Encapsulation and Targeted Delivery of Metallic Species for Biomedical Imaging via Functionalised Carbon Nanotubes Nanocarriers

Hu, Zhiyuan

Award date:
2013

Awarding institution:
University of Bath

Encapsulation and Targeted Delivery of Metallic Species for Biomedical Imaging via Functionalised Carbon Nanotubes Nanocarriers

Zhiyuan Hu

A thesis submitted for the degree of Doctor of Philosophy
University of Bath
Department of Chemistry
April 2012

Declaration

The work presented in this thesis was carried out in the Department of Chemistry between October 2008 and March 2012, under the supervision of Sofia I. Pascu. All of the work is my own unless otherwise indicated, and has not been submitted previously for any other degree at this or any other University.

Zhiyuan Hu
16 April 2012

Abstract

This thesis focuses on designing and synthesis of novel molecular imaging probes based on non-covalent funtionalisation of pure single-walled carbon nanotubes (SWNTs). Several synthetic strategies for the supramolecular chemistry functionalisation of SWNTs, cytotoxicity measurements and cellular imaging of supramolecularly functionalised carbon nanotube probes are discussed.

Chapter one is a literature review as the thesis Introduction. This describes aspects of the physical and chemical properties, structural importance and synthesis methods of single-walled carbon nanotubes (SWNTs), also opens the discussion of the different functionalisation methods to enhance the solubility and biocompatibility of SWNTs for biomedical applications. Several approaches for the design of functionalisation SWNTs for molecular imaging reported in the current literature are highlighted. Techniques and facilities for accessing cell imaging ability and behavior of these synthesized molecular imaging probes, including confocal laser scanning microscopy (CLSM) and fluorescence-lifetime imaging microscopy (FLIM) are described briefly.

Chapter two explores the synthesis of specifically designed naphthalene diimide (NDI). These molecules are known to form 3 dimensional (3D) helical organic nanotubes through hydrogen bonding. In this work an iodine-tagged NDI was allowed to self-assemble onto the surface of SWNTs. The cavities of the NDI organic nanotubes can accommodate SWNTs strands in their hydrophobic interior as observed high-resolution transmission electron microscopy (HR TEM). A new hybrid material, NDI@SWNT, was prepared and characterised as dispersed in organic solvents and aqueous media and in the solid state by HR TEM, tapping mode atomic force microscopy (TM AFM), scanning electron microscopy (SEM), circular dichroism,

Raman and fluorescence spectroscopies (steady-state single and two-photon techniques).

These measurements indicate that amino acid-functionalised NDI interacts strongly with SWNTs in dispersions and forms a donor-acceptor complex denoted NDI@SWNT. The interaction of this nanohybrid with cancer cells was explored using fluorescence microscopies.

Chapter three describes the synthesis of series of molecular imaging agents based on two cancer targeting peptides (bombesin and RGDfK). Two types of NDI-peptide conjugates (Iodine-tagged NDI-Bombesin and Tryptophan-NDI-RGDfK) were designed and synthesized through EDC-coupling method. New compounds synthesized were characterised by mass spectroscopy and also HPLC. Fluorescence lifetime imaging microcopy and confocal laser scanning microscopy were utilised for investigating cellular behaviors (stability, fluorescence intensity and localization) of these molecular imaging probes.

Chapter four describes the synthesis of amphiphilic conjugated thiophenes (dodecathiophene, denoted as T12). In this system, the thiophene backbone structure was chosen as a biocompatible coating for carbon nanotubes as simple molecular mechanics modeling suggested that it would be perfectly fitted to the curvature of SWNTs. T12 showed very good capability for debundling of SWNTs and forming corresponding solution dispersions of T12@SWNTs describes the potential of T12@SWNTs as a stable fluorescent bioimaging nano-probe for tracking cancer cells.

Chapter five describes the successful filling of SWNTs with Cu^{2+} by radiochemistry methods (using "hot" ^{64}Cu ions anchored onto NaOAc) and also by a "cold" optimised procedure for excess $Cu(OAc)_2$. Filling with other metal ions was also tested, for example $KReO_4$ and $Zr(OAc)_4$. The filling experiments with $Zr(OAc)_4$

in solution did not prove successful at normal pH but results were promising when pH was adjusted to *ca.* 2 by adding H_2SO_4. Any significant leakage of metal ions from open SWNTs was avoided by a simultaneous encapsulation of C_{70} molecules at the ends of SWNTs. Functionalisation of SWNTs by the supramolecular wrapping the surface of SWNTs in aqueous media with a naturally occurring glucan (*β*-1,3-1,4-D-glucan, denoted here as *β*-D-glucan) was also explored. Several boronic acid fluorophores were successfully synthesized and tested for the labeling of *β*-D-glucan @SWNTs by molecular recognition between boronic acids and this polysaccharide. Their cellular translocation behaviour and fluorescence properties were investigated by confocal fluorescence imaging and fluorescence lifetime imaging. Both methods show that localisation in sub-cellular (MCF-7 cells) regions and that the glucan coating significantly enhances the cell membrane translocation of SWNTs.

Chapter six reports an efficient and economical strategy of supramolecular complex formulation of thermally reduced graphene. Naphthalene diimide (NDI) was used to form a stable and energy transfer complex which showed efficient quenching and significant red-shift of fluorescence of NDI when adsorbed onto graphene surfaces. The effect of thermally reducing annealing procedure to convert graphene oxides in graphene-nanoflake like materials was investigated. A new hybrid material (denoted here as NDI@TRG) synthesized was characterised by transmission electron microscopy (TEM), Raman spectroscopy, thermogravimetric analysis (TGA) and fluorescence microscopy in the dispersed phase

Chapter seven contains full experimental details for the work described in this thesis.

The Appendix contains details of the crystallographic data and supplementary information on cell imaging photos and fluorescence lifetime point decay data for SWNT nanocomposites.

献给我的父母，还有我伟大的祖国，灿烂的中华传统文明！

Acknowledgements

Firstly, I would like to gratefully acknowledge Dr Sofia I. Pascu who has given me her support and guidance and made this project successful. She has provided the most inspiring and enthusiastic supervision throughout my time here in Bath.

I very much appreciate to Prof. Paul Raithby and members in his group for the warm atmosphere of the lab. I also extend huge thanks you to G. Dan Pantos, Tony James, Rex M. Tyrrell, Julia Zhong, John Fossey and Rory L. Arrowsmith, and especially to Steve Flower for invaluable expertise in glucan boronic acid binding. Dr. Gabriele Kociok-Köhn is acknowledged for crystallography and Dr Adrian Rogers supported cell imaging work, Dr John Mitchels supported for SEM, TEM and AFM at Bath. Dr Justin O'Byrne helped with microscopy and proof-reading of the manuscripts.

The ORS is acknowledged for funding and University of Bath for financial support throughout my three and a half years.

I would like to acknowledge Dr. Stan Botchway and Dr. Pierre Burgos for measuring samples for me at the Laser Facilities at the Rutherford Appleton Laboratory providing the necessary microscope facilities to carry out these studies.

Finally, I thank my friends, families who have provided unstinting support in my study. Now it is the time to break the silence and say 'thank you' very much.

Zhiyuan Hu
Bath
April 2012

Abbreviations

a.u.	Arbitrary units
ACN	Acetonitrile
AFM	Atomic force microscopy
BB3-R	Bombesin subtype-3 receptor
BBN	Bombesin
CD	Circular dichroism
CVD	Chemical vapour deposition
D band	"Diamond" band characteristic of sp^3 carbon
DCC	1,3-Dicyclohexylcarbodiimide
DFT	Density functional theory
DMF	*N,N*-Dimethylformamide
DMF	*N,N*-Dimethylformamide
DMSO	Dimethyl Sulfoxide
ECM	Extracellular matrix
EDC	1-Ethyl-3-(3-dimethylaminopropyl)carbodiimide hydrochloride
EDS	Energy-dispersive X-ray spectroscopy
EMEM	Eagle's minimal essential medium
FBA	Fluorescein boronic acid
Fek-4	Normal human dermal fibroblasts
FLAB	Biotin-tagged fluorescein boronic acid
FLIM	Fluorescence lifetime imaging microscopy
FMCA	Ferrocene monocarboxylic acid
FTIR	Fourier transform infrared spectroscopy
G band	"Graphite" band characteristic of sp^2 carbon
GRP-R	Gastrin-releasing peptide receptor
HiPco	High pressure CO
HOPG	Highly oriented pyrolytic graphite
HRTEM	High-Resolution transmission electron microscopy
IR	Infrared
MBHA	Methylbenzhydrylamine
MCF	Human breast adenocarcinoma cell line
MI50	Concentration that reduces cell metabolism to half that of untreated cells
MTT	3-(4,5-dimethylthiazol-2-yl)-2,5-diphenyl tetrazolium bromide
MWNT	Multi-walled carbon nanotube
NDI	naphthalene diimide
NHS	*N*-Hydroxysuccinimide
NMR	Nuclear magnetic resonance
NMR	Nuclear magnetic resonance
PBS	Phosphate-buffered saline
PET	Positron emission tomography
RBM	Radial breathing mode
RGD	Arginine-glycine-aspartic acid
SAED	Selected area electron diffraction
SDS	Sodium dodecyl sulfate

SEM	Scanning Electron Microscopy
SFM	Serum free medium
SIESTA	Spanish Initiative for Electronic Simulations with Thousands of Atoms
SPG	β-1,3-D-glucan schizophyllan
SWNT	Single wall carbon nanotube
TEM	Transmission electron microscopy
UV	Ultraviolet

List of compounds

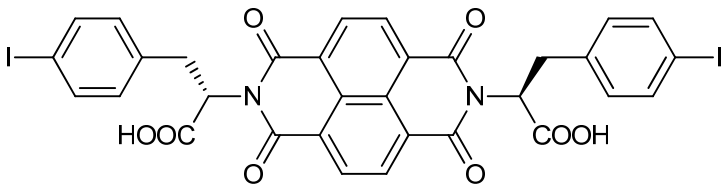

1

Chemical Formula: $C_{32}H_{20}I_2N_2O_8$
Exact Mass: 813.93
Molecular Weight: 814.32
m/z: 813.93 (100.0%), 814.93 (35.3%), 815.94 (7.6%), 816.94 (1.2%)

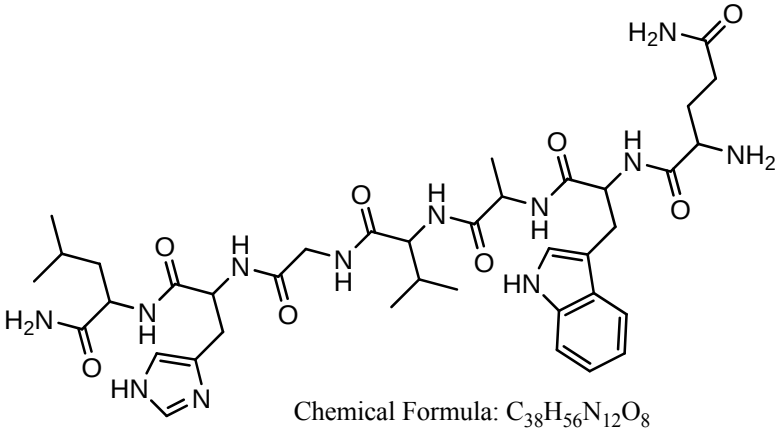

2

Chemical Formula: $C_{38}H_{56}N_{12}O_8$
Exact Mass: 808.43
Molecular Weight: 808.93
m/z: 808.43 (100.0%), 809.44 (42.0%), 810.44 (10.3%), 809.43 (4.4%), 811.44 (2.2%), 810.43 (1.9%)

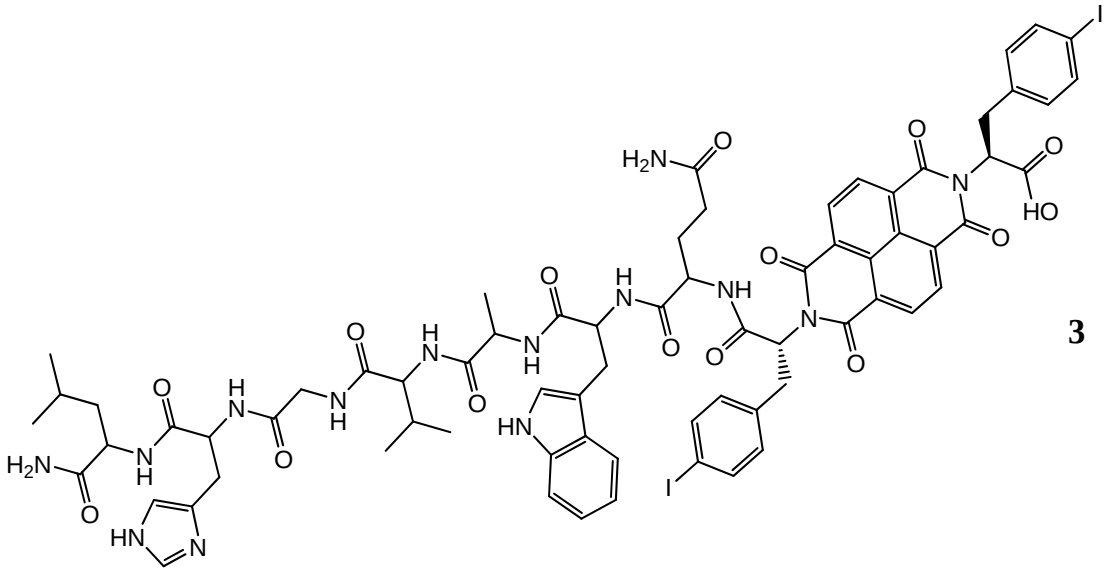

3

Chemical Formula: $C_{70}H_{74}I_2N_{14}O_{15}$
Exact Mass: 1604.35
Molecular Weight: 1605.23
m/z: 1604.35 (100.0%), 1605.36 (77.1%), 1606.36 (36.4%), 1607.36 (11.0%), 1605.35 (5.2%), 1608.37 (2.2%)

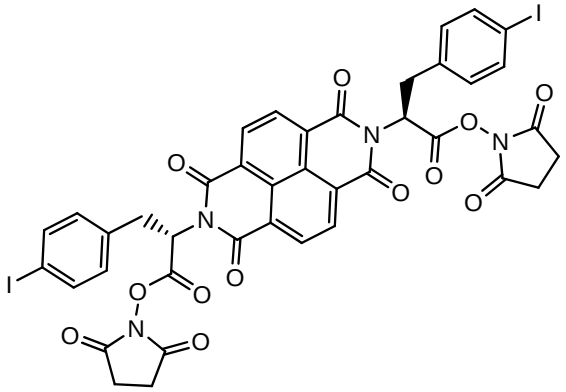

4

Chemical Formula: $C_{40}H_{26}I_2N_4O_{12}$
Exact Mass: 1007.96
Molecular Weight: 1008.46
m/z: 1007.96 (100.0%), 1008.97 (44.0%), 1009.97 (11.9%), 1010.97 (2.5%), 1008.96 (1.5%)

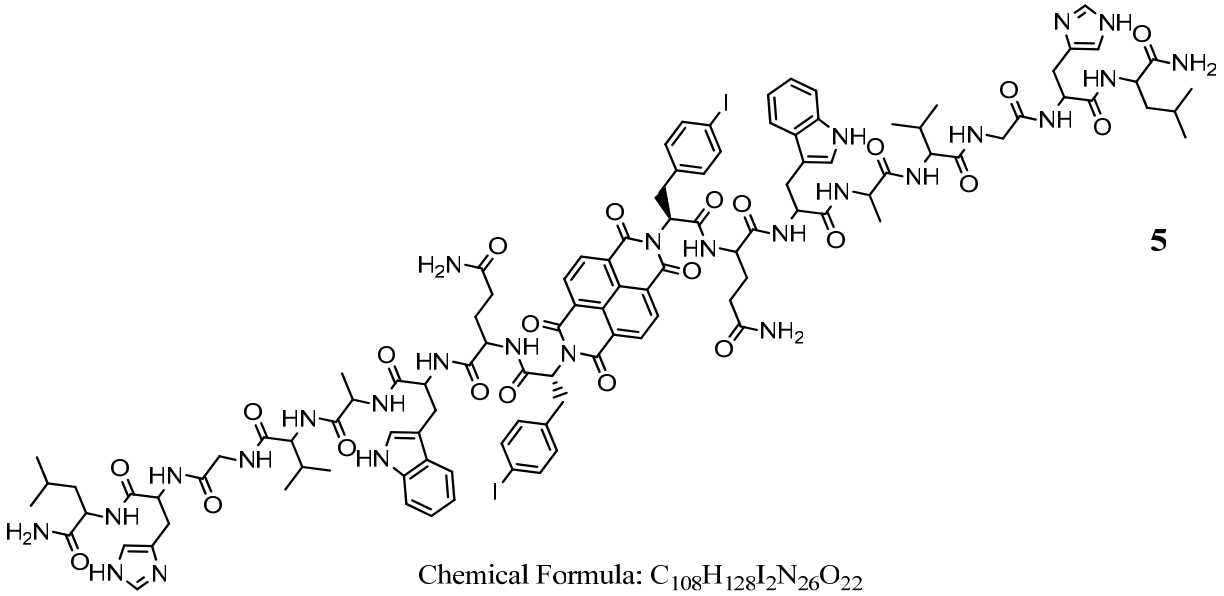

5

Chemical Formula: $C_{108}H_{128}I_2N_{26}O_{22}$
Exact Mass: 2394.78
Molecular Weight: 2396.14
m/z: 2395.78 (100.0%), 2394.78 (77.7%), 2396.79 (54.6%), 2397.79 (25.6%), 2396.78 (12.4%), 2398.79 (10.7%), 2397.78 (5.9%), 2399.79 (1.8%), 2399.80 (1.4%)

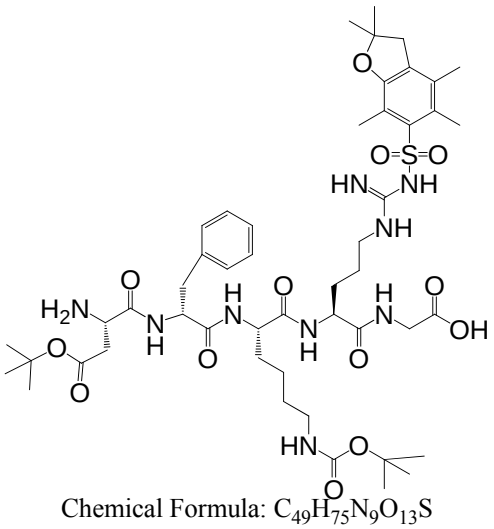

6

Chemical Formula: $C_{49}H_{75}N_9O_{13}S$
Exact Mass: 1029.52
Molecular Weight: 1030.24
m/z: 1029.52 (100.0%), 1030.52 (57.6%), 1031.53 (14.5%), 1031.52 (9.5%), 1032.53 (4.1%), 1032.52 (3.1%)

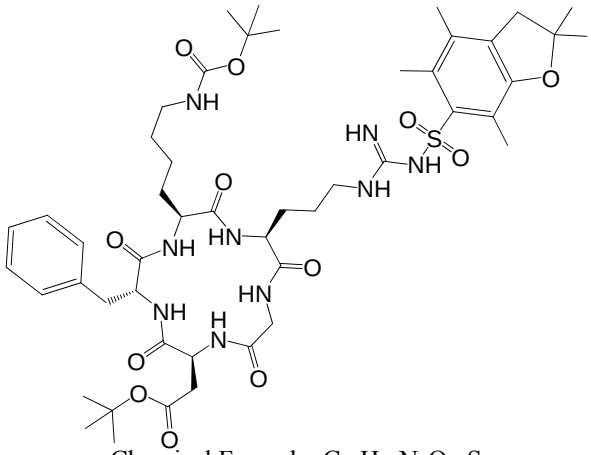

7

Chemical Formula: $C_{49}H_{73}N_9O_{12}S$
Exact Mass: 1011.51
Molecular Weight: 1012.22
m/z: 1011.51 (100.0%), 1012.51 (57.6%), 1013.52 (14.5%), 1013.51 (9.2%), 1014.52 (4.0%), 1014.51 (3.1%)

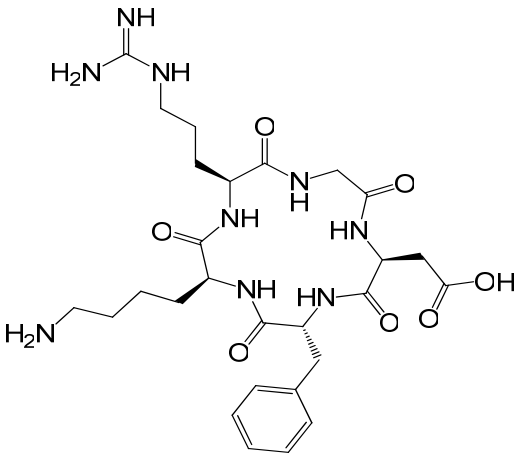

8

Chemical Formula: $C_{27}H_{41}N_9O_7$
Exact Mass: 603.31
Molecular Weight: 603.67
m/z: 603.31 (100.0%), 604.32 (29.9%), 605.32 (5.8%), 604.31 (3.3%), 605.31 (1.0%)

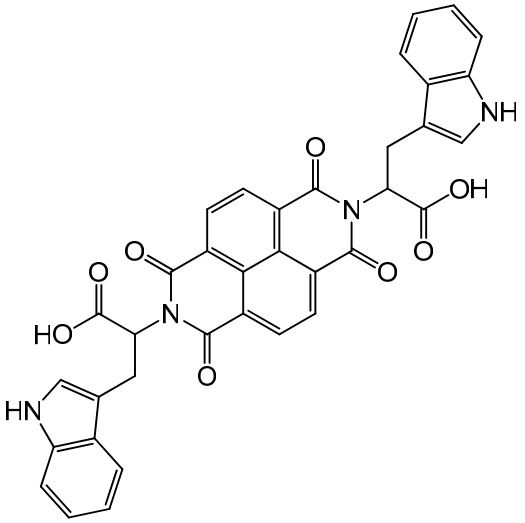

9

Chemical Formula: $C_{36}H_{24}N_4O_8$
Exact Mass: 640.16
Molecular Weight: 640.60
m/z: 640.16 (100.0%), 641.16 (40.7%), 642.17 (7.6%), 642.16 (2.2%), 643.17 (1.6%)

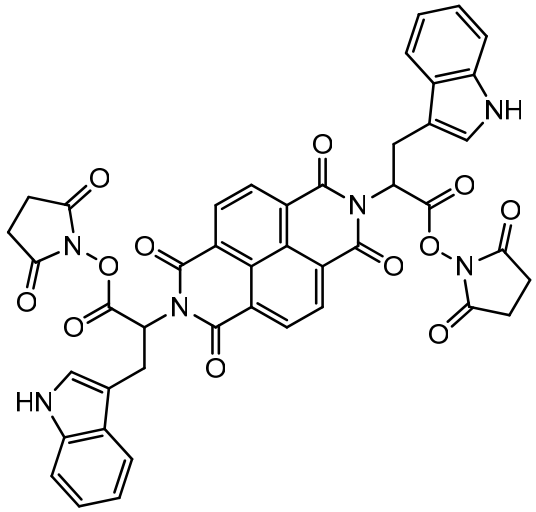

10

Chemical Formula: $C_{44}H_{30}N_6O_{12}$
Exact Mass: 834.19
Molecular Weight: 834.74
m/z: 834.19 (100.0%), 835.20 (48.4%), 836.20 (13.9%), 837.20 (3.2%), 835.19 (2.2%), 836.19 (1.1%)

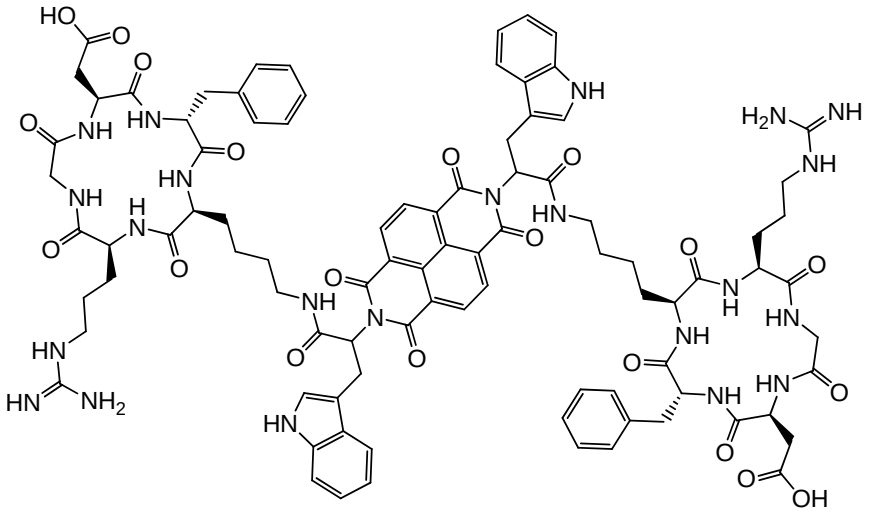

11

Chemical Formula: $C_{90}H_{102}N_{22}O_{20}$
Exact Mass: 1810.76
Molecular Weight: 1811.91
m/z: 1810.76 (100.0%), 1811.77 (99.3%), 1812.77 (53.0%), 1813.77 (23.2%), 1812.76 (8.2%), 1811.76 (8.1%), 1814.78 (5.8%), 1814.77 (1.7%), 1815.78 (1.4%)

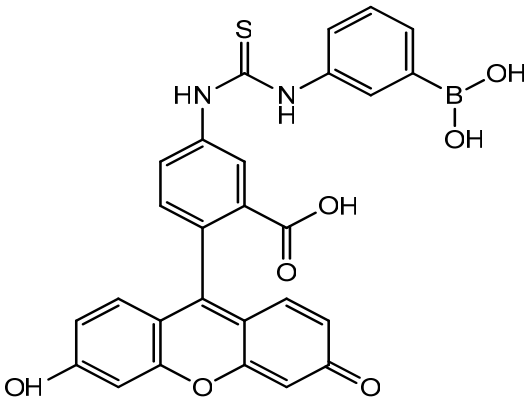

12

Chemical Formula: $C_{27}H_{19}BN_2O_7S$
Exact Mass: 526.10
Molecular Weight: 526.32
m/z: 526.10 (100.0%), 527.10 (32.1%), 525.10 (24.7%), 526.11 (7.3%), 528.10 (6.7%), 528.11 (4.5%), 527.11 (1.7%), 529.10 (1.4%)

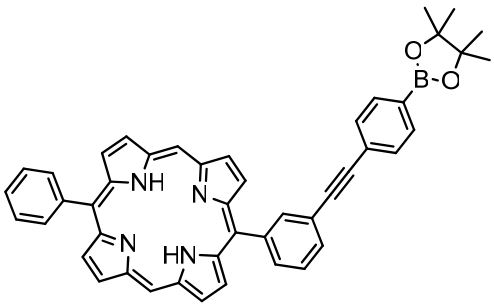

13

Chemical Formula: $C_{46}H_{37}BN_4O_2$
Exact Mass: 688.30
Molecular Weight: 688.62
m/z: 688.30 (100.0%), 689.30 (51.2%), 687.30 (24.8%), 690.31 (13.3%), 688.31 (12.4%), 689.31 (3.7%), 691.31 (2.2%)

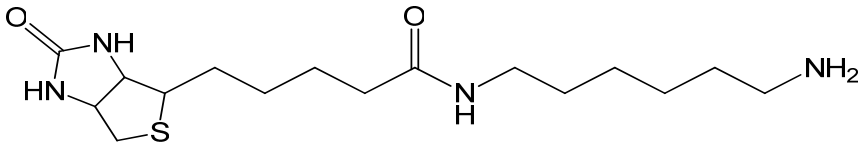

14

Chemical Formula: $C_{16}H_{30}N_4O_2S$
Exact Mass: 342.21
Molecular Weight: 342.50
m/z: 342.21 (100.0%), 343.21 (19.7%), 344.20 (4.5%), 344.22 (1.5%)

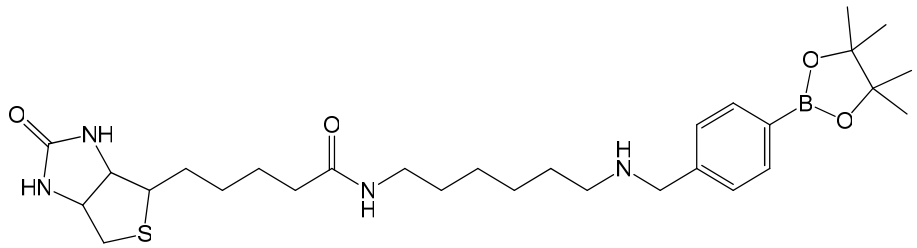

15

Chemical Formula: $C_{29}H_{47}BN_4O_4S$
Exact Mass: 558.34
Molecular Weight: 558.58
m/z: 558.34 (100.0%), 559.34 (34.6%), 557.34 (24.7%), 558.35 (7.9%), 560.35 (6.0%), 560.34 (5.6%), 559.35 (2.3%), 561.34 (1.6%)

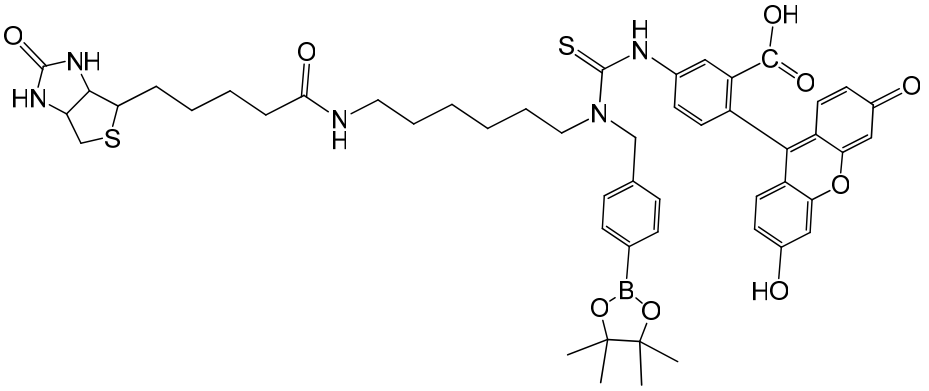

16

Chemical Formula: $C_{50}H_{58}BN_5O_6S_2$
Exact Mass: 947.38
Molecular Weight: 947.96
m/z: 947.38 (100.0%), 948.38 (52.3%), 946.38 (21.7%), 949.38 (17.1%), 949.37 (8.0%), 950.38 (6.1%), 948.39 (3.2%), 950.39 (2.5%), 948.37 (1.6%), 951.38 (1.5%), 949.39 (1.2%)

Table of Contents

Chapter 1 Introduction to functionalised carbon nanotubes……..…… 1

1.1 Introduction…….……. 1

1.2 Single-walled nanotubes (SWNTs)…….. 2

1.3 Structure……..….. 2

1.3.1 Bonding of Carbon Atoms……..… . 2

1.4 Synthesis…….…..… 4

1.4.1 Arc discharge……..…. 4

1.4.2 Laser ablation……..…… 6

1.4.3 Chemical vapour deposition (CVD)……..…….…… 7

1.5 Chemically Functionalised Carbon Nanotubes……. 8

1.5.1 Covalent Methods for modification……..9

1.5.2 Covalent attachment polymers with CNT……..... 12

1.5.2.1 "Grafting to" Method ……12

1.5.2.2 "Grafting from" Method……...… 13

1.5.3 Non-covalent Interactions……..….. 14

1.5.3.1 Glucans as coating materials for SWNTs……..… 16

1.5.3.1.1 Interaction between boronic acids and diols……..…. . 18

1.5.4 Introduction to Filling SWNTs……...….20

1.6 Application of SWNTs in molecular imaging…….……22

1.6.1 Optical imaging using functionalised SWCNTs…….……24

1.6.2 PET and SPECT imaging using functionalised SWCNTs……...25

1.7 Fluorescence spectroscopy……..29

1.7.1 Confocal laser scanning microscopy (CLSM or LSCM) ……...30

1.7.2 Fluorescence-lifetime imaging microscopy (FLIM)……... 31

1.7.2.1 Fluorescent lifetime……....31

1.7.2.2 Time-correlated single-photon counting……..32

1.7.2.3 Applications…….33

1.7.2.3.1 Calcium Ion Concentration Imaging …….33

1.7.2.3.2 Fluorescence Resonance Energy Transfer (FRET) ……...33

1.8 Summary…….34

1.9 References for in troduction …….. 35

Chapter 2 Interactions between amino acid-tagged naphthalenediimide and single walled carbon nanotubes for the design and construction of new bioimaging probes

..……. ……. 43

2.1 Introduction……..43

2.2 Results and Discussions……...45

2.2.1 Synthesis, single crystal X-ray diffraction and molecular modelling of iodine tagged Naphthalenediimides (NDI)……45
2.2.2 Spectroscopic characterization of NDI@SWNT composite……53
2.2.3 Solid state investigations by HR TEM, AFM and SEM……..62
2.2.4 Multiphoton fluorescence imaging of NDI@SWNT in solution and in vitro…….65
2.2.5 Cellular translocation monitoring of NDI@SWNT by MTT assays…….…..75
2.3 Conclusions for Chapter 2 ……..……..…78
2.4 Reference for Chapter 2…….……80
Chapter 3 Synthesis of tumour targeting peptide tagged naphthalenediimide derivatives and their supramolecular complexes with SWNTs …...……. 84
3.1 Introduction……84
3.2 Results and Discussion……89
3.2.1 Synthesis of NDIBBN.....……89
3.2.1.1 Bombesin(7-13) analogue……89
3.2.1.2 Two routes for synthesizing NDIBBN conjugate…….……..89
3.2.1.3 Confocal fluorescence microscopy imaging…….…...92
3.2.1.4 Cytotoxicity of NDIBBN derivatives (compounds **3** and **5**) on fibroblast cells and prostate cancer PC-3 cell line……..…….…….93
3.2.1.5 Fluorescence lifetime microscopy imaging……....95
3.2.2 Synthesis and characterisation of **3**@SWNTs complex……96
3.2.2.1 Highly clear wall surface of Single carbon nanotubes for biomedical functionalisation …… .97
3.2.2.2 Complex of **3** with SWNTs……98
3.2.2.3 Laser scanning confocal imaging and life-time imaging of compound **3**@SWNTs in cells…….....105
3.2.3 Synthesis of tryptophan-NDI-cyclo-(RGDfK) conjugate for biomedical imaging...110
3.2.3.1 Synthesis, single crystal X-ray diffraction determination of tryptophan-NDI……..110
3.2.3.2 Confocal fluorescence microscopy imaging……..112
3.2.3.3 Fluorescence lifetime microscopy imaging……...113
3.3 Conclusion for Chapter 3…..…….116
3.4 Reference for Chapter 3…..……...118
Chapter 4 Synthesis of individual polythiophene functionalised single walled carbon nanotubes as prominent fluorescent nanoprobes for cellular imaging …..…….121
4.1 Introduction……121
4.2 Results and Discussion……..125
4.2.1 Characterizations of T12@SWNT dispersions……..125
4.2.1.1 Absorption spectroscopy and fluorescence spectroscopy……..125
4.2.1.2 Raman Spectroscopy……..128

4.2.1.3 Surface analysis of T12@SWNTs complex……..128

4.2.1.4 Confocal fluorescence microscopy imaging…….…….133

4.2.1.5 In vitro and in solution FLIM studies……136

4.2.1.6 Diffusion-ordered 2D NMR (DOSY) as a tool for analysis of functionalisation of SWNTs ……...140

4.3 Conclusion for Chapter 4…..…….142

4.4 Reference for Chapter 4…...……..144

Chapter 5 Radio-metal filled and fluorescent SWNTs as synthetic platforms for multimodal imaging systems…….…….. ……147

5.1 Introduction ……..147

5.2 Purification and Opening of Carbon Nanotubes Using Steam……...152

5.2.1 Supramolecular nanoprobe scaffold C_{70}@ M@SWNT synthesis……...152

5.2.2 Supramolecular wrapping of the filled carbon nanotubes surface:M@C_{70}@SWNT@glucan synthesis…….....159

5.2.3 Biocompatibility and proliferation effects of β-D-glucan and β-D-glucan@SWNTs towards fibroblast cells…….....162

5.2.4 Reversible covalent chemistry for the attachment of targeting units or fluorophors: Hierarchical nanoprobes flurophor@glucan@M@SWNT synthesis

…….…..165

5.2.5 PET Imaging tracer preparation by radioisotope filling using ^{64}Cu radioactivity encapsulation …….....173

5.3 Conclusion for Chapter 5…..……....176

5.4 References for Chapter 5…..……...……..177

Chapter 6 Synthesis of thermally reduced graphene oxide and of its amino acid naphthalene diimide complex …...……..……182

6.1 Introduction……182

6.2 Results and Discussion……..183

6.3 Conclusion for Chapter 6..…….190

6.4 References for Chapter 6…..……..190

Chapter 7 Experimental details…….. 193

7.1. Instrumentation……...193

7.1.1 Raman spectrometer……..193

7.1. 2 Transmission electron microscope (TEM) with energy dispersive X-ray (EDS) analysis……193

7.1.3 Ultrasonic bath……...193

7.1.4 Scanning electron microscopy (SEM) ……..194

7.1.5 Fluorescence lifetime imaging microscopy (FLIM)……..194

7.1.6 Atomic Force Microscopy (AFM)……195

7.1.7 UV/vis……195

7.1.8 NMR spectra……196
7.2 Materials……196
7.2.1 Chemicals……...196
7.2.2 Glassware……..….197
7.3 Methods……..…197
7.3.1 TEM sample preparation…….…..197
7.3.2 Preparation of amino acid-Tagged Naphthalenediimide functionalised Single Walled Carbon Nanotubes…….…….…197
7.3.2.1 Synthesis of NDI ((2S,2'S)-2,2'-(1,3,6,8-tetraoxobenzo[lmn][3,8]phenanthroline-2,7(1H,3H,6H,8H)-diyl)bis(3-(4-iodophenyl)propanoic acid)) (**1**)……...197
7.3.2.2 Crystal structure determination……..……198
7.3.2.3 Computational methods…….……200
7.3.2.4 Cell culture (FEK-4, MCF-7 and HeLa) and fluorescence imaging……..202
7.3.2.5 In vitro fluorescence lifetime imaging (FLIM)…….204
7.3.2.5 Cell viability tests in FEK-4 and MCF-7 cell lines by MTT assays ……204
7.3.2.6 Epifluorescence Microscopy…….……205
7.3.2.7 MTT assays for MI50 determinations……...205
7.3.2.8 Calculate Fluorescence Quantum Yields of NDI……..……206
7.3.2..9 Staining for nuclear Co-localisation studies…….207
7.3.3 Synthesis of Bombesin-Naphthalenediimide conjugate functionalised Single Walled Carbon Nanotubes ……..208
7.3.3.1 Reagents……208
7.3.3.2 Equipment…….208
7.3.3.3 Reagent setup……208
7.3.3.4 Semi-preparative HPLC system…….208
7.3.3.5 Flow gradient for semi-preparative HPLC……....209
7.3.3.6 Synthesis of bombesin(7-13) peptide (**2**)…….…....209
7.3.3.7 Swelling the resin ……..210
7.3.3.8 Deprotection…….……..210
7.3.3.9 Kaiser-test…….……..211
7.3.3.10 Coupling……211
7.3.3.11 Loading efficiency of the first amino acid to the resin…….....211
7.3.3.12 Synthesis of Naphthalene diimide-Bombesin Conjugates……...…….213
7.3.3.12.1 Method 1: The first route to the synthesis of Naphthalene diimide-Bombesin Conjugates(mono-substituted Naphthalene diimide-Bombesin)(**3**)…...……213
7.3.3.12.2 Method 2: The second route to the synthesis of Naphthalene diimide-Bombesin Conjugates(double-substituted Naphthalene diimide-Bombesin)(**5**)…….…….215
7.3.3.12.2.1Synthesis of NDI-OSu(**4**)……..……...215
7.3.3.12.2.2 Synthesis of Naphthalene diimide-Bombesin Conjugates by coupling of NDI-

OSu with bombesin(7-13) (**5**) ……216

7.3.3.12. 3 Isolation of mono-substituted NDI-Bombesin and double-substituted NDI-Bombesin from impurities by (semi)Preparative HPLC……218

7.3.3.13 Preparation of **5**@SWNT complex, denoted as NDIBBN@SWNT.....218

7.3.3.14 Fluorescence imaging of NDI-Bombesin and NDI-Bombesin@SWNTs.....219

7.3.4 Synthesis of RGDfK-Naphthalenediimide conjugate……220

7.3.4.1 Synthesis of linear RGDfK(Arg(Pbf)-Gly-Asp(OtBu)-D-Phe-Lys(Boc)) (**6**)…..…220

7.3.4.2 Cyclisation of protected RGDfK peptide (Cyclo(-RGDfK), **7**)……222

7.3.4.3 Cyclic deprotected RGDfK peptide (**8**)…… 222

7.3.4.4 Synthesis of tryptophan-NDI (TNDI) (**9**) ……224

7.3.4.5 Synthesis of tryptophan-NDI-OSu (TrypNDI-OSu) (**10**)…… 226

7.3.4.6 Synthesis of Trypotophan-tagged naphthalene diimide-RGDfK conjugates **11** by coupling reaction…… 227

7.3.5 Functionalisation of SWNTs with a dodecathiophene (denoted T12)……...229

7.3.5.1 Materials……229

7.3.5.2 Preparation of T12@SWNT nanohybrid……...229

7.3.5.3 Cell culture and fluorescence imaging……..230

7.3.6 Preparation of metal radiopharmaceuticals filling and biocompatible fluorescent material coating Carbon Nanotubes……230

7.3.6.1 Buffer and Solvents……...230

7.3.6.2 Purification of SWNTs by steaming (Figure 7.14)……..……230

7.3.6.3 "Cold" filling steam-purified SWNTs using the precursors: $Cu(AcO)_2$, $KReO_4$ and $Zr(OAc)_4$……..…232

7.3.6.3.1 Filling with Copper Acetate ……..232

7.3.6.3.2 Filling with Zirconium Acetate $Zr(OAc)_4$……..232

7.3.6.3.3 Filling with Potassium Perrhenate $KReO_4$……...233

7.3.6.4 Synthesis of fuorescein-5-[thioureidyl-(3-phenylboronic acid)] (FBA) (Scheme 7.10)(**12**)…….…233

7.3.6.5 Synthesis of porphyrin-boronic acid (Scheme 7.11) (**13**)……..234

7.3.6.6 Synthesis of FLAB (**16**) (Scheme 7.12)……236

7.3.6.7 Fluorescence Titrations of boronic acid fluorophors FLAB, FBA, Coumarin- and porphyrin-boronic acid and β -D-glucan…….238

7.3.6.8 Titration Data Analysis……..238

7.3.6.9 Boronic acid fluorophore binding with β-D-glucan, β-D-glucan@SWNTs or β-D-glucan@metalical atom@SWNT.....239

7.3.6.10 Preparation of glucan-wrapped SWNTs and encapsulation of radio-metal ions from aqueous media……....240

7.3.6.11 Cells fluorescence imaging and In vitro fluorescence lifetime imaging (FLIM) of Fluorophore@glucan@SWNTs.....243

7.3.7 Synthesis of a thermal reduced graphene oxide-amino acid naphthalene diimide

complex……...245
7.3.7.1 Graphene oxide synthesis, thermal exfoliation and reduction of GO to give TRG.. 245
7.3.7.2 Synthesis of the complex NDI@TRG.....246
7.3.7.3 Thermogravimetric analysis (TGA)……..246
7.4 References to Chapter 7……246
Appendix…… I

Chapter 1 Introduction to functionalised carbon nanotubes

1.1 Introduction

The first objective is to introduce single walled carbon nanotubes (SWNTs) and discuss their physical and chemical properties, structural importance and synthesis methods. The applications of SWNTs in biomedicine with particular focus on their use as targeted drug delivery and molecular imaging will be highlighted. Several different functionalisation methods used to enhance the solubility and biocompatible of SWNTs for biomedical application are also discussed. The final goal of this chapter is introduce several biocompatible compounds related to those used for encapsulating SWNTs within this research.

1.2 Single walled carbon nanotubes (SWNTs)

Since the discovery of carbon nanotube (CNT) by Iijima,[1] many researchers and scientists from different groups all over the world have been attracted to this material and a large number of studies have been carried out to forward potential applications in electricity, advanced material and medicine.

CNTs were first synthesized as a by-product in the synthesis of fullerenes by using an arc-discharge method, and from this method also several other procedures were then derived,[1-7] including laser ablation[8-10] and catalytic decomposition of hydrocarbon.[11-14] Considering the great effort scientists spent on studying on these materials and given the distinctive electrical, mechanical and chemical properties, CNTs could become one of the most important and promising materials in the 21st century. CNTs can be classified into two

categories: One is multi walled carbon nanotubes (MWNTs)[1,7]and the other single walled carbon nanotubes (SWNTs).[1] The MWNTs had been discovered first. An MWNT is comprised of 2 to 30 concentric graphitic layers, diameters of which range from 10 to 50 nm and length of more than 10 pm. On the other hand, SWNTs are much thinner, with the diameters from 1.0 to 1.4 nm. However, the low solubility and the rapid formation of bundles when dispersed in most common solvents have been the obstacle of forwarding for industrial applications. Indeed, as-produced CNT are insoluble in all organic solvents and aqueous solutions. They can be dispersed in some solvents by sonication, but precipitation immediately occurs when this process is interrupted. On the other hand, it has been demonstrated that CNT can interact with different classes of compounds on the aromatic surface of CNT. The formation of supramolecular complex gives the hope for fabricating innovative nanodevices.

1.3 Structure

1.3.1 Bonding of carbon atoms

To understand the structure and properties of nanotubes, the bonding structure and properties of carbon atoms are discussed hereby. A carbon atom has six electrons with two of them filling the 1*s* orbital. The remaining four electrons fill the sp^3 or sp^2 as well as the *sp* hybrid orbital, responsible for bonding structures of diamond, graphite, nanotubes, or fullerenes. A SWNT can be visualised as a hollow cylinder, formed by rolling over a graphite sheet by specified as vector *C* in terms of a set of two integers (n, m) corresponding to graphite vectors $\mathbf{a}_1$ and $\mathbf{a}_2$ (Figure 1.1) ,

$$C = n\mathbf{a}_1 + m\mathbf{a}_2 \qquad (1.1)$$

Where C is the chiral vector, n and m are integers, and $\mathbf{a} = |\mathbf{a}_1| = |\mathbf{a}_2|$ is lattice constant of graphite. The tubes with m = n are commonly referred to as armchair tubes and m = 0 as zigzag tubes. Others are called chiral tubes in general with the chiral angle, θ is defined as the angle between the vector C and the zigzag direction $\mathbf{a}_1$,

$$\theta = \tan^{-1}[3^{0.5} m/(m+2n)] \qquad (1.2)$$

θ ranges from 0 for zigzag (m = 0) and 30° for armchair (m = n) tubes.

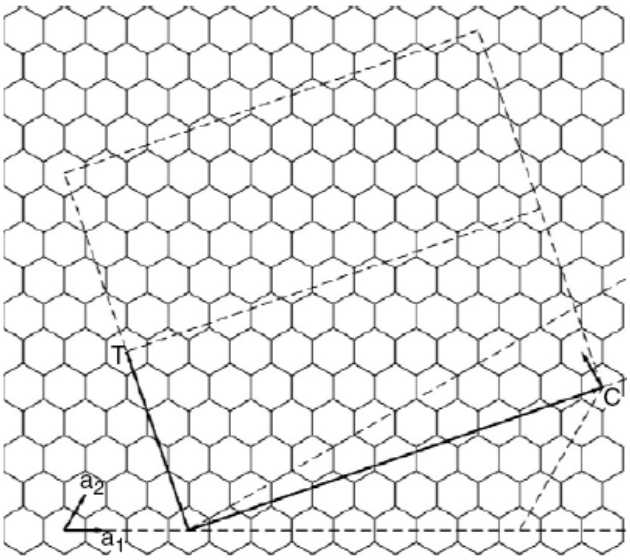

Figure 1.1. A nanotube (n, m) is formed by rolling a graphite sheet along the chiral vector $C = n\mathrm{a}_1 + m\mathrm{a}_2$ on the graphite where a_1 and a_2 are graphite lattice vector. The picture is reproduced from the paper.[15]

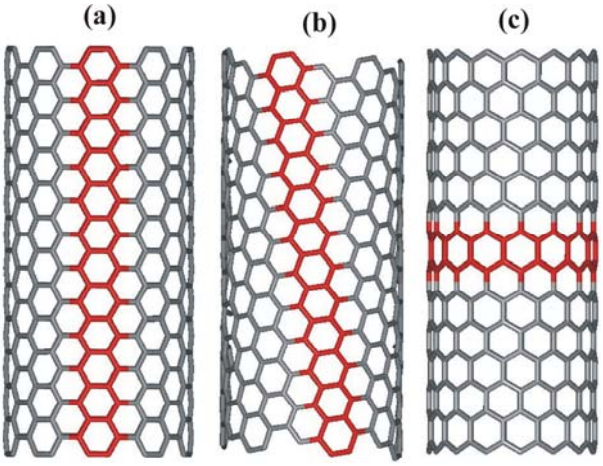

Figure 1.2. Different types of SWNT formed by rolling a graphite sheet in different directions, two typical nanotubes can be obtained: zigzag[16], armchair (m, m) and chiral (n, m) where n>m>0 by definition. In the specific example, they are (10, 10) (a), (12, 7) (b) and (15, 0) (c) nanotubes. The picture is reproduced from the paper.[15]

The tube chirality parameter (n, m) significantly affect the electronic, optical, magnetic, and other properties of a nanotube. Scanning Tunneling Microscopy (STM) can be used to measure tube geometry charactersied by (d, *θ)* which, in turn, can be used to derive the (n, m) parameters.

1.4 Synthesis

Carbon nanotubes are normally synthesized by three main methods. These are arc discharge, laser ablation and chemical vapor deposition (CVD). Scientists are still searching for more economic routes for scale up synthesis and purification of the new material. In the arc discharge method, carbon nanotubes are created through arc-vaporization of two carbon rods placed end to end with or without catalyst. The rods are separated by approximately 1 mm, in an enclosure that is usually filled with inert gas at low pressure. In the laser ablation technique, a high-power laser beam vaporises a graphite target in a high-temperature reactor filled with inert gas in the chamber. At the moment, laser ablation produces a small amount of clean nanotubes, whereas arc discharge methods generally produce large quantities of impure material. In general, chemical vapor deposition (CVD) results in MWNTs or poor quality SWNTs. The SWNTs produced with CVD have a large diameter range, which can be poorly controlled. But on the other hand, this method is very easy to scale up, shows the most promise for industrial-scale production.[15]

1.4.1 Arc discharge

The carbon arc discharge method initially used for producing C_{60} fullerenes by using a current of 100 amps. However the first macroscopic production of carbon nanotubes using this method was made in 1992 by two researchers at NEC's Fundamental Research

Laboratory.[17] In this method, the carbon in the negative electrode sublimates in the high temperature caused by discharge (Figure 1.3). This technique produces a mixture of components. It is required to separate carbon nanotubes from the soot and also the catalytic metals in the crude product. Because nanotubes were initially discovered using this technique, it has been the most widely-used method of nanotube synthesis. This method produces carbon nanotubes by arc-vaporising of two carbon rods also filled with inert gas (helium, argon) at low pressure (50-700 mbar). Recent research also indicates that producing nanotubes by arc-discharging in liquid nitrogen.[18] A direct current of 50 to 100 A driven by approximately 20 V creates a high temperature discharge between the two electrodes. The discharge vaporises one of the carbon rods and forms a small rod shaped deposit on the other rod. Producing nanotubes in high yield depends on the uniformity of the plasma arc and the temperature of the deposit formed on the carbon electrode.[17]

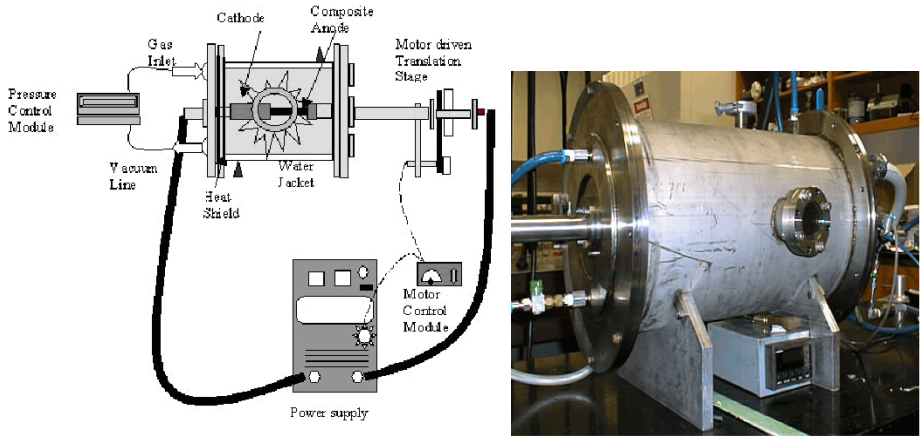

(a) **(b)**

Figure 1.3. Schematic drawings of arc-discharge apparatus (a) for producing SWNTs. Small diameter, single-wall nanotubes can be synthesized in arc chamber (b) using an arc welder to maintain the optimal settings between two horizontal electrodes in helium or argon atmospheres.
(http://www.personal.psu.edu/faculty/p/c/pce3/facilities/arc.htm)

Nanotubes were observed in 1991 in the carbon soot of graphite electrodes during an arc discharge, by using a current of 100 amps, that was intended to produce fullerenes.[16] However the first macroscopic production of carbon nanotubes was made in 1992 by two

researchers at NEC's Fundamental Research Laboratory.[19] During this process, the carbon contained in the negative electrode sublimates because of the high discharge temperatures. It has been the most widely-used method of nanotube synthesis, since nanotubes were initially discovered by this technique. The yield by using this method is up to 30% by weight, including both SWNTs and MWNTs.

1.4.2 Laser ablation for the production of CNTs

This process was developed by Dr. Richard Smalley and co-workers at Rice University in 1995, who at the time of the discovery of carbon nanotubes, were blasting metals with a laser to produce various metal molecules. Upon observation of CNTs formation, they replaced the metals with graphite to create multi-walled carbon nanotubes.[20] The laser vaporisation apparatus used by Smalley's group is shown in Figure 1.4. The graphite target in an oven at 1200 °C is vaporised by a pulsed or continuous laser. The oven is filled with helium or argon gas in order to keep the pressure at 500 Torr. Very hot vapors expand and cool rapidly, and then small carbon molecules and atoms quickly condense to form larger clusters including fullerenes. At the same time, the catalyst also condenses but this process takes place more slowly than the condensation of carbon. Catalysts may form cage structures when they are attached to carbon, then stop carbon nanotube growth. It is believed that tubular carbon structures form around the cage structures and grow into SWNTs, until the whole catalyst particles become too large or there are no carbon atoms that can sufficiently cover the surface of catalyst on cooling. The SWNTs formed in this case are bundled together by *van der Waals* forces.[21]

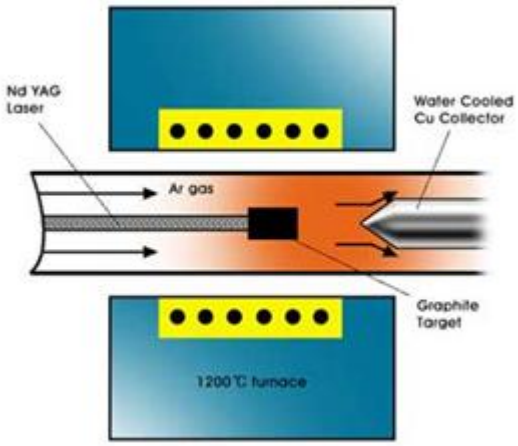

Figure 1.4. Schematic drawing of a laser ablation apparatus.
(http://students.chem.tue.nl/ifp03/synthesis.html)

The optimum gas and catalyst mix is the same as in the arc discharge process, therefore the laser ablation process is similar to the arc discharge: since similar reaction conditions are needed, the chemical transformations probably occur with the same mechanism.

1.4.3 Chemical vapour deposition (CVD) for CNTs synthesis

Carbon nanotubes formed by vapour phase deposition method was first reported in 1993.[22] For CVD method, a layer of metal catalyst particles (nickel, cobalt, iron or a combination) is prepared as a substrate. Also the diameters of nanotubes grown using this method are related to the particles size. Before filling with carbon containing gas, the substrate is heated to approximately 700 °C. Then two types of gases are bled into the reactor: a process gas (such as ammonia, nitrogen or hydrogen) and a carbon-containing gas (such as C_2H_2, CH_4, C_2H_4 and C_2H_6). The carbon-containing gas is broken apart at the surface of the catalyst particle, and the carbon is transported to the edges of the particles, where it forms the nanotubes. In order to promote the yield of carbon nanotubes, scientists mixed the metal nanoparticles with a catalyst support (MgO or Al_2O_3). CVD method has become the most

commercial production of carbon nanotubes because of its low price/unit ratio, and because CVD is capable of growing nanotubes directly on a desired substrate, whereas the nanotubes must be collected in the other growth techniques. Carbon nanotubes products from Baytube Company are produced in a high-yield catalytic process based on chemical vapour deposition. Figure 1.5 shows a schematic diagram of a typical plasma CVD apparatus with a parallel plate electrode structure.

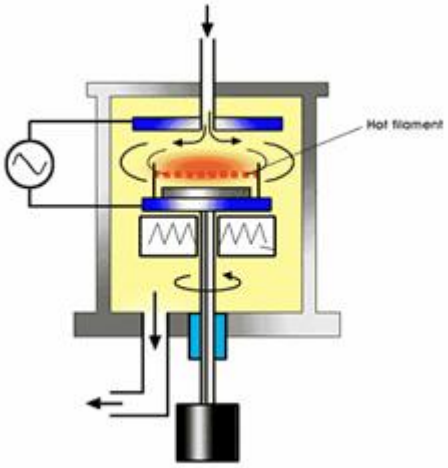

Figure 1.5. Schematic diagram of plasma CVD apparatus (http://students.chem.tue.nl/ifp03/synthesis.html)

1.5 Chemically functionalised carbon nanotubes

SWNTs can severely bundle with each other due to strong *van der Waals* forces and the resulting materials are very difficult to solubilise essentially in any solvent. Insolubility has become the major roadblock forward the potential application of SWNTs due to the difficult to process carbon nanotubes in the liquid state forming devices or complex. Though they can be dispersed in some solvents by using sonication, precipitation happens after a while if there is no continuous sonication applied. Oxidation processing of SWNTs in mixture of concentrated nitric and sulfuric acid is a very important and essential treatment of carbon nanotubes. The final products from this treatment are nanotube fragments. Ends and sidewalls of these 100-300 nm length nanotubes are attached with lots of carboxyl groups.

These abundant carboxyl groups present on carbon nanotubes can be modified again through forming amide and ester bonds for attaching with different functional moieties. The presence of carboxyl groups leads to a reduction of *van der Waals* interactions between the CNTs, which strongly facilitates the separation of nanotube bundles into individual tubes.[23] Additionally, the attachment of suitable groups enhances the solubility in aqueous or organic solvents. A high water solubility of a few tenths of a gram per milliliter has recently been achieved on the basis of the carboxyl-based coupling of hydrophilic polymers such as poly(ethylene glycol) (PEG).[24]

The study of SWNTs and their interaction with different kinds of compound to form supramolecular complexes has been a matter of intense investigation. The most common routes used for modification of these one-dimensional structures can be grouped into two types: The covalent attachment of chemical groups on the aromatic surface of SWNTs. Different kinds of functional molecules (such as polymers) can be non-covalently attached on carbon nanotubes surface through aromatic interactions.

1.5.1 Covalent chemistry methods for surface modification

Direct coupling of functional groups on to the π-conjugated carbon structure are available by thermally activated reactions. Several addition reactions have been published, and these are represented schematically in Figure 1.6.

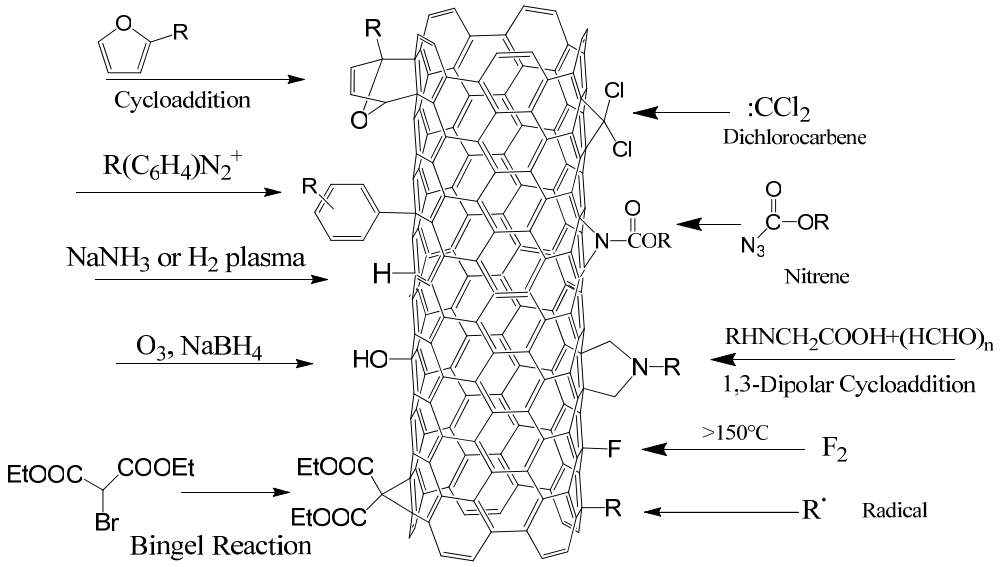

Figure 1.6. Overview of possible addition reactions for the functionalisation of the nanotube sidewall.

Reactions of graphite with elemental fluorine yield several different types of fluorides mainly depending on fluorination temperature. Graphite fluorides $(CF)_n$ and $(C_2F)_n$ with covalent C–F bond are prepared at high temperatures of 350–600 °C.[25] Two possible fluorinated patterns forming two isomers were proposed. One pattern is called the 1,4 isomer which the fluorine atoms occupy the 1,4 positions on every other row of hexagons. Another one is called the 1,2 isomer, i.e. the fluorine atoms occupies the 1,2 positions of the hexagons of alternate rows while the double bonds form a conjugated system along the tube. It has been reported that the 1,4 isomer is more stable than the 1,2 addition pattern.[26] Fluorinated SWNTs can be solvated as individual tubes in various alcohol solvents via ultrasonication. The solubility limit of the solvated fluorinated SWNTs in 2-propanol is at least 1 mg/mL.[27] Terminal alkylidene diamines and OH group-terminated moieties were attached with fluorinated SWNTs through nucleophilic substitution reactions. FTIR, Raman, UV−vis−NIR, SEM/EDS, TEM and TGA analyses were used to determine the sidewall attachment of the N-alkylidene amino groups and hydroxyl groups.[28,29] Hydrogenated SWNTs and MWNTs, as well as graphite were prepared by dissolved metal reduction method in liquid ammonia.

Hydrogenated carbon nanotubes can maintain stable up to 400 °C. Also glow discharge [30-32] or proton bombardment[33] was used for functionalisation of CNT with atomic hydrogen.

Dichlorocarbene has been attached on the surface of carbon nanotubes by stirring in a $CHCl_3$/NaOH mixture or using a phenyl (bromodichloro methyl) mercury reagent (Figure 1.6). The dichlorocarbene-functionalised SWNTs [(s-SWNT)CCl_2] have good solubility in organic solvents such as tetrahydrofuran and dichlorobenzene. The degree of dichlorocarbene functionalisation was from 12% to 23%. The chlorine atoms can be removed by heating treatment above 300°C.[34-36] Organic functionalised of Carbon Nanotubes was described using the 1,3-dipolar cycloaddition of azomethine ylides, prepared remarkably soluble bundles of nanotubes supported by TEM analysis.[37,38] The microwave-induced pyrazoline-modified SWNTs by thermal 1,3-dipolar cycloaddition of nitrile imines was reported by Yubing Wang et al.[39] The 1,3-dipolar cycloaddition of SWNTs was carried out in 15 min under microwave conditions. The final products were characterised by UV−vis, NMR, and FT-IR spectroscopies. The solubility of the functionalised SWNTs in different organic solvents was also observed in Yubing Wang's research work.[39] Molecular dynamics simulations indicated that radicals can be attached on the surface of carbon nanotubes through carbon radicals forming. Diazonium salts have been used to covalently functionalise the sidewall of carbon nanotubes.[37,39,40] Electrochemical reduction of substituted aryl diazonium salts in organic media was used for modification of CNTs.[37,40,41] Electron transfer between CNTs and the aryl diazonium salts leads to the formation of aryl radicals on the surface of CNTs. Confirmation of this type of functionalisation was made easily according to UV−vis spectroscopy. Also Raman spectroscopy and TGA methods suggested that tubes are heavily functionalised. This modification method significantly increased the solubility of CNTs in DMF (0.8 mg/mL). Substituted phenyl groups were attached on the surface of CNT by electrochemical method, in which two types of coupling reactions were proposed, one

was reductive coupling of aryl diazonium salts (Figure 1.10) and another was oxidative coupling of aromatic amines (Figure 1.6).[42-44] The lithium ions were reduced and intercalated with the surface of CNTs in ammonia atmosphere or in polar aprotic solvents.[45,46] Transient alkyl radicals were attached covalently on the surface through electron exchange between negatively charged tubes and long chain alkyl iodides. The successful covalent attachment was confirmed by FT-IR, Raman, and TEM.

1.5.2 Covalent attachment of polymers onto CNT

Polymer covalently wrapping can enhance the solubility CNTs in $CHCl_3$, DMSO, MCB, DCM, H_2O and DMF. Long chain polymer can wrap the tubes uniformly and decrease the CNTs form bundles. According the polymerization before wrapping or after interaction with CNTs, there are two methods for this modification, which are defined as "grafting to" and "grafting from" methods. The former one, polymer chain is synthesized with a specific molecular weight before attached to the surface of CNT. The latter one, polymer precursors are immobilised on the surface of nanotubes first and then propagating the polymer chain by adding monomeric species.

1.5.2.1 "Grafting to" Method

Ultrasonication of SWNTs in a monochlorobenzene (MCB) solution of poly(methyl methacrylate) (PMMA) followed by filtration is an effective way to obtain discrete and single dispersed carbon nanotubes. The damages of ultrasonication to SWNTs can be controlled to the least. The FT-IR spectra indicate that MCB and PMMA were attached with SWNTs chemically.[47] The SWNTs wrapped with poly(vinyl-pyrrolidone) (PVP-1300) was reported by Richard E. Smalley.[48] PVP-1300 forms a monomolecular ~2.5 nm thick layer which is wrapping individual SWNTs by coiling and forming nanotube

bundles. Preparation of polystyrene-wrapped SWNTs using the high-speed vibration milling technique was reported which can help disperse SWNTs in various organic solvents.[49]

1.5.2.2 "Grafting from" Method

CNT-polymer composites were first fabricated by an in situ radical polymerisation process. Poly(methyl methacrylate)/carbon nanotube (PMMA/CNT) composites prepared by using an in situ process was reported.[50-54] CNTs can be initiated by AIBN (Azobisisobutyronitrile) to open their π-bonds. In turn, this is then forming strong interactions between the aromatic surface of CNT and in the presence of the PMMA matrix, at the same time when PMMA polymerization occurs. Carbon nanotubes can be grafted with polystyrene molecules using an in situ radical polymerisation reaction also enhanced their solubility and their suitability for nanocomposite applications. A uniform thin polystyrene wrapping was formed on the wall surface of CNTs. Complexes denoted polystyrene@MWNTs were soluble in dimethylformamide and tetrahydrofuran.[55-58] SWNTs was grafted with poly (4-vinylpyridine by using in situ free radical polymerization of 4-vinylpyridine was reported by Shuhui Qin et al.[59] After centrifugation and ultrafiltration treatment, catalyst particles and unattached polymer were removed. SWNT−PVP can maintain stable in DMF, methanol, and 2-propanol at least 8 months. Raman spectra analysis confirmed that discrete SWNT having PVP covalently attached. MWNTs grafted with a soft shell of brush-like polystyrene was successfully prepared by in situ atom transfer radical polymerization (ATRP), using Cu(I)Br/*N,N,N',N'',N'''*-pentamethyldiethylenetriamine (PMDETA) as the catalyst, at 100°C in diphenyl ether solution. The thickness of the shell layer can be controlled by controlling the molecular weight of polystyrene.[60]

1.5.3 Non-covalent interactions for SWNTs wrapping

CNTs' surfaces adsorb strongly with each other and they can easily form big bundles in solution: this is due to the fact that CNTs have strong surface energy. Non-covalent wrapping of the tubular structure by various species of polymers, polynuclear aromatic compounds, surfactants and biomolecules are also an important method to prepare separated carbon nanotubes. Non-covalent wrapping method is very interesting as this method modifies the CNTs without affecting the electronic network or the tubes. The non-covalent interaction between CNT and shell wrapping material is based on *van der Waals* forces and aromatic stacking.

Nanotube−polymer composites have been be widely used in different kinds of applications. The most important issue for nanotube−polymer composite preparation is efficient and uniform wrapping the core carbon nanotubes with shell species. The efficient load of wrapping species requires homogeneous dispersion and strong interfacial bonding between the host and guest. Chemists have developed several approaches for synthesis of such composites, including physical mixing in solution, *in situ* polymerization of monomers in the presence of nanotubes, surfactant-assisted processing of composites, and chemical functionalisation of the incorporated tubes. Carbon nanotubes were functionalised with polyethylene oxide (PEO) chains for biosensor by immobilizing a wide range of proteins with PEO.[61] It has been reported that zinc protoporphyrin IX (ZnPP) binds non-covalently to SWNTs and renders them solubility in DMF or DMSO.[62,63] Jinyu Chen et al. used water-soluble porphyrin molecules [meso-(tetrakis-4-sulfonatophenyl) porphine dihydrochloride] to wrap SWNTs, resulting in soluble SNWTs@porphyrin solutions that were stable for several weeks.[64]

Earlier work in the Pascu group described a strategy for coating SWNTs by using tripodal porphyrin receptors. These two tripodal porphyrin hosts can solubilise SWNTs in

DMF–toluene mixtures. Also this supramolecular coating material showed intense fluorescence, promise photovoltaic properties and biocompatibility whilst helping to disperse carbon nanotubes in organic solvents.[65] The Soret and Q-bands of porphyrin moieties in the porphyrin@SWNTs composites are significantly broadened and their fluorescence was almost quenched as the strong aromatic stacking between host and guest. Hongjie Die's group reported the use of fluorescein−polyethylene glycol (Fluor-PEG) to noncovalently functionalise SWNTs to enhance water-soluble of Fluor-PEG/SWNT and also afford the fluorescent labeling to nanotubes.[66]

Their interesting physicochemical properties make CNTs good candidates for nanomedicines design, especially for drug delivery applications. These are, for example, ordered structure with high aspect ratio, ultra-light weight, high mechanical strength, high electrical conductivity, high thermal conductivity, metallic or semi-metallic behaviour and high surface area.

However, CNT toxicology to human body and the environment is a big concern for application forward in medicine and industry. Certain experiments *in vivo* and *in vitro* have shown that there is no apparent toxic effect of CNT in the short term if modified in a suitable way.[67] *In vitro* and *in vivo* studies focused on the impact of functionalised carbon nanotubes on cells and animals. There is no size cut-off below which diameter suddenly becomes harmful. There are two factors that act together to induce harm:

(a) Large surface area of CNT

(b) CNTs' reactivity or intrinsic toxicity of the surface.

Additionally, the smaller the diameter of CNT, the more surface area they have per unit mass; therefore the more toxic the CNT. A dispersed CNT phase contains a huge number of tubular, high lengths/diameter ratio particles of even milligrams quantity as the nanometer-scale dimensions, with a concurrent very high total surface area. The total surface

area depends on their degree of bundling and aggregation of nanotubes in solution. Toxicity studies showed that there would be less cytotoxic effects than aqueous dispersions of pristine SWNT stabilised with a surfactant-1% of Pluronic F108 if SWNT are functionalised by phenyl-SO_3H or phenyl-$(COOH)_2$ groups covalently.[68]

In vitro studies indicated that two types of f-CNTs (functionalised through 1, 3-dipolar cycloaddition reaction and the oxidation/amidation treatment) can be taken up by B and T lymphocytes as well as macrophages without affecting cell viability as the solubility of f-CNTs seems high in cell culture medium.[69] Gene delivery using CNTs as a carrier can increase expression up to 10 times higher than the DNA alone. Hongjie Dai's group (Stanford) used CNT as a drug carrier to load anticancer doxorubicin.[70] The anticancer effects evaluation indicated this carrier had ultrahigh loading capacity of doxorubicin while targeted delivery of it selectively to cancer cell lines. The popularly used lipid vesicles for drug delivering can only carry doxorubicin in quantities up to one-eighth of their weight. Covalent binding with biocompatible molecules is an efficient way for bio-functionalisation of CNTs and enhance the possibility of applying CNTs in biomedical research areas.

1.5.3.1 Glucans as coating materials for SWNTs

β-1,3-D-Glucans are polyglucose complexes which can be isolated and purified from yeasts, mushrooms and other fungi. They are normally prepared by enzymatic extraction treatments of yeast cell walls. Curdlan is the simplest *β*-1,3-glucan. *β*-1,3-glucan has been attracting interest from phytochemical research scientists and health professionals since in 1940s, Dr. Louis Pillemer and his colleagues first isolated an immunity activating compound from a yeast cell-wall named 'Zymosan'.[71,72] The active component of Zymosan was not identified. The *β*-1,3-glucan has shown to be able to fortify and magnify the all-important 'primary' immune response in humans and animals. X-ray diffraction patterns of β-

1, 3-glucans in the anhydrous form showed that it adopts a right-handed triple helix.[73,74,75] In the triple helix structure, three glucoses containing different chains are bound together through the hydrogen bonds among the three O-2 atoms, forming the one-dimensional hydrogen-bonding network in the triple helix.[76] (1→3)-linked *β*-D-glucose molecules arranged in a linear polymer backbone with a side glucose group linked at every third main-chain glucose forms schizophyllan (SPG).

The helical structures of β-1,3-glucans helical structure are quite similar with those of double-stranded DNA, but larger than DNA helical tube. There is not enough space in the triple helix structure as it stands to accommodate even small molecular guests. The only way for β-1,3-glucans to encapsulate molecules is to dissociate the original triple helix structure into single strand by losing the hydrogen-bonding network, and dissociated β-1,3-glucan chains can have the ability to include guests and to form nanotubes. Norisuye et al. have reported the interesting solution properties of β-1,3-glucans where denaturing and re-naturing of the triple helix can take place reversibly. In the reported experiment β-1,3-glucans adopted a triple helix in nature, but can be dissociated into a single chain by dissolving in DMSO. When DMSO is exchanged by water, the changes in β-1,3-glucan intermolecular structure are promoted, resulting in the formation of the original triple helix structure.[77]

As mentioned above, since the discovery of SWNTs by lijima, SWNTs have attracted scientists' attention and have been regarded as very ideal materials due to their unique electronic, photochemical and mechanical properties.[1,2] But the strong cohesive nature and poor solubility of SWNTs in the absence of functionalisation is the major obstacle in their application in bioimaging fields. Synthetic or biological polymer solutions can be used for wrapping SWNTs to promote dissociation of the SWNT bundle to give a well dispersed SWNTs solution without damaging SWNT surface. Natural polysaccharide schizophyllan

was found by Shinkai[78] to be an excellent dispersing agent for SWNTs. In addition, polysaccharides do not absorb in the UV-Vis wavelength region, therefore the photochemical properties of the resulting complex composites are not affected by SPG. Hydrophobic interaction and the hydrogen-bonding interaction are main driving forces for the reconstruction of the triple-stranded β-1,3-glucans from the single-stranded ones. On the basis, SWNTs might be encapsulated in the hollow of the β-1,3-glucans helical structure mainly owing to hydrophobic interaction. However the natural β-1,3-glucans do not have enough cavity to accommodate SWNT larger than 1–2 nm diameters. Thus, some conformational change is needed in the β-1,3-glucan main-chain after wrapping the guest, probably with the weakness of the H bonds.

1.5.3.1.1 Interactions between boronic acids and diols

A method for rapid functionalisation of *β*-D-Glucans such as curdlan (an analogue of SPG, used widely) demonstrated by Prof Tony James group.[79] This group also pioneered the rapid tagging and recognition of polysaccharides by boronic acids.[80-82]

A number of research works examined the properties and the synthesis of boronic acids [83,84] and quantitative investigate into the interactions between boronic acids and polyols in 1959.[85] The dissociation of a hydrogen ion from phenylboronic acid occurs from the interaction of the boron atom with a molecule of water. As the phenylboronic acid and water react, a hydrated proton is liberated, thereby defining the acidity constant K_a. [86] The Scheme 1.1 depicts the association between water molecule and the Lewis acidic boron.

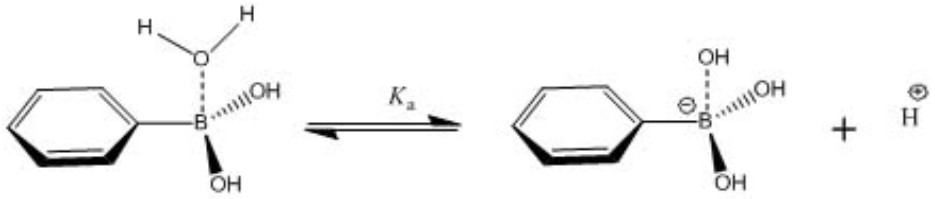

Scheme 1.1. The acid–conjugate base equilibrium for phenylboronic acid in water, diagram reproduced from paper.[87]

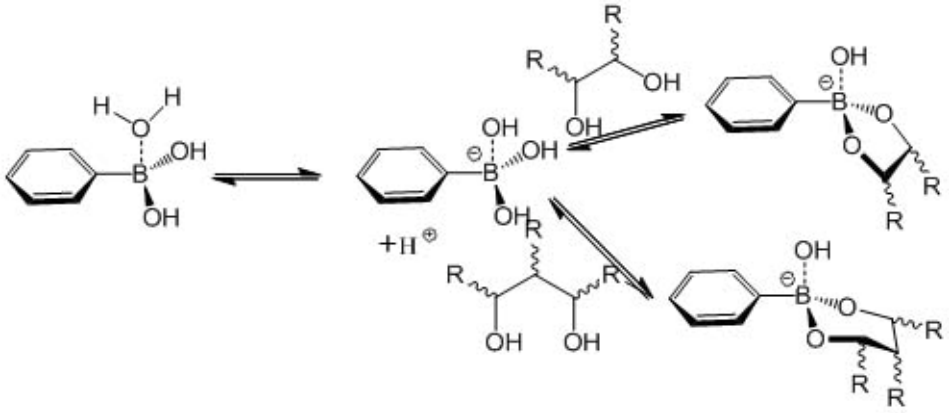

Scheme 1.2. Interaction of the phenylboronate anion with 1,2 diol to form diol–phenylboronate complexes with five membered rings, respectively, diagram reproduced from paper.[87]

Simultaneously, boronic acids have been reported to rapidly and reversibly[88] interact with dicarboxylic acids[89,90] α-hydroxy carboxylic acids and diols to form esters in aqueous media.[91] The most common interaction is with 1, 2 diol to form five-membered ring (Scheme 1.2). From experimental observations, it has been demonstrated that the kinetics of this inter-conversion is fastest in aqueous basic media where the boron is present in its tetrahedral anionic form. Therefore, boronic acids seem to be ideal candidates for rapid and stable functionalisation of polysaccharides such as *β*-D-Glucans.

Early findings by Shinkai for curdlan and SPG clearly showed that *β*-1,3-D-Glucan maintains its inherent ability as a one-dimensional host and can change the cavity to accommodate SWNT. The wrapping of *β*-1,3-D-Glucan provided a novel strategy to create functional polymer composites in a supramolecular manner. Considering a general difficulty in introducing functional groups into the functional polymer backbones without damaging the helical network, the use of boronic acids in combination with the present system may be a new potential path to develop functional polymeric materials formed by SWNT (filled or empty), glucan and targeting/monitoring tag.

1.5.4 Introduction to filling of SWNTs

A number of laboratories in the UK and world-wide are involved in the research of endohedral filling of SWNTs. The first endohedral filling of SWNTs with inorganic compounds was published in 1998,[92] therefore starting the new area of filling SWNTs to give new composite materials. Throughout this work we denoted the SWNT-based hybrid nanocomposite as X@SWNTs (where X is an atom, a molecule, or a chemical compound encapsulated into the cavity or around onto the surface).

The main interest in filling SWNTs was to enforce the filling materials to adopt 1D morphology. Filling SWNTs with 1D metallic wires was expected to promote the synthesis of future electronic devices.[93] Another application of filling SWNTs was to use this SWNT as a container for nano-sized catalysts with delayed action.[94] SWNTs may be partially filled with short nanorod or nanoparticles of catalysts. The carbon shell can protect catalyst from its release to the surrounding medium and help control the reaction due to the chemical and thermal inertness of the carbon layer. After the reaction conditions become oxidising (e.g. an oxidising agent is introduced into the mixture) the carbon layer would be oxidised and broken, then nano-size catalysts are released and activated for reaction. The catalyst efficiency was thus enhanced greatly due to the nano-size effect.

The first successful SWNT filling work with exogenous material was using $RuCl_3$, which was subsequently reduced into metallic Ru by using a heat-treatment (45 °C) under gaseous hydrogen. The group of Professor Malcolm L.H. Green (Oxford Nanotube Group) pioneered in the filling SWNTs with different kinds of halides so far, including $ThCl_4$,[95] $CdCl_2$,[95] $TbCl_3$, $TiCl_4$ and PbI_2, lanthanide halides $LnCl_3$,[96] KI, [97,98] $ZrCl_4$[99] and silver halides.[100]

Most metallic filling proceeded via a melting route, where very harsh condition were needed (T>400 °C) over prolonged periods of time.

The preparation of C_{60}@SWNTs ('peapods') was reported in 1998, the same year as Ru/$RuCl_3$@SWNT. The peapods were synthesized unexpectedly during purification and annealing treatments which were applied at Rice University on raw SWNT materials produced from the pulsed laser vaporisation method (PLV). Both carbon nanotubes and C_{60} molecules are produced when using pulsed laser vaporization of graphite in the presence of certain metallic catalysts. But C_{60} is still trapped inside a nanotube during this rather elaborate synthetic sequence.

We envisage that heavy-elements or radio-elements can be trapped inside the encapsulated fullerene under mild conditions and used as whole body markers for radiography. The application may be promoted for medical trials because fullerenes have been demonstrated to be biologically in active. They would eventually be eliminated from the body while the complex containing the markers (otherwise not very welcome in the body) will be imaged.[101-103]

The synthesis of 'endotubular metallofullerenes' (such as [Gd@C_{82}]@SWNT,[104,105] [La@C_{82}]@SWNT, [La_2@C_{82}]@SWNT and [Sm@C_{82}]@SWNT and [La_2@C_{80}]@SWNT [92] have been achieved already.

The first method for filling SWNTs with molecular species under harsh conditions was by mixing SWNT and the material to be inserted into a glass ampoule sealed under vacuum, and then heat the ampoule beyond the filling material sublimation temperature. Thus the filling materials become gas-phase atoms and enter into the cavity of SNWTs which can open simultaneously. This method has been used widely for preparing peapods and related materials,[106-108] due to the rather low sublimation temperature of fullerenes (～ 350 °C) added to the exceptional thermal stability of the isolated C_{60} and C_{70} molecules (～ 3000–4000 K[109]). Using this method a successful filling of nearly 100%, makes SWNT surfaces adequately clean. In situ filling is another similar method, which SWNTs are

synthesized while the filling material is sublimed, typically during the electric arc process, e.g., by using graphite anodes doped with both Co and Bi.[110] This resulted in the product of Bi@SWNT or resulted with the peapods by using various carbon anodes doped with C_{60}. The yield of this method is very low because of the high speed of the transient phenomena and the restricted volume where SWNT formation occurs in the plasma. Filling via liquid phase is another most common route used for preparing SWNT-based nano-complex. In addition to the above filling procedure, solution phase method is another simple and efficient filling method,[94,110-112] with the advantage that filling temperature is close to the room temperature. In this procedure, the SWNT material is suspended into a solution of the filling material using the suitable solvent depending on the filling material and the specific requirements of the procedure, e.g. HCl for CrO_3,[94] HNO_3 for $Bi(NO_3)_3$,[110] $AgNO_3$ [111,112] and H_2O for $RuCl_3$.[113] After filling, encapsulated metallic SWNTs can be obtained by reducing the inserted salts using a heat treatment under gaseous hydrogen.[110,112] It was reported that Ag@SWNT can be obtained from the heat-treatment of $AgNO_3$@SWNT at 350 °C in air.[111] This method has not yet been exploited a biomedical context.

1.6 Application of functional SWNTs in molecular imaging

The molecular imaging is a new discipline in which probes known as biomarkers are used to visualise, characterise and measure biological processes at the molecular and cellular level in humans and other living systems without perturbing them. This new technique is applicable for diagnosis of diseases such as cancer, and neurological and cardiovascular diseases. The development and improvement of new ideas and methodology in molecular imaging discipline have enhanced the possibility of earlier and more precise diagnosis of various cancers. Generally, molecular imaging modalities include molecular magnetic resonance imaging (MRI), magnetic resonance spectroscopy (MRS), optical

bioluminescence, optical fluorescence, targeted ultrasound, single photon emission computed tomography (SPECT), and positron emission tomography.[99,114] Molecular imaging methods use chemically synthesized probes to target molecular markers at different stages of diseases. These can also give whole-body readout of molecular changes of different diseases which is much more reliable and scientific than popular used *in vitro/ex vitro* assays. Non-invasive detection of various molecular makers can allow for precise and in time diagnosis and earlier treatment in early development stage of most of diseases.

Functionalised SWCNTs have been studied in the context of every single molecular imaging modality, including magnetic resonance (MR), optical, SPECT, and PET imaging.[9] SWNTs were loaded with aquated $Gd^{3+}{}_n$-ion clusters which may occur through the side-wall defects or end-of-tube openings to give linear super-paramagnetic molecular magnets with MRI efficacies 40 to 90 times larger than any Gd^{3+}-based contrast agent (CA) in current clinical use. These ultrasound systems denoted $Gd^{3+}{}_n$@US-tubes led to a new paradigm for high-performance MRI CA design[115]. Michael S. Strano et al.[116] reported that complexes formed by magnetic iron oxide nanoparticles and near-infrared[117] fluorescent SWNTs can be utilised as dual magnetic and fluorescent imaging agents. The iron oxide particle-enriched (Fe-enriched) and iron oxide particle-depleted (Fe-depleted) DNA-SWNT solutions contained 35 wt % of magnetic particles, had a magnetization saturation of 56 emu/g, and a magnetic relaxation time scale ratio (T_1/T_2) of approximately 12 and also a longer spin−spin relaxation time (T_2 :164 ms) than typical ferromagnetic particles. $Gd^{3+}{}_n$@US-tubes was confirmed as ultrasensitive pH-smart probes from pH 7.0−7.4. It indicated that $Gd^{3+}{}_n$@US-tubes might be very good candidates for detecting of early stage of cancer where the extracellular pH value can drop to pH = 7 or below.[118] Hongjie Dai et al. reported the utilization of PL-PEG-NH_2 functionalised and semiconducting SWNTs as near-infrared fluorescent tags for probing of cell surface receptors and simultaneous cell imaging.[119]

Phospholipid-PEG-NH_2 functionalised semiconducting SWNTs were attached to the antibody Rituxan to recognise CD20 cell surface receptor on B-cells and Herceptin aiding the recognition of HER2/neu positive breast cancer cells.

1.6.1 Optical imaging using functionalised SWCNTs

Fluorescent labeling of SWCNTs has been exploited for optical imaging applications. Massimo Bottini et al. reported the application of streptavidin-conjugated quantum dot decorated SWNTs in both optical and confocal fluorescent microscopies.[120] The supramolecular luminescent nano-complex can form stable dispersions under physiological conditions. Complexes were internalized by Jurkat T leukemia cell by multivalent CD3 receptor-mediated endocytosis (adsorption by cell).

Hongjie Dai et al. reported that SWNTs conjugated with various targeting ligands including Herceptin (anti-Her2), Erbitux (anti-Her1), and RGD peptide exhibited distinct Raman G-band peaks which have been used for multiplexed multicolour Raman imaging of biological systems (Figure 1.7).[121] An optimised noninvasive Raman microscope was used to evaluate targeting effects and localization of RGD-SWNT and compare to plain-SWNTs. Results of imaging indicated that increased accumulation of RGD-SWNTs in tumour ($p < 0.05$) compared to plain-SWNTs over the next 72 h was observed. Antibody-functionalised SWCNTs have recently been used as multicolor Raman labels for highly sensitive, multiplexed protein detection in an arrayed format.[122]

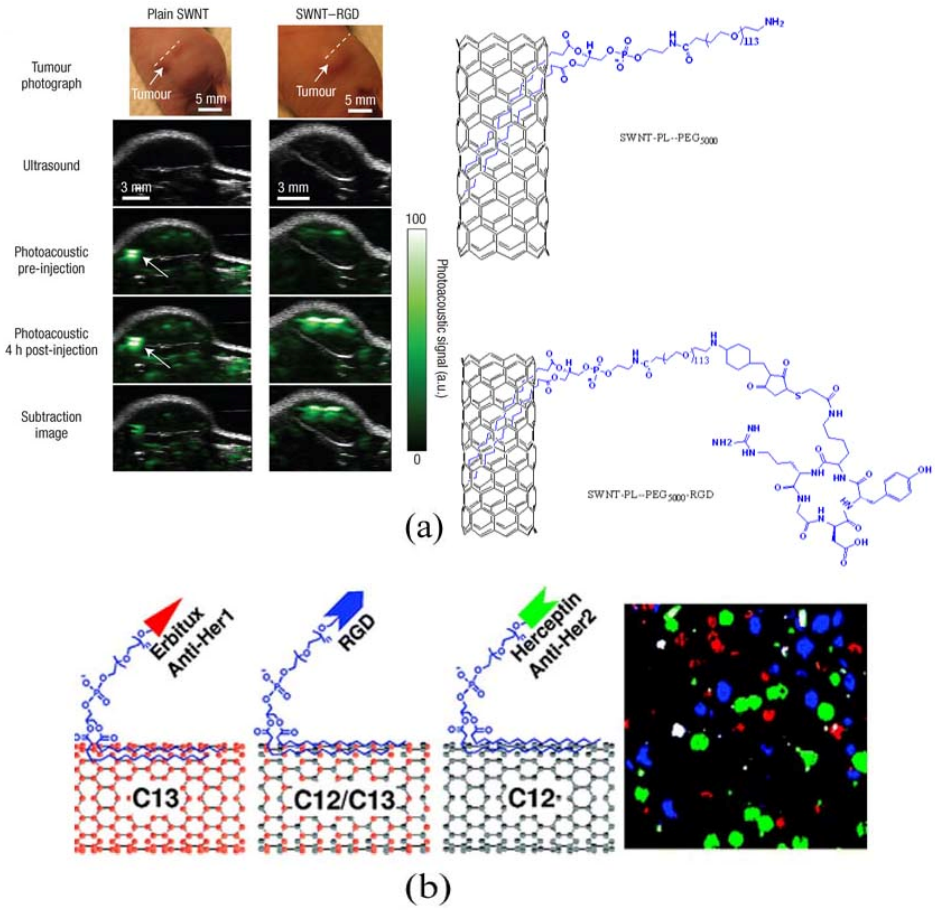

Figure 1.7. (a) Merged Ultrasound (grey) and photoacoustic (green) images of one vertical slice (white dotted line) through the tumour. Injection with SWNT-RGD induces a significantly higher photoacoustic signal than injection with plain SWNT in tumour site. (b)SWNTs tagged with different isotope compositions show distinct Raman single walled carbon nanotubes (SWNTs) with different isotope compositions show distinct Raman G-band peaks and accordingly show different Raman colours. This can be used for multicolour imaging of biological systems. [Image adapted from[121,123,124]]

1.6.2 PET and SPECT imaging using functionalised SWCNTs

PET uses positron emitter-labeled molecules in very low concentrations ($<10^{-9}$ M) to image and measure the function of biological processes with minimal disturbance.[125,126] Normally the sensitivity of PET is significantly higher than SPECT. After the development of micro-PET scanners, scientists can use small-animal imaging studies (which can provide a similar *in vivo* imaging capability in mice, rats, and monkeys) to facilitate and prove clinical

translation of lab derived PET agents.[127] The SPECT images emerge from gamma-ray emissions. 3D images can be obtained from radioisotope decays and emitted gamma rays detected by a gamma camera. Carbon nanotubes are promising candidates for PET or SPET imagines *in vivo*. Haifang Wang et al. studied the distribution of ^{125}I labeled water-soluble hydroxylated carbon single-wall nanotubes in mice.[128] This study, for the first time, affords a quantitative analysis of carbon nanotubes accumulated in animal tissues. Later, ^{111}In labeled DTPA functionalised water-soluble SWNTs were used for PET imaging purposes (DTPA= Diethylene-triamine-pentaacetic acid, Figure 1.8). After intravenous administration of functionalised SWNTs, radioactivity tracing study revealed that SWNTs were not retained in any of the reticulo-endothelial system (RES) organs (liver or spleen) and were rapidly cleared from systemic blood circulation through the renal excretion route.[129] The whole body biodistribution in mice was studied using ^{64}Cu- labeled SWNTs by *in vivo* PET.

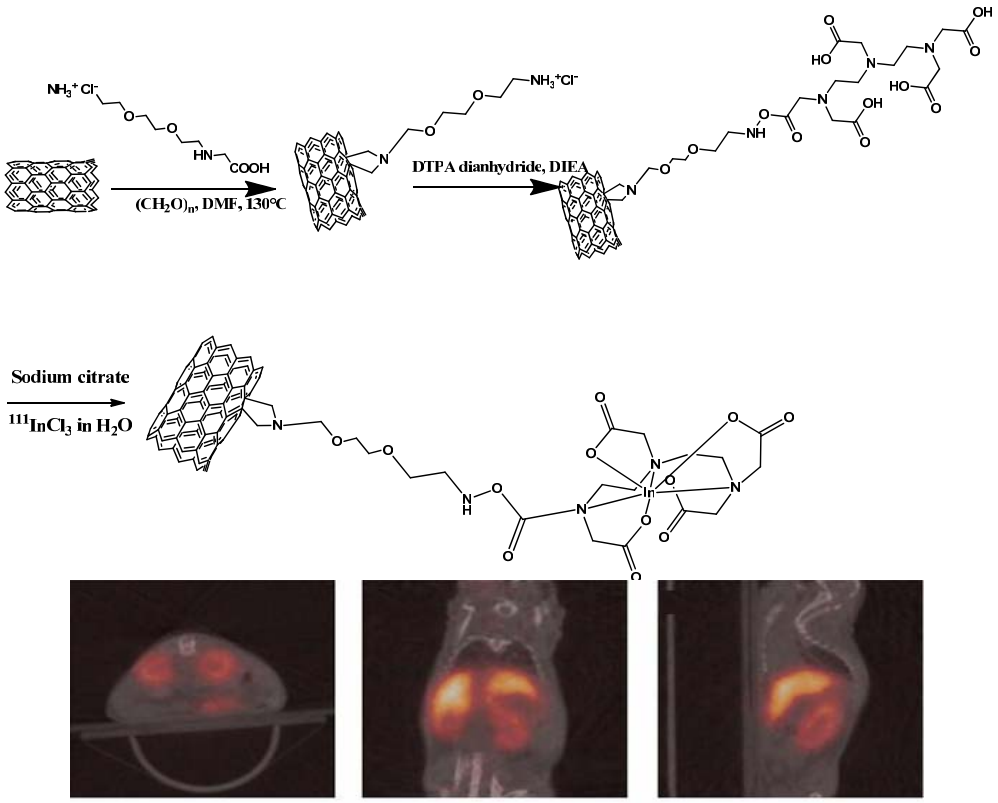

Figure 1.8. Synthesis of ^{111}In-labeled CNT (top diagram) and SPECT imaging applications (bottom diagram). [Image adapted from Reference[130].]

The SWNTs used in this report were non-covalently functionalised with phospholipid–PEG (PL–PEG) and were surprisingly stable *in vivo* (Figure 1.8 a).

PEGylated SWNTs exhibited relatively long blood circulation time and low uptake by the RES. DOTA was attached to the termini of the PEG chains and used to conjugate positron emitting radionuclide ^{64}Cu (radio decay half-life $t_{1/2}$ = 12.7 h). The conjugation of SWNTs to both ^{64}Cu and Cyclo-(RGDyK), a potent integrin $\alpha_v\beta_3$ antagonist, aimed at in vivo targeting of integrin $\alpha_v\beta_3$-positive tumours in mice via specific RGD–integrin $\alpha_v\beta_3$ binding was reported.[123,124] In order to evaluate the potential application of SCNT scaffold for tumour targeted radioisotope drug delivery. Covalently-attached DOTA chelates attached and ^{86}Yttrium labeled SWNT constructs were synthesized from amine-functionalised, water-soluble CNT (Figure 1.9).[131] The whole-body distribution and clearance of yttrium-86 was studied at 3 and 24 hours post-injection using PET. The ^{86}Yttrium disappeared from the blood within 3 hours and accumulated predominantly to the kidneys, liver, spleen and to a less extent in the bone.

Novel radionuclide filled and carbohydrate functionalised SWNTs were prepared and used as radioprobes by Sung You Hong et al. (Figure 1.10).[67] Metal halides (Na^{125}I) were encapsulated inside SWNTs by a molten phase method under harsh conditions. The surface of carbon nanotubes was covalently modified with 'biantennary' carbonhydrates for improving dispersibility and biocompatibility. Intravenous administration of Na^{125}I-filled glyco-SWNTs in mice was tracked by SPECT. High lung accumulation and zero leakage of isotopes to high-affinity organs (thyroid/stomach or excretion) of these radioprobes were demonstrated *in vivo* experiment. It remains the case that the synthetic method applied here was extremely time consuming in the biomedical radioimaging

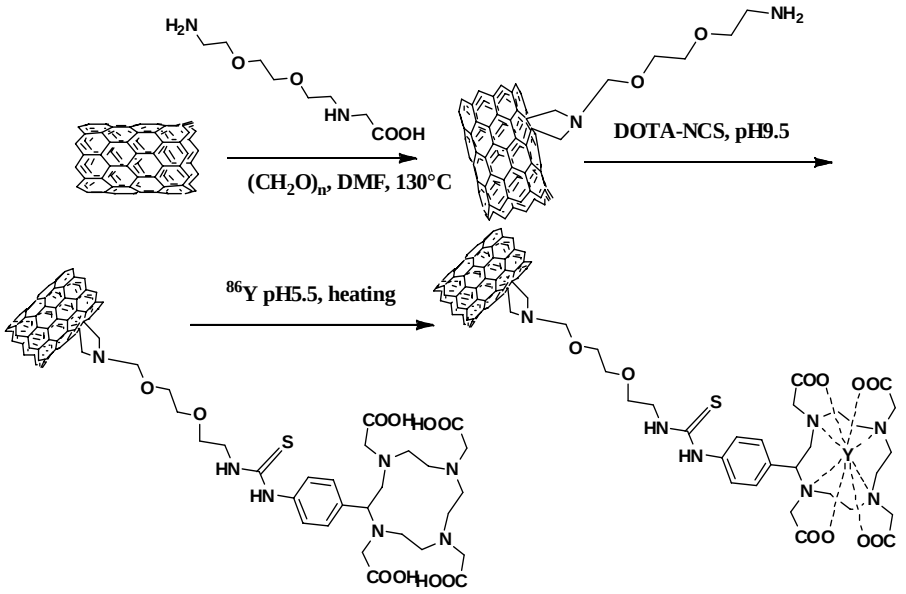

Figure 1.9. Synthetic scheme to prepare ^{86}Y-CNT and fused PET and CT images at 3 hours post-injection of ^{86}Y-CNT. [Image adapted from paper [131]]

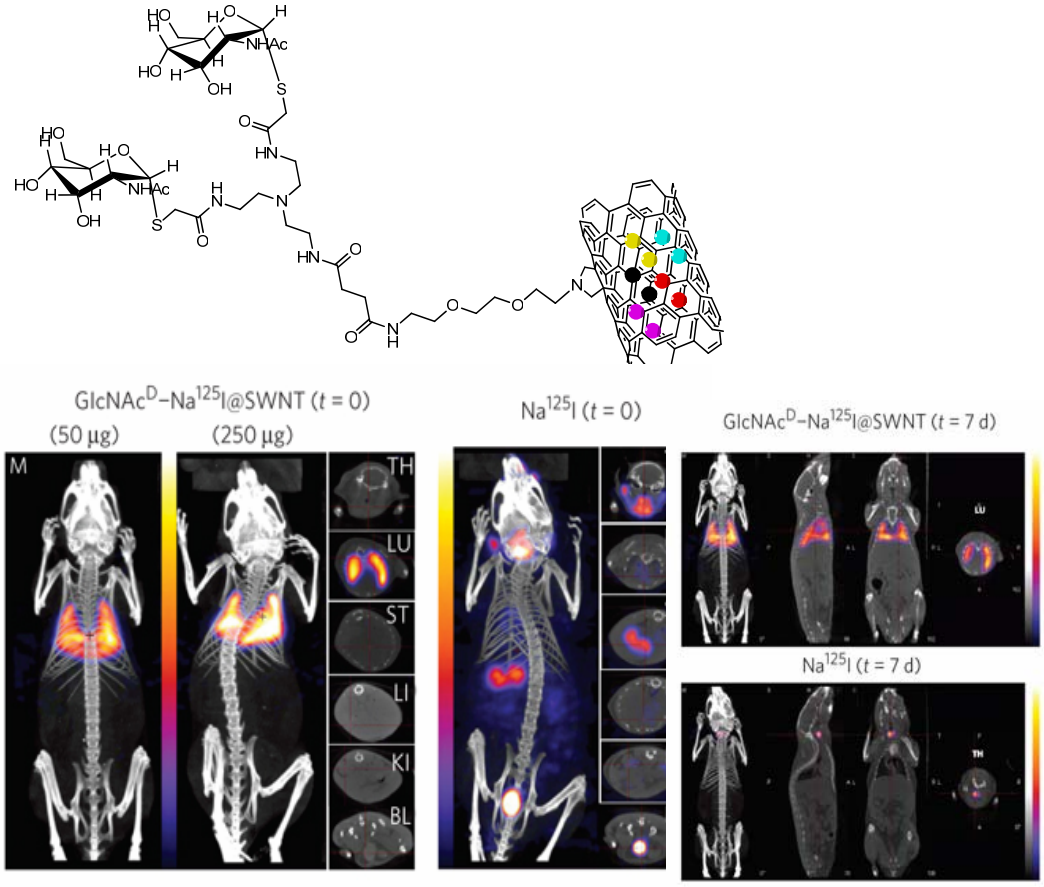

Figure 1.10. Molecular structure of GlcNAcD–X@SWNTs (X=CuBr, NaI or $Na^{125}I$) (Middle). Whole-body SPECT/CT imaging of mice after immediately tail-vein and 7 days post-injection of the GlcNAc^{D}–$Na^{125}I$@SWNTs or $Na^{125}I$ with a scanning time of 40–60 min (Left). [Image adapted from paper [67]]

1.7 Fluorescence spectroscopy

The use of fluorophores in bioimaging applications is an increasingly approach in biological studies. For examples, after the fluorophores are internalised by cells they may bind within cellular structures of interest. Upon irradiation with laser light, fluorophores inside of cells can absorb energy from photons, a valence electron of this molecule is activated to jump to a higher energy orbit. Electrons cannot remain excited at this energy level, they return back to the original level of lower energy, ground level and certain quantified energy will be released from this relaxation giving an emission as fluorescence. [132,133]

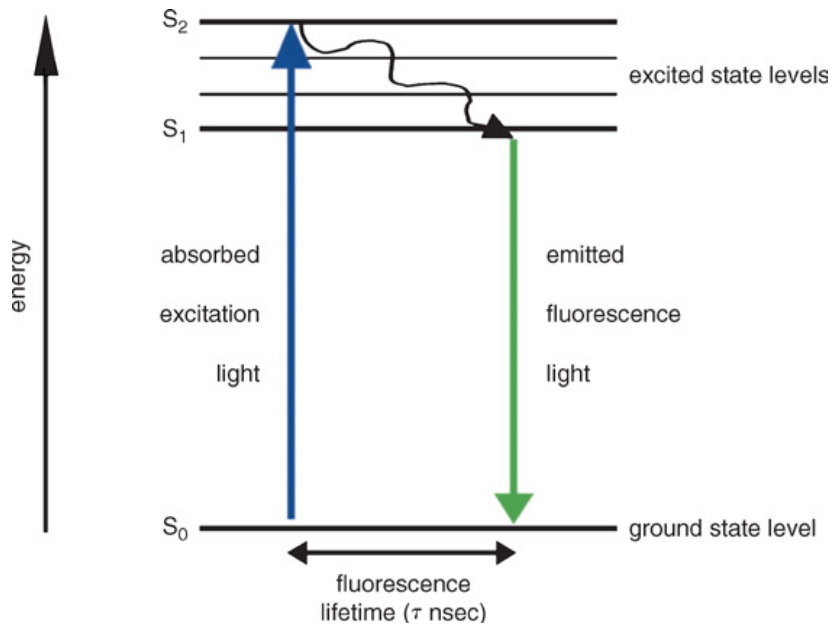

Figure 1.11. Jablonski diagram illustrates the energy states transfer. Fluorophore without absorbing energy stays at the ground state level S_0. After it is excited by photons with certain wavelength, the excited state S_1energy. Normally fluorophore can exist in number of vibrational energy levels at each energy state; one energy state has multiple lines. The fluorophore can not maintain stable in this excited energy level, it will drop back to the stable energy level which gives the emission. The time of fluorophore staying in this excited energy level ranges from nano- to picoseconds for most standard fluorophors.[132,133]

1.7.1 Confocal laser scanning microscopy (CLSM)

Confocal laser scanning microscopy (CLSM) is a technique which can acquire in-focus high-resolution images with depth selectivity. Basically, images are formed by collecting signal point-by-point from the sample and mathematically transferring to two-dimensional or three-dimensional photos. A conventional microscope can collect signals from the whole range as far into the specimen as the light can penetrate, but a confocal microscope just collect signals from one depth level at a time. CLSM can focus on very limited depth level and scan all levels to reconstruct the interior images. This technique can let researcher obtain the three-dimensional profile not just surface profile of the objects of interest. The basic principle of this technique can be traced back to Marvin Minsky's patent in 1961.[134] This technique became a standard technique until the end of the 1980s after the development and utilization of lasers for CLSM. Using laser scanning method for profiling 3D structure of biological species labeled with fluorescent markers was designed by Thomas and Christoph Cremer in 1978.[135] Then this technique has become more and more mature due to instrument development by academics and industry partners.

In a confocal laser scanning microscope, a laser beam enters the system and is focused onto certain depth level of specie by objective lens. In biological application, the specimens are normally fluorescent or labeled with fluorescent reporter. Fluorescent light was generated after excitation by laser light, the emitted signal is collected by the objective lens and relayed to the detector. The confocality is achieved by a pinhole blocking in front of the detector. This pinhole passes the light from the confocal point while rejecting the majority of the light from the outside of the confocal area. After passing the pinhole, the intensity of light is detected by a photodetection device (usually a photomultiplier tube (PMT) or avalanche photodiode), transforming the light signal into an electrical one that is used for reconstructing images by computer.

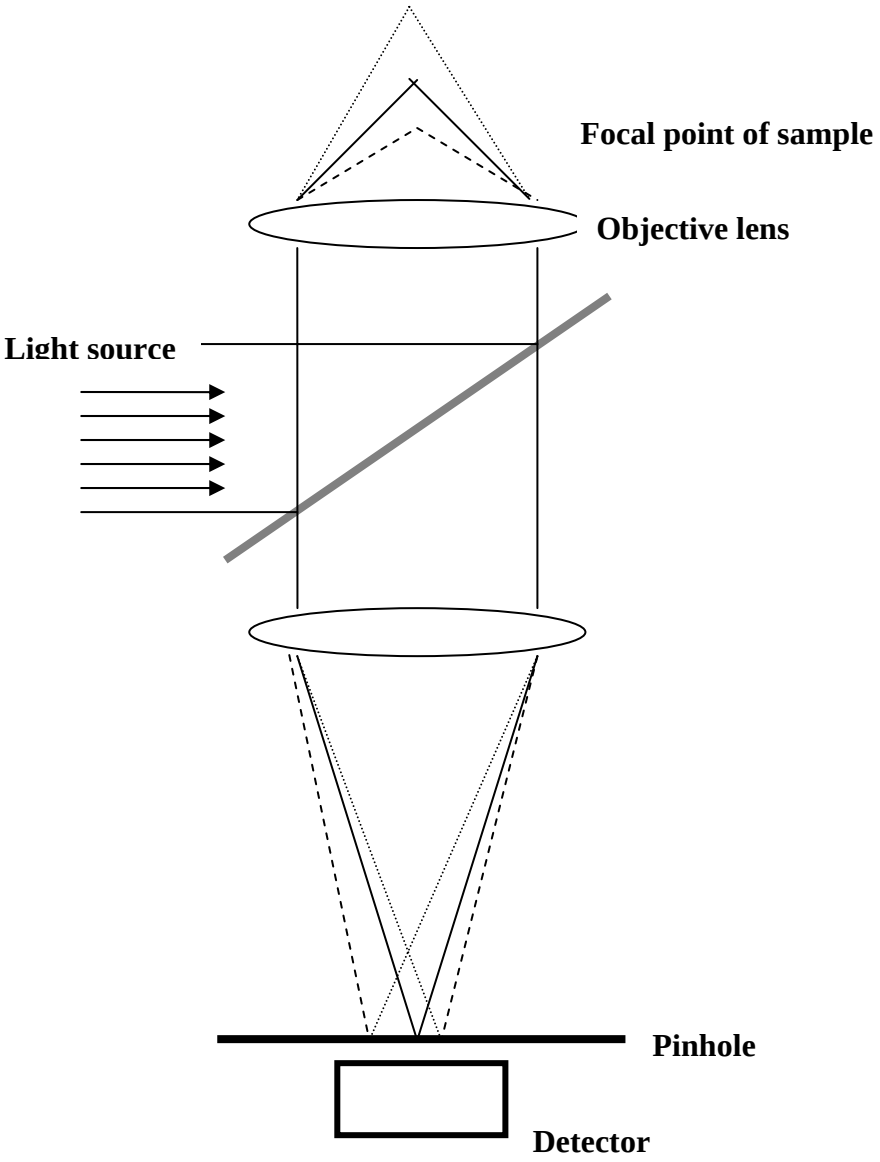

Figure 1.12. The principle of setup of a confocal microscope. Laser light excites fluorescence emission from sample which can be collected by the objective lens and relayed to the detector. Light from out of the focus lane is rejected by the pinhole and the light originating from the focus is detected and transferred to electrical signal.[132,133]

1.7.2 Fluorescence-lifetime imaging microscopy (FLIM)

1.7.2.1 Fluorescent lifetime

A fluorophore which is excited by a photon following the absorption of energy and then jumps to the excited state, after a very short time, it will drop to the ground state. The

average time the molecule remains in its excited state before dropping to the ground state is the fluorescence lifetime.

The fluorescence emitted will decay with time according to this equation

$$F(t) = F_0 e^{-t/\tau}$$

Where

$$\frac{1}{\tau} = \sum k_i$$

In this equation, τ is the fluorescence lifetime, t is time, F_0 is the initial fluorescence at $t = 0$, and k_i are the rates for each decay pathway. Fluorescence-lifetime imaging can be achieved by forming images with intensity of each pixel representing the lifetime τ, which can give the contrast images of objects based on the difference of fluorescence decay rates.

1.7.2.2 Time-correlated single-photon counting

Time-correlated single-photon counting (TCSPC) is a method which can detect single photons of a periodical light signal, also measure of the decay time of the individual photos and reconstruct the waveform from each measurements. Usually, TCSPC records times of corresponding pulse when individual photons are detected by a photo-multiplier tube [136]). The recordings can be repeated for the continual pulses and a histogram of all these recording times can be generated (Figure 1.13). An exponential function contained the lifetime decay function can be fitted based on this histogram. The lifetime parameter can be accordingly extracted. [132,133]

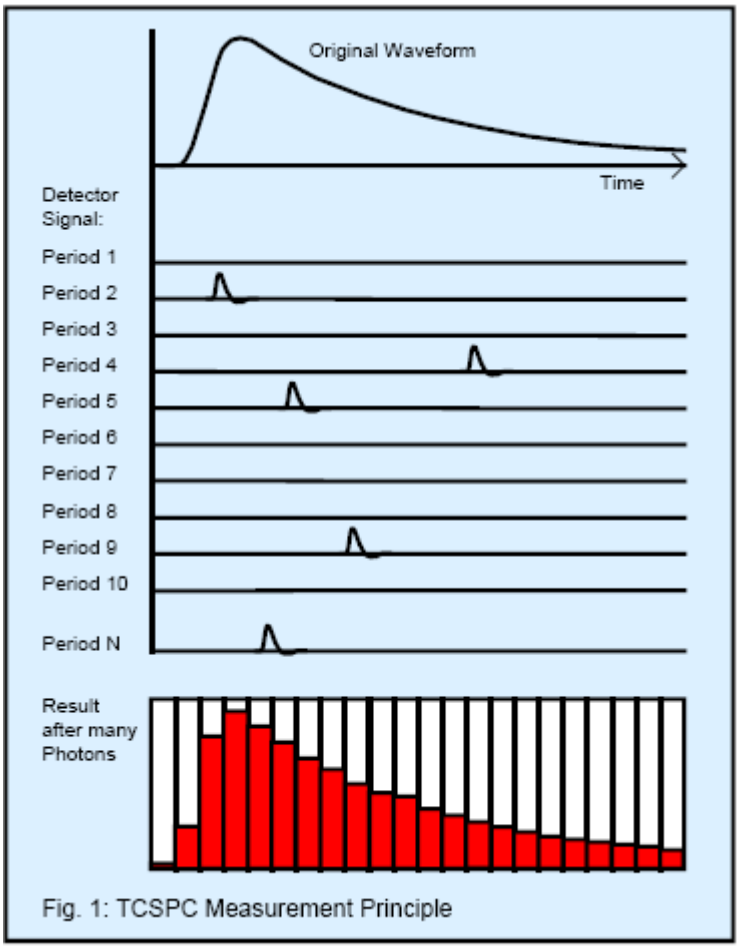

Figure 1.13. Measurement Principle of TCSPC. [Image adapted from paper[137]]

1.7.2.3 Applications

1.7.2.3.1 Calcium Ion Concentration Imaging

This application is based on both fluorescence lifetime and fluorescence intensity change after calcium ion binds to fluorescent probe. The change amplitude of the intensity reflects the change of the calcium concentration influx into the cells because the ratio of bound and unbound calcium leads to the change of fluorescence lifetime and the measure pixel in the specimen. This principle also can be used to probe the cellular pH change.

1.7.2.3.2 Fluorescence Resonance Energy Transfer (FRET)

When mapping the lifetime of a population of fluorophores in single cell, a key factor will interfere with lifetime of individual fluorophore, in which a second fluorophore (acceptor) with the appropriate spectral properties can absorb energy from the first fluorophore (donor) by fluorescence resonance energy transfer.[138] The decrease of the lifetime and fluorescence quenching of the donor, accompanied with an increase in acceptor fluorescence emission can be used to judge whether the FRET interaction happen or not between donor and acceptor. Also, FRET can be utilised as a tool for measuring distances between two biomolecules labeled with an appropriate donor and acceptor fluorochrome.[138] For example labeling two interested biomolecules with two spectrally distinct fluorophores and combining with FLIM imaging technique can provide a powerful tool to visualise the spatial distribution and also the interaction between these two biomolecules. Fluorescence microscope can give a maximum resolution of about 5 μm. Using fluorescence resonance energy transfer can increase the spatial resolution of the fluorescence microscope to below 10 nm. This amazing leap in resolution makes FRET technique so attractive for studying co-localization of two interesting biomolecules in live cells.

1.8 Summary

The introduction provided a brief overview of some recent developments in the fields of synthesis, functionalisation and characterization of carbon nanotubes with an emphasis on their biomedical imaging applications. Several methods used for the monitoring of the interactions between carbon nanotubes and living cells and organisms have been also highlighted. The reminder of this thesis describes the synthesis, characterization and cellular

imaging of novel nanohybrid materials based on single walled carbon nanotubes with potential biological applications.

1.9 References for introduction

(1) Iijima, S. *Nature* **1991**, *354*, 56.

(2) Bethune, D. S.; Kiang, C. H.; Devries, M. S.; Gorman, G.; Savoy, R.; Vazquez, J.; Beyers, R. *Nature* **1993**, *363*, 605.

(3) Journet, C.; Maser, W. K.; Bernier, P.; Loiseau, A.; delaChapelle, M. L.; Lefrant, S.; Deniard, P.; Lee, R.; Fischer, J. E. *Nature* **1997**, *388*, 756.

(4) Kiang, C. H.; Goddard, W. A.; Beyers, R.; Bethune, D. S. *Carbon* **1995**, *33*, 903.

(5) Lin, X.; Wang, X. K.; Dravid, V. P.; Chang, R. P. H.; Ketterson, J. B. *Appl. Phys. Lett.* **1994**, *64*, 181.

(6) Seraphin, S. *J. Electrochem. Soc.* **1995**, *142*, 290.

(7) Zhao, X.; Ohkohchi, M.; Wang, M.; Iijima, S.; Ichihashi, T.; Ando, Y. *Carbon* **1997**, *35*, 775.

(8) Kroto, H. W.; Heath, J. R.; Obrien, S. C.; Curl, R. F.; Smalley, R. E. *Nature* **1985**, *318*, 162.

(9) Thess, A.; Lee, R.; Nikolaev, P.; Dai, H. J.; Petit, P.; Robert, J.; Xu, C. H.; Lee, Y. H.; Kim, S. G.; Rinzler, A. G.; Colbert, D. T.; Scuseria, G. E.; Tomanek, D.; Fischer, J. E.; Smalley, R. E. *Science* **1996**, *273*, 483.

(10) Hsu, W. K.; Hare, J. P.; Terrones, M.; Kroto, H. W.; Walton, D. R. M.; Harris, P. J. F. *Nature* **1995**, *377*, 687.

(11) Endo, M.; Takeuchi, K.; Kobori, K.; Takahashi, K.; Kroto, H. W.; Sarkar, A. *Carbon* **1995**, *33*, 873.

(12) Muller, T. E.; Reid, D. G.; Hsu, W. K.; Hare, J. P.; Kroto, H. W.; Walton, D. R. M. *Carbon* **1997**, *35*, 951.

(13) Li, W. Z.; Xie, S. S.; Qian, L. X.; Chang, B. H.; Zou, B. S.; Zhou, W. Y.; Zhao, R. A.; Wang, G. *Science* **1996**, *274*, 1701.

(14) Terrones, M.; Grobert, N.; Olivares, J.; Zhang, J. P.; Terrones, H.; Kordatos, K.; Hsu, W. K.; Hare, J. P.; Townsend, P. D.; Prassides, K.; Cheetham, A. K.; Kroto, H. W.; Walton, D. R. M. *Nature* **1997**, *388*, 52.

(15) Terrones, M. *Annu. Rev. Mater. Res.* **2003**, *33*, 419.

(16) Wikipedia In *Carbon nanotube*; Wikipedia: 2012.

(17) Ebbesen, T. W.; Ajayan, P. M. *Nature* **1992**, *358*, 220.

(18) Jung, S. H.; Kim, M. R.; Jeong, S. H.; Kim, S. U.; Lee, O. J.; Lee, K. H.; Suh, J. H.; Park, C. K. *Appl. Phys. A* **2003**, *76*, 285.

(19) Dresselhaus M. S., Dresselhaus G., Phaedon A. *Carbon Nanotubes: Synthesis, Structure, Properties, and Applications* **2001**, 297.

(20) Guo, T.; Nikolaev, P.; Rinzler, A. G.; Tomanek, D.; Colbert, D. T.; Smalley, R. E. *J. Phys. Chem.* **1995**, *99*, 10694.

(21) Scott, C. D.; Arepalli, S.; Nikolaev, P.; Smalley, R. E. *Appl. Phys. A* **2001**, *72*, 573.

(22) Joseyacaman, M.; Mikiyoshida, M.; Rendon, L.; Santiesteban, J. G. *Appl. Phys. Lett.* **1993**, *62*, 657.

(23) Balasubramanian, K.; Burghard, M. *Small* **2005**, *1*, 180.

(24) Fernando, K. A.; Lin, Y.; Sun, Y. P. *Langmuir* **2004**, *20*, 4777.

(25) Nakajima, T.; Koh, M.; Gupta, V.; Zemva, B.; Lutar, K. *Electrochim. Acta* **2000**, *45*, 1655.

(26) Kelly, K. F.; Chiang, I. W.; Mickelson, E. T.; Hauge, R. H.; Margrave, J. L.; Wang, X.; Scuseria, G. E.; Radloff, C.; Halas, N. J. *Chem. Phys. Lett.* **1999**, *313*, 445.

(27) Margrave, J. L.; Mickelson, E. T.; Chiang, I. W.; Zimmerman, J. L.; Boul, P. J.; Lozano, J.; Liu, J.; Smalley, R. E.; Hauge, R. H. *Abst. Paper. Ameri. Chem. Soc.* **1999**, *218*, 13.

(28) Stevens, J. L.; Huang, A. Y.; Peng, H. Q.; Chiang, L. W.; Khabashesku, V. N.; Margrave, J. L. *Nano Lett.* **2003**, *3*, 331.

(29) Zhang, L.; Kiny, V. U.; Peng, H. Q.; Zhu, J.; Lobo, R. F. M.; Margrave, J. L.; Khabashesku, V. N. *Chem. Mater.* **2004**, *16*, 2055.

(30) Khare, B. N.; Meyyappan, M.; Cassell, A. M.; Nguyen, C. V.; Han, J. *Nano Lett.* **2002**, *2*, 73.

(31) Khare, B. N.; Meyyappan, M.; Kralj, J.; Wilhite, P.; Sisay, M.; Imanaka, H.; Koehne, J.; Baushchlicher, C. W. *Appl. Phys. Lett.* **2002**, *81*, 5237.

(32) Kim, K. S.; Bae, D. J.; Kim, J. R.; Park, K. A.; Lim, S. C.; Kim, J. J.; Choi, W. B.; Park, C. Y.; Lee, Y. H. *Adv. Mater.* **2002**, *14*, 1818.

(33) Khare, B.; Meyyappan, M.; Moore, M. H.; Wilhite, P.; Imanaka, H.; Chen, B. *Nano Lett.* **2003**, *3*, 643.

(34) Chen, Y.; Haddon, R. C.; Fang, S.; Rao, A. M.; Lee, W. H.; Dickey, E. C.; Grulke, E. A.; Pendergrass, J. C.; Chavan, A.; Haley, B. E.; Smalley, R. E. *J. Mater. Res.* **1998**, *13*, 2423.

(35) Chen, J.; Hamon, M. A.; Hu, H.; Chen, Y. S.; Rao, A. M.; Eklund, P. C.; Haddon, R. C. *Science* **1998**, *282*, 95.

(36) Kamaras, K.; Itkis, M. E.; Hu, H.; Zhao, B.; Haddon, R. C. *Science* **2003**, *301*, 1501.

(37) Georgakilas, V.; Kordatos, K.; Prato, M.; Guldi, D. M.; Holzinger, M.; Hirsch, A. *J. Am. Chem. Soc.* **2002**, *124*, 760.

(38) Tagmatarchis, N.; Prato, M. *J. Mater. Chem.* **2004**, *14*, 437.

(39) Wang, Y. B.; Iqbal, Z.; Mitra, S. *Carbon* **2005**, *43*, 1015.

(40) Tagmatarchis, N.; Zattoni, A.; Reschiglian, P.; Prato, M. *Carbon* **2005**, *43*, 1984.

(41) Coleman, K. S.; Bailey, S. R.; Fogden, S.; Green, M. L. H. *J. Am. Chem. Soc.* **2003**, *125*, 8722.

(42) Kooi, S. E.; Schlecht, U.; Burghard, M.; Kern, K. *Angew. Chem. Int. Ed.* **2002**, *41*, 1353.

(43) Balasubramanian, K.; Friedrich, M.; Jiang, C. Y.; Fan, Y. W.; Mews, A.; Burghard, M.; Kern, K. *Adv. Mater.* **2003**, *15*, 1515.

(44) Balasubramanian, K.; Sordan, R.; Burghard, M.; Kern, K. *Nano Lett.* **2004**, *4*, 827.

(45) Liang, F.; Sadana, A. K.; Peera, A.; Chattopadhyay, J.; Gu, Z. N.; Hauge, R. H.; Billups, W. E. *Nano Lett.* **2004**, *4*, 1257.

(46) Borondics, F.; Bokor, M.; Matus, P.; Tompa, K.; Pekker, S.; Jakab, E. *Fuller. Nanotube. Carb. N* **2005**, *13*, 375.

(47) Koshio, A.; Yudasaka, M.; Zhang, M.; Iijima, S. *Nano Lett.* **2001**, *1*, 361.

(48) Didenko, V. V.; Moore, V. C.; Baskin, D. S.; Smalley, R. E. *Nano Lett.* **2005**, *5*, 1563.

(49) Shin, J. Y.; Kim, C.; Geckeler, K. E. *Polym. Int.* **2009**, *58*, 579.

(50) Jia, Z. J.; Wang, Z. Y.; Xu, C. L.; Liang, J.; Wei, B. Q.; Wu, D. H.; Zhu, S. W. *Mater. Sci. Eng., A* **1999**, *271*, 395.

(51) Choi, H. J.; Lim, J. Y.; Zhang, K. *Diam. Relat. Mater.* **2008**, *17*, 1498.

(52) Huang, Y. L.; Yuen, S. M.; Ma, C. C. M.; Chuang, C. Y.; Yu, K. C.; Teng, C. C.; Tien, H. W.; Chiu, Y. C.; Wu, S. Y.; Liao, S. H.; Weng, F. B. *Compos. Sci. Technol.* **2009**, *69*, 1991.

(53) Kumar, S.; Rath, T.; Khatua, B. B.; Dhibar, A. K.; Das, C. K. *J Nanosci Nanotechno.* **2009**, *9*, 4644.

(54) Liu, M. H.; Zhu, T.; Li, Z. C.; Liu, Z. F. *J. Phys. Chem. C* **2009**, *113*, 9670.

(55) Yang, Y. K.; Xie, X. L.; Wu, J. G.; Mai, Y. W. *J. Polym. Sci., Part A: Polym. Chem.* **2006**, *44*, 3869.

(56) Fragneaud, B.; Masenelli-Varlot, K.; Gonzalez-Montiel, A.; Terrones, M.; Cavaille, J. Y. *Compos. Sci. Technol.* **2008**, *68*, 3265.

(57) Nayak, R. R.; Shanmugharaj, A. M.; Ryu, S. H. *Macromol. Chem. Phys.* **2008**, *209*, 1137.

(58) Sui, K. Y.; Yang, C. J.; Gao, S.; Shan, X.; Xia, Y. Z.; Zheng, Q. *J. Appl. Polym. Sci.* **2009**, *114*, 1914.

(59) Qin, S. H.; Qin, D. Q.; Ford, W. T.; Herrera, J. E.; Resasco, D. E. *Macromolecules* **2004**, *37*, 9963.

(60) Kong, H.; Gao, C.; Yan, D. Y. *Macromolecules* **2004**, *37*, 4022.

(61) Chen, R. J.; Bangsaruntip, S.; Drouvalakis, K. A.; Kam, N. W. S.; Shim, M.; Li, Y. M.; Kim, W.; Utz, P. J.; Dai, H. J. *Proc. Natl. Acad. Sci. U. S. A.* **2003**, *100*, 4984.

(62) Murakami, H.; Nomura, T.; Nakashima, N. *Chem. Phys. Lett.* **2003**, *378*, 481.

(63) Kubat, P.; Lang, K.; Janda, P.; Frank, O.; Matulkova, I.; Sykora, J.; Civis, S.; Hof, M.; Kavan, L. *J Nanosci Nanotechno.* **2009**, *9*, 5795.

(64) Chen, J. Y.; Collier, C. P. *J. Phys. Chem. B* **2005**, *109*, 7605.

(65) Pascu, S. I.; Kuganathan, N.; Tong, L. H.; Jacobs, R. M. J.; Barnard, P. J.; Chu, B. T.; Huh, Y.; Tobias, G.; Salzmann, C. G.; Sanders, J. K. M.; Green, M. L. H.; Green, J. C. *J. Mater. Chem.* **2008**, *18*, 2781.

(66) Nakayama-Ratchford, N.; Bangsaruntip, S.; Sun, X.; Welsher, K.; Dai, H. *J. Am. Chem. Soc.* **2007**, *129*, 2448.

(67) Hong, S. Y.; Tobias, G.; Al-Jamal, K. T.; Ballesteros, B.; Ali-Boucetta, H.; Lozano-Perez, S.; Nellist, P. D.; Sim, R. B.; Finucane, C.; Mather, S. J.; Green, M. L.; Kostarelos, K.; Davis, B. G. *Nat Mater* **2010**, *9*, 485.

(68) Sayes, C. M.; Liang, F.; Hudson, J. L.; Mendez, J.; Guo, W. H.; Beach, J. M.; Moore, V. C.; Doyle, C. D.; West, J. L.; Billups, W. E.; Ausman, K. D.; Colvin, V. L. *Toxicol. Lett.* **2006**, *161*, 135.

(69) Dumortier, H.; Lacotte, S.; Pastorin, G.; Marega, R.; Wu, W.; Bonifazi, D.; Briand, J. P.; Prato, M.; Muller, S.; Bianco, A. *Nano Lett.* **2006**, *6*, 1522.

(70) Liu, Z.; Fan, A. C.; Rakhra, K.; Sherlock, S.; Goodwin, A.; Chen, X.; Yang, Q.; Felsher, D. W.; Dai, H. *Angew Chem Int Ed Engl* **2009**, *48*, 7668.

(71) Pillemer, L.; Schoenberg, M. D.; Blum, L.; Wurz, L. *Science* **1955**, *122*, 545.

(72) Pillemer, L.; Blum, L.; Lepow, I. H.; Ross, O. A.; Todd, E. W.; Wardlaw, A. C. *Science* **1954**, *120*, 279.

(73) Kanagawa, M.; Satoh, T.; Ikeda, A.; Adachi, Y.; Ohno, N.; Yamaguchi, Y. *J. Bio. Chem.* **2011**, *286*, 29158.

(74) Deslandes, Y.; Marchessault, R. H.; Sarko, A. *Macromolecules* **1980**, *13*, 1466.

(75) Marchessault, R. H.; Deslandes, Y.; Ogawa, K.; Sundararajan, P. R. *Can. J. Chem.Rev. Can. Chim.* **1977**, *55*, 300.

(76) Atkins, E. D. T.; Parker, K. D. *Nature* **1968**, *220*, 784.

(77) Yanaki, T.; Norisuye, T.; Fujita, H. *Macromolecules* **1980**, *13*, 1462.

(78) Numata, M.; Asai, M.; Kaneko, K.; Bae, A. H.; Hasegawa, T.; Sakurai, K.; Shinkai, S. *J. Am. Chem. Soc.* **2005**, *127*, 5875.

(79) Regina, A.; Demeule, M.; Che, C.; Lavallee, I.; Poirier, J.; Gabathuler, R.; Beliveau, R.; Castaigne, J. P. *Brit. J. Pharm.* **2008**, *155*, 185.

(80) Zhao, J.; James, T. D. *Chem. Commun.* **2005**, 1889.

(81) Huang, Y. J.; Jiang, Y. B.; Bull, S. D.; Fossey, J. S.; James, T. D. *Chem. Commun.* **2010**, *46*, 8180.

(82) Phillips, M. D.; Fyles, T. M.; Barwell, N. P.; James, T. D. *Chem. Commun.* **2009**, 6557.

(83) M. I. Wolfrom; Solms, J. *J. Org. Chem.* **1956**, *21*, 815.

(84) Lappert, M. F. *Chem. Rev.* **1956**, *56*, 959.

(85) Porand, J. P. *J. Org. Chem.* **1959**, *24*, 769.

(86) Hartley, J. H.; Phillips, M. D.; James, T. D. *New J. Chem.* **2002**, *26*, 1228.

(87) R.J. Ferrier *Adva. Carbo. Chem. Biochem.* **1978**, *35*, 31.

(88) DiCesare, N.; Lakowicz, J. R. *Anal. Biochem.* **2001**, *294*, 154.

(89) Friedman, S.; Pizer, R. *J. Am. Chem. Soc.* **1975**, *97*, 6059.

(90) Babcock, L.; Pizer, R. *Inorg. Chem.* **1983**, *22*, 174.

(91) Pizer, R.; Tihal, C. *Inorg. Chem.* **1992**, *31*, 3243.

(92) Smith, B. W.; Luzzi, D. E.; Achiba, Y. *Chem. Phys. Lett.* **2000**, *331*, 137.

(93) Hu, J. Q.; Bando, Y.; Golberg, D. *J. Mater. Chem.* **2009**, *19*, 330.

(94) Mittal, J.; Monthioux, M.; Allouche, H.; Stephan, O. *Chem. Phys. Lett.* **2001**, *339*, 311.

(95) Hutchison, J. L.; Sloan, J.; Kirkland, A. I.; Green, M. L. *J. Electron Microsc. (Tokyo).* **2004**, *53*, 101.

(96) Xu, C. G.; Sloan, J.; Brown, G.; Bailey, S.; Williams, V. C.; Friedrichs, S.; Coleman, K. S.; Flahaut, E.; Hutchison, J. L.; Dunin-Borkowski, R. E.; Green, M. L. H. *Chem. Commun.* **2000**, 2427.

(97) Meyer, R. R.; Sloan, J.; Dunin-Borkowski, R. E.; Kirkland, A. I.; Novotny, M. C.; Bailey, S. R.; Hutchison, J. L.; Green, M. L. H. *Science* **2000**, *289*, 1324.

(98) Wilson, M.; Madden, P. A. *J. Am. Chem. Soc.* **2001**, *123*, 2101.

(99) Brown, G.; Bailey, S. R.; Sloan, J.; Xu, C. G.; Friedrichs, S.; Flahaut, E.; Coleman, K. S.; Hutchison, J. L.; Dunin-Borkowski, R. E.; Green, M. L. H. *Chem. Commun.* **2001**, 845.

(100) Sloan, J.; Terrones, M.; Nufer, S.; Friedrichs, S.; Bailey, S. R.; Woo, H. G.; Ruhle, M.; Hutchison, J. L.; Green, M. L. *J. Am. Chem. Soc.* **2002**, *124*, 2116.

(101) Fu, W.; Xu, L.; Azurmendi, H.; Ge, J.; Fuhrer, T.; Zuo, T.; Reid, J.; Shu, C.; Harich, K.; Dorn, H. C. *J. Am. Chem. Soc.* **2009**, *131*, 11762.

(102) Shu, C.; Corwin, F. D.; Zhang, J.; Chen, Z.; Reid, J. E.; Sun, M.; Xu, W.; Sim, J. H.; Wang, C.; Fatouros, P. P.; Esker, A. R.; Gibson, H. W.; Dorn, H. C. *Bioconj. Chem.* **2009**, *20*, 1186.

(103) Shu, C. Y.; Ma, X. Y.; Zhang, J. F.; Corwin, F. D.; Sim, J. H.; Zhang, E. Y.; Dorn, H. C.; Gibson, H. W.; Fatouros, P. P.; Wang, C. R.; Fang, X. H. *Bioconj. Chem.* **2008**, *19*, 651.

(104) Hirahara, K.; Suenaga, K.; Bandow, S.; Kato, H.; Okazaki, T.; Shinohara, H.; Iijima, S. *Phys. Rev. Lett.* **2000**, *85*, 5384.

(105) Suenaga, K.; Tence, T.; Mory, C.; Colliex, C.; Kato, H.; Okazaki, T.; Shinohara, H.; Hirahara, K.; Bandow, S.; Iijima, S. *Science* **2000**, *290*, 2280.

(106) Kataura, H.; Maniwa, Y.; Kodama, T.; Kikuchi, K.; Hirahara, K.; Suenaga, K.; Iijima, S.; Suzuki, S.; Achiba, Y.; Kratschmer, W. *Synth. Met.* **2001**, *121*, 1195.

(107) Smith, B. W.; Luzzi, D. E. *Chem. Phys. Lett.* **2000**, *321*, 169.

(108) Luzzi, D. E.; Smith, B. W. *Carbon* **2000**, *38*, 1751.

(109) M.S. Dresselhaus, G. D. a. P. C. E. I. *Science of fullerenes and carbon nanotubes*; Academic Press, San Diego, CA, 1995.

(110) Kiang, C. H.; Choi, J. S.; Tran, T. T.; Bacher, A. D. *J. Phys. Chem. B* **1999**, *103*, 7449.

(111) Zhang, Z. L.; Li, B.; Shi, Z. J.; Gu, Z. N.; Xue, Z. Q.; Peng, L. M. *J. Mater. Res.* **2000**, *15*, 2658.

(112) Govindaraj, A.; Satishkumar, B. C.; Nath, M.; Rao, C. N. R. *Chem. Mater.* **2000**, *12*, 202.

(113) Sloan, J.; Hammer, J.; Zwiefka-Sibley, M.; Green, M. L. H. *Chem. Commun.* **1998**, 347.

(114) Massoud, T. F.; Gambhir, S. S. *Genes & Development* **2003**, *17*, 545.

(115) Sitharaman, B.; Kissell, K. R.; Hartman, K. B.; Tran, L. A.; Baikalov, A.; Rusakova, I.; Sun, Y.; Khant, H. A.; Ludtke, S. J.; Chiu, W.; Laus, S.; Toth, E.; Helm, L.; Merbach, A. E.; Wilson, L. J. *Chem. Commun.* **2005**, 3915.

(116) Choi, J. H.; Nguyen, F. T.; Barone, P. W.; Heller, D. A.; Moll, A. E.; Patel, D.; Boppart, S. A.; Strano, M. S. *Nano Lett.* **2007**, *7*, 861.

(117) Worle-Knirsch, J. M.; Pulskamp, K.; Krug, H. F. *Nano Lett* **2006**, *6*, 1261.

(118) Hartman, K. B.; Laus, S.; Bolskar, R. D.; Muthupillai, R.; Helm, L.; Toth, E.; Merbach, A. E.; Wilson, L. J. *Nano Lett.* **2008**, *8*, 415.

(119) Welsher, K.; Liu, Z.; Daranciang, D.; Dai, H. *Nano Lett.* **2008**, *8*, 586.

(120) Bottini, M.; Cerignoli, F.; Dawson, M. I.; Magrini, A.; Rosato, N.; Mustelin, T. *Biomacromolecules* **2006**, *7*, 2259.

(121) Liu, Z. A.; Li, X. L.; Tabakman, S. M.; Jiang, K. L.; Fan, S. S.; Dai, H. J. *J. Am. Chem. Soc.* **2008**, *130*, 13540.

(122) Chen, Z.; Tabakman, S. M.; Goodwin, A. P.; Kattah, M. G.; Daranciang, D.; Wang, X. R.; Zhang, G. Y.; Li, X. L.; Liu, Z.; Utz, P. J.; Jiang, K. L.; Fan, S. S.; Dai, H. J. *Nat. Biotechnol.* **2008**, *26*, 1285.

(123) Liu, Z.; Cai, W.; He, L.; Nakayama, N.; Chen, K.; Sun, X.; Chen, X.; Dai, H. *Nat Nanotechnol* **2007**, *2*, 47.

(124) Liu, Z.; Tabakman, S. M.; Chen, Z.; Dai, H. *Nat. Prot.* **2009**, *4*, 1372.

(125) Phelps, M. E.; Hoffman, E. J.; Mullani, N. A.; Terpogossian, M. M. *J. Nucl. Med.* **1975**, *16*, 210.

(126) Phelps, M. E. *J. Nucl. Med.* **2000**, *41*, 661.

(127) Cherry, S. R.; Shao, Y.; Silverman, R. W.; Meadors, K.; Siegel, S.; Chatziioannou, A.; Young, J. W.; Jones, W. F.; Moyers, J. C.; Newport, D.; Boutefnouchet, A.; Farquhar, T. H.; Andreaco, M.; Paulus, M. J.; Binkley, D. M.; Nutt, R.; Phelps, M. E. *IEEE Trans. Nuc. Sci.* **1997**, *44*, 1161.

(128) Wang, H. F.; Wang, J.; Deng, X. Y.; Sun, H. F.; Shi, Z. J.; Gu, Z. N.; Liu, Y. F.; Zhao, Y. L. *J Nanosci Nanotechno.* **2004**, *4*, 1019.

(129) Singh, R.; Pantarotto, D.; Lacerda, L.; Pastorin, G.; Klumpp, C.; Prato, M.; Bianco, A.; Kostarelos, K. *Proc. Natl. Acad. Sci. U. S. A.* **2006**, *103*, 3357.

(130) McDevitt, M. R.; Chattopadhyay, D.; Kappel, B. J.; Jaggi, J. S.; Schiffman, S. R.; Antczak, C.; Njardarson, J. T.; Brentjens, R.; Scheinberg, D. A. *J. Nucl. Med.* **2007**, *48*, 1180.

(131) McDevitt, M. R.; Chattopadhyay, D.; Jaggi, J. S.; Finn, R. D.; Zanzonico, P. B.; Villa, C.; Rey, D.; Mendenhall, J.; Batt, C. A.; Njardarson, J. T.; Scheinberg, D. A. *PLoS One* **2007**, *2*, e907.

(132) Royer, C. A. *Biophys. J.* **1995**, *68*, 1191.

(133) Oheim, M.; Michael, D. J.; Geisbauer, M.; Madsen, D.; Chow, R. H. *Adv. Drug Del. Rev.* **2006**, *58*, 788.

(134) Minsky, M. *USPTO* **19/12/1961**, *US3013467A*.

(135) Cremer, C.; Cremer, T. *Microsc. Acta* **1978**, *81*, 31.

(136) Li, Z.; Hulderman, T.; Salmen, R.; Chapman, R.; Leonard, S. S.; Young, S. H.; Shvedova, A.; Luster, M. I.; Simeonova, P. P. *Environ. Health Perspect.* **2007**, *115*, 377.

(137) Chang, C. W.; Sud, D.; Mycek, M. A. *Methods Cell Biol.* **2007**, *81*, 495.

(138) Sekar, R. B.; Periasamy, A. *J. Cell Biol.* **2003**, *160*, 629.

Chapter 2 Interactions between amino acid-tagged naphthalenediimide and single walled carbon nanotubes for the design and construction of new bioimaging probes

2.1 Introduction

New synthetic routes to functionalised fullerenes and carbon nanotubes using molecular recognition and encapsulation techniques can lead to optoelectronic materials with nanotechnological applications ranging from future photovoltaics[1] to nanoreactors for controlled chemical reactions[2] and to sensors and drug delivery devices.[3-7] Single walled carbon nanotubes (SWNTs) have been studied for their potential as electronic nanodevices with unique electron transport properties on the nano-scale.[4,8] The supramolecular encapsulation of fluorescent molecules inside the hollow cavity of SWNTs (e.g. polythiophenes[9]) and their self-assembly onto the surface of aromatic carbon nanomaterials (e.g. tailor-made porphyrin hosts [10] or water soluble perylenes[11,12]) has been a lively area of exploration in the quest for new nano-hybrids with potential applications ranging from new luminescent materials to molecular imaging tools.[4,5,7-9,12-33] Naphthalenediimides (NDI) are emerging both as a building block for organic nanotube creation[34] and as a promising class of chromophores because of their strong absorption and fluorescence emission at visible and near IR wavelengths.[35] NDI fluorescence emissions show maxima between 300-800 nm, including in the spectral region where the interference from the autofluorescence of living cells (300-650 nm) may be bypassed; this makes them attractive candidates as building blocks for optical imaging probes.[35-42] NDI derivatives have been recently explored as DNA intercalators by virtue of their aromatic stacking with purines and pyrimidines[40,43,44] and as fluorescent tags for hypoxia-targeting probes such as nitroimidazoles.[45-47] Due to their aromatic stacking ability, fluorescence and

electrochemical properties, NDIs are of interest as building blocks for biomimetic supramolecular and functional materials.[48-50] Amino acid-functionalised NDI molecules self-assemble into helical nanotubular, supramolecular structures from weakly polar solvents.[51,52] These dynamic structures are capable of recognising and solubilising fullerenes and ion pairs:[53] the Sanders group has shown that carbon materials such as C_{60} sense the helicity of the NDI host environment[54] whereas C_{70} provoked an entirely unexpected reorganisation to give a hexameric receptor.[55] The NDI supramolecular nanotubes which have cavities with diameters in the range of 1-2 nm created by hydrogen bonding have been shown to act as receptors for aromatic molecules including naphthalene-based guests or fullerenes.[42,56]

Fluorescence imaging studies on fluorescent carbon nanotubes have thus far focused primarily on the measurement of the steady state spatial changes in emission intensity or wavelength.[3,13-17,19,21,57-64] The use of fluorescence lifetime imaging microscopy (FLIM) in combination with multiphoton excitation and near infrared[65] femtosecond laser pulses is widely used in the study of small molecule fluorophores.[66-69] To date FLIM has been used primarily on endogenous molecules such as tryptophan and common fluorescent dyes (e.g. GFP-tagged proteins and fluorescein-based derivatives),[70,71] with recent work exploring lifetime imaging of fluorescent platinum complexes permitting for the first time microsecond resolved emission imaging microscopy.[70] There are, to the best of our knowledge, thus far no reports on supramolecular assemblies involving carbon nanomaterials studied by this method. The combination of two-photon excitation with fluorescence lifetime imaging techniques (FLIM) allows the use of near IR light to provide deeper tissue penetration, reduced cellular cytotoxicity and scattering and improved signal detection. Due to the defined nature of the emission lifetime and the sensitivity of lifetime measurements, excited state lifetime measurements could provide a powerful means by which to study donor-acceptor complexes in cells.

We have been interested in the design and spectroscopic investigation of new nanomaterials with light emitting properties.[63] The NDI nanotubular receptor recently developed[52] has the ability to bind via donor-acceptor interactions to carbon nanomaterials, therefore we investigated the formation of a new nano-hybrid, denoted NDI@SWNT, in solution and on a preparative scale. We report here for the first time, the recognition and coating of the aromatic surface of steam-purified SWNTs (Thomas Swan Ltd, Elicarb SWNTs, free of catalytic impurities or carbonaceous materials from the nanotube synthesis, see Experimental section Chapter 7) by a new iodine- and amino acid-derivatised NDI. Investigations into the properties of the new material synthesized (in bulk and in dispersions in $CHCl_3$, EtOH, DMSO and serum free aqueous cell culture media such as EMEM) have been carried out by Raman, circular dichroism, FT IR, UV-Vis-NIR and fluorescence spectroscopies and imaged at the nano-scale by HR TEM, SEM, EDS and TM AFM. The cellular translocation of the resulting NDI@SWNT complex was investigated by a combination of fluorescence microscopy techniques including fluorescence lifetime imaging and cytotoxicity assays (MTT) in cancerous and non-cancerous cell lines. Here we have used such techniques to probe the integrity of a new nanocomposite denoted NDI@SWNT *in vitro*. Such an approach could aid the future understanding of the mechanism of action of supramolecular materials at the cellular level and improve the synthetic design of nano-hybrids for biomedical imaging and therapeutic applications.

2.2 Results and Discussions

2.2.1 Synthesis, single crystal X-ray diffraction and molecular modeling of new iodine-tagged naphthalenediimides (NDI)

To facilitate the direct observation of these nanodimensional aggregates by electron microscopy techniques coupled with energy dispersive X-ray spectroscopy (EDS) analysis, we designed a new NDI molecule which includes iodine (Z = 53) as a high scattering heavy element.

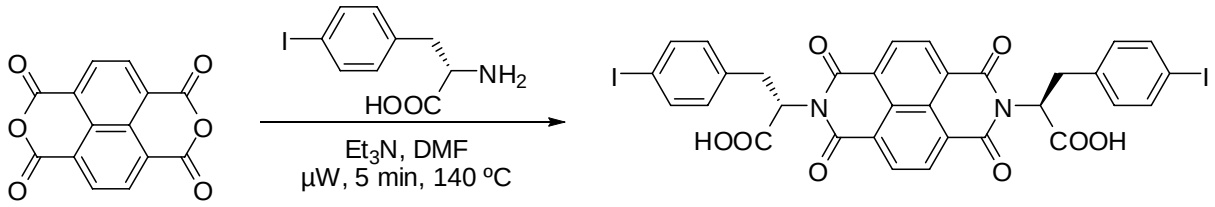

Scheme 2.1. Synthesis of iodine-derivatised NDI

The new amino acid-derivatised and iodine-tagged NDI was synthesized from L-4-iodophenylalanine and 1,4,5,8-naphtalene-tetracarboxylic dianhydride, using a microwave-assisted method(**Scheme 2.1**).[51,52]

The molecular structure and supramolecular architecture of NDI was determined in the solid state by single crystal X-ray crystallography (Figure 2.1). The NDI molecules are oriented face-on and show two amino acid groups placed anti with respect to the aromatic core. No aromatic stacking was observed in the unit cell but intramolecular and intermolecular dipole interactions link up stacks of NDI molecules, whereby the I···(O)COH dipole interactions have rather short (3.184 Å) separations. Thus, the NDI supramolecular structure shows weakly linked, hence flexible and likely to act as adaptive, tubular arrangements in the solid state, with cavities of ca 1.24 nm filled with disordered crystallizing solvents.

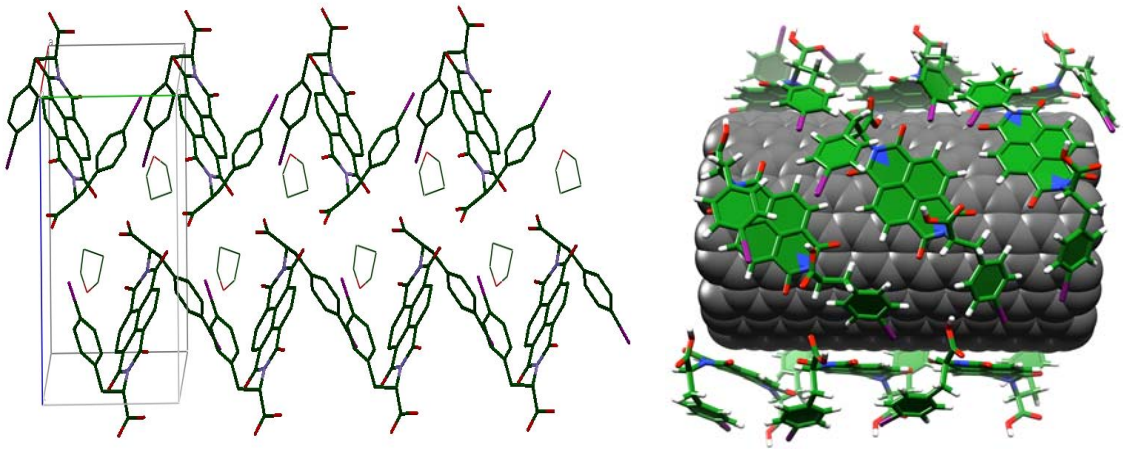

a **b**

Figure 2.1. a) X-ray structure of NDI: unit cell fragment, view over axis a; **b**) Proposed structure of a fragment of NDI@SWNT composite: molecular mechanics minimised representation (Forcite) of NDI stacks self-assembled on the surface of a [10:10] SWNT fragment. [Color code: purple: I, grey/green: C, white:H, red:O, blue:N].

To isolate NDI@SWNT composites on a preparative scale, a solution of NDI dissolved in $CHCl_3$: EtOH 4:1 (6 mg/mL) was treated with 1 mg of purified single walled carbon nanotubes (Elicarb©, Thomas Swann). The mixture was sonicated for 30 min (340 W), followed by centrifugation (1500 rotations/min) and filtration (a 200 nm pore diameter membrane). The separated solid material was dispersed in minimum amount of $CHCl_3$: EtOH 4:1 and the sonication, centrifugation and filtration sequence was repeated at least 3 times (stages 1-3 of dispersion experiment). The resulting liquid phases were analysed by UV-Vis, UV-Vis-NIR and steady state fluorescence spectroscopies (Figure 2.3, *vide infra*), which confirmed the removal of excess and weakly bound NDI and the presence of dispersible SWNTs. After at least 3 cycles of dispersion/filtration, the resulting solid residue denoted NDI@SWNT was redispersed in $CHCl_3$: EtOH 4:1 (with 30 min sonication, stage 4) to give a transparent dispersion (0.2 mg/mL, Appendix Figure 8.1) which was stable for days without precipitation. Formation of stable and clear dispersions was also observed when DMSO or aqueous cell medium (EMEM, Eagle's Modified Essential Medium, phenol-red free) were used to 'solubilise' the NDI@SWNT hybrid.

In an attempt to describe the structure of NDI@SWNT, we propose a molecular mechanics (MM+, Forcite) model of SWNT encapsulated within the supramolecular nanotubular receptor framework of NDI based on the X-ray structure determination of the NDI (Figure 2.1). It has already been shown that certain NDI networks may adjust their adaptable tubular cavities in order to encapsulate via aromatic stacking guests with diameters in the range of 1 nm (for C_{60} [54] or C_{70} [55]). DFT computational modeling was used to aid our understanding of the geometry adopted by an isolated NDI molecule in the presence of a SWNT and the nature of its interactions with this aromatic guest. Here, the simplified SWNT model used was 1.6 nm wide. A hierarchy of DFT-based codes (SIESTA, Spanish Initiative for Electronic Simulations with Thousands of Atoms[72]) allowed the *ab initio* total energy calculations of these large systems, thus aiding investigations of the structural and electronic behavior of NDI absorbed onto SWNTs (Figure 2.2). To examine more closely the interaction between an isolated NDI molecule and SWNT surface we modeled at the DFT level a simplified capped model of a short [10,10] SWNT and two possible geometries for the corresponding NDI:SWNT 1:1 complex:

(**A**) NDI decorates the sidewall of the SWNT and

(**B**) NDI is bound face-on to the tip of the SWNT.

Table 2.1 shows calculated distances at the binding of NDI to SWNTs. These compare well with the known, simpler model of NDI molecule bound to C_{60}. The calculated binding energies for the NDI interaction with the sidewall of the SWNT and to the tip of the SWNT are −0.84 eV and −0.66 eV respectively, indicating a π-orbital interaction between the NDI aromatic ring and the aromatic network of the model SWNT. According to the DFT estimated binding energies (Table 2.1), it is clear that the interaction between NDI and SWNT is of a similar order of magnitude to that between NDI and C_{60} and these are both of a rather weak non-covalent nature. In terms of binding energy values the NDI molecule binds more strongly to a single strand of a short and idealised [10,10] SWNT than to a C_{60} molecule. One of the

limitations in the DFT model used is the overestimation of the binding energy caused by weak interactions.[73] This has been first highlighted for the modeling of a supramolecular benzene dimer.[74] For this simple aromatic stacking model interaction DFT calculations yielded an inter-ring distance of 3.06 Å and a binding energy of −0.48 eV, whereas higher level modeling (CCSD (T)) calculations gave corresponding values of 4.1 Å and −0.05 eV respectively.[74] A similar computational approach was applied hereby by our collaborator Dr Navaratnarajah Kuganathan (UCL) and was detailed in a previous publication by the Pascu group.[63]

Table 2.1. DFT-calculated binding energies Eb(eV) and NDI-aromatic guest distances in the optimised composite geometries. For a comparison, the gas-phase DFT estimated charge transfer at the absorbtion of NDI onto C60 (NDI:SWNT 1:1) is also given.

System	**Charge transfer [NDI/aromatic surface]**	**Closest C-C distances between aromatic surface and NDI (Å)**	**Uncorrected binding energy (eV) E_b (unc) [a]**	**Corrected binding energy (eV) $E_{b\ (CP)}$ [b]**
NDI@C_{60}	0.024	3.230, 3.294, 3.307, 3.334, 3.462, 3.484, 3.523	−0.66	−0.31
NDI@SWNT (Configuration **A,** *middle of SWNT*)	0.086	3.150, 3.310, 3.455, 3.700, 4.020, 4.090, 4.140	−1.03	−0.84
NDI@SWNT (Configuration **B,** *tip of SWNT*)	0.044	2.926, 3.104, 3.360, 3.398, 3.587, 3.853, 3.920	−0.95	−0.66

Note:

a) Defined as described in Appendix Determined by the counterpoise correction (CP) method [75]

First-principles computational studies using density functional theory (DFT) were performed on a naphthalenediimide (NDI) molecule anchored onto a model single strand of a [10. 10] SWNT. Table 2.1 lists the binding energies calculated for the NDI@SWNT where the configurations shown in Figure 2.2 were optimised. These were compared with the simpler case

of NDI binding to C_{60} giving a model complex NDI: C_{60} 1:1.The interaction between the NDI and C_{60} molecules is −0.31 eV indicating a π-orbital interaction between the NDI aromatic ring and the C-ring of the C_{60}. The calculated binding energies for the NDI interaction with the sidewall of the SWNT and to the tip of the SWNT are −0.84 eV and −0.66 eV respectively. According to these estimated binding energies, it is clear that the interactions between NDI with C_{60} or SWNT are both of a rather weak non-covalent nature. However, in terms of binding energy values the NDI molecule binds stronger to a single strand of a short and idealised [10,10] SWNT than to a C_{60} molecule. The closest C-C distances (Table 2.1) were measured in optimised geometries of the NDI@SWNT and NDI@C_{60} composites to further explore the nature of bonding in simplified 1:1 model complexes. Table 2.1 summarises the amount of charge transfer between a molecule of NDI and the aromatic guest (C_{60} or the model SWNT considered). Calculations show that the interactions between either C_{60} or SWNT and a single molecule of NDI occur with a negligible charge transfer in the gas phase. For the C_{60}: NDI complex, the estimated charge transfer between one NDI and one C_{60} molecule was 0.024 electrons. For the NDI@SWNT composite where an NDI molecule is bound to the middle of the SWNT strand (configuration **A,** Figure 2.2), 0.086 electrons were transferred between a molecule of NDI and the [10, 10] SWNT model. For the NDI@SWNT composite in the tip-binding configuration **B** (Figure 2.2), 0.044 electrons were transferred between NDI and the [10, 10] SWNT model. In order to investigate the charge transfer between two adjacent NDI molecules (in the absence of SWNT) we performed a control calculation on two stacked NDI molecules using a fragment of the asymmetric unit for the X-ray structure determination: this showed that a negligible NDI-NDI charge transfer occurs.

Since the DFT-optimised model used for computational studies, considered only a very short length for the SWNT modeled (200 nm): this allows maximum 6 NDI molecules to bind

in configuration **A** (to the middle part of the SWNT) and a further 4 NDI molecules to bind in configuration **B** (coating the tip of the SWNTs).

Observations from HR TEM coupled with EDS (*vide infra*) showed that NDI molecules coating both the surface and the tips of the SWNT are giving a monolayer of NDI@SWNTs. NDI@SWNT composites with dimensions of 200-500 nm length have been observed by microscopy (AFM, SEM and HR TEM, *vide infra*) in samples deposited on supports from $CHCl_3$: EtOH dispersions, Thus, DFT calculations estimate that overall approximately 2 *electrons* are transferred between the nano-receptor formed by 10 molecules of NDI absorbed onto the outer surface of a 500 nm long capped SWNT fragment. Since fluorescence spectroscopy showed a significant quenching of NDI emission in the presence of SWNTs this is likely to be due to the donor-acceptor interactions and DFT calculations support this hypothesis.

Calculations showed that for a model NDI@SWNT composite with configuration **A** (Figure 2.2 c, where an NDI molecule is bound to the middle of the SWNT strand, 0 0.086 electrons were transferred between a molecule of NDI and the [10, 10] SWNT. For the NDI@SWNT composite in the tip-binding configuration **B** (Figure 2.2 d), 0.044 electrons were transferred between NDI and the carbon nanotube. In order to investigate the charge transfer between two adjacent NDI molecules we performed a control calculation in the absence of SWNT, where only two stacked NDI molecules were modeled. Initial geometries for the NDI-NDI complex were generated using a fragment of the asymmetric unit for the X-ray structure determination. This showed that a negligible NDI-NDI charge transfer occurs in the absence of the aromatic guest (C_{60} or SWNT).

Our DFT-optimised model used for computational studies considered only a very short length for the SWNT modeled (200 nm): this allows maximum 6 NDI molecules to bind in configuration **A** (to the middle part of the SWNT) and a further 4 NDI molecules to bind in configuration **B** (coating the tip of the SWNTs). According to gas-phase DFT modeling, NDI

and SWNTs are held together by non-covalent interactions whereby approximately 2 electrons are transferred between the nano-receptor formed by 10 molecules of NDI absorbed onto the outer surface of a 500 nm long capped SWNT fragment. In solution, steady-state fluorescence spectroscopy showed a significant quenching of NDI emission in the presence of SWNTs. DFT calculations support the hypothesis that donor-acceptor interactions may occur between NDI and SWNTs and that these are similar in nature to those found in known NDI-C_{60} complexes.[54]

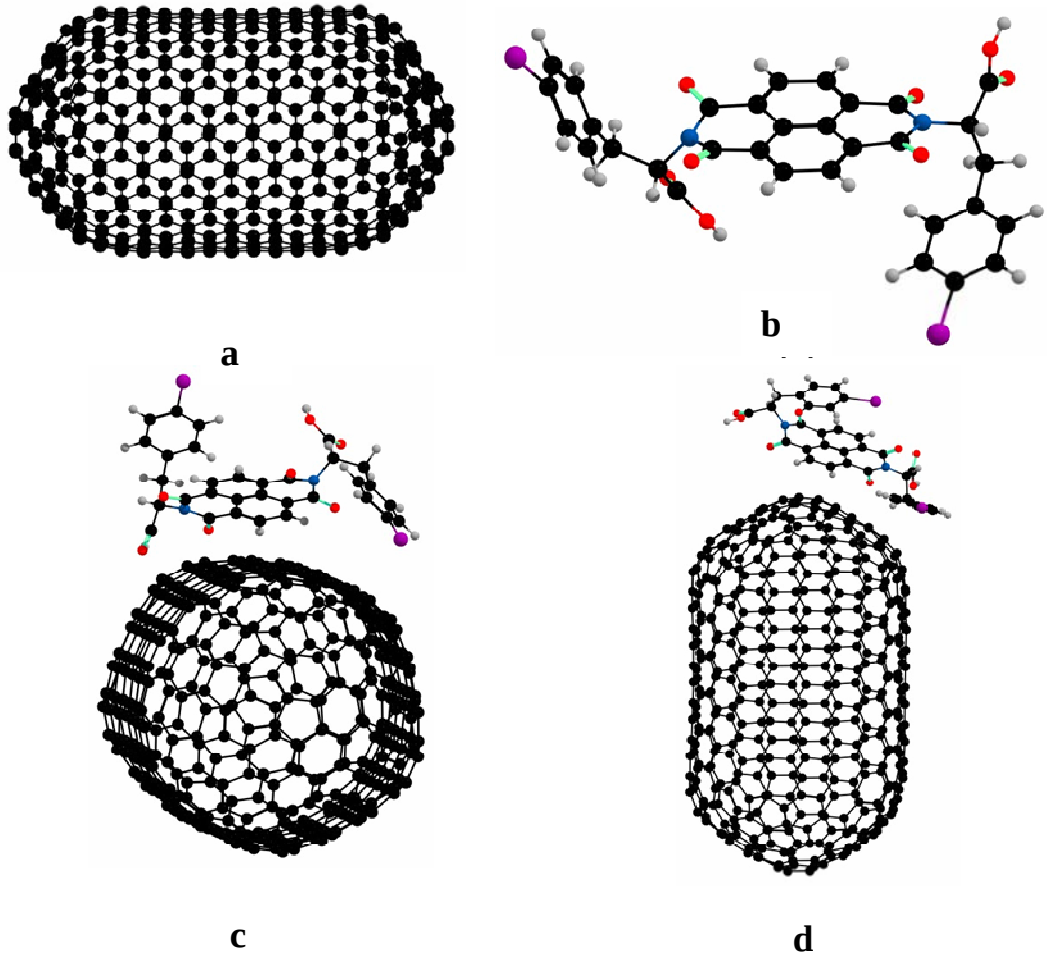

Figure 2.2. DFT-level optimised geometries (SIESTA) of model compounds: (**a**) a short [10,10] capped SWNT; (**b**) NDI molecule; (**c**) NDI molecule bound supramolecularly onto the middle part of a [10,10] capped SWNT (configuration a); (**d**) NDI molecule bound to the tip of a [10,10] capped SWNT (configuration b). [Colour code: black – carbon, red – oxygen, nitrogen – blue, violet– iodine, grey – hydrogen]

2.2.2 Spectroscopic characterisation of NDI@SWNT composite

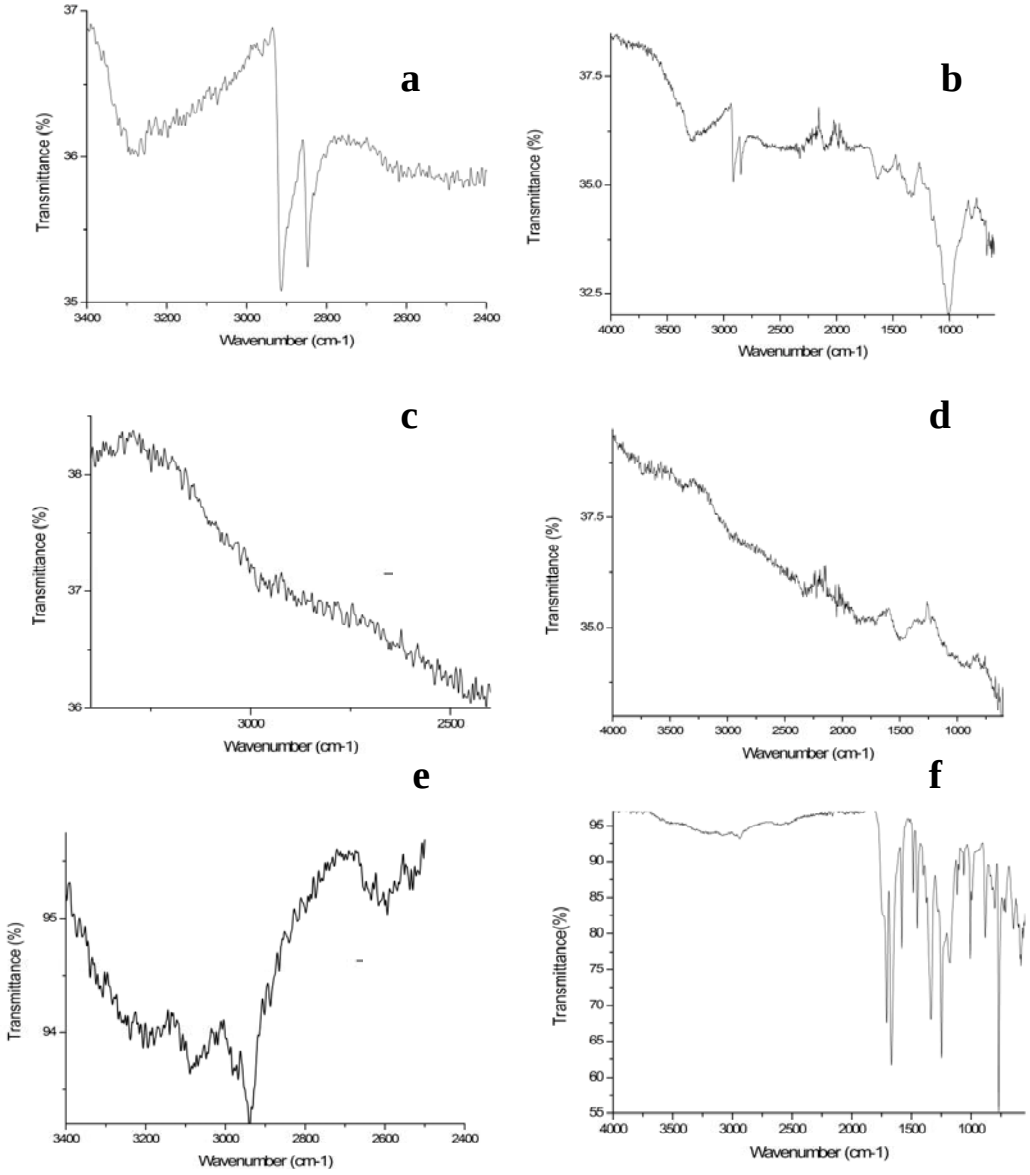

Figure 2.3. Solid state FT IR spectroscopy of (**a**) and (**b**) NDI@SWNT composite; (**c**) and (**d**) free SWNT; (**e**) and (**f**) free NDI. Images **a, c** and **d** represent expansion in the 3400-2400 cm^{-1} region of the spectrum, show the presence of –COOH in free NDI and in NDI@SWNT.

Solid state FT-IR spectroscopy (Figure 2.3) of the solid composite prepared as above suggested functionalisation associated with nanotubes, with the spectrum clearly showing the carbonyl (C=O) stretching at 1730 cm^{-1}, the C-O stretching at 1100 cm^{-1} and O-H band at 3300 cm^{-1}. Thus the presence of carboxylic groups associated with the tubes due to the amino acid tagged NDI was confirmed.

Raman spectroscopy is a powerful tool for characterising functionalised carbon nanomaterials:[76,77] spectra shown in Figure 2.4 were recorded for dispersed samples deposited from $CHCl_3$:EtOH (4:1) or DMSO using λ_{ex}= 830 nm, i.e. a region of the emission spectra of the NDI@SWNT without interference from fluorescence emission from NDI. NDI@SWNT showed features consistent with the occurrence of defects in the tube surface post-functionalisation with respect to free SWNTs. The G band (which corresponds to a splitting of the E2g stretching mode of graphite and reflects the structural intensity of the sp^2-hybridised carbon atoms) at ~1590 cm^{-1} and a disordered D band (generally attributed to the disordered graphite structure of the nanotubes) at ~1330 cm^{-1} were observed. For dried samples, deposited from $CHCl_3$:EtOH 4:1, an increase in the I_D/I_G band intensity ratio of the NDI@SWNT solid composite (15%) was observed compared to the I_D/I_G of free SWNTs (9.5%), confirming that the supramolecular functionalisation of SWNTs has occurred.[78-79].

Raman spectra of NDI@SWNT also showed a G' band at ca. 2600 cm^{-1} as well as the radial breathing modes (RBM) between 140-300 cm^{-1}. The latter signal remained largely unchanged with respect to that of the starting material steam-purified SWNTs in DMSO or EMEM. Several broad peaks centered at 150, 165, 189, 235, 239 and 270 cm^{-1} are observed for pristine SWNTs samples and are also visible in the spectra of NDI@SWNT particles deposited on borosilicate glass slides from all solvents investigated, i.e. $CHCl_3$:EtOH 4:1, DMSO and aqueous media EMEM (Figure 2.5). The pristine SWNT sample contains tubes with a broad diameter ranging between 1.8 and 0.8 nm. RBM maxima indicate that tubes with diameters of 1.6, 1 and 0.86 nm are mainly present (Footnote 1) in the starting material used. The spectrum of NDI@SWNT showed significant enhancement and sharpening of the RMB peaks at 147.5, 165 and 240 cm^{-1} respectively, with respect to the RBMs of the pristine SWNTs used. This indicates that in $CHCl_3$: EtOH 4:1, NDI@SWNTs dispersions contain tubes with diameters of 1.65, 1.47 and 0.93 nm.

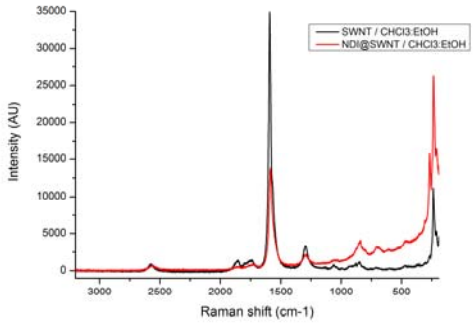

a

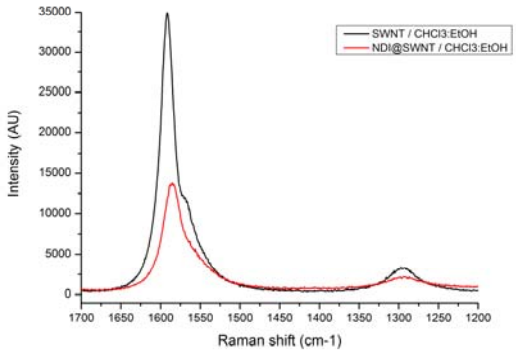

b

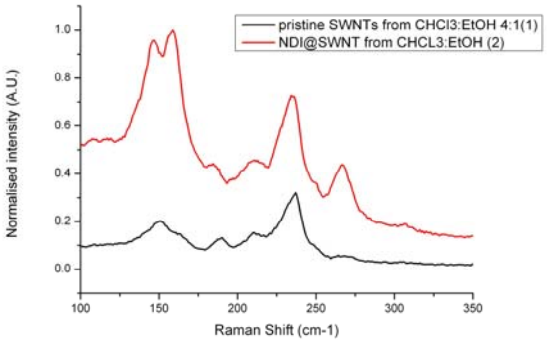

c

Figure 2.4. Raman spectroscopy of purified SWNT and NDI-functionalised SWNTs (λ_{ex}=830 nm, laser power at the sample 220 mW spot size 100 μm. (**a**) Full spectra for materials deposited on borosilicate glass from $CHCl_3$:EtOH 4:1, 0.2 mg/mL dispersions; (**b**) expansion diagnostic of surface functionalisation of SWNT, showing D and G bands for $CHCl_3$:EtOH 4:1. (**c**) RBM of SWNT upon NDI complexation. Spectra of solid materials were recorded three times from different areas of the nanomaterial and the average spectra reported.

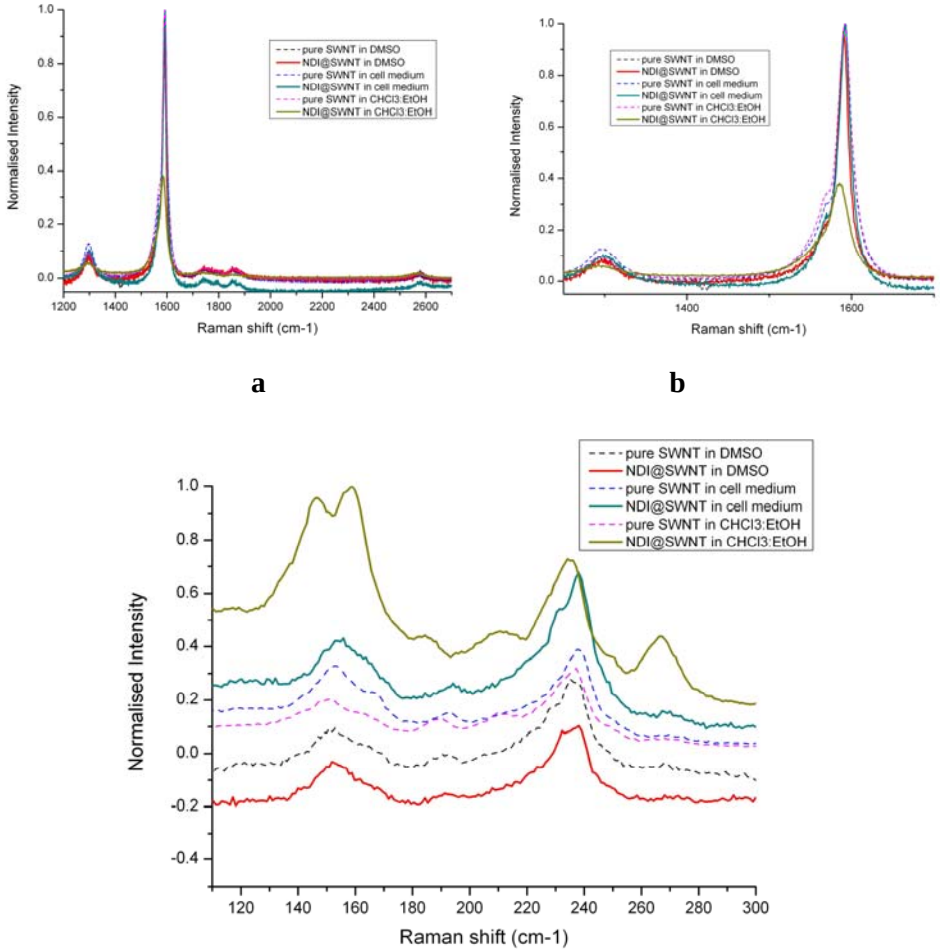

Figure 2.5. Raman spectrum of solid NDI@SWNT deposited from several solvents (λ_{ex}=830 nm) showing the intensity of G and D bands vs Raman shift (cm-1) (**a** and **b**) as well as RMB frequency modes (**c**).

Several broad peaks centred at 150, 165, 189, 235, 239 and 270 cm^{-1} are observed for pristine SWNTs deposited from all investigated solvents (Figure 2.5 c). These signals correspond to SWNTs with a rather broad diameter range, from 1.7 to 0.85 nm but the main components of the pristine SWNT sample used (steam-purified Thomas Swann Elicarb) have diameters of 1.6, 1 and 0.86 nm (estimated according to the equation ϖ= [(223.5/dt)+12.5], where constants 223.5 and 12.5 were taken from literature[80]). In $CHCl_3$:EtOH 4:1, NDI 'solubilises' SWNTs of diameters 1.65, 1.47, 0.93 and 0.87 nm, which are only very minor components of the SWNTs starting material used. This was evidenced from the significant enhancement of the

coresponding RMB and the sharpening of the peaks at 147.5, 165 , 240 and 270 cm^{-1} respectively.

To determine the most reliable NDI:SWNT mass ratio likely to lead to a complete binding of NDI to SWNT and stable dispersions (with respect to nanoparticle precipitation over 24 h) in common solvents, fluorescence and UV-Vis spectroscopic titrations of NDI solutions onto SWNTs dispersions were carried out in several common solvents ($CHCl_3$, EtOH, DMSO). First, aliquots of 2 μg/mL of NDI were added followed by 5 minutes sonication prior to recording each spectrum. The optimum NDI: SWNT mass ratio was obtained when a solution of 26 μM of NDI (21 μg/mL) was anchored onto 35 μg/mL SWNTs dispersed in $CHCl_3$: EtOH 4:1, DMSO or aqueous medium EMEM (containing up to 5 % DMSO) giving the NDI: SWNT mass ratio 0.6. The titration experiment was also repeated by the addition of SWNTs (dispersed in $CHCl_3$:EtOH, 20 μg/mL aliquots) to a solution of NDI (26 μM). The direct spectroscopic observation for the SWNT surface recognition by NDI was thus achieved: NDI@SWNT formation on a preparative scale (using excess of NDI and the filtration /redispersion procedure described above) as well as titration experiments showed an extremely rapid quenching (with ca. 80% decrease in fluorescence intensity) of the NDI fluorescence emission in the presence of SWNTs. Titration curves obtained were typical of very strong binding, as shown in appendix Figure 8.3. The binding of NDI to SWNTs appears to be too tight in solution and did not allow an accurate determination of the association constant using standard binding isotherms. [81] Similar binding curves with extremely sharp end-points were recently observed at the tight non-covalent binding of porphyrin oligomers to SWNTs: the binding constant was believed to be higher than 10^7 M^{-1} in such cases.[81]

The UV-Vis spectroscopy of NDI@SWNT recorded in aqueous medium (EMEM) or in organic solvents $CHCl_3$, $CHCl_3$/EtOH, DMSO and EtOH showed very similar features (Figure 2.6). UV-Vis spectroscopy showed that both NDI@SWNT and free dye NDI have broad and

complex excitation spectra with three characteristic maxima in the 300-400 nm region. The occurrence of a new band was observed in the UV-Vis spectra of samples containing SWNTs (λ_{max} = 280 nm), as well as significant broadening and red-shifting of the bands in the 388 nm region. In DMSO or in aqueous cells media (EMEM containing 1% DMSO), NDI@SWNT dispersions showed a ca. 6 nm red-shift of the band at 388 nm compared with the organic solvents investigated ($CHCl_3$, EtOH). This suggests that the interaction between SWNTs and the NDI molecules absorbed is stronger in biocompatible environment (the cell culture media EMEM or in DMSO) than in the standard organic solvents investigated ($CHCl_3$, EtOH).

The fluorescence spectra of NDI@SWNTs were recorded for excitation wavelengths between 200-800 nm in $CHCl_3$: EtOH, DMSO or aqueous media (EMEM, of relevance for bioimaging investigations) and are broader than those of the free NDI. Both NDI and NDI@SWNT show two emission maxima in the range 300-700 nm (Appendix materials). The position of these bands seems strongly influenced by the nature of the solvent and concentration. As stated above, the severe quenching of the fluorescence emission intensity was observed after adding SWNT (Figure 2.6c), indicating the strong absorption of the aromatic coating material onto the surface of the nanotube.[41] A red-shift in the emission maxima of NDI (20 nm) was also observed upon its anchoring onto SWNTs (Figure 2.7 and Figure 2.8). The broadening in the UV-Vis spectra as well as decay in the fluorescence emission intensity with time was observed, and this behavior stabilises after 24 h presumably as the NDI absorption onto SWNTs reaches completion. The presence of the SWNT as the aromatic guest within the NDI supramolecular network (which acts as a nano-receptor) makes the dispersion phase determination of the fluorescence quantum yield of NDI@SWNT difficult to ascertain with precision. The quantum yield of the free dye was estimated as 2.4 % in $CHCl_3$ and 1.6 % in EtOH (relative to $[Ru(bipy)_3][PF_6]_2$ in H_2O,[82] which is within the range expected for this class of compounds.[83]

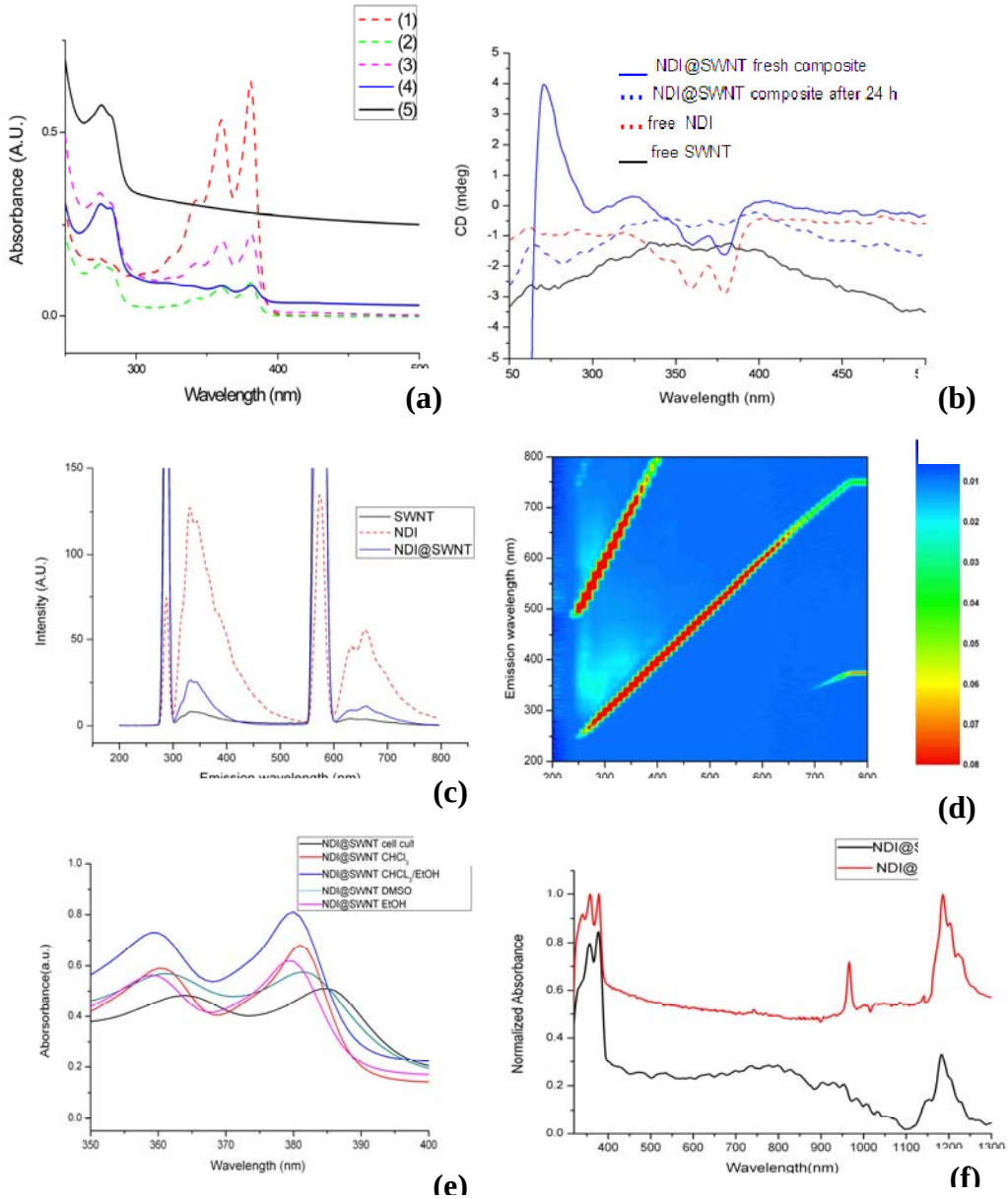

Figure 2.6. **a**) Preparation of NDI@SWNT monitored by UV-Vis spectroscopy in $CHCl_3$:EtOH 4:1. (1)-(3): NDI@SWNTs composites during the stages 1-3 of the synthetic experiment; (4): redispersed NDI@SWNT composite from stage 4 (0.2 mg/mL) and (5): free SWNT (0.35 mg/mL); **b**) CD spectra of NDI@SWNT composite, recorded in fresh dispersions (20 min, followed by filtration through a 200 nm pore PTFE membrane) or after storing at r.t. for 24 h (0.2 mg/mL, $CHCl_3$:EtOH 4:1); **c**) Typical fluorescence emission spectra showing the NDI fluorescence quenching upon treatment of a diluted solution of NDI (26 μM in $CHCl_3$:EtOH 4:1, λ_{ex}=280 nm) with SWNT (35 μg/mL); **d**) Emission/excitation map (normalised intensity) showing that the redispersed NDI@SWNT composite resulting after the stage 4 of the redispersion experiment retains fluorescence (0.2 mg/mL $CHCl_3$:EtOH 4:1). **e**) UV-Vis spectroscopy of NDI@SWNT (0.2 mg/mL) in organic and in aqueous cell culture media (EMEM). **f**) UV-Vis-NIR spectroscopy of NDI@SWNT composite (0.2 mg/mL, $CHCl_3$:EtOH 4:1 and pure $CHCl_3$ dispersions).

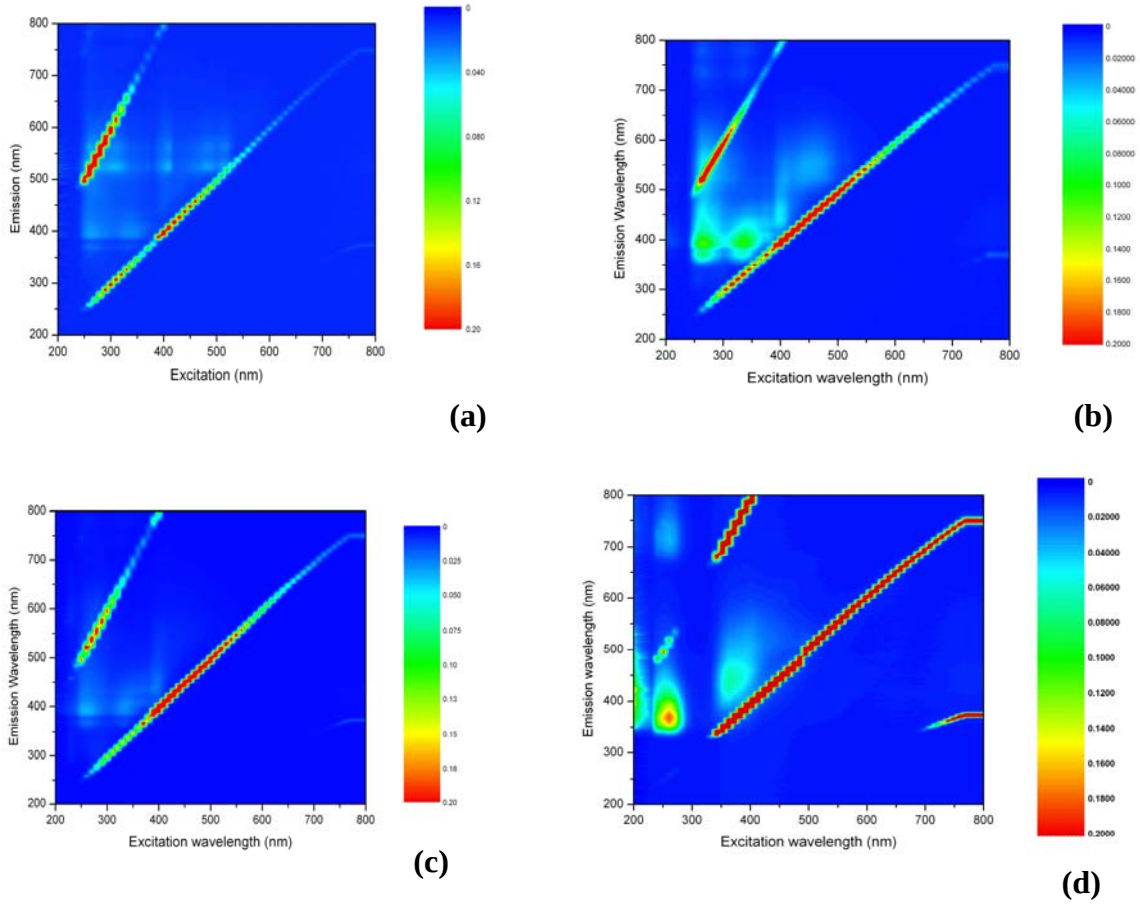

Figure 2.7. Fluorescence spectroscopy (2-D excitation/emission wavelengths plots, with normalised intensities) for free NDI (26 μM) in $CHCl_3$:EtOH 4:1 (**a**), $CHCl_3$ (**b**), EtOH (**c**) and in EMEM: DMSO 99:1 (**d**), showing significant solvent-dependent behaviour.

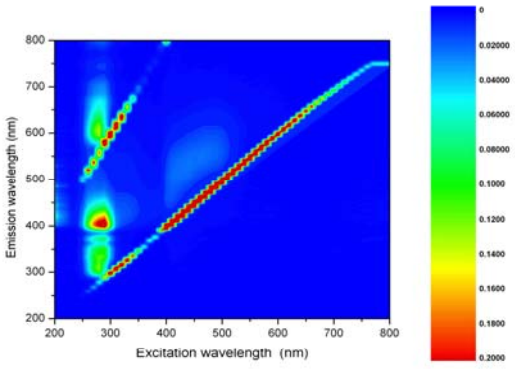

Figure 2.8. Fluorescence spectroscopy (2-D excitation/emission wavelengths plot, normalised intensity) of NDI@SWNT containing 26 μM NDI anchored onto 35 μg/mL SWNTs (mass ratio NDI:SWNT ca 0.6) in EMEM:DMSO 99:1. Fluorescence spectroscopy showed a significant red-shifting of NDI@SWNT emission maxima compared with that of the free NDI.

The circular dichroism (CD) spectrum at the free NDI absorbance (330 – 400 nm) was assigned to interactions between the NDI couplets of sequential interacting NDI chromophores.[84] Changes in the relative position of these moieties lead to changes in the CD fingerprint of the supramolecular assembly. CD spectroscopy showed new features for the NDI@SWNT composite which are due to NDI upon absorption onto the carbon nanomaterial, i.e. the sequential interacting NDIs change their relative position, leading to changes in the 380 nm region of circular dichroism spectrum and the appearance of a new signal in the 260-280 nm region (Figure 2.6 b). CD spectroscopy shows that the initial aggregation motif of free NDI in solution is being altered by the presence of SWNT. The chirality of the amino acid-derivatised NDI molecule is also observed in the NDI@SWNT composites: this is consistent with earlier reports on DNA@SWNT composites studied by this method, whereby DNA helicity was believed to be sensed by carbon nanotubes in dispersions. [20,85,86]

The UV-Vis-NIR spectra of NDI@SWNT (recorded in pure $CHCl_3$ or mixtures of $CHCl_3$:EtOH 4:1) shows the lowest-energy van Hove transition S_{11} for NDI@SWNT (at 1204 nm), and also typical S_{22} transitions at in the 960 nm region (Figure 2.6 f). Partially overlapping of S_{22} and metallic M_{11} transitions characteristic to SWNTs can be seen at 500-1000 nm in NDI@SWNT dispersions. The S_{22} and S_{11} band are sharp compared to those observed in other supramolecularly functionalised SWNT composites (for example those of peptides[78,87,88] or porphyrin oligomers[81]) absorbed onto the SWNTs, and closely similar to those observed in perylene-SWNTs composites[11,12] Since these transition energies are related to the size of the SWNT bundles and the presence of isolated tubes in solution have been reported to give rise to sharp, well-resolved peaks,[26] UV-Vis-NIR spectroscopy of the NDI@SWNT composite suggests that NDI is capable of efficient de-bundling of the SWNT strands in these common organic solvents.

2.2.3 Solid state investigations by HR TEM, AFM and SEM

High resolution transmission microscopy (HR TEM, JEOL 3000F) provided direct evidence for the presence of a monolayer of NDI coating the walls of the SWNTs (Figure 2.69 a and Figure 2.69 b). Areas of strong contrast due to heavy elements, attributable to iodine atoms, are clearly visible with respect to the lighter regions (due to the lower scattering elements present, i.e. carbon, hydrogen, nitrogen, oxygen) and in contrast to the initially clean SWNT surface observed for the high purity, SWNTs used (raw Elicarb SWNTs provided by Thomas Swann Ltd.). HR TEM also showed that NDI coated the ends of the SWNTs and that the NDI layer is less than 2 nm thick, consistent with the qualitative molecular mechanics model proposed in Figure 2.1 for a NDI-wrapped single strand of a [10,10] SWNT. The presence of amorphous carbon created by beam damage of the soft coating under the HR TEM working conditions cannot be fully discounted, but both low resolution TEM and HR TEM coupled with EDS allowed us to probe locally the surface of nanotubes where such dark spots were observed (Figure 2.9a). Characteristic peaks corresponding to iodine were detected in the EDS spectra in the 4 keV region. By contrast with the large bundles typically observed for purified but unfunctionalised SWNT starting material the NDI coated nanotubes tended to aggregate into much smaller bundles or form only single strands in polar solvents.

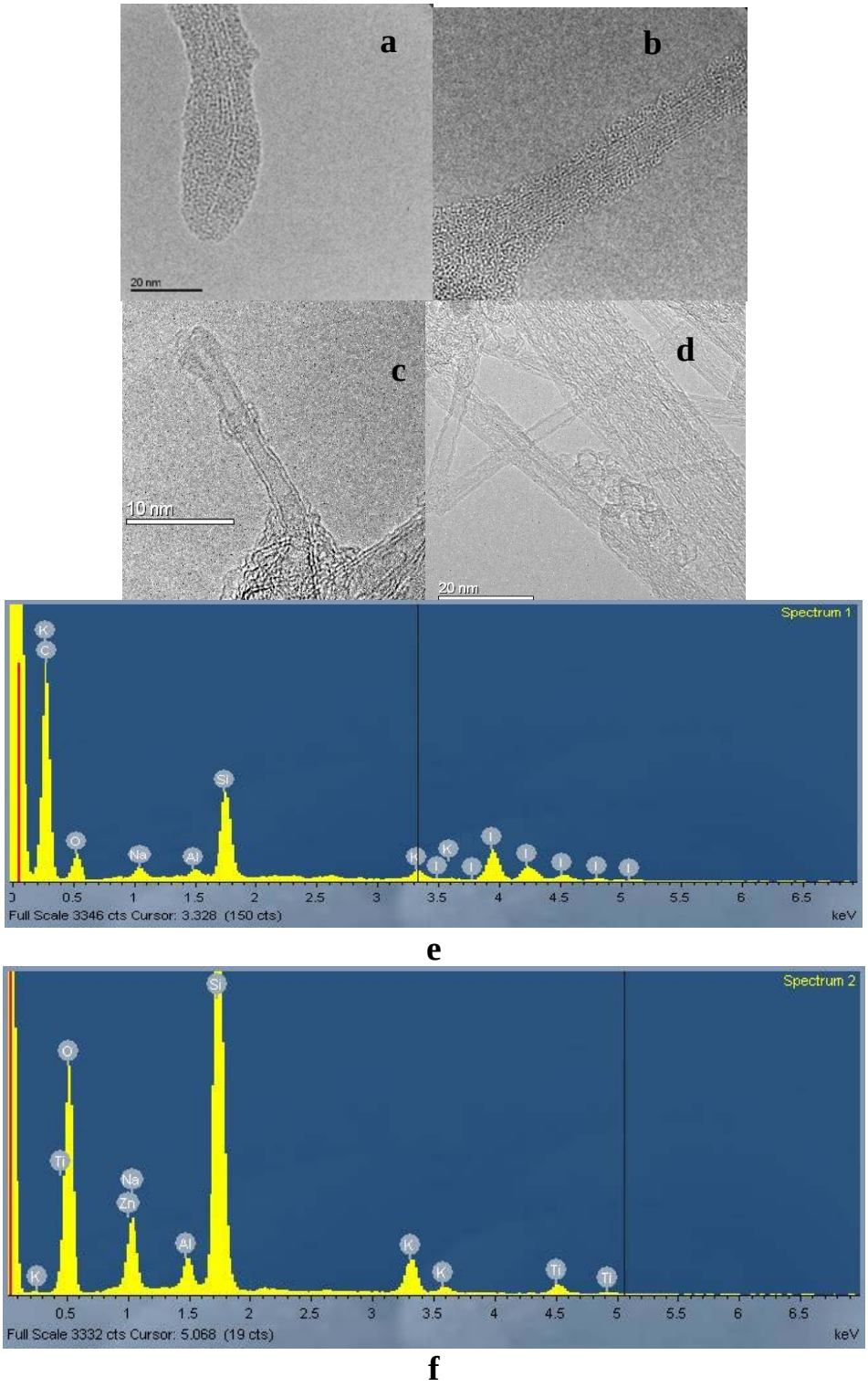

Figure 2.9. (a-c): Typical HR TEM images of the NDI@SWNT composite showing the uniform coating of SWNTs, including its tips (**a** and **b**), and the presence of 'dark dots' assignable to the heavy element iodine (Z = 53) in uniform layers on the aromatic surface; **(d)**: TEM of free, purified, SWNT used. The EDS spectrum of NDI@SWNT composite deposited on glass support **(e)** and control EDS spectrum **(f)**.

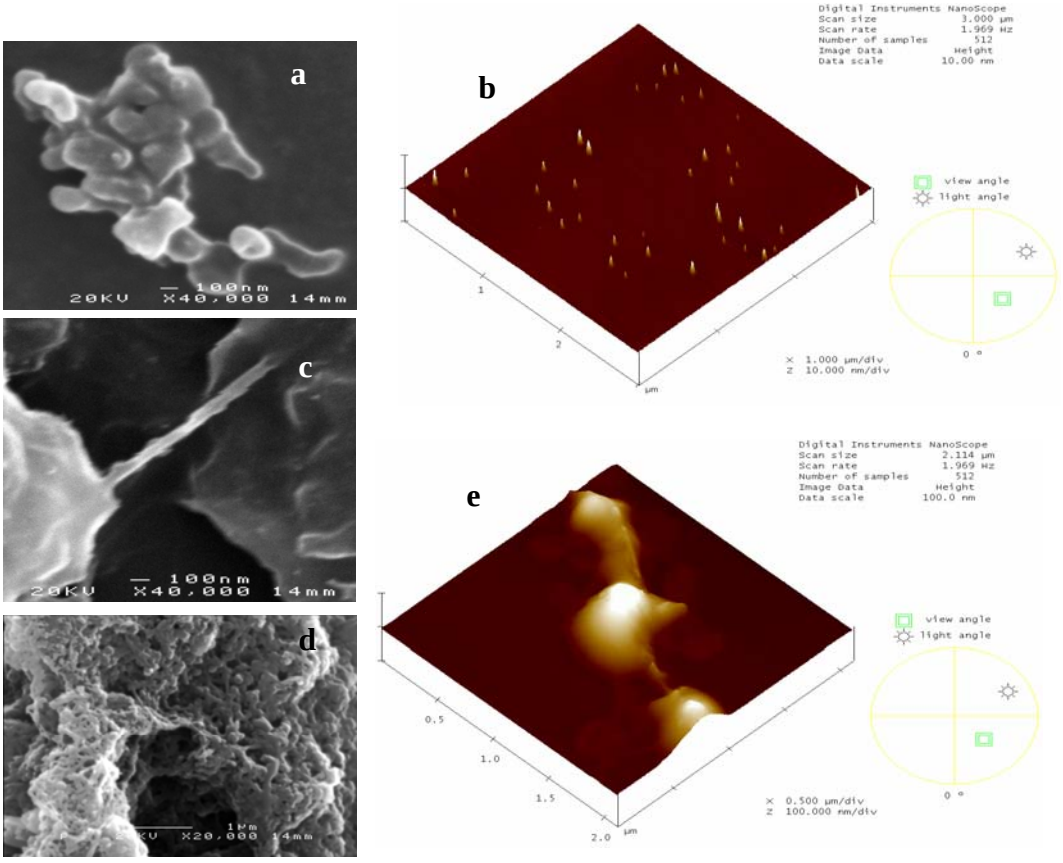

Figure 2.10. SEM and TM AFM imaging of NDI and NDI@SWNT deposited from $CHCl_3$:EtOH. Aggregates of free NDI formed upon spin-coating onto a mica substrate, imaged by SEM (**a**) and TM AFM (**b**) showing formation of nanodimensional tower-like objects on mica; SEM micrographs showing a small bundle of NDI-coated SWNTs (**c**) and the morphology of NDI@SWNT (**d**); TM AFM imaging of NDI@SWNT (**e**). All SEM measurements were carried out on samples coated with ca. 2 nm gold layer. Concentrations: free NDI 26 µM; NDI@SWNT composite dispersion containing 21 µg/mL NDI (26 µM) anchored onto 35 µg/mL SWNT.

The morphology of these new aggregates was confirmed by SEM and tapping mode AFM (TM AFM) (Figure 2.10). The coating with NDI was uniform and covered the entire aromatic surface of SWNTs. TM AFM of free NDI (spin-coated on mica surfaces from 0.2 mg/mL solutions in $CHCl_3$:EtOH 4:1) showed formation of tower-like aggregates with heights of ca. 10 nm and diameters of ca. 2 nm. TM AFM of the NDI@SWNT composite (spin-coated on a mica surface from the ca. 0.2 mg/mL dispersion in $CHCl_3$:EtOH) confirmed the complete

coating of the SWNTs and formation of small NDI@SWNT bundles with lengths of ca. 500 nm, and heights ranging from 10-50 nm, without free (unbound) NDI aggregates on the mica surface.

2.2.4 Multiphoton fluorescence imaging of the NDI@SWNT complex in solution and *in vitro*

To probe the potential of NDI@SWNT somposite as a precursor for future applications towards traceable imaging probes inside living cells, two-photon emission lifetime decay spectra were recorded by time-correlated single photon counting using pulsed laser excitation (λ_{ex}= 910 nm in DMSO). DMSO was chosen as the solvent of use here for both NDI and NDI@SWNT showed minimum scattering due to aggregation within the experimental timescale in this solvent and due to its low volatility. Both systems exhibited more than one lifetime component: calculations (SPC Image analysis software) indicated a long component on the order of several nanoseconds and a much shorter component on the order of several hundred picoseconds. There are several differences between the lifetime decay spectra profiles of free NDI and NDI@SWNT (Figure 2.11), i.e. the lifetime of the long component drops by ca. 10%, from 2.67 ns (36 % weighting) in free NDI to 2.33 ns (27 % weighting) in NDI@SWNT. Only a slight increase in the short component lifetime and weighting was found for the dominant component, from 0.43 ns (64 % weighting) in free NDI to 0.41 ns (73 % weighting) for NDI@SWNT dispersions. The decrease in fluorescence lifetime of NDI upon immobilisation onto the SWNT (in DMSO) confirmed the fluorescence quenching by the SWNT surface via non-radiative pathways, in agreement with earlier reports on polythiophene-SWNTs nano-hybrids.[89]

For the high resolution laser scanning confocal fluorescence imaging of NDI@SWNT fresh dispersions (0.2 mg/mL in $CHCl_3$:EtOH 4:1) were dropcast on a borosilicate glass cover slip and the solvent evaporated under air. High-resolution confocal imaging under single-photon

(488 nm) or two-photon excitation (910 nm), using a mode-locked Ti-sapphire laser (see Appendix), generated images of the solid NDI@SWNT film by the raster scanning of the laser spot in the xy plane.

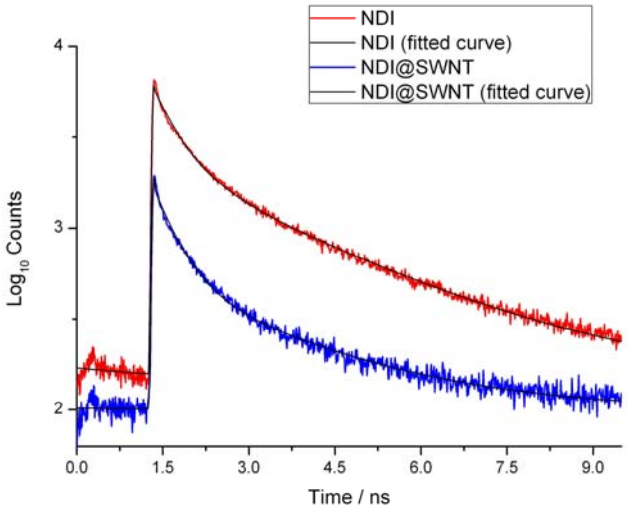

Figure 2.11. Two-photon fluorescence spectroscopy: fluorescence decay traces and corresponding fitted curves for the lifetime determinations (λex = 910 nm, NDI 26 μM, pure DMSO, NDI@SWNT composite dispersion containing 21 μg/mL NDI or 26 μM anchored onto 35 μg/mL SWNT).

Two photon fluorescence imaging and emission lifetime measurements were carried out, using FLIM in solid state composite (deposited on borosilicate glass from $CHCl_3$:EtOH 4:1 dispersions) and in HeLa and MCF-7 cell lines (*vide infra*) for NDI and NDI@SWNT. Single photon laser scanning confocal fluorescence imaging showed solid NDI@SWNT particles retaining some fluorescence emission under single photon excitation (λ_{ex}=488 nm) but this composite is a rather weak fluorophore with respect to standard organic dyes and the signal to noise ratio is normally dramatically improved when using 2-photon excitation. Within the NDI@SWNT film, fluorescent aggregates with irregular shapes and sizes ranging from ca. 200 nm to 1 μm were observed in the differential interference contrast (DIC) micrographs, in the red (λ_{em} = 606 nm) and green (λ_{em} = 516 nm) channels of the single photon fluorescence emission images (λ_{ex}=488 nm), as well as by two-photon fluorescence intensity and lifetime imaging

(λ_{ex}=910 nm). Intensity images of NDI@SWNT obtained from two-photon fluorescence excitation gave better signal to noise than one-photon excitation and fluorescence lifetime imaging and corresponding data fitting was obtained when 2-photon FLIM measurements were used (Figure 2.12). The fluorescence lifetime imaging shows lifetime emission maps for NDI@SWNT together with intensity maps showing the spatial variations in fluorescence emission and the lifetime distribution plots for the major lifetime component. For NDI@SWNT, the maximum fluorescence lifetime in the solid state of the major component (0.42 ns, with width at half-height WHH of +/-0.12 ns) is similar to the fluorescence lifetime measured in pure DMSO solution (0.41 ns).

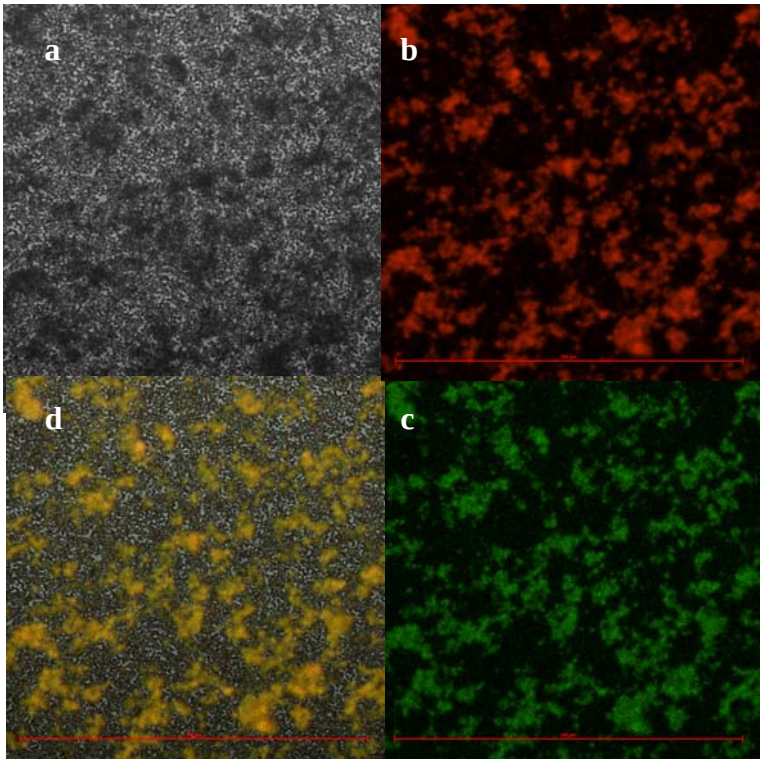

Figure 2.12. Single photon confocal imaging (scale-bar 100 μm, λ_{ex} = 488 nm) of solid NDI@SWNT composite drop-cast on borosilicate glass from a $CHCl_3$:EtOH 4:1 mixture showing: (**a**) bright-field micrograph (**b**) red channel emission (606 nm); (**c**) green channel emission (516 nm) and d) overlay of (**a**)-(**c**) micrographs

To test the biocompatibility and *in vitro* stability of the NDI@SWNT composite, cancerous (breast carcinoma MCF-7 and cervical carcinoma HeLa) and healthy (fibroblast Fek-4) cells were treated with the composite dispersed in cell medium EMEM over a range of concentrations. Despite the strong quenching observed with respect to the free NDI fluorescence emission, some residual emission of the NDI absorbed onto SWNTs was sufficient to enable the observation of the nanocomposite in living cells (Figure 2.13, Figure 2.14, Figure 2.15 and Figure 2.16). Cell uptake was monitored in living cells by epi-fluorescence microscopy (following 30 min, 2 h, 3 h or 5 h incubation with NDI@SWNTs at 4 °C and 37 °C, λ_{ex} 450 nm) and by single-photon laser scanning confocal fluorescence imaging (λ_{ex} = 488 nm, 30 min, 1 h and 2 h incubation at 37 °C, Figure 2.13). The composites penetrate cell membranes at 37 °C but not at 4 °C, suggesting active uptake, possibly endocytosis, as the likely uptake mechanism.[20] Colocalisation experiments showed some nuclear uptake for free NDI in all cell lines and this seems to increase in cells after 1 h incubation, as indicated by co-staining with Hoechst nuclear stain and fluorescence lifetime imaging (*vide infra*). To verify whether the supramolecular NDI@SWNT composites remain stable *in vitro* with respect to NDI loss, fluorescence emission lifetime measurements were carried out using 2-photon FLIM in HeLa or MCF-7 cell lines (1 h incubation, 37 °C, using 910 nm excitation from a mode locked Mira titanium sapphire laser, 180 fs pulse, 75 MHz) and data was compared with FLIM of the free NDI under identical conditions (Figure 2.15, Figure 2.16). Similar to the case of FLIM of the solid NDI@SWNT composite, data fitting for FLIM measurements of NDI@SWNT in cells was significantly more reliable for 2-photon excitation than compared to the 1-photon measurements. Figure 2.165 shows lifetime emission maps for NDI and NDI@SWNT in HeLa cells together with 2-photon intensity maps showing the spatial variations in fluorescence emission, the lifetime imaging maps and corresponding distribution plots for the predominant

lifetime component (τ_1) for either free NDI or NDI@SWNT composite. Similar images are included for the FLIM of NDI and NDI@SWNT in the MCF-7 cell line (Figure 2.16).

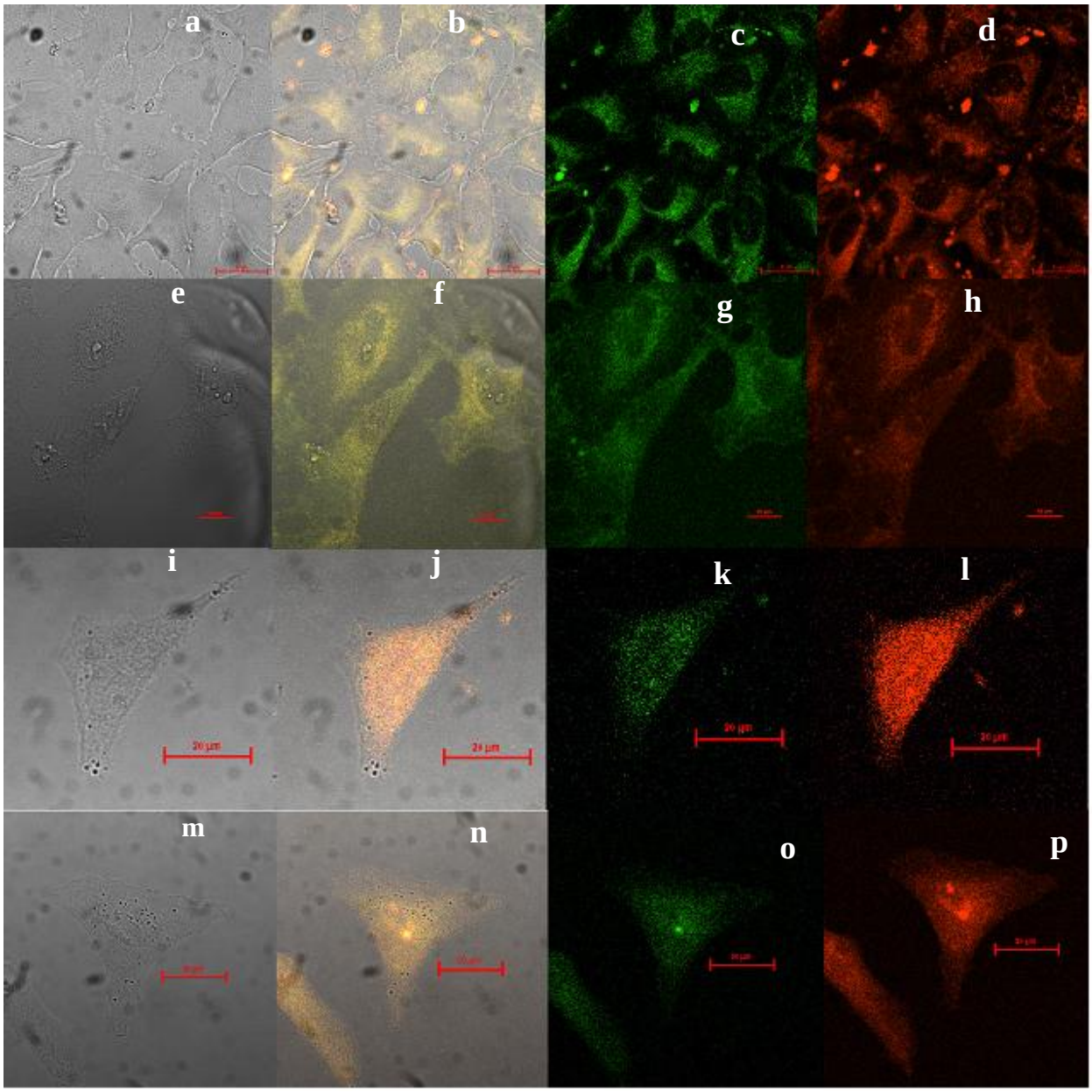

Figure 2.13. Single Photon Laser scanning confocal imaging of cancerous (HeLa) cells incubated at 37 °C where λ_{ex} = 488 nm with: (**a-l**) NDI imaging (26 μM or 21 μg/mL in 1: 99% DMSO:EMEM) - 30 min incubation showing DIC (**a**), DIC-green-red channel overlay (**b**), green channel (515-530 nm) (**c**) and red channel (605-675 nm) (**d**); (**e-h**) 1 h incubation showing DIC (**e**), DIC-green-red channels overlay (**f**), green channel (515-530 nm) (g) and red channel (605-675 nm) (**h**); (**i-l**) 2 h incubation showing DIC (**i**), DIC-green-red channels overlay (**j**), green channel (515-530 nm) (**k**) and red channels (605-675 nm) (**l**); (**m-p**) NDI@SWNT composite dispersion (in 1:99% DMSO:EMEM) containing 21 μg/mL NDI anchored onto 35 μg/mL SWNT: DIC (**m**), DIC-green-red channels overlay (n), green channel (515-530 nm) (**o**) and red channel (605-675 nm) (**p**). Scalebar 20 μm.

The lifetime distributions measured inside cells are within the same order of magnitude with the values acquired from studies in pure DMSO (Figure 2.12) for both the NDI and the NDI@SWNTs and compare well with the FLIM of the solid NDI@SWNT. The major lifetime components measured in cells incubated for 1 h (37 °C) were 0.65±0.15 ns for free NDI inside cells and 1.10±0.10 ns for NDI@SWNT in HeLa cells. A much broader lifetime distribution inside the cells than in solution or solid state was observed, and images of NDI@SWNT in HeLa cells showed regions of extremely high fluorescence intensity, corresponding to particles of ca 4 μm with extremely short emission lifetimes by 2-photon FLIM (0.07 ns or less). As expected, the relative weightings of the lifetime components obtained were somewhat different under the different conditions employed for cellular vs. solution lifetime estimations.[90] An inspection of the DIC and confocal images suggest that these large aggregates contain SWNTs coated in fluorescent materials and are concentrated in the proximity of the cell membrane and also bound on the outer surface of the cell.

Initial tests on the colocalisation of NDI and NDI@SWNT with the mitochondrial stains Mitotracker Red, and lysosome stain Lysotracker Red (Invitrogen) were carried out but results did not show any conclusive mitochondrial or lysosomal colocalisation (Figure 2.17). There was evident nuclear uptake both in the HeLa and in Fek-4 cell lines and this seems to increase in cells after 2 h incubation, as indicated by co-staining with Hoechst and fluorescence lifetime imaging. Further colocalisation tests using alternative stains to fully identify the specific sites of cellular localisation for these compounds and their effect on the cellular organelles are underway.

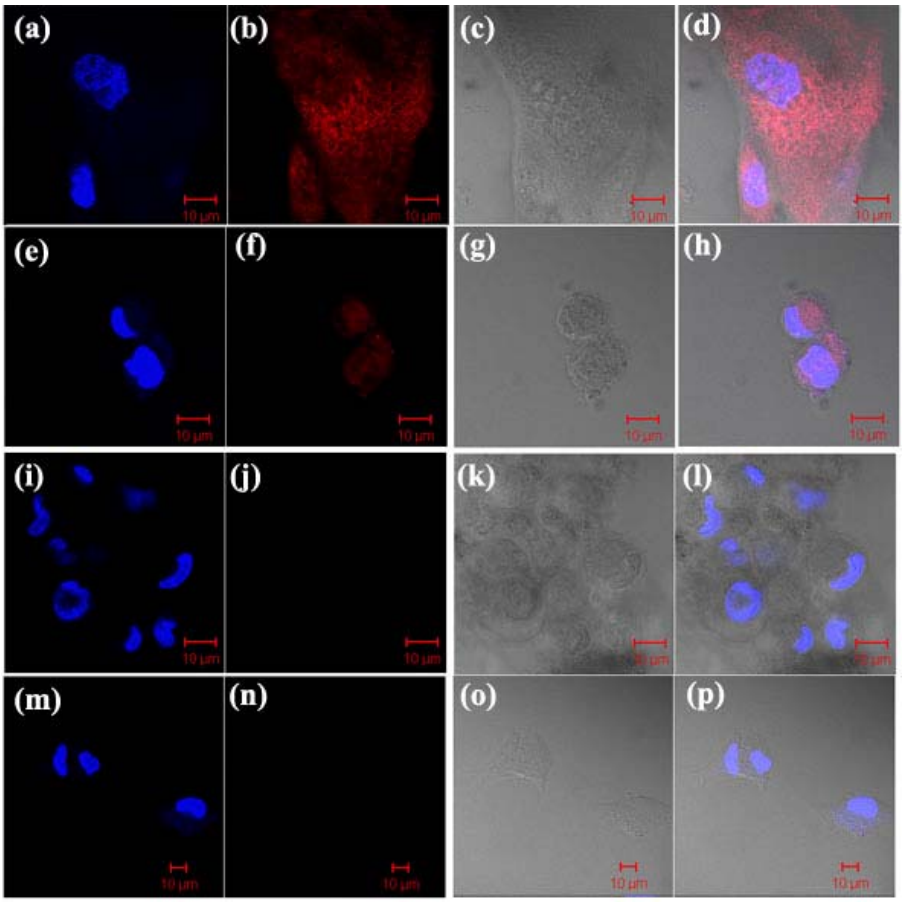

Figure 2.14. Single Photon Laser scanning confocal imaging of Fek-4 cells incubated for 2 h at 37 °C in cells incubated for 2 h at 37 °C with: (**a-d**) NDI@SWNT composite dispersion (in 1: 99% DMSO : EMEM) containing 21 μg/mL NDI (26 μM) 'anchored' onto 35 μg/mL SWNT; (**e-h**): 21 μg/mL (26 μM) NDI in 1: 99% DMSO: EMEM (**i-l**): 35 μg /mL free SWNT scaffold (dispersed in 1: 99% DMSO: EMEM). (**m-p**): Control experiment where the cell nucleus was stained with Hoechst (λ_{ex} 405 nm) prior to the experiment. Images (**i-l**) and [91] show significantly more damage to the cell morphology upon treatment than (**a-d**); images (**a-d**) and (**e-h**) show significant localisation of probe within the cell nucleus. Images show nuclear uptake for free NDI and significant deterioration of cells morphology. Scalebar 10 μm.

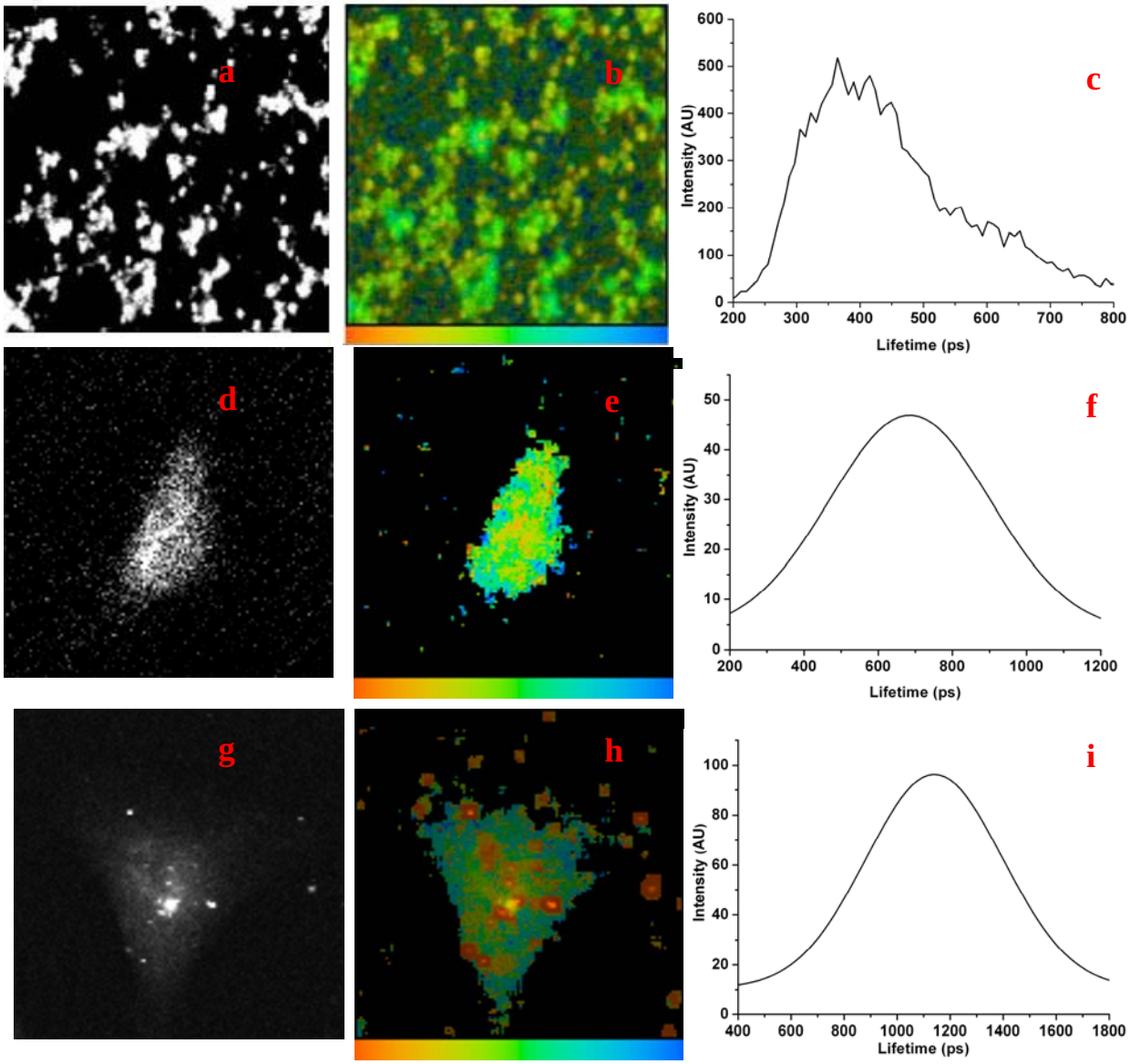

Figure 2.15. Two-photon laser confocal fluorescence (λ_{ex}= 910 nm):(**a-c**) solid NDI@SWNT composite (drop-cast on borosilicate glass from a $CHCl_3$:EtOH 4:1 mixture): intensity image (a), lifetime mapping and scalebar (**b**) and corresponding lifetime distribution curve (**c**); (**d-f**) Typical micrograph of adherent cancerous cells (HeLa) incubated for 2 h at 37 °C with NDI (26 µM or 21 µg/mL in 1: 99% DMSO EMEM) showing NDI uptake throughout cytoplasm and cell nucleus, intensity image (**d**), lifetime mapping and scalebar (**e**) and corresponding lifetime distribution curve (**f**); (**g-i**) Typical micrographs of adherent cancerous cells (HeLa) incubated for 2 h at 37 °C with NDI@SWNT composite (dispersions in 1: 99% DMSO : EMEM contained 21 µg/mL NDI (26 µM) 'anchored' onto 35 µg/mL SWNT. Intensity image (**g**), lifetime mapping and scalebar (**h**) and corresponding lifetime distribution curve (**i**). Bright spots show fluorescent NDI@SWNT composites translocated into cells as intact objects (Scalebar / Micrographs width = 100 µm). A key is provided for direct correlation between the lifetime colour map and lifetime histogram.

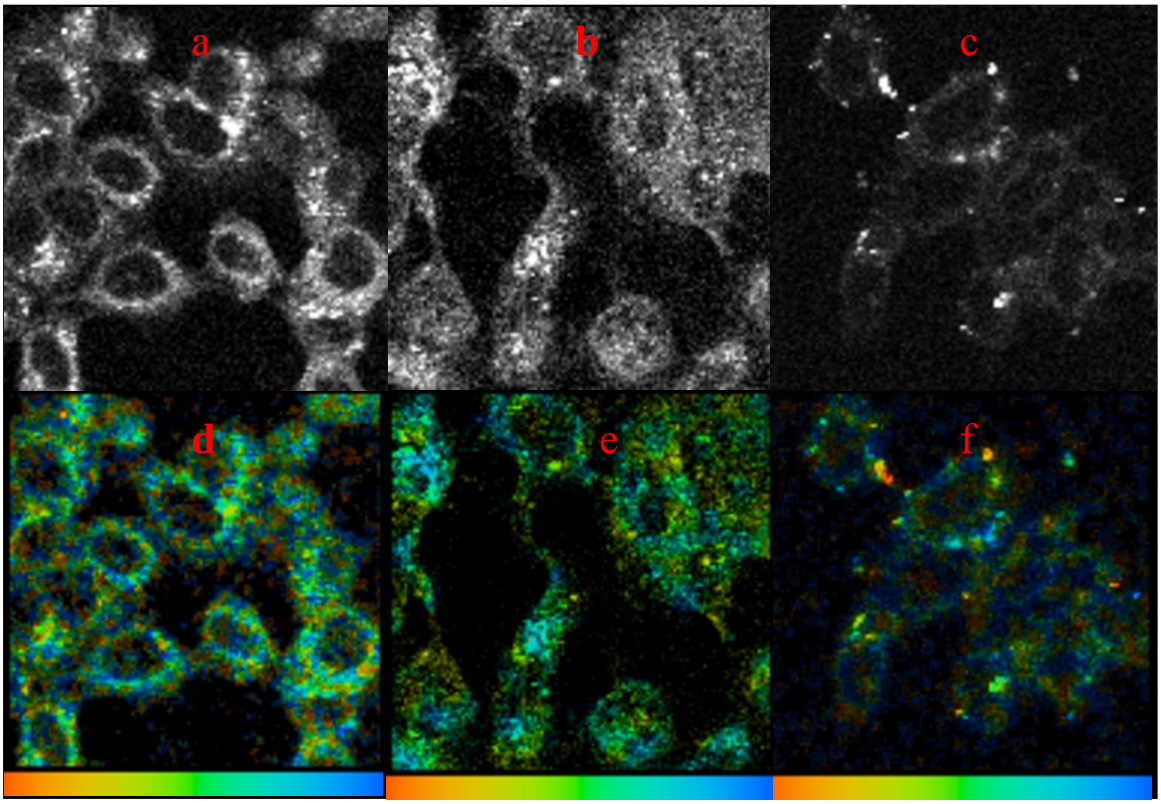

NDI 20 min incubation	NDI 1 h incubation	NDI@SWNT 1 h incubation
	Average lifetime (WHH):	
1562 ps	1568 ps	1224 ps

Figure 2.16. Two photon intensity images (**a-c**) and FLIM (**d-f**) for NDI and NDI@SWNT in MCF-7 cells (incubation at 37 °C, λ_{ex}=910 nm).

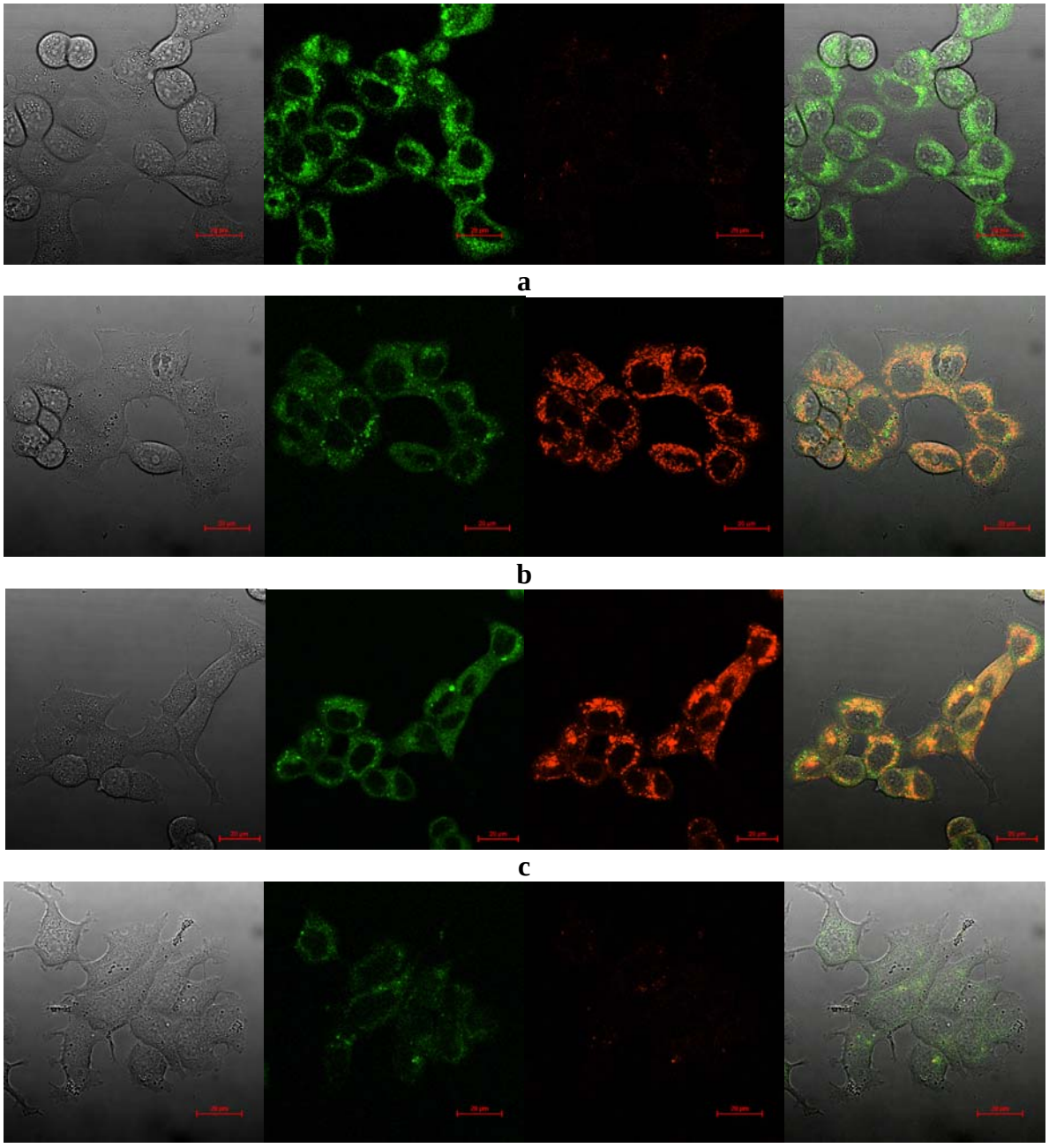

Figure 2.17. (**a**): INDI alone (no dye imaged in ex. 488 nm channel,); (**b**): NDI colocalised with mitotracker red. Only mitotracker emission visible in the red channel (ex. 543 nm) without NDI emission in this channel; (**c**): NDI colocalised with lysotracker red. Only lysotracker emission in the red channel (ex. 543 nm) without NDI emission visible on this channel; (**d**) NDI@SWNT alone (no dye imaged in ex. 488 nm channel). Scalebar 20 μm.

2.2.5 Cellular translocation monitoring of NDI@SWNT by MTT assays

The different spatial distributions observed by DIC imaging coupled with fluorescence imaging and FLIM for the free NDI and NDI@SWNT *in vitro* suggests that the nanocomposite translocates into cells as a distinct intact entity and remains largely intact in the cellular environment within the timescale of these imaging experiments, i.e. is kinetically stable with respect to de-complexation by loss of NDI *in vitro* within the timescale of this experiment. Since the naphthalene diimides and structurally related monoimides are known to show cell toxicity and potent antitumour activities by virtue of their DNA binding[38,92] standard MTT assays were used here to verify the cell viability in the presence of NDI, SWNT and NDI@SWNT under conditions similar to those used in the fluorescence microscopy studies(Figure 2.18). Assays showed that the materials investigated (free SWNTs, free NDI and NDI@SWNT hybrid) had only a moderate impact on cell viability at the 1 h time point at the same concentration used in the fluorescence studies. In separate experiments, cell metabolism MI_{50} values (the concentration that reduces cell metabolism to half that of untreated cells) were also determined via MTT assays over the traditional 24 h period. Dispersions of NDI, NDI@SWNT and free SWNT (1% DMSO in Eagle's Modified Essential Medium EMEM containing 15% foetal calf serum FCS) were incubated with HeLa cells for 24 h at concentrations of 1 nM, 100 nM, 1 μM, 10 μM, 50 μM, 100 μM and 250 μM for NDI or NDI-anchored onto SWNTs (whereby the mass ratio of NDI:SWNT was kept at 0.6, consistent with observations from fluorescence titrations) and concentrations ranging from 1 μg/mL to 250 μg/mL for the pristine SWNT. MI_{50} values were estimated in each case from five repeat experiments (see Appendix Figure 8.9). It was interesting to note that after 24 h incubation at 37 °C the pristine SWNTs seem to be significantly more cytotoxic than the NDI-functionalised SWNTs. MI_{50} values for free and functionalised SWNTs are within the same order of magnitude with earlier reports of the uptake of functionalised carbon nanotubes *in*

vitro.[7,30,58,60,93,94] Confocal imaging experiments already showed that both free NDI and NDI@SWNTs localise in the cell cytoplasm and partially in the nucleus too. Interestingly, an inspection of the cell morphology of free NDI treated cells suggested that these are significantly more damaged than of those treated with the NDI@SWNT composite or free NDI within 2 h incubation time. MTT assays suggest that NDI@SWNTs has a somewhat lower cytotoxicity compared to that of the free SWNTs and free NDI healthy cells (Fek-4) vs in cancerous (MCF-7). Interestingly, MI_{50} data estimated by MTT assays over the traditional 24 h observation period showed significantly lower toxicity of NDI@SWNT towards FEK4 when compared to MCF-7. Cell viability tests support the hypothesis from imaging experiments that that free NDI, NDI@SWNT and free SWNTs all act upon healthy (Fek-4) and cancerous cells (Figure 2.13, Figure 2.14) over a wide range of concentrations, but that the NDI modulates the biocompatibility of the SWNTs and the resulting composite localises in the cell cytoplasm as an intact object. The NDI@SWNT composite has a higher cytotoxicity to cancer cells MCF-7 than to normal cells Fek-4, as shown both by MI_{50} determinations (Table 2.2, Figure 2.19 and in Appendix Figure 8.9) and via time-lapse MTT experiments(Figure 2.18). Both free NDI and SWNT-supported NDI (NDI@SWNT) exhibit low toxicity up to 6 h incubation in Fek-4 cells, with cell viability higher than 89% and 96% respectively. After 24 h incubation with NDI and NDI@SWNT, Fek-4 cells showed lower viability by comparison to that of controls, of 25% and 45% respectively. Cell viability for the group treated with NDI@SWNT was 5% higher than for the case when free SWNTs were used, suggesting an increase of the SWNT biocompatibility upon wrapping and the significantly altered behavior of NDI@SWNT composite *in vitro* with respect to its individual components, *i.e.* free NDI or SWNT. In MCF-7 cells, free NDI as well as SWNT-supported NDI showed notable cytotoxicity at shorter time points. Cells treated with the NDI@SWNT composite show 53% viability after 6 h incubation for MCF-7 *vs* 96% observed for Fek-4. Pristine SWNTs showed cytotoxicity after 1-3 h incubation for both cell

lines, with the faster inhibition observed in Fek-4 cells. The cell viability after 6 h incubation with NDI@SWNT was higher than that of pristine SWNT (96 % vs 63 %, Figure 2.18). Further investigations are underway in our laboratories to fully establish the precise mechanism for these differences, and whether size and/or shape of this new nanoparticle are influencing the biolocalisation and ultimately their toxicity *in vivo*.[31,94-98]

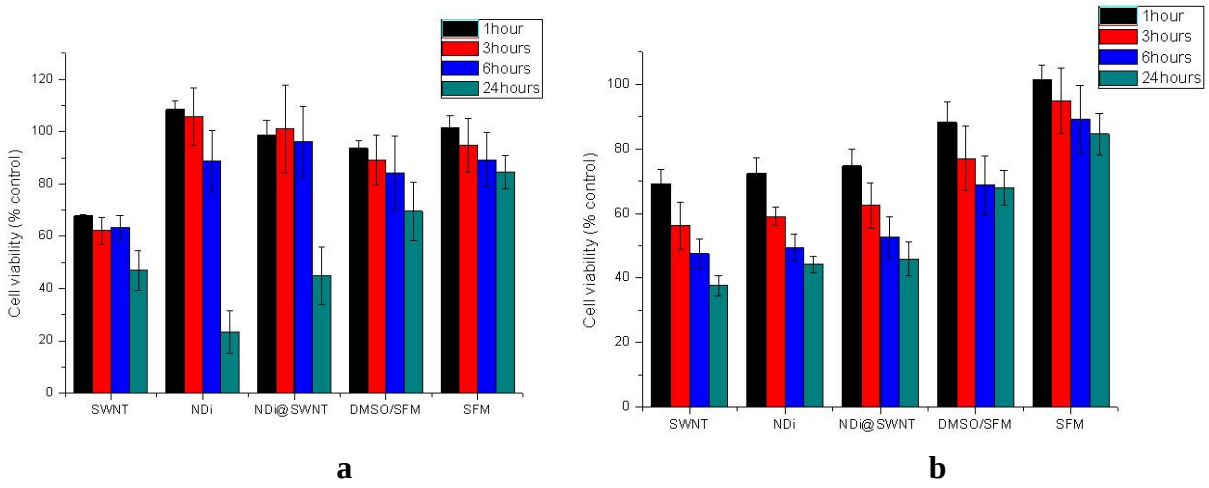

Figure 2.18. Cell viability is expressed as the percentage of viability measured for untreated cells (control) for MCF-7 (left) and Fek-4 cells cultured with purified SWNT, free NDI and the NDI@SWNT composite. Data were recorded after 1, 3, 6 and 24 hours incubation time (37 ^{o}C). In control experiments the cells were cultured in SFM (phenol-red free EMEM with 1% DMSO and also without DMSO). Concentrations (in 1: 99 % DMSO :serum free medium EMEM): **a**) 0.70 μg SWNT dispersed in 100 μL solvent **b**) 0.42 μg free NDI dispersed in 100 μL solvent (5.15 μM); c) NDI@SWNT composite, formed in situ by anchoring 0.42 μg NDI onto 0.70 μg SWNT and dispersed in 100 μL medium. Two control groups were used consisting of 100 μL solvent / well, i.e. 1:99 % serum free medium, as well as 100% serum free medium. Each bar/value corresponds to the average result from three repeated experiments with three culture wells for each experiment.

We observed that the surface functionalisation of carbon nanotubes with NDI reduces the SWNT toxicity behavior significantly both in cancerous and non-cancerous cell lines and mediates the biocompatibility of pristine SWNTs. Supramolecular wrapping is rapid and uniform thus bypassing the need for complex covalent synthetic procedures to be performed directly on the SWNT surface.[99-101] The new NDI reported hereby is a biocompatible nano-receptor that may be derivatised further by virtue of the carboxylic groups: this method of SWNTs wrapping could facilitate the rapid incorporation of targeting peptides onto the surface

of SWNTs for precise cancer cell delivery *in vitro*. Future experiments are underway in our laboratories to construct and test *in vitro* and *in vivo* future nanotherapeutics based on this optically traceable NDI@SWNT scaffold.

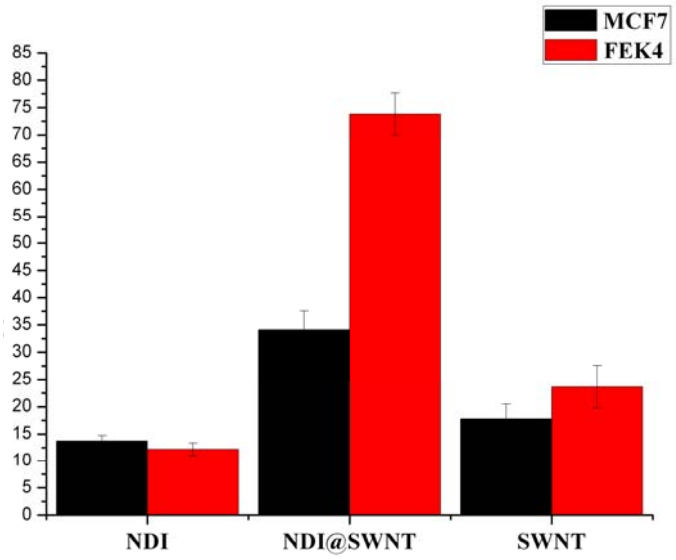

Figure 2.19. A comparison of MI_{50} values (μg/mL, shown on Y axis) for free NDI, NDI@ SWNT and free SWNT in healthy (Fek-4) and cancerous cells (MCF-7). Cells were cultured in EMEM % FCS containing was 15% for Fek-4 and 10% for MCF-7 as this is standard for these cell lines ; each experiment was repeated five times.

Table 2.2. Calculated MI_{50} (± SEM values, μg/mL, the concentration that reduces cell metabolism to half that of untreated cells, 24 h MTT assay) for free NDI, NDI@ SWNT and free SWNT. Cells were cultured in EMEM each experiment was repeated five times.

MI_{50} μg/mL	**MCF-7** Breast carcinoma	**Fek-4** Normal human fibroblast cell line
NDI	13.76 ± 1.00	12.21 ± 1.17
NDI@SWNT	34.08 ± 3.46	73.79 ± 3.87
SWNT	17.81 ± 2.71	23.66 ±3.90

2.3 Conclusions to Chapter 2

In summary, we have developed a rapid and reliable method for the surface functionalisation of SWNTs via encapsulation by a new nano-receptor, NDI, which acted as a supramolecular host. A new supramolecularly functionalised fluorescent nanomaterial was

synthesized on a preparative scale. Iodine atoms featured as a key design motif in the NDI structure to aid the identification by TEM of the uniform coating of the surface of the carbon nanotubes. [2,101] The 'host' is tightly wrapped around the carbon nanotube, forming a monolayer of NDI held to the aromatic surface by aromatic stacking reinforced by solvophobic effects. The NDI network adapts its geometry in order to accommodate a guest with diameters as wide as 1.6 nm (i.e. a [10,10] SWNT). Charge transfer interactions are likely to occur between host (NDI) and guest (SWNT) in these composites in dispersions as suggested by significant quenching in fluorescence emission and DFT calculations in the gas phase.

The NDI@SWNT hybrid is biocompatible, translocates in cells as an intact object and shows fluorescence emission in the visible range. Confocal fluorescence imaging showed that localisation in sub-cellular (Fek-4 and MCF-7) regions and that the NDI coating significantly enhances the biocompatibility of SWNTs and mediates its intracellular localisation. The excited state lifetime of the probes in cells versus solution phase indicates that the probes are not affected by the change in their chemical environment. The new amino acid functionalised NDI is amenable for further rapid derivatisation with functional groups and/or biomolecules[92] via simple peptide coupling chemistry. Supramolecular coating led to the controlled and uniform functionalisation of the whole of SWNTs surface, including the coating of the SWNTs ends in a manner analogous to the fullerene binding by similar NDI-based nano-receptors and without the disruption of the aromatic network. This new nano-hybrid showed a significant output in the visible spectrum, opening up future possibilities for its incorporation in the next generation optoelectronic devices for both photovoltaic and biomedical imaging applications. We are now investigating further amino acid- and targeting peptide-derivatised NDI molecules as key components for the rapid assembly of imaging and drug delivery devices based on carbon nanomaterials.

2.4 References for Chapter 2

(1) Guldi, D. *Phys. Chem. Chem. Phys.* **2007**, *9*, 1400.

(2) Eliseev, A. A.; Chernysheva, M. V.; Verbitskii, N. I. *Chem. Mater.* **2009**, *21*, 5001.

(3) Ali-Boucetta, H.; Al-Jamal, K. T.; McCarthy, D. *Chem. Commun.* **2008**, 459.

(4) Chen, R. J.; Bangsaruntip, S.; Drouvalakis, K. A. *Proc. Nat. Acad. Sci. USA* **2003**, *100*, 4984.

(5) Choi, J. H.; Nguyen, F. T.; Barone, P. W. *Nano Lett.* **2007**, *7*, 861.

(6) Dhar, S.; Liu, Z.; Thomale, J.; Dai, H. J.; Lippard, S. J. *J. Am. Chem. Soc.* **2008**, *130*, 11467.

(7) Heller, D. A.; Baik, S.; Eurell, T. E.; Strano, M. S. *Adv. Mat.* **2005**, *17*, 2793.

(8) Balasubramanian, K.; Sordan, R.; Burghard, M.; Kern, K. *Nano Lett.* **2004**, *4*, 827.

(9) Loi, M. A.; Gao, J.; Cordella, F. *Adv. Mater.* **2010**, *22*, 1635.

(10) Pascu, S. I.; Kuganathan, N.; Tong, L. H. *J. Mat. Chem.* **2008**, *18*, 2781.

(11) Backes, C.; Hauke, F.; Schmidt, C. D.; Hirsch, A. *Chem. Commun.* **2009**, 2643.

(12) Backes, C.; Schmidt, C. D.; Hauke, F.; Boettcher, C.; Hirsch, A. *J. Am. Chem. Soc.* **2009**, *131*, 2172.

(13) Arnold, M. S.; Guler, M. O.; Hersam, M. C.; Stupp, S. I. *Langmuir* **2005**, *21*, 4705.

(14) Balasubramanian, K.; Friedrich, M.; Jiang, C. Y. *Adv. Mat.* **2003**, *15*, 1515.

(15) Bayazit, M. K.; Coleman, K. S. *J. Am. Chem. Soc.* **2009**, *131*, 10670.

(16) Chen, J. Y.; Collier, C. P. *J. Phys. Chem. B* **2005**, *109*, 7605.

(17) Cherukuri, P.; Gannon, C. J.; Leeuw, T. K. *Proc. Nat. Acad. Sci. USA* **2006**, *103*, 18882.

(18) De, M.; Ghosh, P. S.; Rotello, V. M. *Adv. Mat.* **2008**, *20*, 4225.

(19) Didenko, V. V.; Moore, V. C.; Baskin, D. S.; Smalley, R. E. *Nano Lett.* **2005**, *5*, 1563.

(20) Jin, H.; Heller, D. A.; Strano, M. S. *Nano Lett.* **2008**, *8*, 1577.

(21) Lee, Y.; Geckeler, K. E. *Adv. Mater.* **2010**, *22*, 4076.

(22) Liu, Z.; Chen, K.; Davis, C. *Cancer Res.* **2008**, *68*, 6652.

(23) Liu, Z.; Fan, A. C.; Rakhra, K. *Angew. Chem.-Int. Ed.* **2009**, *48*, 7668.

(24) Murakami, H.; Nomura, T.; Nakashima, N. *Chem. Phys. Lett.* **2003**, *378*, 481.

(25) Nakayama-Ratchford, N.; Bangsaruntip, S.; Sun, X.; Welsher, K.; Dai, H. *J. Am. Chem. Soc.* **2007**, *129*, 2448.

(26) O'Connell, M. J.; Bachilo, S. M.; Huffman, C. B. *Science* **2002**, *297*, 593.

(27) Ou, Z. M.; Wu, B. Y.; Xing, D. *Nanotech.* **2009**, *20*.

(28) Tamesue, S.; Numata, M.; Kaneko, K.; James, T. D.; Shinkai, S. *Chem. Commun.* **2008**, 4478.

(29) Welsher, K.; Liu, Z.; Daranciang, D.; Dai, H. *Nano Lett.* **2008**, *8*, 586.

(30) Yang, W. R.; Thordarson, P.; Gooding, J. J.; Ringer, S. P.; Braet, F. *Nanotechnology* **2007**, *18*.

(31) Zavaleta, C.; de la Zerda, A.; Liu, Z. *Nano Lett.* **2008**, *8*, 2800.

(32) Zhu, W. H.; Minami, N.; Kazaoui, S.; Kim, Y. *J. Mater. Chem.* **2003**, *13*, 2196.

(33) Zu, S. Z.; Sun, X. X.; Liu, Y. Q.; Han, B. H. *Chem. Asian J.* **2009**, *4*, 1562.

(34) Pantos, G. D.; Pengo, P.; Sanders, J. K. M. *Angew. Chem.-Int. Ed.* **2007**, *46*, 194.

(35) Bell, T. D. M.; Yap, S.; Jani, C. *Ultrasensitive Single-Molec. Detection Techn. II* **2007**, *6444*, 44404.

(36) Bevers, S.; O'Dea, T. P.; McLaughlin, L. W. *J. Am. Chem. Soc.* **1998**, *120*, 11004.

(37) Bhosale, S. V.; Jani, C. H.; Langford, S. J. *Chem.Soc. Rev.* **2008**, *37*, 331.

(38) Brana, M. F.; Castellano, J. M.; Moran, M. *Anticancer. Drug Des.* **1993**, *8*, 257.

(39) Gianolio, D. A.; McLaughlin, L. W. *Bioorg. Med. Chem.* **2001**, *9*, 2329.

(40) Matsugo, S.; Kawanishi, S.; Yamamoto, K. *Angew. Chem., Int. Ed. Engl.* **1991**, *30*, 1351.

(41) Singh, T. B.; Erten, S.; Gunes, S. *Organic Electronics* **2006**, *7*, 480.

(42) Tamanini, E.; Ponnuswamy, N.; Pantos, G. D.; Sanders, J. K. M. *Faraday Discuss.* **2009**, *doi: 10.1039/b907538k.*

(43) Guelev, V.; Sorey, S.; Hoffman, D. W.; Iverson, B. L. *J. Am. Chem. Soc.* **2002**, *124*, 2864.

(44) Lokey, R. S.; Kwok, Y.; Guelev, V. *J. Am. Chem. Soc.* **1997**, *119*, 7202.

(45) Abdel-Jalil, R. J.; Aqarbeh, M.; Loffler, D. *J. Radioanal. Nucl. Chem.* **2010**, *283*, 239.

(46) Koch, C. J.; Evans, S. M. *Oxygen Transport to Tissue Volume Xxiii* **2003**, *510*, 285.

(47) Riche, F.; d'Hardemare, A. D.; Sepe, S. *Bioorg. Med. Chem. Lett.* **2001**, *11*, 71.

(48) Ashkenasy, N.; Horne, W. S.; Ghadiri, M. R. *Small* **2006**, *2*, 99.

(49) Chu, Y.; Sorey, S.; Hoffman, D. W.; Iverson, B. L. *J. Am. Chem. Soc.* **2007**, *129*, 1304.

(50) Martinez, R.; Chacon-Garcia, L. *Curr. Med. Chem.* **2005**, *12*, 127.

(51) Pantos, G. D.; Pengo, P.; Sanders, J. K. *Angew. Chem., Int. Ed.* **2007**, *46*, 194.

(52) Pengo, P.; Pantos, G. D.; Otto, S.; Sanders, J. K. *J. Org. Chem.* **2006**, *71*, 7063.

(53) Tamanini, E.; Pantos, G. D.; Sanders, J. K. *Chemistry* **2010**, *16*, 81.

(54) Pantos, G. D.; Wietor, J. L.; Sanders, J. K. *Angew. Chem.-Int. Ed.* **2007**, *46*, 2238.

(55) Wietor, J. L.; Pantos, G. D.; Sanders, J. K. M. *Angew. Chem.-Int. Ed.* **2008**, *47*, 2689.

(56) Bulheller, B. M.; Pantos, G. D.; Sanders, J. K. M.; Hirst, J. D. *Phys. Chem. Chem. Phys.* **2009**, *11*, 6060.

(57) Bianco, A.; Kostarelos, K.; Prato, M. *Exp. Op. Drug Deliv.* **2008**, *5*, 331.

(58) Bottini, M.; Bruckner, S.; Nika, K. *Toxicol. Lett.* **2006**, *160*, 121.

(59) Bottini, M.; Cerignoli, F.; Dawson, M. I. *Biomacromolec.* **2006**, *7*, 2259.

(60) Cui, D. X.; Tian, F. R.; Ozkan, C. S.; Wang, M.; Gao, H. J. *Toxicol. Lett.* **2005**, *155*, 73.

(61) Kubat, P.; Lang, K.; Janda, P. *J. Nanosci. Nanotech.* **2009**, *9*, 5795.

(62) Lin, S. J.; Keskar, G.; Wu, Y. N. *Appl. Phys. Lett.* **2006**, *89*.

(63) Pascu, S. I.; Kuganathan, N.; Tong, L. H. *J. Mater. Chem.* **2008**, *18*, 2781.

(64) Porter, A. E.; Gass, M.; Muller, K. *Nature Nanotech.* **2007**, *2*, 713.

(65) Worle-Knirsch, J. M.; Pulskamp, K.; Krug, H. F. *Nano Lett* **2006**, *6*, 1261.

(66) Konig, K. *J. Microsc. (Oxford)* **2000**, *200*, 83.

(67) Suhling, K.; French, P. M. W.; Phillips, D. *Photochem. Photobiol. Sci.* **2005**, *4*, 13.

(68) Stutzmann, G. E.; Parker, I. *Physiology* **2005**, *20*, 15.

(69) Oheim, M.; Michael, D. J.; Geisbauer, M.; Madsen, D.; Chow, R. H. *Adv. Drug Delivery Rev.* **2006**, *58*, 788.

(70) Bisby, R. H.; Crisostomo, A. G.; Botchway, S. W.; Parker, A. W. *Photochem. Photobiol.* **2009**, *85*, 353.

(71) Treanor, B.; Lanigan, P. M. P.; Suhling, K. *J. Microsc.* **2005**, *217*, 36.

(72) Artacho, E.; Sanchez-Portal, D.; Ordejon, P.; Garcia, A.; Soler, J. M. *Phys. Status Solidi B* **1999**, *215*, 809.

(73) Sceats, E. L.; Green, J. C. *J. Chem. Phys.* **2006**, *125*, 154704.

(74) Hobza, P.; Selzle, H. L.; Schlag, E. W. *J. Phys. Chem.* **1996**, *100*, 18790.

(75) Boys, S. F.; Bernardi, F. *Mol. Phys.* **1970**, *19*, 553.

(76) Dresselhaus, M. S.; Jorio, A.; Hofmann, M.; Dresselhaus, G.; Saito, R. *Nano Lett.* **2010**, *10*, 751.

(77) Salzmann, C. G.; Chu, B. T. T.; Tobias, G.; Llewellyn, S. A.; Green, M. L. H. *Carbon* **2007**, *45*, 907.

(78) Lee, G. K. C.; Sach, C.; Green, M. L. H.; Wong, L. L.; Salzmann, C. G. *Chem. Commun.* **2010**, *46*, 7013.

(79) Ikeda, A.; Totsuka, Y.; Nobusawa, K.; Kikuchi, J. *J. Mater. Chem.* **2009**, *19*, 5785.

(80) Araujo, P. T.; Pesce, P. B. C.; Dresselhaus, M. S. *Physica E-Low-Dimensional Systems & Nanostructures* **2010**, *42*, 1251.

(81) Sprafke, J. K.; Stranks, S. D.; Warner, J. H.; Nicholas, R. J.; Anderson, H. L. *Angew. Chem. Int. Ed. Engl.* **2011**, *50*, 2313.

(82) Caspar, J. V.; Meyer, T. J. *J. Am. Chem. Soc.* **1983**, *105*, 5583.

(83) Thalacker, C.; Roger, C.; Wurthner, F. *J. Org. Chem.* **2006**, *71*, 8098.

(84) Wietor, J. L.; Pantos, G. D.; Sanders, J. K. M. *Angew. Chem., Int. Ed.* **2008**, *47*, 2689.

(85) Heller, D. A.; Jeng, E. S.; Yeung, T. K. *Science* **2006**, *311*, 508.

(86) Dukovic, G.; Balaz, M.; Doak, P. *J. Am. Chem. Soc.* **2006**, *128*, 9004.

(87) Salzmann, C. G.; Lee, G. K. C.; Ward, M. A. H.; Chu, B. T. T.; Green, M. L. H. *J. Mat. Chem.* **2008**, *18*, 1977.

(88) Salzmann, C. G.; Ward, M. A. H.; Jacobs, R. M. J.; Tobias, G.; Green, M. L. H. *J. Phys. Chem. C* **2007**, *111*, 18520.

(89) Loi, M. A.; Gao, J.; Cordella, F. *Adv. Mater.* **2010**, *22*, 1635.

(90) Botchway, S. W.; Charnley, M.; Haycock, O. W. *Proc. Natl. Acad. Sci. U. S. A.* **2008**, *105*, 16071.

(91) Sarkar, S.; Sharma, C.; Yog, R. *J. Nanosci. Nanotech.* **2007**, *7*, 584.

(92) Nojima, T.; Ohtsuka, K.; Nagamatsu, T.; Takenaka, S. *Nucleic Acids Res Suppl* **2003**, 123.

(93) Isobe, H.; Tanaka, T.; Maeda, R. *Angew. Chem. Int. Ed. Engl.* **2006**, *45*, 6676.

(94) Zhao, Y. L.; Xing, G. M.; Chai, Z. F. *Nature Nanotechn.* **2008**, *3*, 191.

(95) McDevitt, M. R.; Chattopadhyay, D.; Jaggi, J. S. *PLoS One* **2007**, *2*, e907.

(96) Poland, C. A.; Duffin, R.; Kinloch, I. *Nature Nanotech.* **2008**, *3*, 423.

(97) Wang, H. F.; Wang, J.; Deng, X. Y. *J. Nanosci. Nanotech.* **2004**, *4*, 1019.

(98) Welch, M. J.; Hawker, C. J.; Wooley, K. L. *J. Nucl. Med.* **2009**, *50*, 1743.

(99) Balasubramanian, K.; Burghard, M. *Small* **2005**, *1*, 180.

(100) Coleman, K. S.; Bailey, S. R.; Fogden, S.; Green, M. L. H. *J. Am. Chem. Soc.* **2003**, *125*, 8722.

(101) Coleman, K. S.; Chakraborty, A. K.; Bailey, S. R.; Sloan, J.; Alexander, M. *Chem. Mater.* **2007**, *19*, 1076.

(102) Hurwitz, H.; Fehrenbacher, L.; Novotny, W. *New Engl. J. Med.* **2004**, *350*, 2335.

Chapter 3 Synthesis of tumour targeting peptide tagged naphthalenediimide derivatives and their supramolecular complexes with SWNTs

3.1 Introduction

Fluorescence imaging technologies have become powerful research tools for cellular imaging and diagnosis as a result of the development of modern epifluorescence, confocal, and multiphoton microscopes. With the aid of these modern imaging facilities and in combination with fluorescent probe development, fluorescent-labeled organelles, molecules, and enzymes can be visualised with precision *in vitro*. The further chemical modification with specific targeting molecules attached to the fluorescent label is usually needed to localise specific targets *in vivo* and *in vitro*.

In the past decades, synthetic peptide-based targeting fluorescence probes have been developed for diagnostic imaging and therapy. This is because of their advantages compared with large-sized antibodies: specific peptides are easily synthesized and modified, and they are less likely to be immunogenic, also they have rapid blood clearance.[1-5] Bombesin peptides have attracted lots of research groups to investigate since many types of human cancer have been found to over-express bombesin receptors.[6] This receptor family comprises three members in humans: the neuromedin B receptor (NMB-R), the gastrin-releasing peptide receptor (GRP-R), and the orphan bombesin subtype-3 receptor (BB3-R).[7] GRP-R is the prominent subtype because its high expression has been detected on prostate, non-small cell lung carcinoma, breast and gastrointestinal stromal tumours.[8] NMB-R and BB3-R also have been found over-expressed in intestinal carcinoids and small cell lung carcinomas.[9] The same type of carcinoma even co-expresses two bombesin receptor subtypes. This suggests that bombesin peptide is a very good candidate for visualising these tumours in earlier

diagnosis. It is more and more important to develop GRP receptor targeting agents including the bombesin peptide for both diagnostic imaging and therapeutic application. Previous research studies have revealed that bombesin, a 14-amino-acid analogue of mammalian gastrin-releasing peptide, binds to the GRP-R with very high affinity and specificity. This compound, BBN (7−13) NH_2 is the most popular peptide sequence used for designing tumour-specific radiotracers for early diagnosis or systemic radiotherapy of the GRPR-positive tumours.

Tumour angiogenesis is the process of growing new blood vessels that can assist cancerous growths through supplying nutrients and oxygen also removing waste products.[10,11] Angiogenesis is an important mechanism involved in the of spreading of a tumour, and in a simplified explanation, cancer cells can invade into the blood vessel, and also can then be transported to a distant site.[12-14] A secondary tumour will grow once cancer cell invade the normal tissue in this new site. Angiogenesis is a potential target for combating tumour as it plays a key factor in tumour metastasis and growth. Application of specific compounds that may inhibit new blood vessels at tumour site may help switching off the metastasis.

The biomolecule called $\alpha_v\beta_3$ integrin is one of important molecular markers which involved in the mechanism of cell adhesion to the extracellular matrix (ECM). They are highly expressed during angiogenesis and playing an important role of transferring signals from extra-cellular environment to the intracellular compartment.[15] $\alpha_v\beta_3$ integrin is absent in resting endothelial cells and most normal organ systems, rendering it a very potential target for anti-angiogenic cancer therapy. Tumour progression, invasion and metastasis of breast cancer, glioma, melanoma and ovarian carcinoma are all linked to $\alpha_v\beta_3$ integrin overexpression during tumour angiogenesis. It has been found that several proteins like vitronectin, fibrinogen and fibronectin can bind with $\alpha_v\beta_3$ integrin via the same amino acid

sequence arginine-glycine-aspartic acid or RGD.[16-19] Based on this finding, pentapeptide cyclo(-Arg-Gly-Asp-DPhe-Val-) was developed by Kessler and co-workers and shows high affinity and selectivity for $\alpha_v\beta_3$ integrin.[20-22] It has shown that cyclo-(RGDfK) is one the most prominent structures for development of molecular imaging agents for the assessment of $\alpha_v\beta_3$ expression.

As described in Chapter 2, amino acid tagged naphthalene diimide (NDI) has attracted particular attention because of its electron accepting properties and good solubility properties.[23] NDIs and their derivatives are relatively easily-functionalised materials[24,25] which have strong absorption and fluorescence emission at visible and near IR wavelengths. These make NDI-based derivatives attractive candidates as building blocks for optical imaging probes.

In this chapter, two types of promising NDI-peptide imaging probes incoparating naphthalene fluorophore core, cancer specific targeting peptide (RGDfK and Bombesin[7-13]) and an amino acid linking the NDI core with peptide chain were designed and synthesized through a EDC-mediated coupling (EDC=1-Ethyl-3-(3-dimethylaminopropyl)carbodiimide. (Scheme 3.1)

The rational reason that these probes were designed to incorporate cyclo-(RGDfK) or Bombesin[7-13] is that these are known to selectively bind to breast cancer cells and prostate cancer cells that overexpress specific receptor aiming to perform *in vitro* experiments. Furthermore, in this work, the conjugates of NDI dye with cyclo-(RGDfK) or Bombesin[7-13] was used to image cancer cells *in vitro* in preliminary tests.

The application of two-photon fluorescence microscopy has become a very potential tool for studying biological function in living cells and tissue as their many advantages compared with conventional imaging microcopies.[26,27] Neuroscientists in particular prefer to use two-photon fluorescence microscopy to investigating subcellular neural structures and

their physiological function as this technique can image deep tissue with spatial resolution and reduced photodynamic tissue damage and fluorophore photo-bleaching effect.[28,29]

Two photon excited fluorescence spectroscopy is a method that differs from single photon excited fluorescence in the first stage of normal fluorescence process (three stage process, normally consisting of: (1) excitation, (2) internal conversion, and (3) emission).[30] For two photon excitation, the transition of fluorophore from its ground state to an excited state happens by the near-simultaneous ($\sim 10^{-16}$ s) absorption of two photons. One photon excites the fluorophore to a 'virtual' intermediate state while the second photon further excites the fluorophore to the excited state before the virtual state decays (dephases), hence highly focused, very fast pulsed lasers are required (< 1 ps) so that instantaneous irradiation in the focal volume is high. Two photon excitation uses half of the energy needed for one photon excitation to excite a fluorophore in a one-quantum event.

Two photon absorption has already been extensively used for developing a new technique: two photon excitation microscopy, which allows the imaging of living tissue up to a very high depth (up to about one millimeter) and also allows the imaging of targeting processes to specific cells or tissue, making it possible to obtain the imaging of delicate sites, such as the retina and avoiding damage to healthy tissue.[31]

In addition, exciting the fluorophore by two photon absorption requires photons with half the energy and double wavelength for the transition. This allows the diagnosis and treatment of deeper tissue with spectral windows between 800-1100 nm. Two photon excitation can be a potential and powerful alternative to confocal microscopy technique due to its deeper tissue penetration, efficient light detection and reduced phototoxicity.[32]

Until now, very few studies investigated small molecule fluorophores in cells using two photon fluorescence lifetime microscopy (FLIM). For example, cell uptake behaviour of

BODIPY (for boron-dipyrromethene) conjugates and diethynyl dipyrromethene- boron dyes were studied in HeLa cells using two photon excitation lifetime microscopy.[33,34]

The potential of two photon fluorescence imaging technique combined with single photon confocal imaging provide powerful tool to study the peptide-derivatised fluorescence probes for cellular targeting applications. The potential of this technique for providing information on the stability under *in vitro* conditions of the peptide-based targeting NDI probes was discussed here.

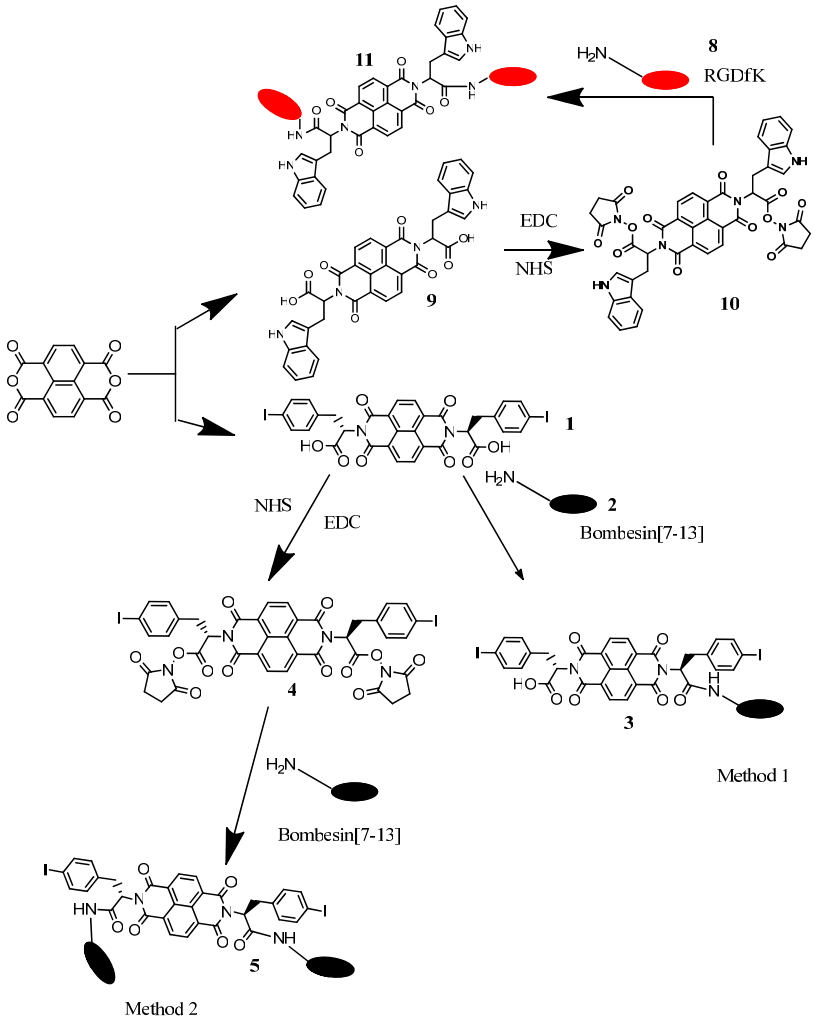

Scheme 3.1. Schematic representation of the methods applied for synthesis of peptide-based targeting NDI probes based on two cancer targeting specific peptides: Bombesin[7-13] and RGDfK.

3.2 Results and Discussion

3.2.1 Synthesis of NDIBBN

3.2.1.1 Bombesin [7-13] analogue

The peptide analog used here is a GRP-receptor binding peptide, bombesin[7 – 13], (denoted BBN, **2**). This amino acids sequence has been studied broadly and shown to bind to all four GRP receptor sub-types with high affinity.[6] These GRP receptors are over-expressed in a variety of tumours, including prostate cancer, making BBN a potentially important labeling tag for both cancer diagnosis and therapy.

The targeting BBN peptide **2** was synthesized using standard Fmoc solid phase synthesis, cleavage, deprotection and purification on an insoluble polystyrene Rink amide 4-methylbenzhydrylamine (MBHA) resin. The resulting BBN peptides **2** used in this study were characterised by electrospray ionisation-MS and HPLC (Table 3.1, Figure 3.2).

3.2.1.2 Two routes for synthesizing the NDIBBN conjugate

A new naphthalene diimide-bombesin conjugate was synthesized by coupling NDI (synthesized as described in Chapter 2 and in appendix) to the amino group of glutamine residue of the conjugates. In here, two routes were designed to couple NDI with BBN.

In the first route (**Method 1**), peptide **2** was attached to NDI in one reaction with EDC·HCl, HOBt·H_2O in DMF. In the second route (**Method 2**), the NHS-activated NDI intermediate, the NDI succinate ester (NDI-OSu, **4**) was synthesized in the first step. This intermediate is stable enough to be purified and stored at low temperatures in the absence of water. The success synthesis of **4** was confirmed by ^{1}H NMR and HPLC characterisation. For the next step, **4** can react with amino group of glutamine residue of BBN peptide in DMF.

All of the intermediate and resulting NDIBBN conjugates were purified by semipreparative HPLC and characterised by electrospray ionisation-MS (Table 3.1). ESI/MS and HPLC traces reveal that only mono-substituted NDIBBN (**3**) was produced in the **Method 1** while double-substituted NDIBBN (compound **5**) can be seen from the **Method 2** (see Experimental Details).

We propose that in the **Method 1** reaction, the steric crowding induced by BBN peptide when attached to one side carboxylic acid group of NDI leads prevents the effective activation of the second carboxylic acid group of NDI, which in turn cannot be effectively activated by NHS and this results in the production of only compound **3**.

However, a double NHS activated NDI intermediate was synthesized firstly in the second route, in which it is likely to avoid this steric hindrance by the peptide chain.

Figure 3.1 shows the UV/Vis absorption and fluorescence emission profile of compounds **5** and **3** in pure DMSO (1 mg/mL concentration). Absorbance spectra show no significant differences between these two dyes which both have two maxima absorption around 360 nm and 378 nm.

Compound 5 (resulting from **Method 2**) shows a small red-shift (1 nm) compared with compound **3** which may arise from the significant structural differences. Accordingly, the fluorescence emission spectra show no apparent difference of these two NDIBBN dyes with maxima emission peak at 396 nm (mono-substituted NDI, compound **3**) and 400 nm (double-substituted NDI, compound **5**), in which compound **5** has a 4 nm red-shift compared with compound **3**.

The formation of compound **5** and their intermediates were confirmed by ^{1}H and ^{13}C NMR wherever the solubility allowed this, and by ESI-MS and HPLC (Table 3.1, Figure 3.2, Figure 3.3).

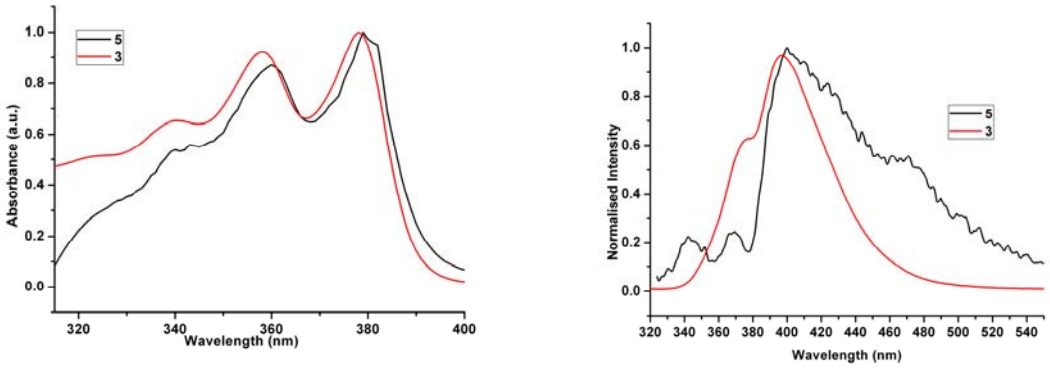

（a） （b）

Figure 3.1. Normalised absorption and emission spectra of compounds **5** and **3** recorded in DMSO at 37 °C.

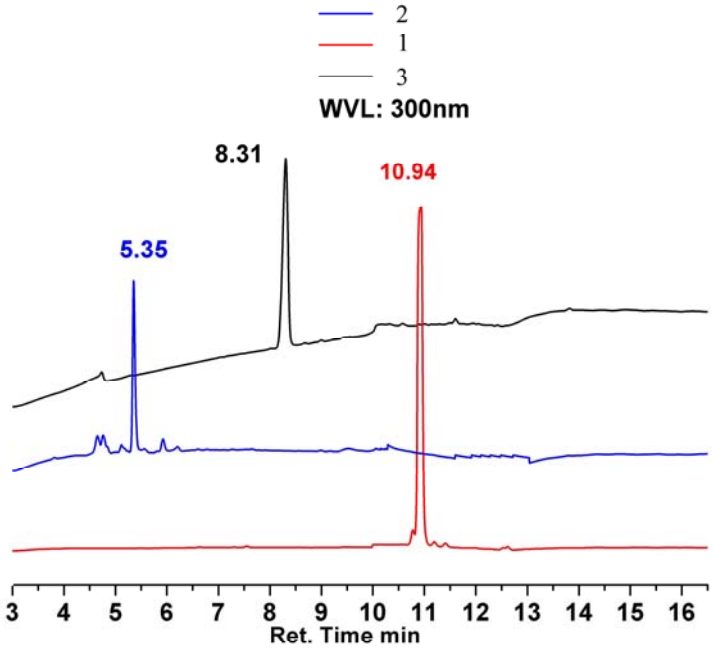

Figure 3.2. HPLC chromatogram comparing of compound **3** with their starting materials (Mobile phase for column: 95 % 0.01 % water; 5 % CH_3CN. Loading solvent for HPLC: DMSO. RP-column flow rate: 0.300 μL min^{-1}.)

Table 3.1. Mass spectroscopy and HPLC analysis (reverse phase) of NDIBBN derivatives and their starting materials

Molecule	Molecular formula	$[M+H]^+$ calculated	MS observed m/z	RP-HPLC retention time(min)
1	$C_{32}H_{20}I_2N_2O_8$	814.93	813.9251 $[M^-]$	10.94
2	$C_{38}H_{56}N_{12}O_8$	809.44	809.44 $[M + H]^+$ 831.42 $[M + Na]^+$	5.35
3	$C_{70}H_{74}I_2N_{14}O_{15}$	1605.36	1627.0 $[M+Na]^+$ 1643.0 $[M+ K]^+$	8.31
4	$C_{40}H_{26}I_2N_4O_{12}$	1008.97	1031.31 $[M+Na]^+$ 1047.28 $[M+K]^+$ 1067.41 $[M+CH_3CN+NH_4]^+$	12.56
5	$C_{108}H_{128}I_2N_{26}O_{22}$	2395.78	2434.43 $[M+ K]^+$	8.71

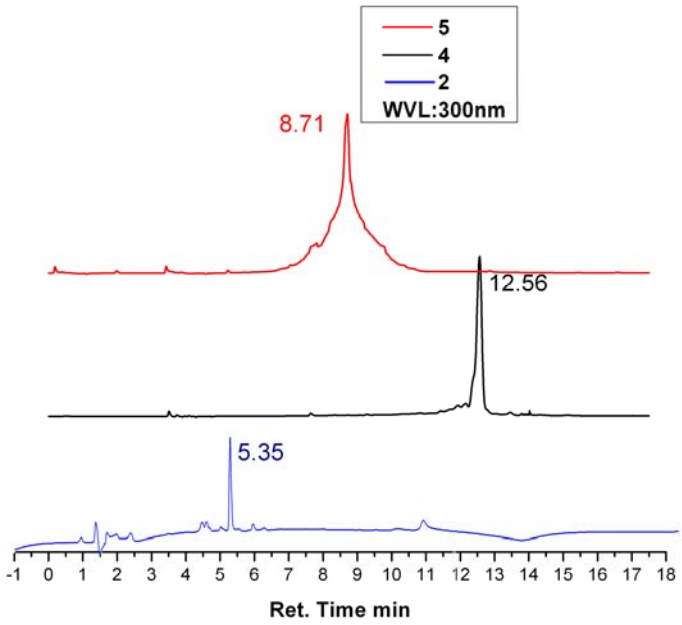

Figure 3.3. HPLC chromatogram compare of compound **5** with their starting materials (Mobile phase for column: 95:5, (0.1% TFA in water): (0.1% TFA in CH_3CN, Loading solvent for HPLC: DMSO. RP-column flow rate: 0.300 μL/min.)

3.2.1.3 Confocal fluorescence microscopy imaging

Confocal fluorescence microscopy images showed that both compounds studied mono-NDIBBN (Compound **3**) and double-NDIBBN (compound **5**) were internalised by

PC-3 cancer cells after 25 minutes of incubation at 37 °C (Figure 3.4). Both dyes mainly localise in the cytoplasm without penetrating the nuclear membrane.

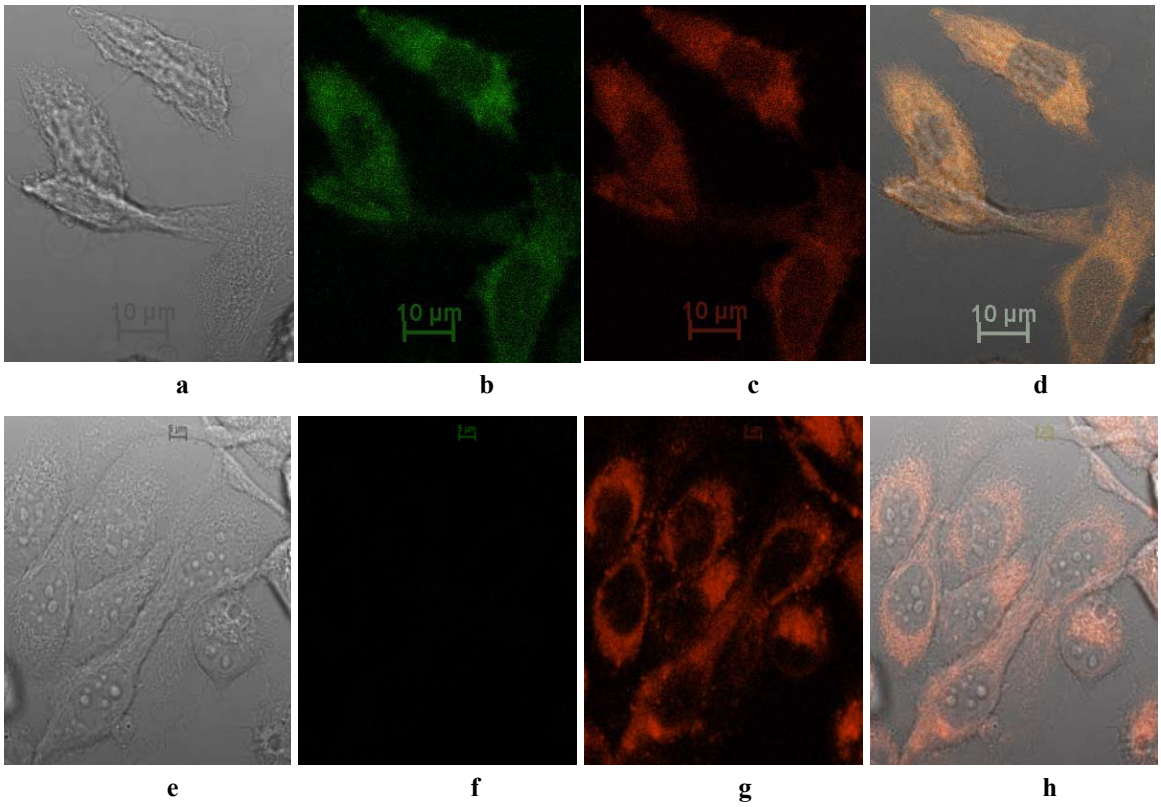

Figure 3.4. Single Photon Laser scanning confocal imaging (λ_{ex} =543 nm) of PC-3 cells incubated for 25 mins at 37 ^{o}C with 38.9 µM mono-NDIBBN (Compound **3**) in 5: 95 % DMSO: serum free medium (**a-c**) and 38.9 µM compound **5** in 5: 95 % DMSO: serum free medium (**e-h**). Scalebar 10 µm

*3.2.1.4 Cytotoxicity of NDIBBN derivatives (compounds **3** and **5**) on fibroblast cells and prostate cancer PC-3 cell line*

In order to evaluate the cytotoxicity of compounds **3** and **5**, the typical MTT assay was used here, in which the conversion of soluble MTT into formazan is directly related to mitochondrial activity and subsequently to cell viability. As shown in Figure 3.5 and Figure 3.6, both compounds **3** and **5** show high cytotoxicity to prostate cancer PC-3 cells with IC_{50} value of 22.53±3.1 µM and 6.38±0.9 µM, while they show low cytotoxicity to fibroblast Fek-4 cells with IC_{50} value of 380.4±14.8 µM and 809.81±50.8 µM after 24h incubation.

The selective inhibition behavior observed seems to suggest that both peptide-substituted NDIBBN have anticancer activity to PC-3 cells. Data indicates that these compounds have significant potential towards prostate cancer therapeutic applications. Moreover, data indicates that the double peptide functionalisation of the NDI core reduces the cytotoxicity towards a healthy cell line (Fek-4) and simultaneously shows increased growth inhibition towards prostate cancer PC-3 cells.

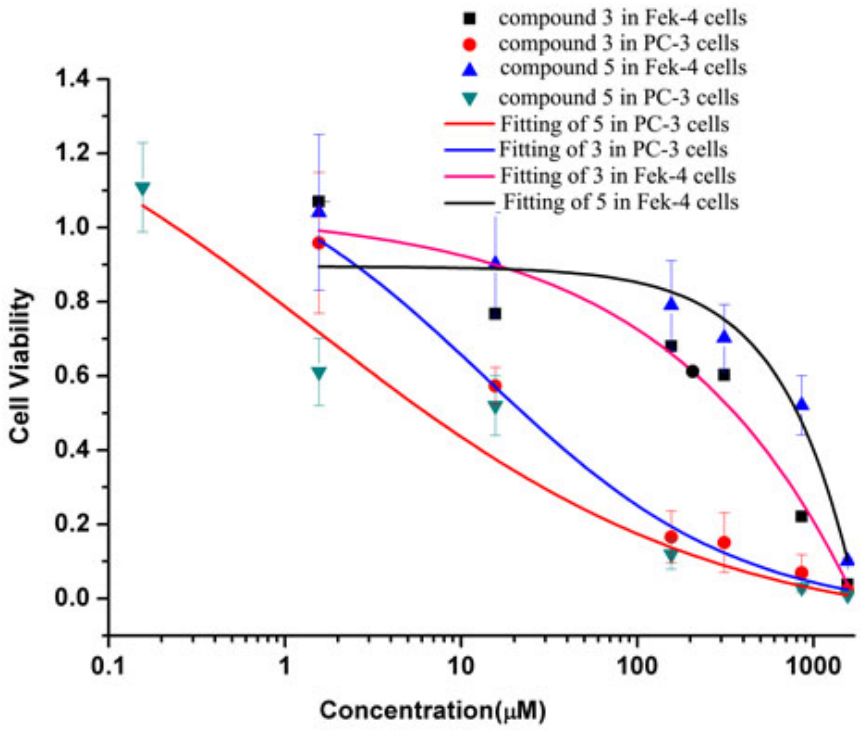

Figure 3.5. Cell viability (fibroblast cell line Fek-4 and Prostate cell line PC-3) as a function of compounds **5** and **3** by typical MTT assay. Cells were cultured in 96-well plates for 24 h the day before the experiment at a density of 7×10^3 cells/well. Then the cells were treated with NDIBBN compounds with varying concentrations for 24 h, respectively. Error bars represent the standard deviation of three measurements. [NDIBBN]= 0−1000 μM, [MTT] =1.0 mg/mL (100 mL/well).

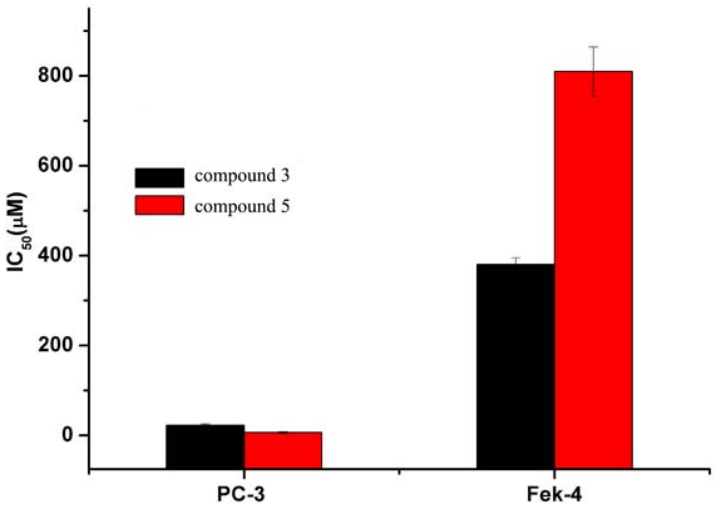

Figure 3.6. IC_{50} (μM) of compounds **5** and **3** towards fibroblast cells Fek-4 and prostate cancer cells PC-3.

3.2.1.5 Fluorescence lifetime microscopy imaging

We are also interested of the lifetime distribution and fluorescence intensity of both NDIBBN dyes in cancer and healthy cells. Figure 3.7 shows lifetime emission maps for compounds **3** and **5** in PC-3 cells together with 2-photon intensity maps showing the spatial variations in fluorescence emission, the lifetime imaging maps and corresponding distribution plots for the predominant lifetime component (τ_1) for both dyes. Lifetime analysis indicates that both compounds **3** and **5** show two components in PC-3 cells. The long lifetime decay component of compounds **3** and **5** in PC-3 cells are 1.92 ± 0.92 ns and 1.66 ± 0.81 ns, separately (Table 3.2), in which compound **5** shows less lifetime compared with compound **3** but not too much. The FLIM mapping of compound **5** shows a homogenous distribution of the fluorescence lifetimes throughout the cytoplasm area but not penetrating the nuclear membrane.

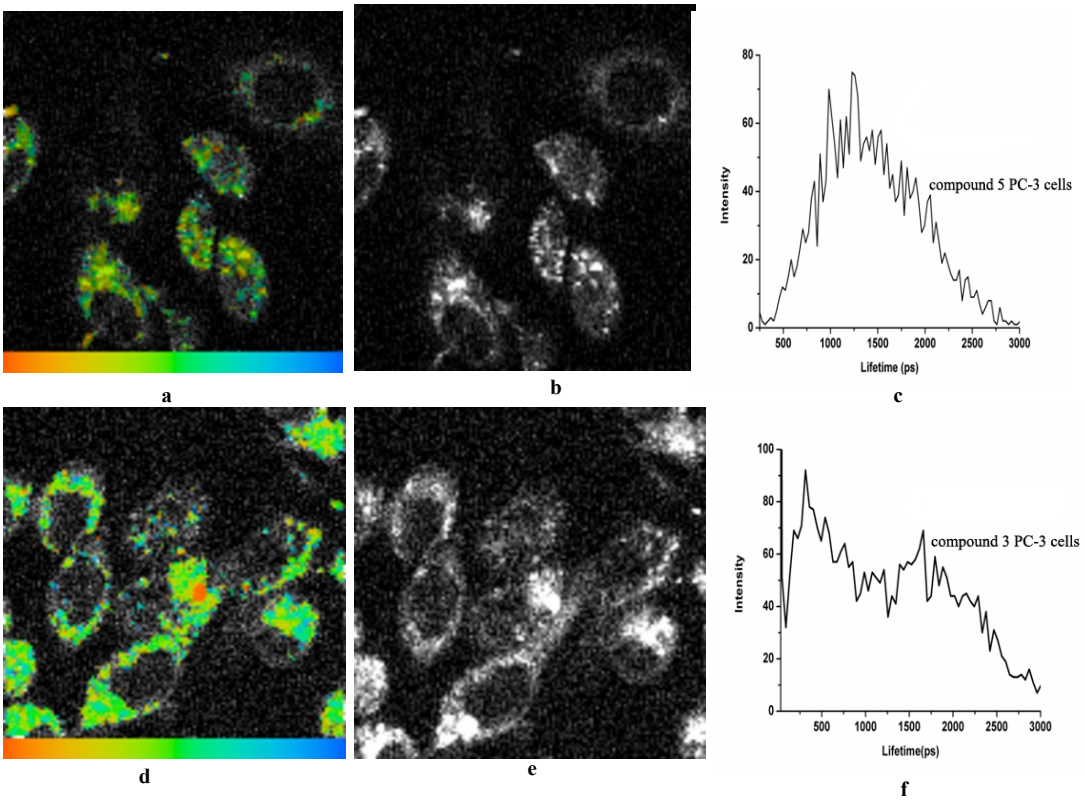

Figure 3.7. Two-photon laser confocal fluorescence (λ_{ex} = 910 nm): fluorescence lifetime (a), fluorescence intensity (b) and corresponding lifetime distribution curve (**c**) of PC-3 cells incubated with compound **5** (38.9 μM in 5: 95 % DMSO: EMEM). Lifetime mapping and scalebar (**d**), intensity image (**e**), and corresponding lifetime distribution curve (**f**) of PC-3 cells incubated with compound **3** (38.9 μM in 5: 95 % DMSO: EMEM).

Table 3.2. Lifetime decay constants for compounds **3** and compound **5** in PC-3 cell

Compound	τ_1 / ns	WHHM / ns	τ_1 %	τ_2 / ns	WHHM / ns	τ_2 %	χ^2
3	0.31	0.16	77.5	1.66	0.81	22.5	1.43
5	0.71	0.18	84.9	1.92	0.92	15.1	1.20

3.2.2 Synthesis and characterisation of 3@SWNTs supramolecular hybrid

One important strategy for tracing the early stage of cancer cells is to using highly luminescent nano-vectors for qualitative or even quantitative *in vitro* detection of tumour cells. Quantum-Dot and gold rods decorated luminescent carbon nanotubes have been made for cancer cell imaging.[35] The shortage of these methods is the high cytotoxicity of the decorated luminescent QD and gold rods. Even overcoming the cytotoxicity of popular CdSe/ZnS quantum dots is a major problem of this material application.[36] In this research,

we report a novel strategy to develop fluorescent tracers with the properties of precise detecting and low cytotoxic by wrapping carbon nanotubes with NDIBBN conjugate. We are aiming to use coat the entire aromatic surface of nanotubes by benign materials in order to decrease the toxicity of SWNTs, and render it traceable *in vitro.* Bombesin-derivatised NDIs were synthesised as described in Experimental section (Chapter 7) and used for the supramolecular functionalisation of carbon nanotubes.

Upon mixing the peptide-NDI compounds with solid SWNTs in ethanol (0.125 mg/mL), we observed the formation of clear carbon nanotube dispersions. Since the peptide-NDI complexes are fluorescent they were also chosen to act as fluorescent tags for tracing the dispersed SWNTs hybrid in cells. The fluorescence emission was expected to be quenched by carbon nanotubes. As discussed in Chapter 2, some residual NDI fluorescence is retained and allows the tracing of the composite in cells. The protocol involving in the use of bombesin as a peptide coupled to naphthalene diimide was investigated with a view to exploring its possible function as a vehicle for delivering this complex to tumour sites. The design engages to introduce the amino acid group of bombesin peptide to imide position of NDI and therefore reduce the cytotoxicity of carbon nanotubes. It is hoped that, as shown in Chapter 2, the NDI will cover the entire area of carbon nanotubes avoiding the exposure of aromatic surface to biomolecules *in vitro* and thus reducing the SWNTs' cytotoxicity.

3.2.2.1 High purity single carbon nanotubes for biomedical funtionalisation

Different methods have been exploited to remove amorphous carbon, catalyst, such as gas phase reaction, acid oxidation, electrochemical oxidation, filtration, and chromatography.[37] In this work, the objective was to use carbon nanotubes of highest purity as a vector for cellular delivery. Then the clear aromatic surface of carbon nanotube can be functionalised with biomolecules to decrease their cytotoxicity. Briefly, the cytotoxicity of

SWNTs can be due to several factors: metal impurities, surface area, dispersion and aggregation status, coating or functionalisation.[38] Metal catalysts used in synthesis can be removed by acidic oxidising and converting to Fe(II), then washing with water at neutral pH. As also discussed in previous chapters, in this chapter we also used carbon nanotubes from Thomas Swann, purified by a steam-based method to remove the amorphous carbon and open the end of tubes, pioneered by the research group of Prof Malcolm Green (Oxford Nanotube Group).[39,40] During the steam purification the graphitic shells which are normally coating the catalytic metal particles and amorphous carbon on the surface of carbon nanotubes are known to be removed without introducing further defects on the nanotubes walls. [39,40] Further purification gives SWNTs characterised by clear outer surfaces, as shown by HRTEM (see Chapter 5 Figure 5.1). This substrate, available from Thomas Swann Ltd (Elicarb), was used for all supramolecular functionalisation methods described hereby.

*3.2.2.2 Complex of compound **3** with SWNTs*

In this report, mono-NDIBBN (compound **3**) was selected for functionalising SWNTs forming imaging probes due to its high solubility and because it was available in highest yield. The **3**@SWNT complex was prepared by mixing compound **3** water solution (2.4 mg, 1 μmol, 2 mL) with SWNT (0.25 mg, 2 mL) EtOH dispersion, then sonicating 20 mins, solution was stirred at room temperature for 2 days. Dialysis of compound **3** and SWNTs mixture against phosphate-buffered saline (PBS, 50 mM, pH 7.4) was carried out at 27 ^{o}C which can results in removal of unbound compound **3**. Centrifuging was performed to remove the aggregate since the large, insoluble aggregates (> 1 μm size) are unlikely to be suitable for biomedical imaging applications.

Approximately, 90% of the initial SWNTs sample was dispersed in aqueous media as described above in the presence of NDIBBN based on the UV-vis-NIR absorption analysis.

The UV-visible absorption spectra of NDIBBN in a DMSO solution (*ca.* 1mg/mL), compound **3**@SWNT DMSO suspension and SWNT are presented in Figure 3.8. This shows that the lowest energy absorption band of compound **3**@SWNT solution in DMSO is red-shifted from 378 nm to 383nm relative to the spectrum of the pure compound **3** solution (1 mg/mL dispersions). The red-shift of π- π* transition band of *ca.* 5 nm was observed: this was due to the possibility that charge-transfer interactions may occur between compound **3** and SWNT.

Severe quenching of the fluorescence emission intensity and a large red-shift in the emission maxima of compound **3** were observed after compound **3** anchoring onto SWNT from the 2D fluorescent contour plotting and fluorescence spectroscopy (Figure 3.8 b and Figure 3.9, emission shifts observed were from $\lambda_{em\ max}$=396.5 nm to $\lambda_{em\ max}$ = 417 nm).

Compared with the sharpness of the maxima emission peak of compound **3**, the emission peak of compound **3**@SWNT is much broader. The maxima emission peak of compound **3** around 396 nm was not seen in 2D fluorescence contour plotting of functionalised SWNTs. These observations confirm that free, unattached, compound **3** coating can be successfully removed after 3 cycles of the filtration/dispersion procedure described in Chapter 2 and above.

This red-shift behaviour observed in the spectrum of compound **3**@SWNT dispersions can be rationalised by the mechanism of fluorescence resonance energy transfer (FRET) a physical process resulting from induced dipole-induced dipole interactions at a close proximity (< 10 nm) between SWNTs and absorbed compound **3**.

The red-shift of emission suggests that more photon energy is required for compound **3** fluorescence excitation due to SWNT absorption. The broadening of compound **3**@SWNT emission spectrum was possibly due to the non-homogeneity of isolated or small bundled SWNTs present in dispersions.

Despite this quenching of fluorescence by SWNT, the residual fluorescence of bound compound **3** adequate for cell imaging, as described below.

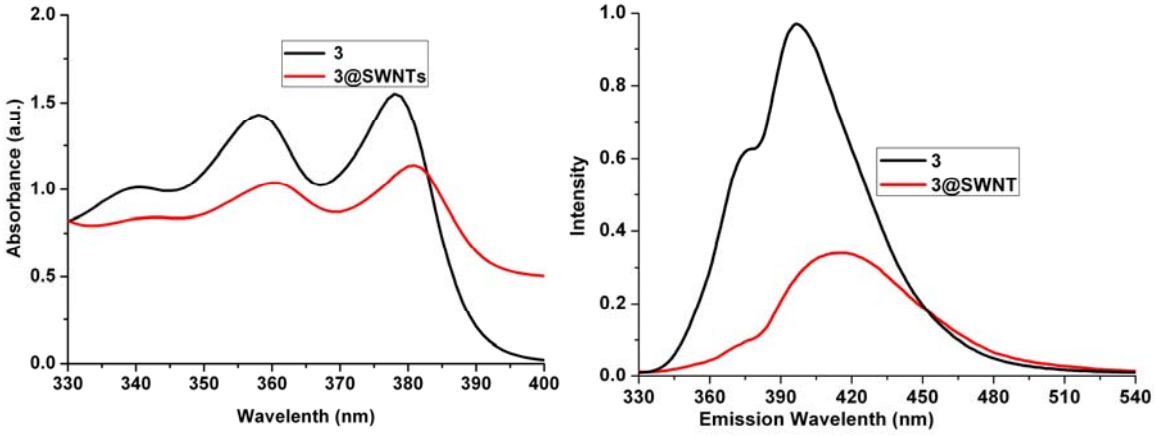

(a) **(b)**

Figure 3.8. UV-Vis spectrum comparison of compound **3** and **3**@SWNT (**a**), Fluorescence spectrum compare of compound **3** and **3**@SWNT (**b**) (Dispersions concentration of *ca.* 1 mg/mL).

Raman spectroscopy is a powerful tool in the study and characterisation of functionalised carbon nanotubes. The Raman spectra (excitation 830 nm) of compound **3**, steam purified SWNT and compound **3**@SWNT are shown in Figure 3.11. The expected G band at *ca.* 1585 cm^{-1}, disordered D band at *ca.* 1287 cm^{-1} and radial breathing modes (RBM) at 232 cm^{-1}. The D-band is known from disordered sp^2 carbon structure and has been considered as probe for C-atom vacancies, amorphous carbon stacking on the surface of nanotubes, chemical groups' substitution and other symmetry-breaking phenomena.[41] The dramatic decrease of the D-band intensity in compound **3**@SWNT compared to the starting material, indicating that the covalent functionalisation route reported here can efficiently remove defects formed during purification. This represents an advantage compared to chemical modification on the sidewall which can cause a partial destruction of SWNTs. The significant peaks observed in NDIBBN Raman Spectrum (303-380 cm^{-1}, 609-694 cm^{-1}, 1038 cm^{-1}, 1415 cm^{-1} and 2117 cm^{-1}) are all present in compound **3**@SWNT spectrum. This

indicates that SWNTs remain successfully functionalised by compound **3** after removing excess **3**.

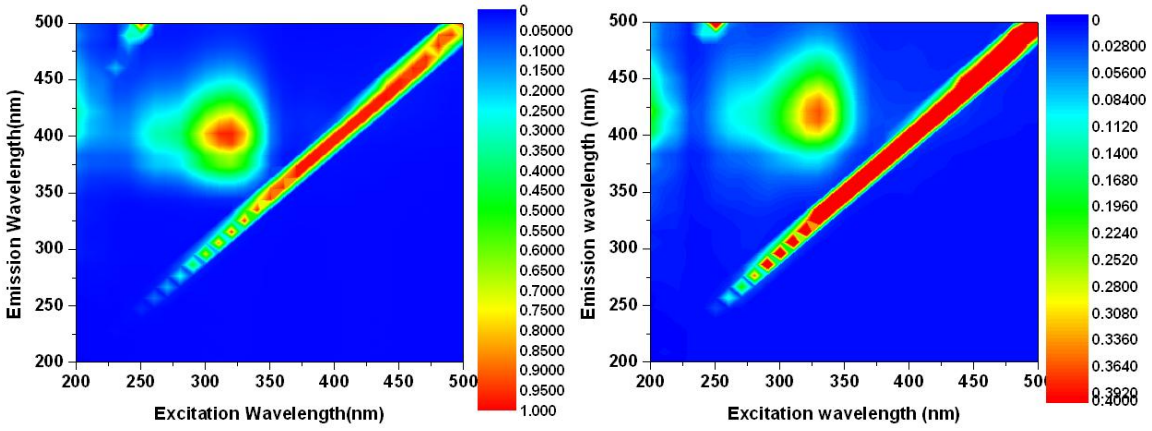

(a) **(b)**

Figure 3.9. 2D Emission/excitation contour plotting (normalised intensity) of free compound **3** (a) (38.9 μM in DMSO) and re-dispersed **3**@SWNT composite (b) resulting after the *stage 4* of the re-dispersion experiment (38.9 μM compound **3** binding with 60 μg/mL SWNTs in DMSO).

Steam purified SWNTs used here were dispersed in EtOH by ultrasonication and deposited onto a lacey carbon coated TEM grid. Figures 3.10 a shows a typical HRTEM image of an individual debundled SWNTs with pretty clean wall surface. To examine the successful wrapping of **3** on SWNTs, **3**@SWNTs composites were dispersed in EtOH using ultrasonication and deposited onto a lacey carbon/copper grid. Figure 3.10b shows a typical TEM image of a bundle of CNTs with **3** attached on the outside of the SWNTs compared to Figure 3.10a. The presence of **3** attached on surface of SWNTs was also can be confirmed by energy dispersive X-ray spectroscopy (EDS) analysis, Figure 3.10c clearly shows the iodine atom peaks are present in the **3**@SWNTs EDS spectrum compared with control EDS spectrum.

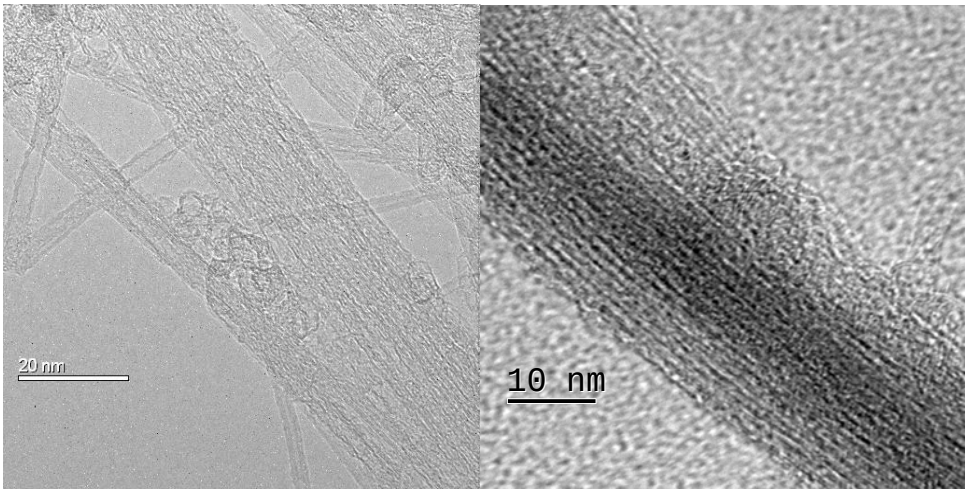

(**a**) (**b**)

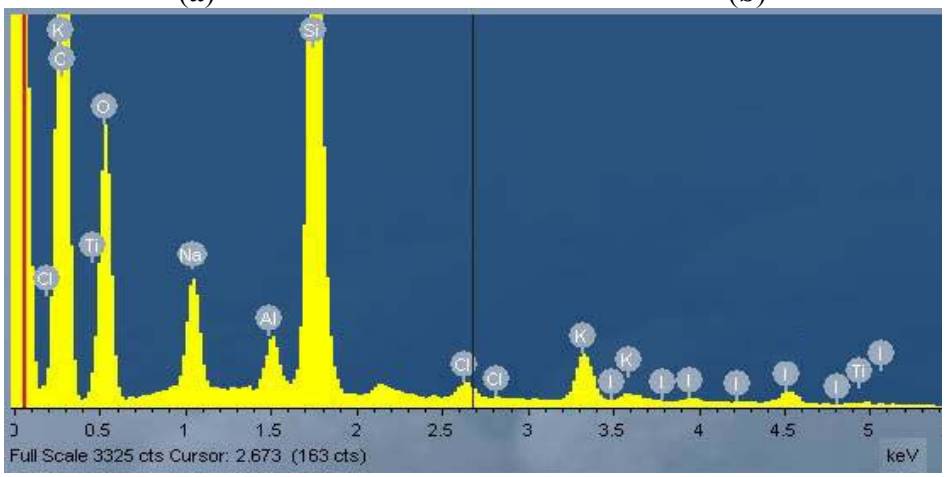

(**c**)

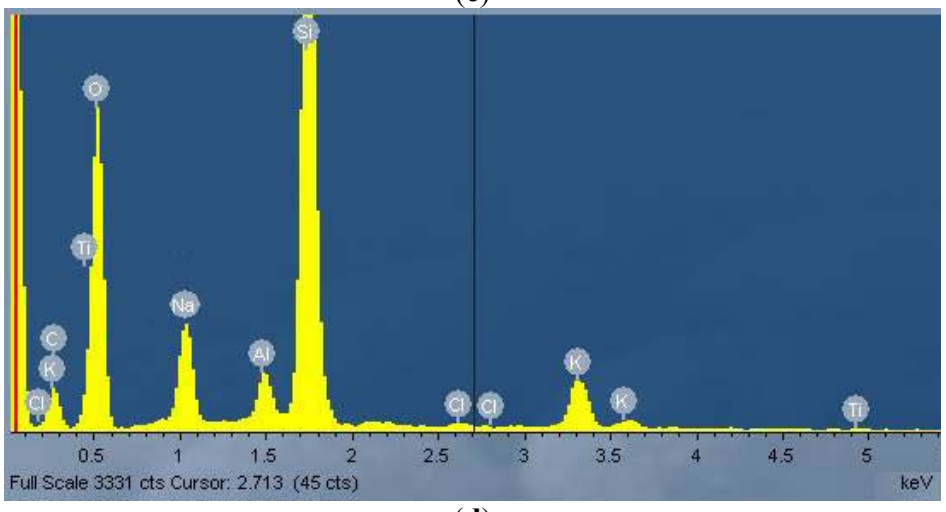

(**d**)

Figure 3.10. Representative images from TEM (recorded as supported on lacey carbon/copper grids) of steam purified SWNTs (**a**) and compound **3**@SWNT composites (**b**). The EDS spectrum of compound **3**@SWNT composites deposited on glass support (**c**) and control EDS spectrum (**d**).

Raman spectroscopy was carried out to probe the presence of compound **3**@SWNTs in cells. MCF-7 cells were incubated with compound **3**@SWNT for 20 min, washed with 3×PBS. Cells were suspended in 2 mL PBS prior to the measurement. Raman scattered light was collected using an ISA Triax 550 spectrometer equipped with a 41 liquid-nitrogen cooled CCD. Intense G-bands centred around 1590 cm^{-1} and RMB range from 100 cm^{-1} to 350 cm^{-1} were easily observed from spectrum collected from cytoplasmic region area of MCF-7 cells incubated with compound **3**@SWNT. This measurement confirmed that this SWNTs-peptide hybrid was indeed translocated into MCF-7 cells (Figure 3.12).

Several regions "black dots" can be observed in cytoplasm region from this optical image of MCF-7 cells. Control cells incubated in medium (without SWNTs) had no detectable SWNT Raman signatures under the same conditions. The higher noise level in the Raman spectrum in MCF-7 cells is possibly due to the Rayleigh and Raman scatterings of lipids and cell organelles.

From this optical image of MCF-7 cells, black dots can be observed within cytoplasm region. Control cells incubated in medium (without SWNTs) had no detectable SWNT Raman signatures under the same conditions. The higher noise level in the Raman spectrum in MCF-7 cells is possibly due to the Rayleigh and Raman scatterings of lipids and cell organelles.

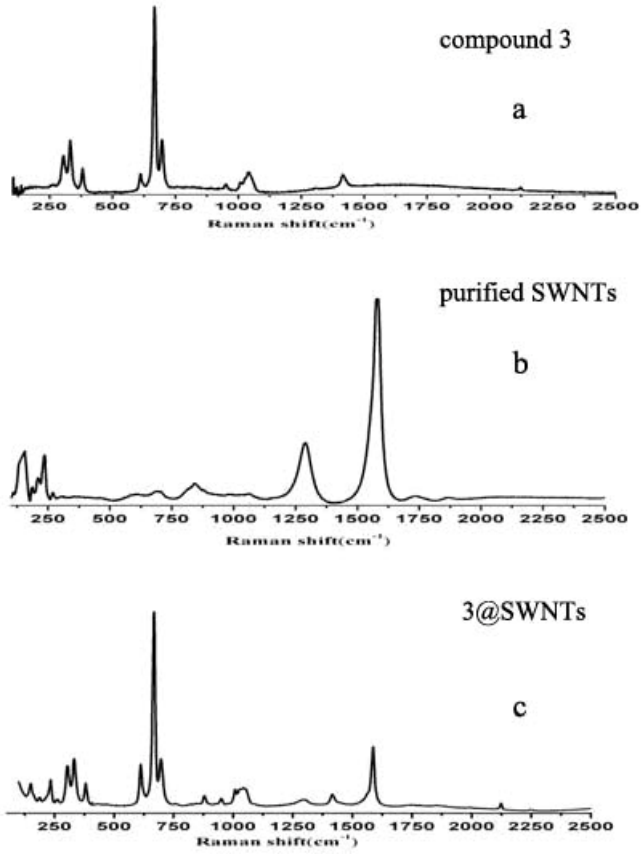

Figure 3.11. Raman spectroscopy of compound **3** (**a**), purified SWNT (**b**) and compound **3** functionalised SWNTs(**c**) (λ_{ex}=830 nm, laser power at the sample 220 mW spot size 100 μm).

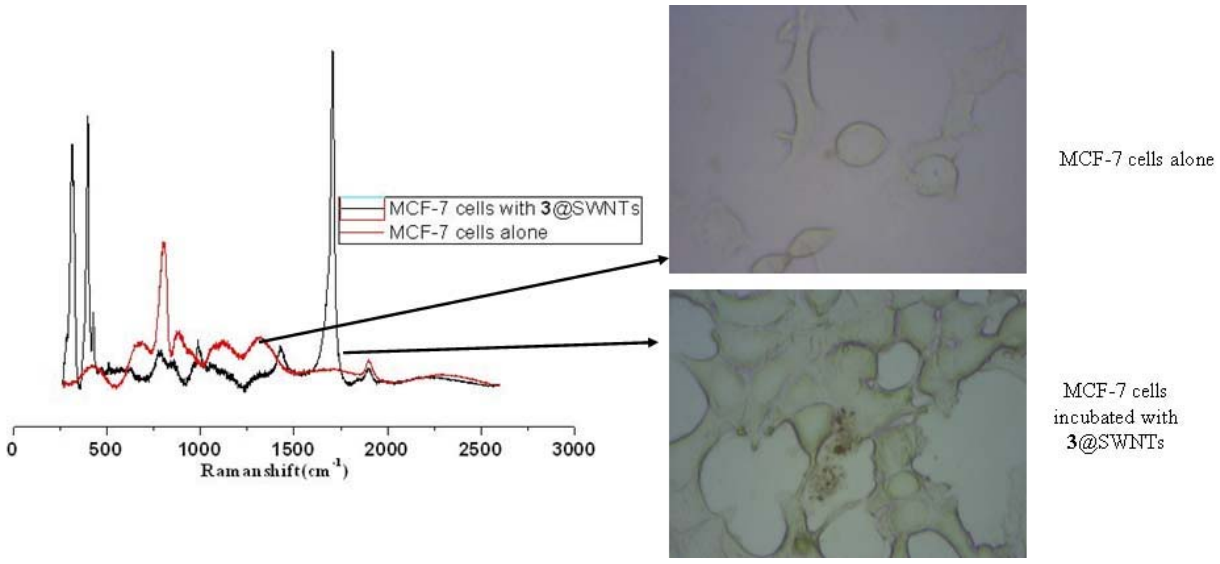

Figure 3.12. Raman spectra acquired from cytoplasmic regions of the live MCF-7 cells alone and MCF-7 cells that were incubated at 37°C for 20 mins with compound **3**@SWNT. The arrows in the optical micrographs denote the specific regions of the MCF-7 cells where spectra were acquired.

*3.2.2.3 Laser scanning confocal imaging and life-time imaging of compound **3**@SWNTs in cells*

Despite the strong quenching of the compound **3** by SWNTs, the residual emission of the absorbed compound **3** was sufficient for mapping the distribution of SWNT in living cells using single- and two-photon fluorescence microscopy.

Cell uptake was monitored in PC-3 (Figure 3.13 and Figure 3.14) and HeLa cells (Figure 3.15) by single-photon laser scanning confocal fluorescence imaging (λ_{ex}= 488 nm, 25 min incubation at 37 °C). The luminescent nanocomposites mainly localise in the cytoplasm (for both PC-3 and HeLa cells) without entering into the nucleus which can be confirmed by the fluorescent mapping.

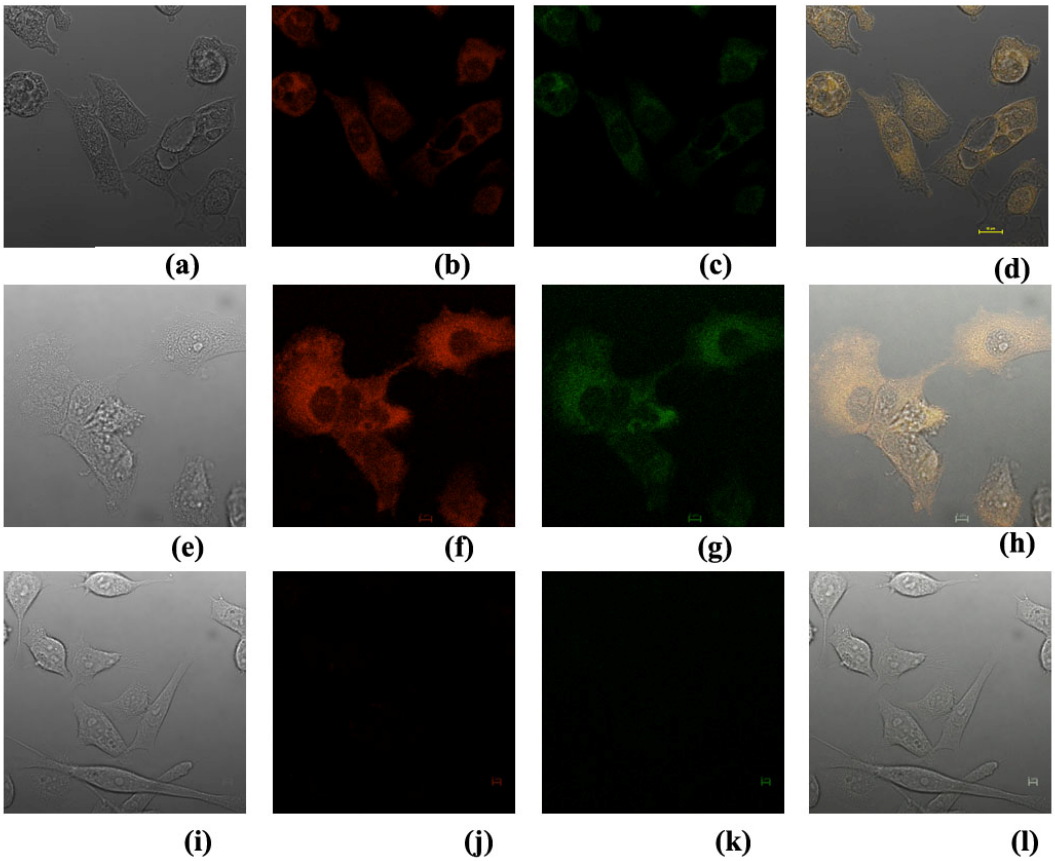

Figure 3.13. Single Photon Laser scanning confocal imaging (λ_{ex} =488 nm) of PC-3 cells incubated for 25mins at 37 ^{o}C with: (**a-d)** compound **3** 38.9 µM in 5: 95 % DMSO: serum free medium; (**e-h**): compound **3**@SWNT in (38.9 µM compound **3** binding with 60 µg/mL SWNTs in 5: 95 % DMSO : serum free medium); (i-l): 5: 95 % DMSO : serum free medium control. Scalebar 5 µm

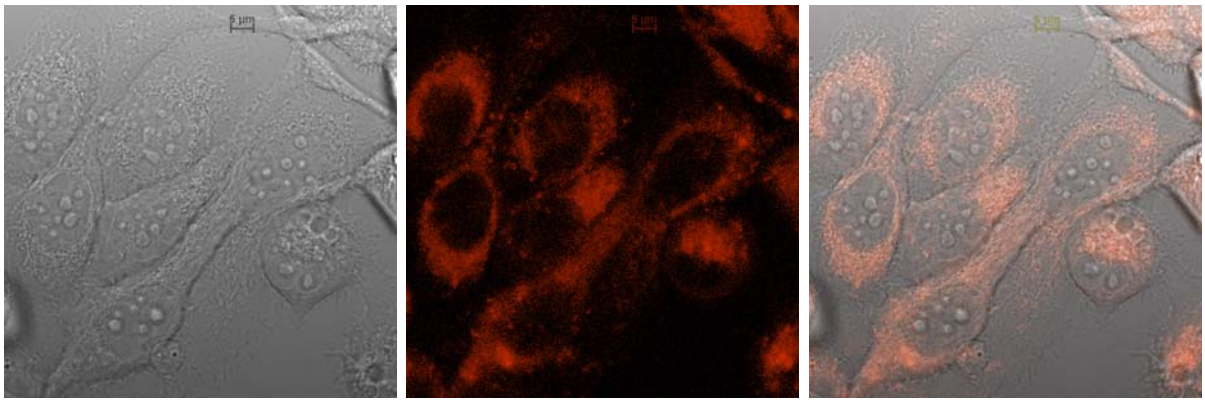

(a) **(b)** **(c)**

Figure 3.14. Single Photon Laser scanning confocal imaging (λ_{ex} =543 nm) of PC-3 cells incubated for 25 mins at 37 ^{o}C with: (a-c) Compound **5** 38.9 µM in 5: 95 % DMSO : serum free medium, Scalebar 5 µm

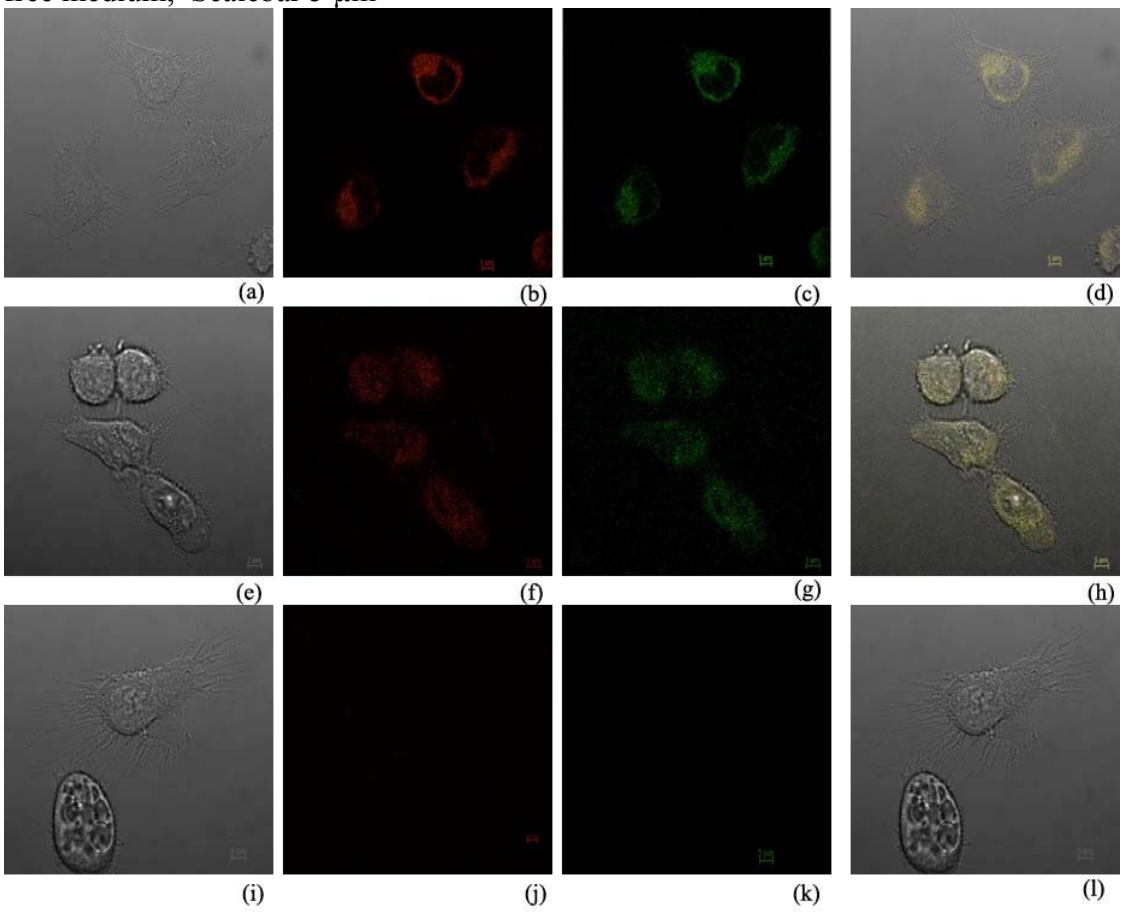

Figure 3.15. Single Photon Laser scanning confocal imaging (λ_{ex} =488 nm) of HeLa cells incubated for 25 mins at 37 ^{o}C with: (**a-d**) compound **3** 38.9 µM in 5: 95 % DMSO : serum free medium; (**e-h**): **3**@SWNT (38.9 µM compound **3** binding with 60 µg/mL SWNTs) in 5: 95 % DMSO: serum free medium (**i-l**): 5: 95 % DMSO : serum free medium control. Scalebar 5 µm

To probe the potential of NDI@SWNT as a precursor for future applications as traceable imaging probes inside living cells, two-photon emission lifetime decay spectra were recorded by time-correlated single photon counting using pulsed laser excitation (λ_{ex} = 910 nm in DMSO). To compare the lifetime of NDI and compound **3**, two-photon emission lifetime decay spectra of these two solid was recorded in DMSO by time-correlated single photon counting using pulsed laser excitation (λ_{ex}= 910 nm). Clearly, the lifetime of compound **3** (1.23 ns) is significantly shorter than that of NDI (lifetime 2.67 ns) under the same condition and can be rationalised due to NDI fluorescence quenching by neighboring peptide chain, causing additional non-radiative pathways for the loss of fluorescence, perhaps through additional H bonding involving the peptide chain.

To verify the cellular behaviour of the supramolecular compound **3**@SWNT nanohybrid in terms of stability, fluorescence intensity and biolocalisation, fluorescence emission lifetime measurements were carried out using 2-photon FLIM in HeLa and PC-3 cell lines (20 min incubation, 37 ^{o}C, using 910 nm excitation from a mode locked Mira titanium sapphire laser, 180 fs pulse, 75 MHz) and data was compared with FLIM of the free compound **3** under identical conditions.

Figure 3.16 shows lifetime emission maps for compound **3** and **3**@SWNT in PC-3 cells together with 2-photon intensity maps showing the spatial variations in fluorescence emission, the lifetime imaging maps and corresponding distribution plots for the predominant lifetime component (τ_1) for either free compound **3** or **3**@SWNT composite.

Similar images are included for the FLIM of compound **3** and **3**@SWNT in the HeLa cell line (Figure 3.17). Lifetime imaging shows that both compound **3** and **3**@SWNT have two lifetime components in HeLa and PC-3 cells (long component and short component). The long lifetime component of free compound **3** measured in PC-3 cells, HeLa cells and DMSO are 1.66 ± 0.81 ns, 1.93 ± 1.28 ns and 1.23 ± 0.19 ns respectively. These values are

rather close in terms of order of magnitude and suggest that the cellular environment does not interfere significantly on the lifetime of this compound.

The short and long lifetime components of **3**@SWNT are 0.24±0.11 ns (83 %) and 1.45±0.72 ns (17 %) for PC-3 cells, while 0.56±0.38 ns (81.7 %) and 1.47±1.03 ns (18.3 %) for HeLa cells (Table 3.3 and Table 3.4).

The short lifetime component is believed to be a contribution from intact **3**@SWNT composite, which is due to the fluorescence of the NDIBBN (Compound **3**) coating which was quenched by SWNTs. Also It was found that the long lifetime component is present - this is supposed to be from NDIBBN (compound **3)** dissociation, breaking free from composite in the cell. Based on the above analysis, we postulate that the "host" and "guest" components of compound **3**@SWNT composites are separated to a certain degree during this incubation time inside of cell, but this level of dissociation was estimated at only *ca.* 20% within 20 minutes incubation.

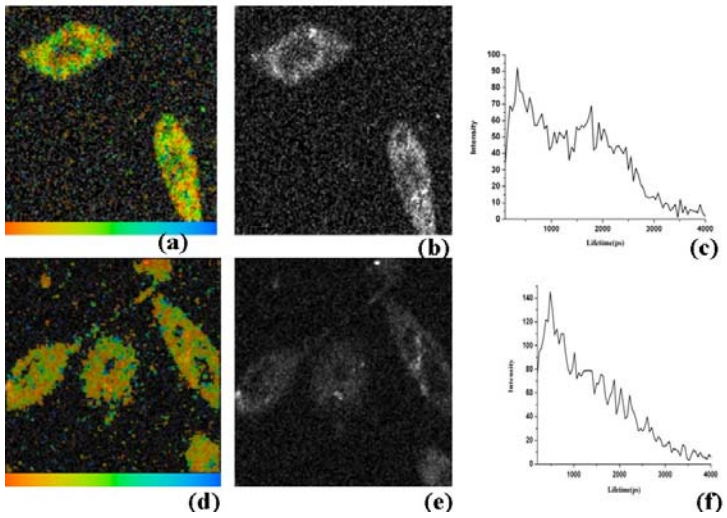

Figure 3.16. Two-photon laser confocal fluorescence (λ_{ex}= 910 nm):(**a,c,e)** Typical micrograph of PC-3 cells incubated for 20 min at 37 ^{o}C with compound **3** (38.9 μM in 5: 95 % DMSO: EMEM showing NDIBBN mainly stay in cytoplasm surrounding nucleus, lifetime mapping and scalebar (**a**), intensity image (**b**), and corresponding lifetime distribution curve (**c**); (**b, d, f**) Typical micrographs of PC-3 cells incubated for 20 min at 37 ^{o}C with compound **3**@SWNT composite dispersion (5: 95 % DMSO: EMEM contained 38.9 μM compound **3** binding with 60 μg/mL SWNTs). Lifetime mapping and scalebar (**d**), Intensity image (**e**), and corresponding lifetime distribution curve (**f**).

Table 3.3. Lifetime decay constants for compounds **3** and **3**@SWNT in PC-3 cell

Compound	τ_1 / ns	WHHM / ns	τ_1 %	τ_2 / ns	WHHM / ns	τ_2 %	χ^2
3	0.31	0.16	77.5	1.66	0.81	22.5	1.43
3@SWNT	0.24	0.11	83.0	1.45	0.72	17.0	1.60

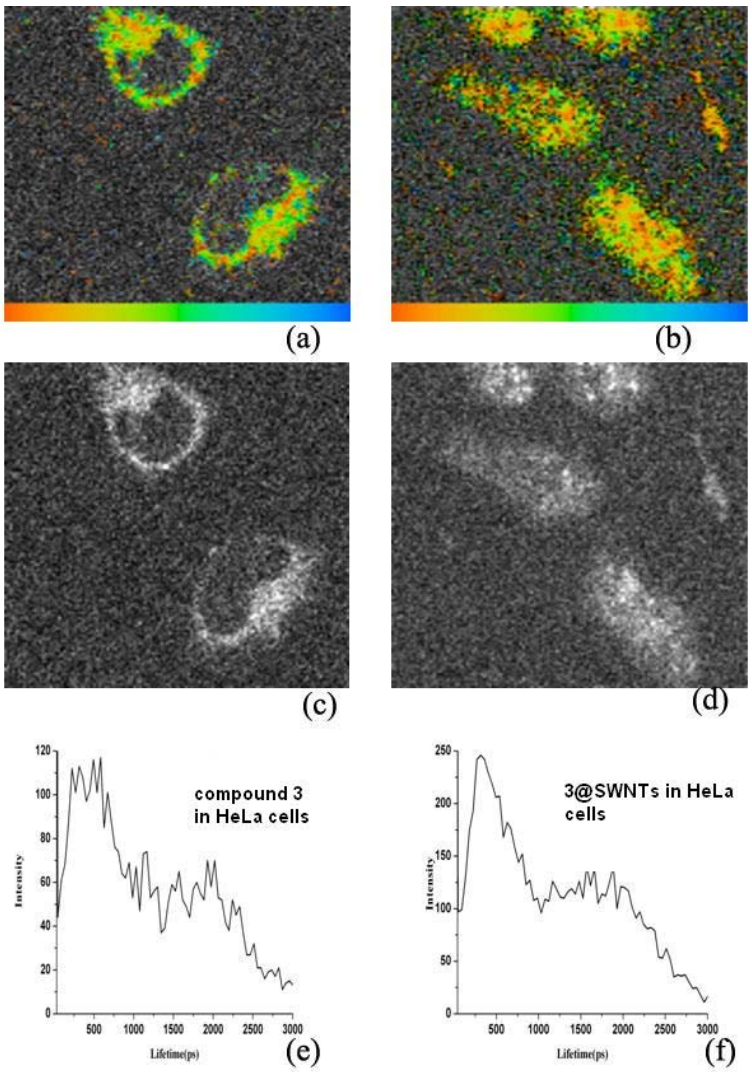

Figure 3.17. Two-photon laser confocal fluorescence (λ_{ex} = 910 nm):(**a,c,e**) Typical micrograph of HeLa cells incubated for 20 min at 37 ^{o}C with compound **3** (38.9 µM in 5: 95 % DMSO: EMEM showing NDIBBN mainly stays in cytoplasm surrounding nucleus, lifetime mapping and scalebar (**a**), intensity image (**c**), and corresponding lifetime distribution curve (**c**); (**b, d** and **f**) Typical micrographs of PC-3 cells incubated for 20 min at 37 ^{o}C with compound **3**@SWNT composite dispersion (5: 95 % DMSO : EMEM contained 38.9 µM compound **3** binding with 60 µg/mL SWNTs. lifetime mapping and scalebar (**b**), Intensity image (**d**), and corresponding lifetime distribution curve (**f**).

Table 3.4. Lifetime decay constants for compounds **3** and **3**@SWNT in HeLa cell

Compound	τ_1 / ns	WHHM / ns	τ_1 %	τ_2 / ns	WHHM / ns	τ_2 %	χ^2
3	0.49	0.29	77.5	1.93	1.28	22.5	1.19
3@SWNT	0.56	0.38	81.7	1.47	1.03	18.3	1.03

3.2.3 Synthesis of tryptophan-NDI-cyclo-(RGDfK) conjugate for biomedical imaging

*3.2.3.1 Synthesis, single crystal X-ray diffraction determination of tryptophan-NDI(TrypNDI, **9**)*

A new compound, tryptophan substituted NDI (TrypNDI, **9)**, was synthesized from L-Tryptophan and 1,4,5,8-naphtalenetetracarboxylic dianhydride, using a microwave-assisted method as described in Experimental section (Chapter 7). The molecular structure and supramolecular architecture of compound **9** was determined in the solid state by single crystal X-ray crystallography (Figure 3.18). Single crystal X-ray diffraction data was obtained for tryptophan-NDI by Dr Gabriele Kociock-Köhn. Crystals suitable for analysis were grown from DMSO.

A typical crystal was mounted using the oil drop technique, in perfluoropolyether oil at 150(2) K with a Cryostream N_2 open-flow cooling device. Single crystal X-ray diffraction data were collected using graphite monochromated Mo-Kα radiation (λ = 0.71073 Å) on a Nonius KappaCCD diffractometer. The structures were solved by direct methods and refined using the program WinGX[42] and representations drawn using CCDC Mercury 3.0. In general, coordinates and anisotropic displacement parameters of all non-hydrogen atoms were refined except where this was not possible due to the presence of disorder.

Abbreviated crystal data and structure refinement parameters are included in in Experimental section. The cif file is available in the appended CD.

The new tryptophan NDI-RGDfK conjugate (TrypNDI-RGDfK, **11)** was also synthesized by coupling compound **9** to the amino group of lysine residue of peptide RGDfK (compound **8**). The formation of compound **11** and their intermediates were confirmed by ESI-MS, MALDI and HPLC (Table 3.5).

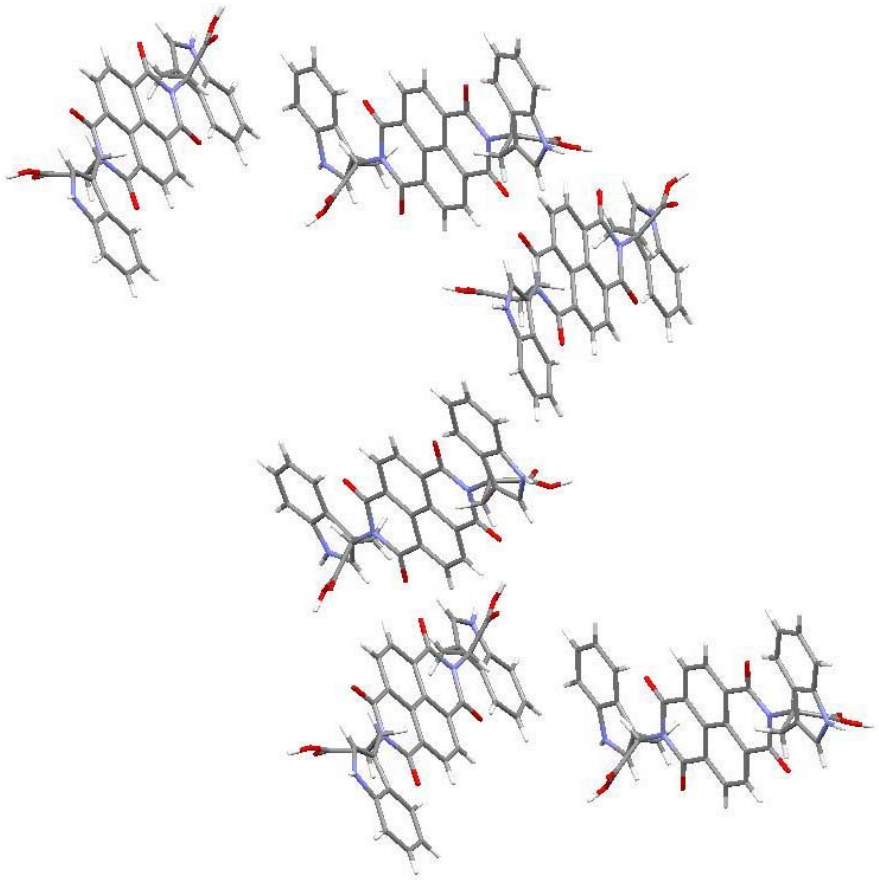

Figure 3.18. a) X-ray structure of TrypNDI (Compound **9**)– view over axis *c*

Table 3.5. Mass spectrometry and RP-HPLC analysis of TrypNDI-RGDfK (Compound **11**) and relevant starting materials

Molecule	Molecular formula	MS calculated	MS observed m/z	RP-HPLC retention time(min)
8	$C_{27}H_{41}N_9O_7$	603	604.3910 $[M+H]^+$	7.95
10	$C_{44}H_{30}N_6O_{12}$	834	857.45 $[M+Na]^+$, 873.46 $[M+K]^+$, 893.33 $[M+K+NH_4+2H]^{4+}$	10.63
11	$C_{90}H_{102}N_{22}O_{20}$	1810.76	1812.75 $[M+2H]^{2+}$	8.62

3.2.3.2 Confocal fluorescence microscopy imaging

Figure 3.19 and Figure 3.20 give the confocal laser scanning microscopy images of compound **9** and **11** in PC-3 cells (λ_{ex} =543 nm). Compound **9** shows emission in all channels after excitation at either 405 nm, 488 nm or 543 nm. By contrast, **11** only shows emission in the red channel after exciting at 543 nm. This indicates that after the compound **9** tagging with two c(RGDfK) peptide groups, the excitation wavelength range narrows significantly.

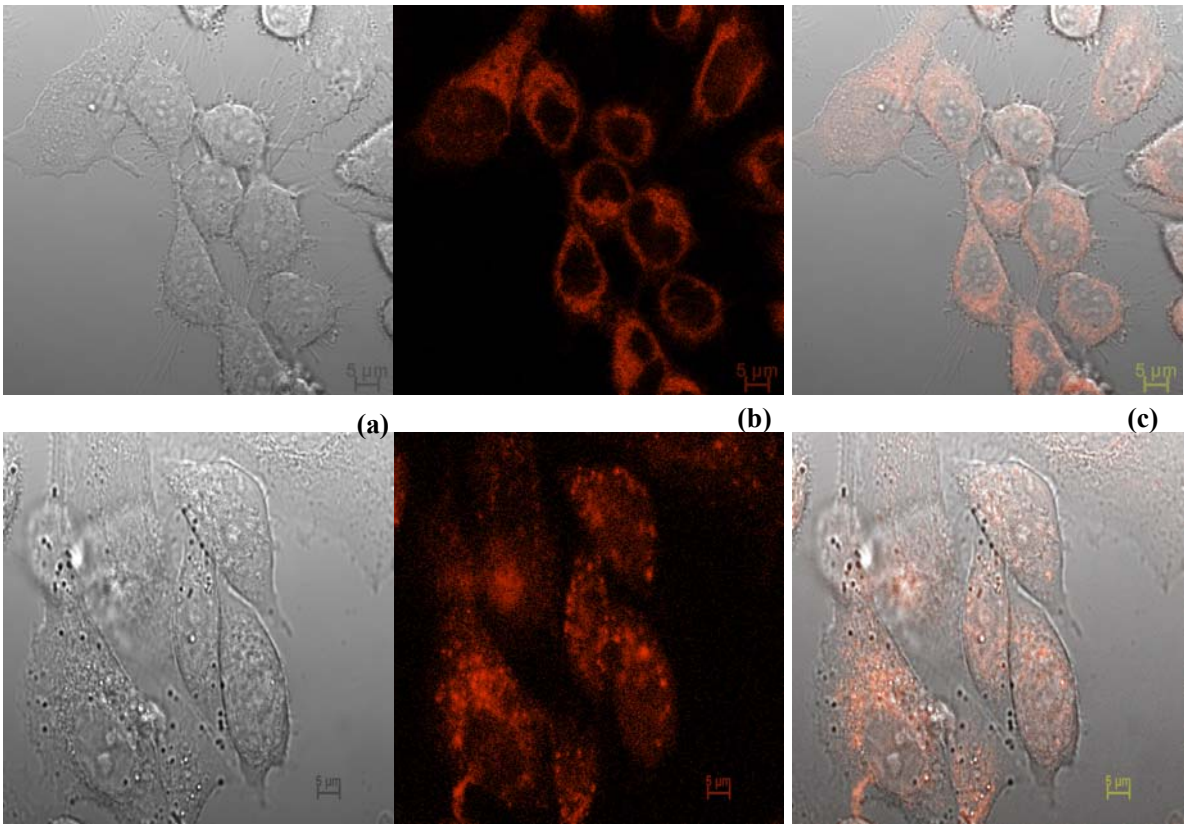

Figure 3.19. Single Photon Laser scanning confocal imaging (λ_{ex} =543 nm) of PC-3 cells incubated for 25mins at 37 ^{o}C with: (**a-c**) Compound **9** (10 μM in 5: 95 % DMSO: serum free medium); (**d-f**): Compound **11** (10 μM in 5: 95 % DMSO: serum free medium). Scalebar 5 μm

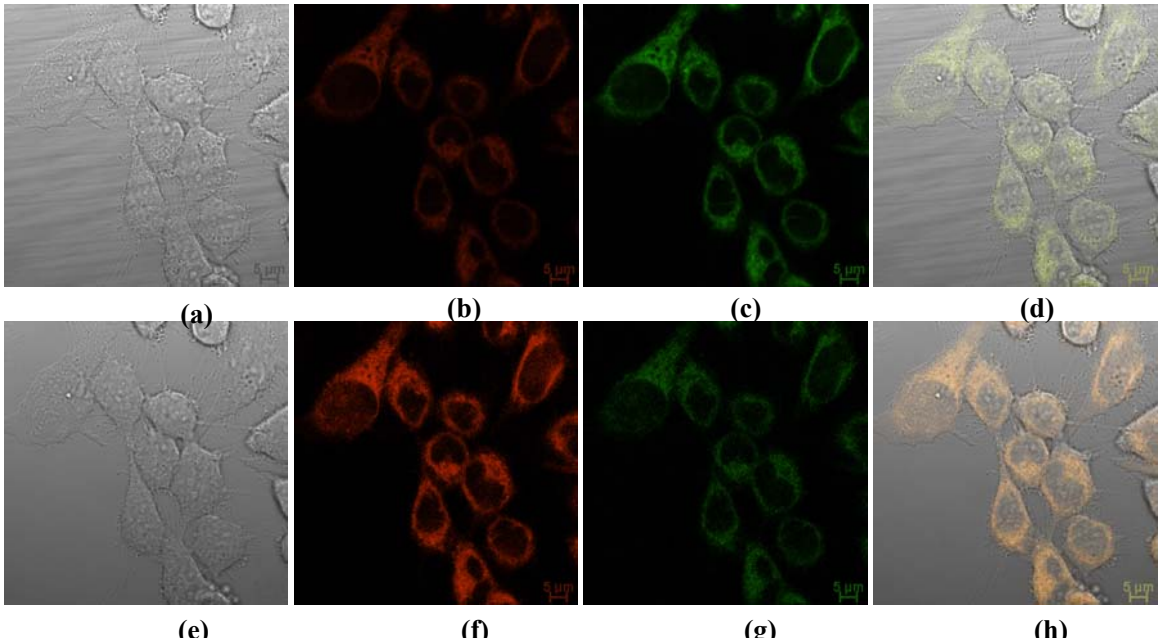

Figure 3.20. Single Photon Laser scanning confocal imaging of PC-3 cells incubated for 25 mins at 37 ^{o}C with Compound **9** (10 μM in 5: 95 % DMSO: serum free medium): (**a-d**) (λ_{ex} =405 nm); (**e-h**) (λ_{ex} =488 nm);

3.2.3.3 Fluorescence lifetime microscopy imaging

To demonstrate the potential of compound **9** and its RGDfK derivative compound **11** for imaging applications, two photon fluorescence lifetime imaging microscopy technique was used here for mapping cellular distribution of compounds.

Experiments were carried out at the Rutherford Appleton Laboratory with assistance and supervision from Dr. S Botchway.

Lifetime measurements were recorded using time-correlated single photon counting with an excitation wavelength of 810 nm and the emission measured at 360-580 nm. The measurements of compounds **9** and **11** were carried out in DMSO solvent with concentration of 10 μM. Emission spectral detection was carried out using an Acton Research Component 275 spectrograph and an Andor iDus 740-BU CCD camera.

Cell uptake studies were performed using HeLa cells and PC-3 cells. Cells were plated on Petri dishes incorporating a glass cover slip and left to adhere for 12 h. Background

lifetime images were recorded before the addition of compound. Cell dishes were then mounted on the microscope stage and kept at 37 °C.

Compounds were dissolved in DMSO as solvent and added to the cells to achieve a final concentration of 10 μM dye in EMEM medium containing 5 % DMSO (*v/v*). Cell uptake was monitored after 25 min incubation, in which dyes reached a maximum after this time. Measurements were recorded for the complete field of view.

The fluorescence lifetime images (FLIM) obtained for compound **9** and its RGDfK derivative compound **11** are displayed in Figure 3.21 and Figure 3.22 including an intensity map showing spatial variations in fluorescence emission, the lifetime map which displays the distribution of different fluorescence decay lifetimes over the cell and also the profile of corresponding lifetime distribution. Lifetime decay data (Table 3.6) shows that both compounds **9** and **11** have two lifetime components.

Compound **11** shows relatively poor uptake in PC-3 cells considering the lifetime distribution. It is apparent from confocal fluorescence microscopy studies that both NDIBBN (compounds **3** and **5**) and compound **11** predominantly localise in the cytoplasm with negligible nuclear uptake. It is clear from the lifetime distribution maps that the distribution of lifetimes over the cells is not homogeneous.

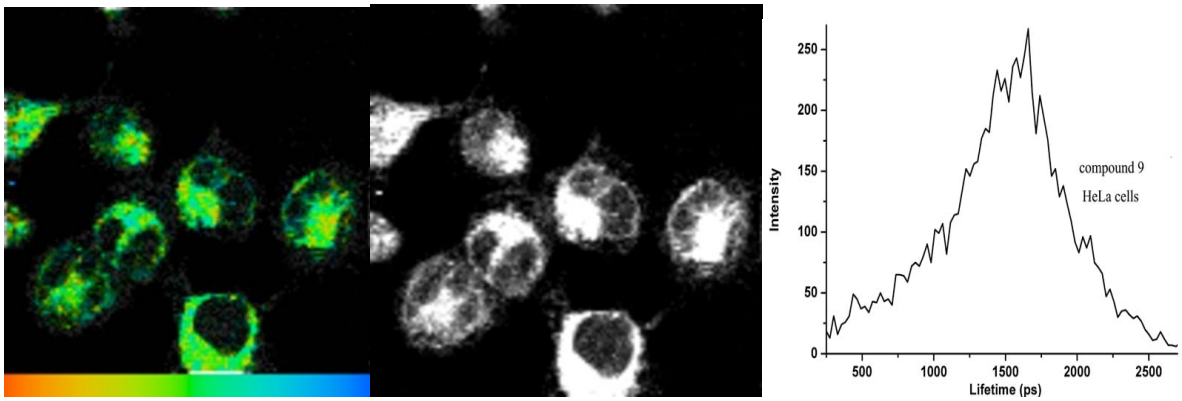

(a) **(b)** **(c)**

Figure 3.21. Two-photon laser confocal fluorescence (λ_{ex} = 810 nm):(**a, b** and **c)** Typical micrograph of HeLa cells incubated for 20 min at 37 ^{o}C with compound **9**(10 μM in 5: 95 % DMSO: EMEM) showing: lifetime mapping and scalebar (**a**), intensity image (**b**), and corresponding lifetime distribution curve (**c**).

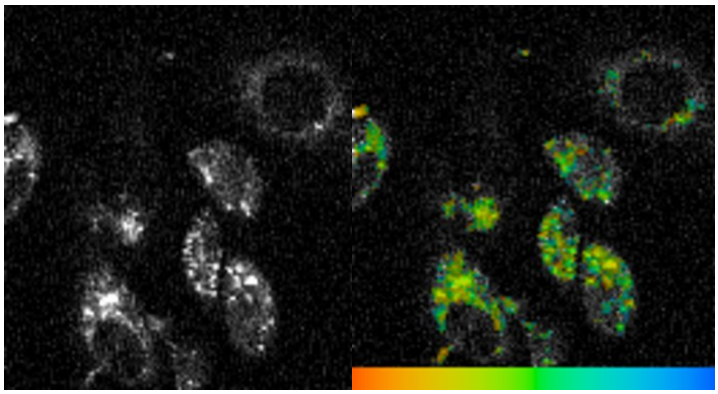

(a) **(b)** **(c)**

Figure 3.22. Two-photon laser confocal fluorescence (λ_{ex} = 810 nm):(a, b and c) Typical micrograph of PC-3 cells incubated for 20 min at 37 ^{o}C with compound 11 (10 μM in 5: 95 % DMSO: EMEM showing compound 11 mainly stays in cytoplasm surrounding nucleus, lifetime mapping and scalebar (**a**), intensity image (**b**), and corresponding lifetime distribution curve (**c**).

Table 3.6. Lifetime decay constants for compounds **9** and **11** in cell

Compound	Cell line	τ_1 / ns	WHHM / ns	τ_1 %	τ_2 / ns	WHHM / ns	τ_2 %	χ^2
9	HeLa	0.56	0.10	62.4	2.46	0.71	37.6	1.21
11	PC-3	0.27	0.12	75.7	1.94	0.73	24.3	1.00

Figure 3.23 gives an overlay of the two photon emission lifetime decay spectra for compounds **9** and **11** with lifetime decay values provided in Figure 3.7 for each compound. The data profile includes the goodness of fit of the decay curves as χ^2 the lifetime of each component and their weighting of each component. The χ^2 value of 1.0 corresponds to an optimal single exponential fit of this measurement. χ^2 value of more than 1.3 means an incomplete single exponential fit of this measurement. High χ^2 values (>1.5) means either significant noise within the TCSPC setup (electronics and/or excitation source) or more than one component decay profile. Lifetime components data were processed using SPCImage analysis software (Becker and Hickl, Germany) or Edinburgh Instruments F900 TCSPC analysis software.

The fluorescence lifetimes of both compounds **9** and **11** measured in the solution phase (DMSO) were found to decay as two component systems, with a long component on

the order of several nanoseconds and a much shorter component on the order of several hundred picoseconds. Compound **11** shows a longer lived component with 3.21ns (44.6 %) compared with 2.83ns (54.1 %) for compound **9**. However compound **11** shows a decreased shorter component with 0.55 ns (55.4 %) compared with 0.61 ns (45.9 %) for compound **9**. The presence of the short components in such high percentage was attributed to aggregation in solution and scattering due to the possibility that organic NDI nanotubes or related nanodimensional objects may form in solution, as demonstrated by Dan Pantos and Jeremy Sanders.[43]

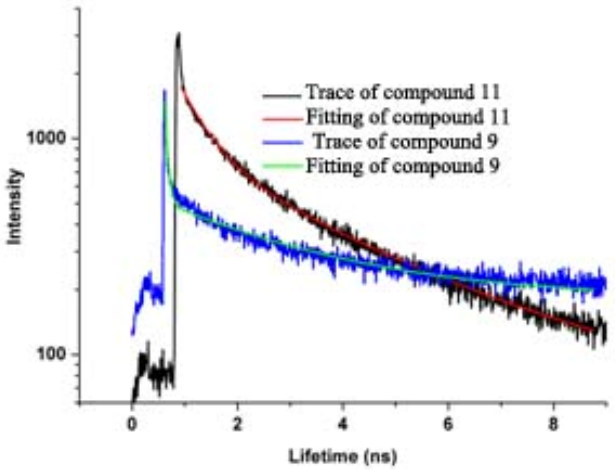

Figure 3.23. Two-photon fluorescence spectroscopy: fluorescence decay traces and corresponding fitted curves for the lifetime determinations of compounds **9** and **11** (λ_{ex} = 810 nm, 10 μM, pure DMSO).

Table 3.7. Lifetime decay constants for compounds **9** and **11** point decay

Compounds	τ_1 / ns	τ_1 %	τ_2 / ns	τ_2 %	χ^2
9	0.61	45.9	2.83	54.1	1.66
11	0.55	55.4	3.21	44.6	1.40

3.3 Conclusion for Chapter 3

In summary, we explored the development of a new series of molecular imaging agents based on using cancer targeting peptides (bombesin and RGDfK) coupled to NDI. Firstly, specific peptides bombesin[7-13] and RGDfK were synthesized using standard Fmoc

solid phase synthesis protocol. The resulting peptides were characterised and confirmed by ESI/MASS, MALDI and HPLC. Then, two type of NDI-peptide conjugates (NDI–bombesin and Tryp-NDI-RGDfK) were designed and synthesized through EDC-coupling route. Two routes were designed to couple NDI with bombesin, compound **3** was prepared from the **Method 1** when compound **5** was formed from the **Method 2**. Also, compound **3**@SWNT supramolecular complex was prepared through non-covalent interaction between NDIBBN with SWNTs by mixing compound **3** water solution with SWNT in EtOH dispersed phase. Fluorescence quenching and significant red-shift in the emission maxima of NDIBBN were observed after anchoring compound **3** onto SWNT in the 2D fluorescent contour plotting, which suggests that the charge-transfer interaction between compound **3** and SWNT and a successful binding between these two components occurs. The quenching is too strong to allow the successful determination of a binding constant by fluorescence titrations suggesting that the binding interaction is likely higher than 10^9 M^{-1}.[44] Raman spectroscopy probing the presence of intracellular carbon nanotubes also confirms the membrane translocation of NDI@SWNTs in MCF-7 cells.

Tryptophan-NDI-RGDfK was also synthesized based on an analogous procedure to that applied in the NDIBBN synthesis. Both NDI-Peptide conjugates were purified and collected by semipreparative-HPLC and characterised by MALDI mass spectrometry. Fluorescent lifetime imaging and confocal laser scanning microscopies were utilised as spectroscopic tools for investigating cellular behaviour (e.g. stability, fluorescence emission and biolocalisation) of these new molecular imaging probes. Fluorescent lifetime mapping, fluorescence intensity profile, lifetime components and lifetime decay profile were all employed in an attempt to qualitatively estimate the integrity of these molecular imaging in cancer cells (HeLa, MCF-7 and PC-3 cell lines).

3.4 References to Chapter 3

(1) Chowdhury, P.; Gondry, M.; Genet, R.; Martin, J. L.; Menez, A.; Negrerie, M.; Petrich, J. W. *Photochem. Photobiol.* **2003**, *77*, 151.

(2) Miller, S. J.; Joshi, B. P.; Feng, Y.; Gaustad, A.; Fearon, E.; Wang, T. D. *Gastroenterology* **2011**, *140*, S104.

(3) Sahoo, H.; Nau, W. M. *ChemBioChem* **2007**, *8*, 567.

(4) Scheffler, S.; Sauer, M.; Neuweiler, H. *Z. Phys. Chem.* **2005**, *219*, 665.

(5) Voglino, L.; Simon, S. A.; McIntosh, T. J. *Biochemistry (Mosc).* **1999**, *38*, 7509.

(6) Cuttitta, F.; Carney, D. N.; Mulshine, J.; Moody, T. W.; Fedorko, J.; Fischler, A.; Minna, J. D. *Nature* **1985**, *316*, 823.

(7) Battey, J. F.; Way, J. M.; Corjay, M. H.; Shapira, H.; Kusano, K.; Harkins, R.; Wu, J. M.; Slattery, T.; Mann, E.; Feldman, R. I. *Proc. Natl. Acad. Sci. U. S. A.* **1991**, *88*, 395.

(8) Wen, X.; Chao, C.; Ives, K.; Hellmich, M. R. *BMC Mol. Biol.* **2011**, *12*.

(9) Reubi, J. C.; Wenger, S.; Schmuckli-Maurer, J.; Schaer, J. C.; Gugger, M. *Clin. Cancer Res.* **2002**, *8*, 1139.

(10) Acker, T.; Plate, K. H. *Journal of Molecular Medicine* **2002**, *80*, 562.

(11) Fraisl, P.; Mazzone, M.; Schmidt, T.; Carmeliet, P. *Dev. Cell* **2009**, *16*, 167.

(12) Gadaleta, C. D.; Ranieri, G. *Crit. Rev. Oncol./Hematol.* **2011**, *80*, 40.

(13) Lequerrec, A.; Duval, D.; Tobelem, G. *Baillieres Clin. Haematol.* **1993**, *6*, 711.

(14) Rmali, K. A.; Puntis, M. C. A.; Jiang, W. G. *Colorectal Disease* **2007**, *9*, 3.

(15) Pedchenko, V.; Zent, R.; Hudson, B. G. *J. Biol. Chem.* **2004**, *279*, 2772.

(16) Buerkle, M. A.; Pahernik, S. A.; Sutter, A.; Jonczyk, A.; Messmer, K.; Dellian, M. *Br. J. Cancer* **2002**, *86*, 788.

(17) Cressman, S.; Sun, Y.; Maxwell, E. J.; Fang, N.; Chen, D. D. Y.; Cullis, P. R. *Int. J. Pep.Res.Ther.* **2009**, *15*, 49.

(18) Fani, M.; Psimadas, D.; Zikos, C.; Xanthopoulos, S.; Loudos, G. K.; Bouziotis, P.; Varvarigou, A. D. *Anticancer Res.* **2006**, *26*, 431.

(19) Romanov, V. I.; Goligorsky, M. S. *Prostate* **1999**, *39*, 108.

(20) Dechantsreiter, M. A.; Planker, E.; Matha, B.; Lohof, E.; Holzemann, G.; Jonczyk, A.; Goodman, S. L.; Kessler, H. *J. Med. Chem.* **1999**, *42*, 3033.

(21) Haubner, R.; Wester, H. J.; Weber, W. A.; Mang, C.; Ziegler, S. I.; Goodman, S. L.; Senekowitsch-Schmidtke, R.; Kessler, H.; Schwaiger, M. *Cancer Res.* **2001**, *61*, 1781.

(22) Hersel, U.; Dahmen, C.; Kessler, H. *Biomaterials* **2003**, *24*, 4385.

(23) Albota, M.; Beljonne, D.; Bredas, J. L.; Ehrlich, J. E.; Fu, J. Y.; Heikal, A. A.; Hess, S. E.; Kogej, T.; Levin, M. D.; Marder, S. R.; McCord-Maughon, D.; Perry, J. W.; Rockel, H.; Rumi, M.; Subramaniam, C.; Webb, W. W.; Wu, X. L.; Xu, C. *Science* **1998**, *281*, 1653.

(24) Asir, S.; Demir, A. S.; Icil, H. *Dye. Pigm.* **1993**, *84*, 1.

(25) Katz, H. E.; Johnson, J.; Lovinger, A. J.; Li, W. J. *J. Am. Chem. Soc.* **2000**, *122*, 7787.

(26) Denk, W.; Strickler, J. H.; Webb, W. W. *Science* **1990**, *248*, 73.

(27) Xu, C.; Webb, W. W. *J. Opt. Soc. Am. B: Opt. Phys.* **1996**, *13*, 481.

(28) Konig, K. *J. Microsc.* **2000**, *200*, 83.

(29) Xu, C.; Zipfel, W.; Shear, J. B.; Williams, R. M.; Webb, W. W. *Proc. Natl. Acad. Sci. U. S. A.* **1996**, *93*, 10763.

(30) Zoumi, A.; Yeh, A.; Tromberg, B. J. *Proc. Natl. Acad. Sci. U. S. A.* **2002**, *99*, 11014.

(31) Helmchen, F.; Denk, W. *Nat. Method* **2005**, *2*, 932.

(32) Schwille, P.; Haupts, U.; Maiti, S.; Webb, W. W. *Biophys. J.* **1999**, *77*, 2251.

(33) Benda, A.; Fagul'ova, V.; Deyneka, A.; Enderlein, J.; Hof, M. *Langmuir* **2006**, *22*, 9580.

(34) Harriman, A.; Izzet, G.; Ziessel, R. *J. Am. Chem. Soc.* **2006**, *128*, 10868.

(35) Georgakilas, V.; Gournis, D.; Tzitzios, V.; Pasquato, L.; Guldi, D. M.; Prato, M. *J. Mater. Chem.* **2007**, *17*, 2679.

(36) Zhang, Y.; Qin, W.; Tang, H.; Yan, F.; Tan, L.; Xie, Q.; Ma, M.; Zhang, Y.; Yao, S. *Colloids Surf. B. Biointerfaces* **2011**, *87*, 346.

(37) Feng, Y.; Zhang, H.; Hou, Y.; McNicholas, T. P.; Yuan, D.; Yang, S.; Ding, L.; Feng, W.; Liu, J. *ACS Nano* **2008**, *2*, 1634.

(38) Cui, H.-F.; Vashist, S. K.; Al-Rubeaan, K.; Luong, J. H. T.; Sheu, F.-S. *Chem. Res. Toxicol.* **2010**, *23*, 1131.

(39) Ballesteros, B.; Tobias, G.; Shao, L.; Pellicer, E.; Nogues, J.; Mendoza, E.; Green, M. L. *Small* **2008**, *4*, 1501.

(40) Shao, L.; Tobias, G.; Salzmann, C. G.; Ballesteros, B.; Hong, S. Y.; Crossley, A.; Davis, B. G.; Green, M. L. *Chem Commun* **2007**, 5090.

(41) Brown, S. D. M.; Jorio, A.; Dresselhaus, M. S.; Dresselhaus, G. *Physical Review B* **2001**, *64*, 73403.

(42) Ellis, D.; Farrugia, L. J.; Peacock, R. D. *Polyhedron* **1999**, *18*, 1229.

(43) Pantos, G. D.; Pengo, P.; Sanders, J. K. M. *Angew. Chem.-Int. Edit.* **2007**, *46*, 194.

(44) Sprafke, J. K.; Stranks, S. D.; Warner, J. H.; Nicholas, R. J.; Anderson, H. L. *Angew. Chem.-Int. Edit.* **2011**, *50*, 2313.

Chapter 4 Synthesis of individual polythiophene functionalised single walled carbon nanotubes as prominent fluorescent nanoprobes for cellular imaging

4.1 Introduction

In comparison with the widely used fluorescent proteins and dyes in biology, nanotechnology imaging probes have the potential to substantially improve the specificity and sensitivity of diagnostic imaging. They could, under correct conditions, provide non-invasive and targeted detection *in vivo*.[1] Nanotechnology-based bioimaging probes are predicted to generate a new era in molecular imaging.

Carbon nanotubes can be classed as one-dimensional nanomaterials possessing unique electronic and mechanical properties because of their very high length-to-diameter ratios. The application of CNTs for potential bioimaging tools has seen very promising progress in recent years.[2-5] CNTs' high length-to-diameter ratio of up to 132000000:1 and also a tremendously high surface area (~1000 m^2/g) which are ideal constructs for coupling biomolecules and drugs. They are also naturally photo-luminescent in the near-infrared region. However, CNTs also form aggregates which inhibit their usage in advanced biomedical applications. Separating nanotube bundles to form individual nanotubes in solution and then forming stable CNT suspensions is a key factor for their usage as bioimaging agents.[6] As discussed in Chapter 1, surface functionalisation is a popular method for dispersing CNTs. The known methods for CNTs' functionalisation are normally divided into two types, covalent functionalisation and noncovalent functionalisation as descriped in Chapter 1.[7]

Non-covalent functionalisation is an ideal route for enhancing CNT solubility without damaging its sp^2 molecular structure as covalent functionalisation involves local destruction

of the sp^2 hybridization. Non-covalent functionalisation includes polymer wrapping,[8,9] the use of biocompatible surfactants,[5] the encapsulation by supramolecular systems of small molecules such as surfactant micelles,[10] and π-stacking by rigid, conjugated macromolecules.[11] Hongjie Dai's group at Stanford University reported an alternative, gentler technique of making a multimodal imaging probe for fluorescence, Raman and photoacoustic imaging by coating the CNT with a layer of phospholipids coupled with fluorescent molecules.[12] Carbon dots are a type of emerging carbon substrate for cell imaging, individually as bright as quantum dots.[13] According to preliminary work carbon dots[14,15] can be internalized into cells much more easily than quantum dots. However, quantum dots have advantages over carbon dots in terms of brightness and the ability to emit a range of colors while the fluorescence of carbon dots is exclusively in the green range.

An ideal class of fluorophores should have large differences from absorption, high absorbance values and photoluminescence frequencies (Stokes shifts), and high fluorescence (quantum yields). Oligothiophenes with more than two thiophene rings or a substituted thiophene ring have interesting optical and electronic properties such as: fluorescence, semiconductance, and light emission if excited with light at the appropriate wavelength. Oligothiophenes are widely used in organic electronic devices and fluorescent probes because oligothiophene shows high absorbance values and large Stokes shifts.[16] Time-resolved experiments confirmed their fluorescent lifetimes are in the order of nanoseconds and it has been found that they can reach high quantum yields in solution as well as in the solid state.[17] Additionally their photoluminescence frequencies can be tuned from the visible range to near-IR by changing the oligomer size and the position of substituents.[18,19] Oligothiophenes are soluble in both organic solvents and even in water after particular functionalization. Oligothiophenes have shown highly varying characteristics as a suitable fluorescent probes for detecting biomolecules. Oligothiophenes have been used as probes for

targeting and identification of intra- or extra-cellular protein aggregates which exist in a wide range of neurodegenerative conditions including prion, Parkinson's, Huntington's, and Alzheimer's diseases.[20]

Fluorescence imaging studies on fluorescent carbon nanotubes have thus far focused primarily on the measurement of the steady state spatial changes in emission intensity or wavelength.[21-36] The use of fluorescence lifetime imaging microscopy (FLIM) in combination with multi-photon excitation and near infrared[37] femtosecond laser pulses is widely used in the study of small molecule fluorophores.[38-41] To date FLIM has been used primarily on endogenous molecules such as tryptophan and common fluorescent dye-tagged proteins and fluorescein-based derivatives), with recent work exploring lifetime imaging of fluorescent platinum complexes permitting for the first time microsecond resolved emission imaging microscopy.[42-44] Prior to this work and to the best of our knowledge so far there are no reports of using FLIM for studying the fluorescent behaviors of fluorescent carbon nanotube complexes after entering into cells. Due to the defined nature of the emission lifetime and the sensitivity of lifetime measurements, excited state lifetime measurement could provide a powerful mean to probe interaction between fluorescent carbon nanotubes with components in cells.

Recently, our collaborator Dr Peter Van Rijn in Delft have reported the synthesis of new amphiphilic conjugated thiophenes[45], which in water can self-assemble into micelles, and can create an energy transfer (ET) system by incorporation of suitable hydrophobic acceptor molecules into the hydrophobic micelle interior.[46] No attempts to study their interactions with carbon materials have been made prior to this thesis and a discussion of this collaborative project carried out at Bath is given here (*vide infra*).

In this chapter, a fluorescent conjugated dodecathiophene (denoted T12) oligomer (Figure 4.1) provided by Dr Peter Van Rijn at the University of Delft was successfully

utilised for helically non-covalent wrapping of SWNTs aiming for the generation of individual and stable SWNTs in the dispersed phase.

The amphipathic conjugated oligothiophene T12 shows excellent dispersant abilities for de-bundling SWNTs in organic solvents as demonstrated by these experiments. The backbone structure of T12 can adapt to the curvature of SWNTs very well. The highest debundling of carbon nanotubes in solution was achieved by wrapping SWNTs with T12. T12 also acts as a fluorescent coating on the surface of carbon nanotubes for tracking their trajectory *in vivo* and *in vitro*. Investigation of the properties of T12@SWNT complex has been carried out by Raman, UV-vis-NIR and fluorescence spectroscopy and also by AFM, TEM and SEM. The biocompatibility of T12 and T12@SWNTs in mammalian cells were evaluated by MTT assay to investigate the effect of coating on carbon nanotubes' cytotoxicity. The cellular translocation behavior and intracellular fluorescent properties of the resulting T12@SWNT complex were investigated by a combination of fluorescence microscopy techniques of fluorescence lifetime imaging and confocal laser scanning microscopy. The aim of this work is to develop a luminescent conjugated polythiophene functionalized CNT probe for cell imaging.

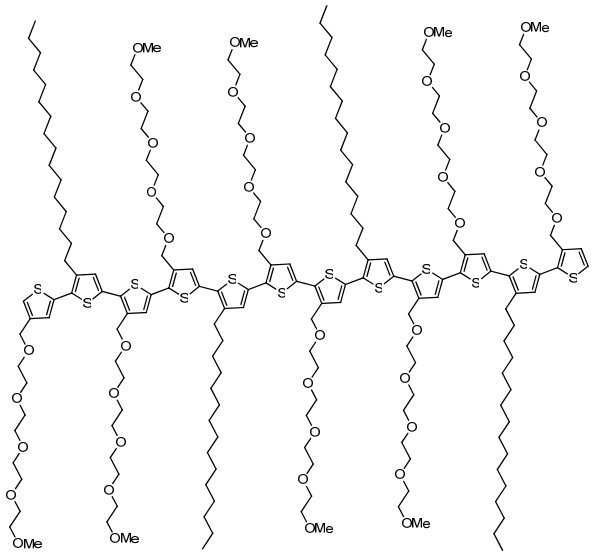

Figure 4.1. Molecular structure of T12 provided by Dr Peter Van Rijn at the University of Delft

4.2 Results and Discussion

4.2.1 Synthesis and characterizations of T12@SWNT dispersions

A typical procedure for preparing T12@SWNT dispersion is as follows: a mixture of SWNTs (0.1 mg) and the T12 polymer (0.1 mg) in $CHCl_3$ (4 mL) was sonicated for 20 min and stirred for 2 days. After centrifugation (10000 rpm) of the resultant yellow-brown suspension for 30 min, the supernatant was taken and filtrated and washing with $CHCl_3$ three times. The black complex on PTFE filter membrane was collected and dried in the oven at 60 °C overnight. The T12@SWNT composite can be dissolved again in $CHCl_3$ and DMSO easily. As shown in Figure 4.2, transparent solution of T12@SWCNT system was observed, which remains stable for 3 months.

4.2.1.1 Absorption spectroscopy and fluorescence spectroscopy

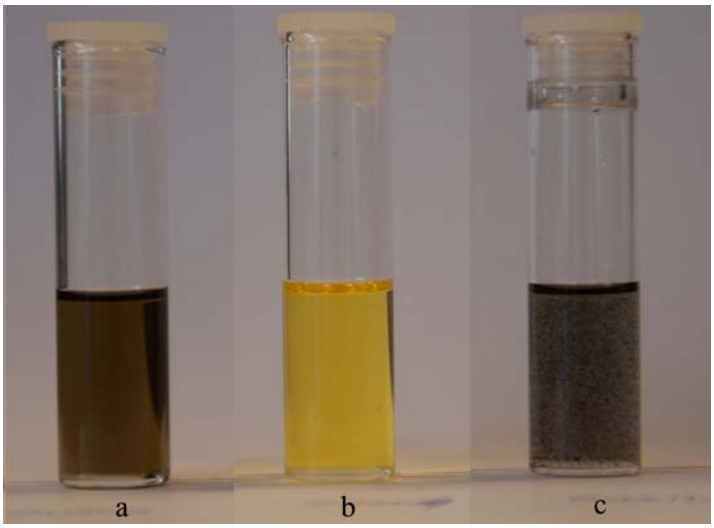

Figure 4.2. Images of T12 solutions in $CHCl_3$ (**b**) and T12@SWNT dispersions in $CHCl_3$ (SWNT~0.05 mg/mL) (**a**), SWNT (~1 mg/mL) (**c**) in $CHCl_3$.

Figure 4.3 c depicts the fluorescence emission spectra of free T12 oligomer in a $CHCl_3$ solution (70 μg/mL) compared to the spectra of T12@SWNT before ($[SWNT]_i$=70μg/mL, $[T12]_i$=70μg/mL) and after ($[SWNT]_i$=70μg/mL, $[T12]_i$=46μg/mL)

filtration. The maxima emission of T12 in $CHCl_3$ is at 560 nm. After mixing and interaction of T12 and SWNTs, it shows that the binding of the T12 in the solution results in a broadening of emission at 560 nm. The new emission peak around 436 nm arises from T12 bound on the SWNT surface. Disappearance of free T12 emission indicates that excess T12 was removed after 3 filtration/dispersion cycle treatments. This blue-shift of 124 nm is due to the conformation change of T12 after its helical wrapping on the surface of SWNT. The well resolved peaks of SWNTs (Figure 4.3 d) in the NIR range originate from electronic transitions between the first (S_{11}) or second (S_{22}) van Hove singularities of the nanotubes. The well-defined peaks also suggest that SWNTs are debundled very well without a significant amount of large aggregated SWNTs in the final dispersion. During the experiment, the solution phase was removed by 3 cycles of dispersion/filtration treatment.

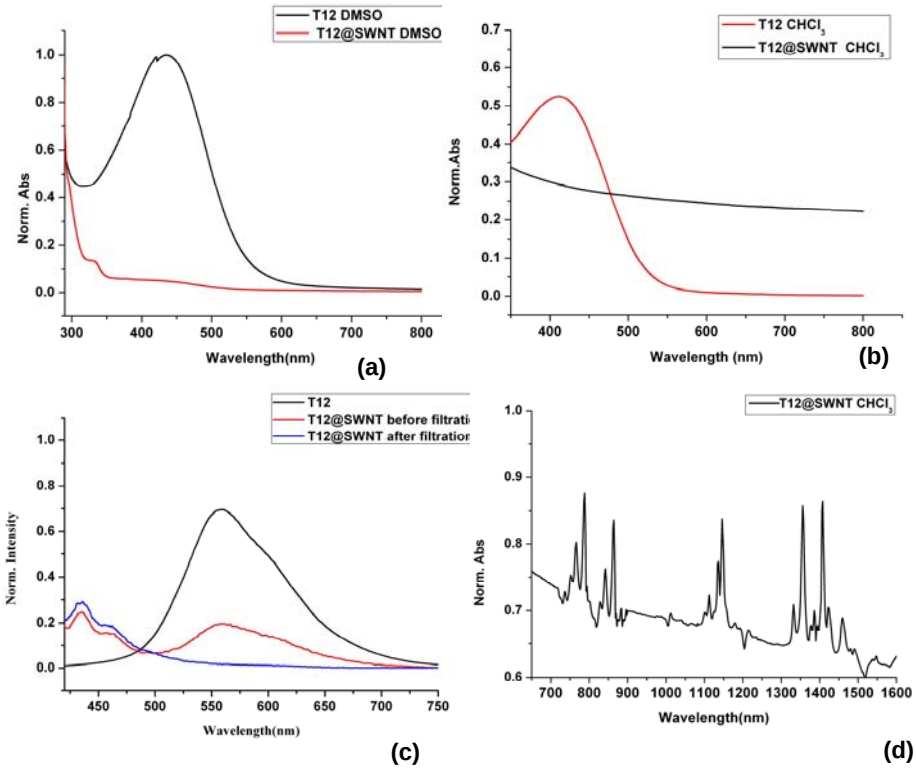

Figure 4.3. **(a)** UV-Vis spectroscopy of T12 and T12@SWNT (7.5 nM) in DMSO. **(b)** UV-Vis spectroscopy of T12 and T12@SWNT (7.5 nM) in $CHCl_3$. **(c)** Typical fluorescence emission spectra showing the T12 fluorescence quenching and significant blue shift after interaction with SWNT. (**d**) UV-Vis-NIR spectroscopy of T12@SWNT composite (7.5 nM or 27.3 µg/mL T12, 70 µg/mL SWNT in $CHCl_3$).

Figure 4.4 shows the contour plot fluorescence spectrum of free T12 and T12@SWNT. It shows that free T12 has emission maxima around 560 nm, this peak also appeared in T12@SWNT complex solution before 3 cycles' washing/filtration (Figure 4.4 b).

The washing/filtration cycle significantly reduce the emission intensity of T12 while most of T12 was washed away and adsorbed onto the SWNTs, whereas the broad peaks with emission maxima between 420 nm and 470 nm originate from T12 adsorbed onto the SWNTs. The blue-shift due to the decreasing planarity of the polymer backbone after helical wrapping on the surface of SWNTs is about 90 nm in the emission spectra which corresponds to the distance from the highest energy emission peaks of free T12 to the peak maxima of the adsorbed T12 molecules.

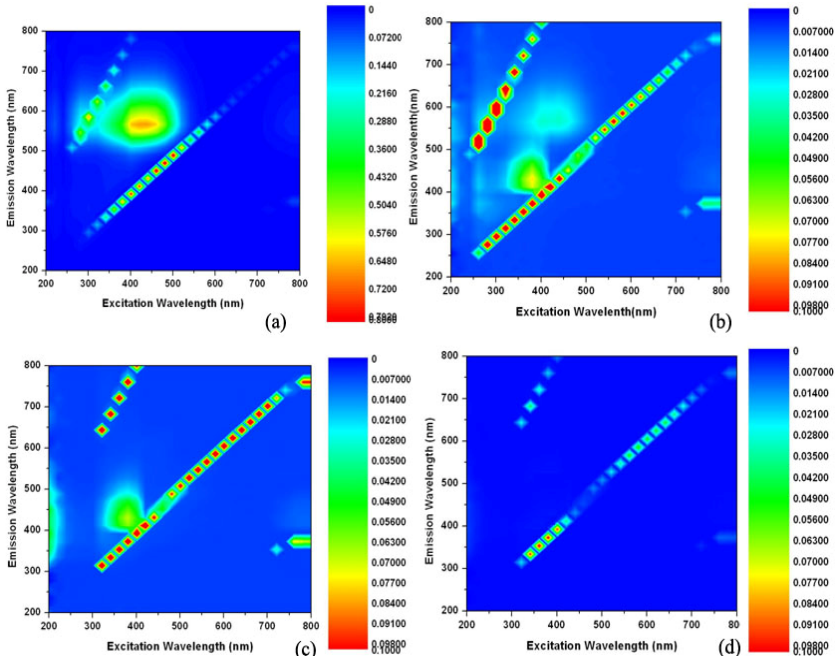

Figure 4.4. Contour plots (linear color gradient) of the fluorescence spectra of (**a**) the T12 $CHCl_3$ solution (19.2 nM or 70 μg/mL), (**b**) the T12@SWNT $CHCl_3$ solution before filtrate (70 μg/mL T12, 70 μg/mL SWNT), (**c**) the T12@SWNT $CHCl_3$ solution after filtrate (7.5 nM or 27.3 μg/mL T12, 70 μg/mL SWNT), (**d**) the SWCNT dispersion in $CHCl_3$ (70 μg/mL SWNT).

The idealised structure of the regioregular polymer should be planar and has the conjugation of π electrons distributed along the whole polymer backbone. We propose here

that the strong aromatic interaction between the thiophene oligomer and the aromatic surface of carbon nanotubes increases the twisting distortion of the polymer backbone. This type of conformational defect decreases the planarity and length of the conjugated system, leading to a blue shift of the emission maximum, analogous in its effect to the thermo-chromism effect, in which increasing temperature enhances the conformational defects, causing a blue shift in the UV-Vis spectra.

4.2.1.2 Raman Spectroscopy investigation

The Raman spectra (excitation 830 nm) of both the T12@SWNT composite and steam purified SWNT are shown in Figure 4.5. Both showed the expected G band at *ca.* 1590 cm^{-1}, a disordered D band at *ca.* 1300 cm^{-1} (consistent with the occurrence of defects in the tube post-functionalization), radial breathing modes (RBM) at *ca.* 265 cm^{-1} and G' band at 2600 cm^{-1}. The D (I_D) band is attributed to a disordered graphite structure of the nanotubes, whereas the G (I_G) band corresponds to a splitting of the E_2g stretching mode of graphite, which reflects the structural intensity of the sp^2-hybridized carbon atoms. The intensity of the D-band of T12@SWNT decreases compared to the starting material, indicating that the defects present in the starting material were removed during the functionalisation process. The increase in the band intensity ratio (I_D/I_G) of T12@SWNT (0.12) compared to free SWNTs (0.09) in the solid state reflects the relative degree of functionalisation of SWNTs.

4.2.1.3 Surface analysis of T12@SWNTs complex

Before the washing/filtration treatment of the T12@SWNT composite dispersion, the AFM imaging shows that excess T12 formed a film and most T12@SWNTs were trapped beneath this film (Appendix Figure 8.12). After 3 washing/filtration treatment cycles, most of the free unbound T12 was removed successfully leaving the tubular T12@SWNT exposed

(Figure 4.6 a). The AFM height profiles show that the single layer coating of carbon nanotubes with a height of 3.5 - 5 nm (Figure 4.6 c, profile 1, 2) and a multilayer coating carbon nanotube with a height 10-12 nm (Figure 4.6 c, profile 3). It also reveals that polymer coats the surface of SWNTs evenly with an average repeat distance of thiophene units every 8.3 nm (Figure 4.6d). T12 acts as a highly efficient dispersing agent capable of debundling SWNTs strands. Some T12 crystals were attached to the tip of SWNTs even after 3 cycles of filtration/dispersion in $CHCl_3$, which can increase fluorescence emission. A chart representation of T12@SWNT length distribution shows that 65% of tubes range from 200 to 650 nm due to the sonication breaking SWNTs into fragments (Figure 8.10 in Appendix).

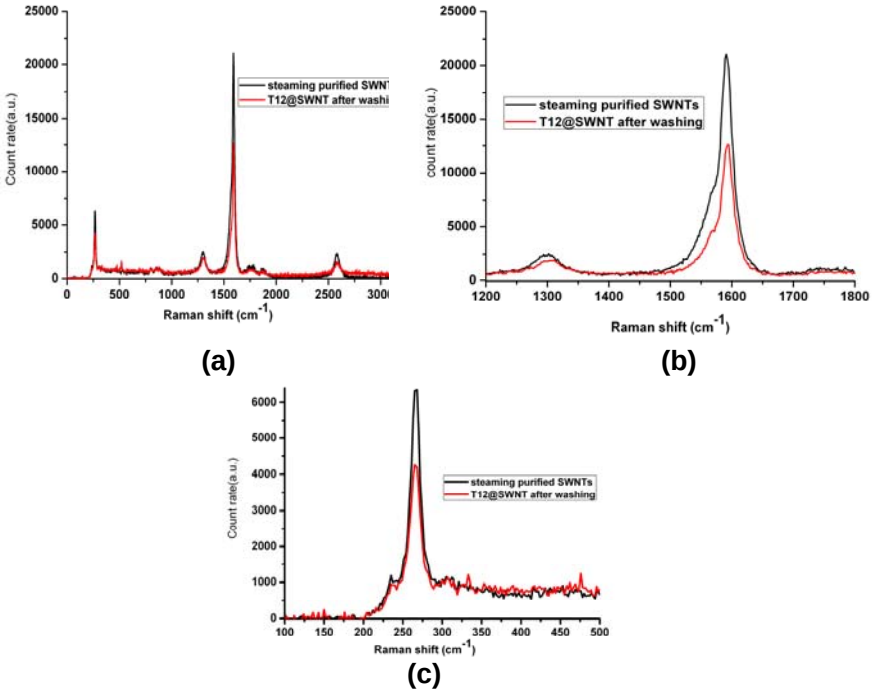

Figure 4.5. Raman spectroscopy of steaming purified SWNT and T12@SWNT after washing (λ_{ex}=830 nm, laser power at the sample 220 mW spot size 100 μm. **(a)** Full spectra for materials deposited silica wafer from $CHCl_3$, 2 mg/mL; **(b)** Expanded Raman spectra showing D and G bands of SWNT and T12@SWNT. **(c)** RBM of SWNT upon T12 complexation. Spectra of solid materials were recorded three times from different areas of the nanomaterial solid and the average spectra reported.

The HRTEM images give the morphology of T12 functionalized SWNTs prepared in $CHCl_3$ solvent (Figure 4.8). The worm-like materials attached onto the surface of SWNTs are presumably the T12 polymers which interact with aromatic carbon surface through

aromatic interactions. Due to the presence of its two neighbouring hydrophilic and hydrophobic-functionalised thiophene groups, T12 seems to adopt a *cis*-conformation in aqueous environments resulting in a curved shape of oliogothiophene. This curved oliogothiophene would self-assemble to a "rod-like" structure as hydrophilic interaction (Figure 4.7 b).[45,46]

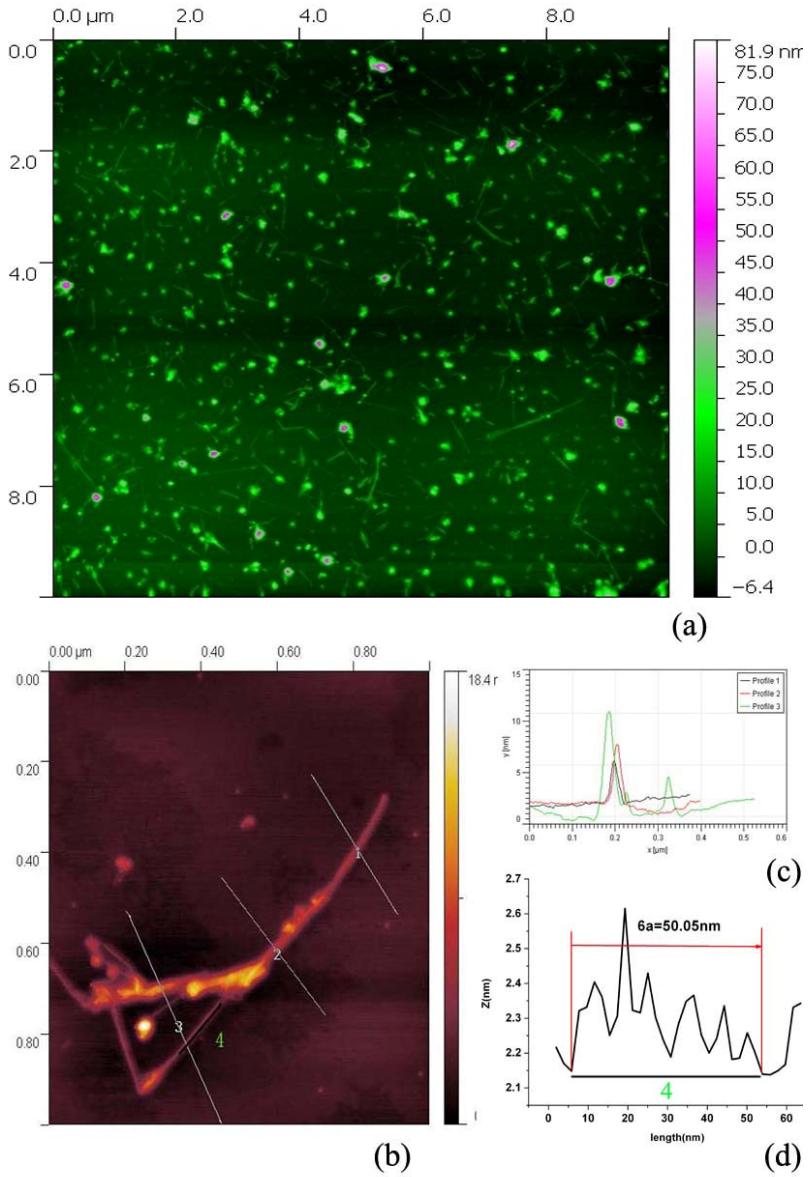

Figure 4.6. **(a)** AFM imaging of T12@SWNT after 3 cycles' filtration/dispersion treatment which shows most of free T12 was removed compared with the T12@SWNT solution before treatment. (**b**) typical imaging of single T12@SWNT, (**c**) Line profile along the lines No 1, 2 and 3 respectively. (**d**) Line profile along the line No 4.

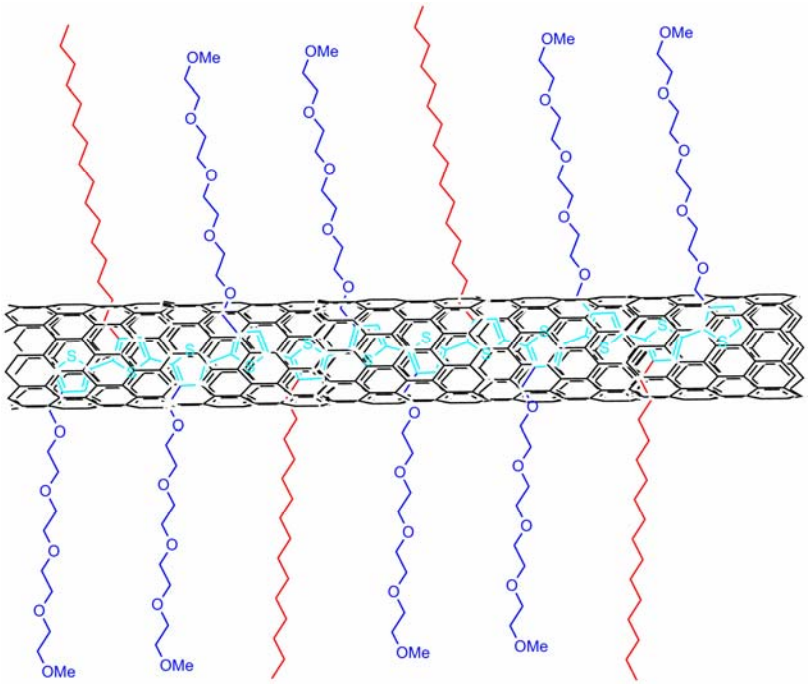

(**a**)

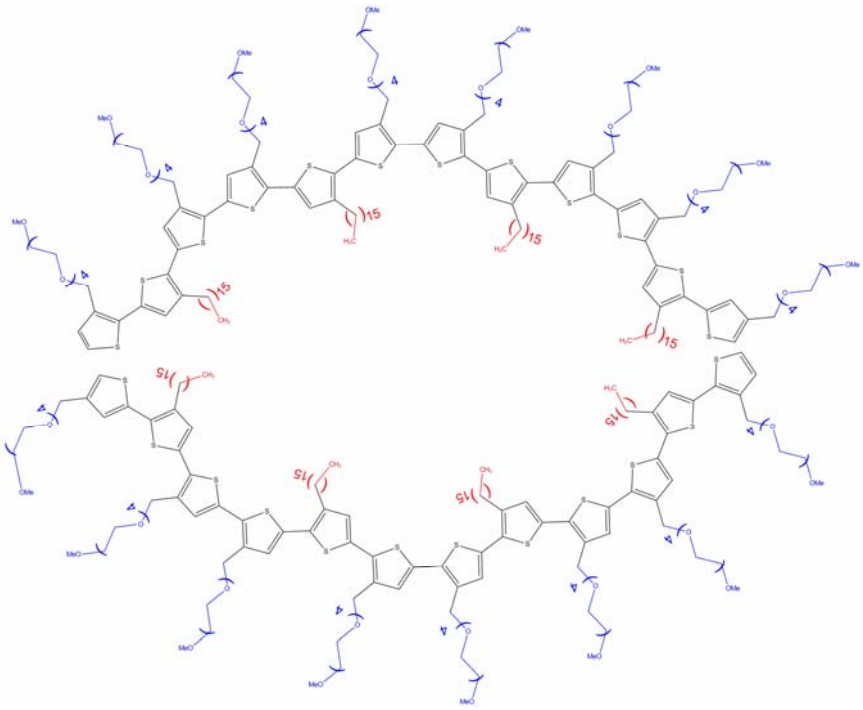

(b)

Figure 4.7. Schematic presentation of T12 polythiophene chain stacking on the surface of SWNTs (**a**). T12 which is amphiphilic in nature folds into "rod-like" structure in aqueous solvents with the curvature obtained from the *trans* to *cis* reorientation of the thiophene (**b**).

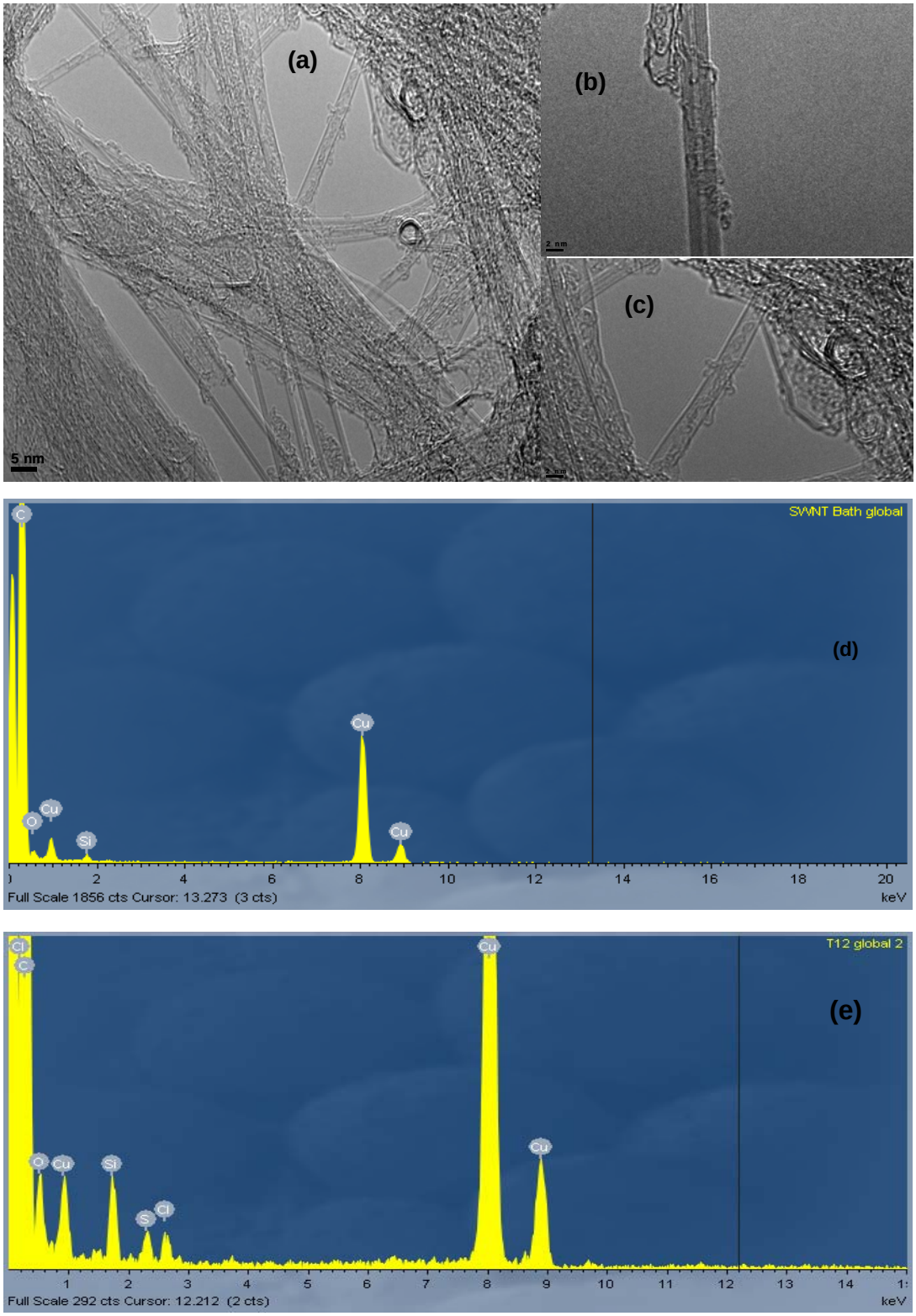

Figure 4.8. Typical HRTEM images of sample T12@SWNTs (dispersed in EtOH) (**a-c**). (**a**) global view; (**b**),(**c**) single SWNTs wrapped by T12 conjugated polymer, (**d**) EDS spectrum of SWNT control and (**e**) EDS spectrum of T12@SWNT.

In weakly polar solvents ($CHCl_3$), T12 is believed to adopt well-ordered, linearly shaped geometries which can aid the adsorption onto carbon nanotubes' surface through

aromatic interactions (Figure 4.7 a). This also indicates that repeated sonication-centrifugation methods enable isolation of T12@SWNTs in $CHCl_3$ through strong interaction between polythiophene with carbon nanotubes.

4.2.1.4 Confocal fluorescence microscopy imaging

Confocal fluorescence microscopy images show that both T12@SWNT and T12 were internalized by HeLa cells after 20 mins of incubation at 37 °C (Figure 4.9). The dye mainly localizes in the cytoplasm without entering into the nucleus. The arrows in Figure 8.18 (see Appendix) clearly show that the black carbon nanotubes aggregate inside cells, confirming that the carbon nanotube can successfully translocate into the cell membrane. The level of the green fluorescence channel decreased in both T12@SWNT and T12 incubation. The red fluorescence channel can maintain a similar level of illumination when exciting at 405 nm, 488 nm and 543 nm for the T12@SWNT and T12 incubation, while there is a significant decrease of the green fluorescence channel (see Appendix Figure 8.14 and 8.16). The total fluorescence intensity profiles of crossing-line in HeLa cells show that both T12 and T12@SWNT have the maximum total fluorescence intensity using the laser excitation channel 405 nm in comparison to 488 nm and 543 nm (see Appendix Figure 8.14 and 8.16). The fluorescence spectroscopy concluded that T12 gives maximum emission when exciting at 488 nm. However, cell images show both T12@SWNT and T12 have the strongest emission when exciting at 405 nm in HeLa cells, in which it is a blue-shift of the maximum excitation. T12 does not enter the nucleus of HeLa cells after 20 minute incubation, however the T12's diffusion into the nucleus can be observed after 1.5 h incubation, as highlighted in in Figure 4.10.

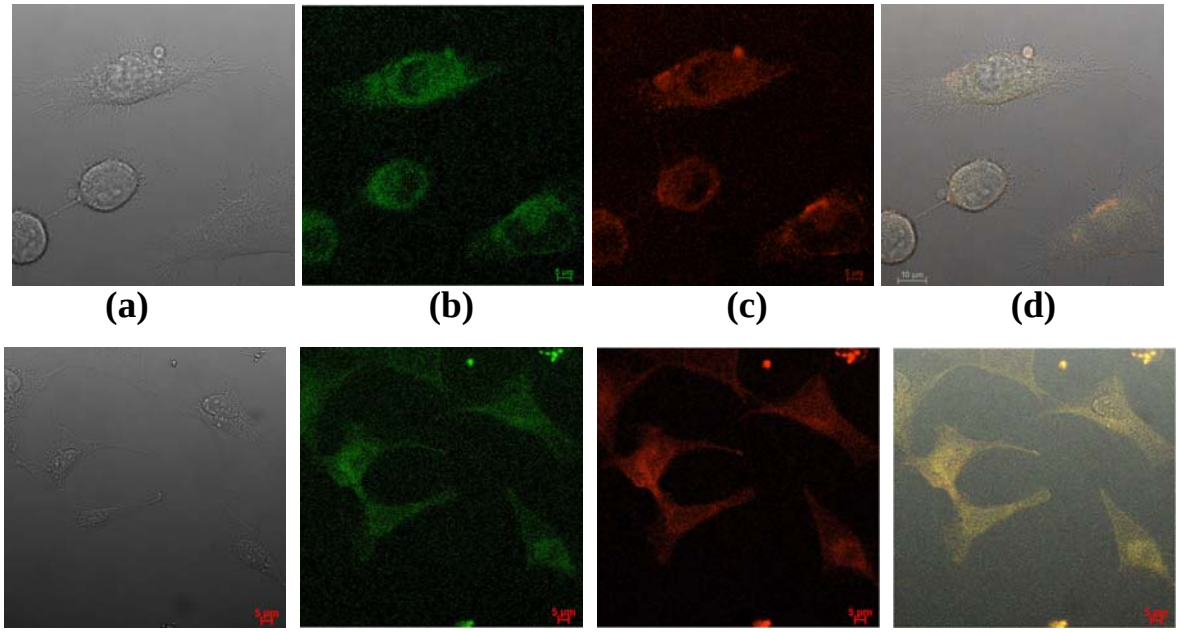

Figure 4.9. Single Photon Laser scanning confocal imaging of cancerous (HeLa) cells incubated at 37 ^{o}C for 20 min where λ_{ex} = 488 nm with: **(a-d)** T12 (1.92 nM or 7 μg/mL in 5: 95 % DMSO: EMEM), showing DIC (**a**), green channel (b), red channel (605-675 nm) (c) and DIC-green-red channel overlay (**d**). **(e-h)** T12@SWNT composite dispersion (in 5:95 % DMSO: EMEM) containing 7 μg/mL T12 anchored onto 18 μg/mL SWNT: DIC (**e**), green channel (515-530 nm) (**f**), red channel (605-675 nm) (**g**) and DIC-green-red channels overlay (**h**), Scalebar 5 μm.

Figure 4.11 shows that T12 in PC-3 cell has nearly zero emission in the red fluorescence channel compared to in HeLa cells. Additionally it is difficult to detect emission when exciting at 543 nm (Figure 8.19, see Appendix). Both T12 and T12@SWNT show that the dye mainly distributes in the cytoplasm not in the nucleus after 20 minute incubation (Figure 4.11). The red channel (605-675 nm) emission can not be detected in PC-3 cells incubated with T12 alone while T12@SWNT gives significant red emission at the same condition. The mechanism why T12 alone in PC-3 cells not gives red emission is still investigated (Figure 8.19 and 8.21, see Appendix).

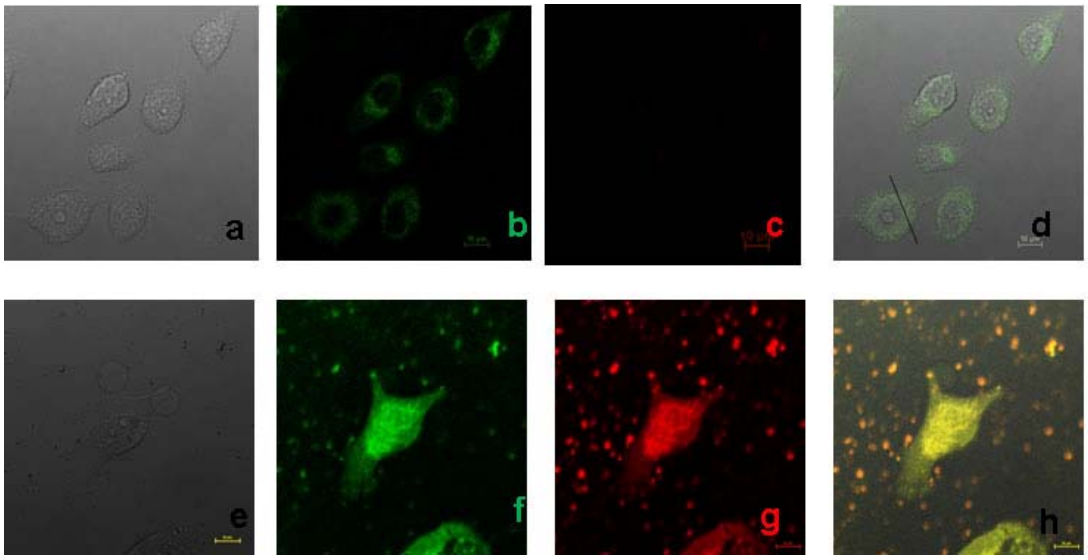

Figure 4.10. Single Photon Laser scanning confocal imaging of cancerous (HeLa) cells incubated at 37 ^{o}C where λ_{ex} = 488 nm with: **(a-d)** T12 for 20 min (1.92 nM or 7 μg/mL in 5: 95% DMSO: EMEM), showing DIC (**a**), green channel (b), red channel (605-675 nm) (c, very weak emission in red channel) and DIC-green-red channel overlay (**d**). **(e-h)** T12 for 1.5 h (1.92 nM or 7 μg/mL in 5: 95% DMSO: EMEM), showing DIC (**e**), green channel (515-530 nm) (**f**), red channel (605-675 nm) (**g**) and DIC-green-red channels overlay (**h**), Scalebar 5 μm.

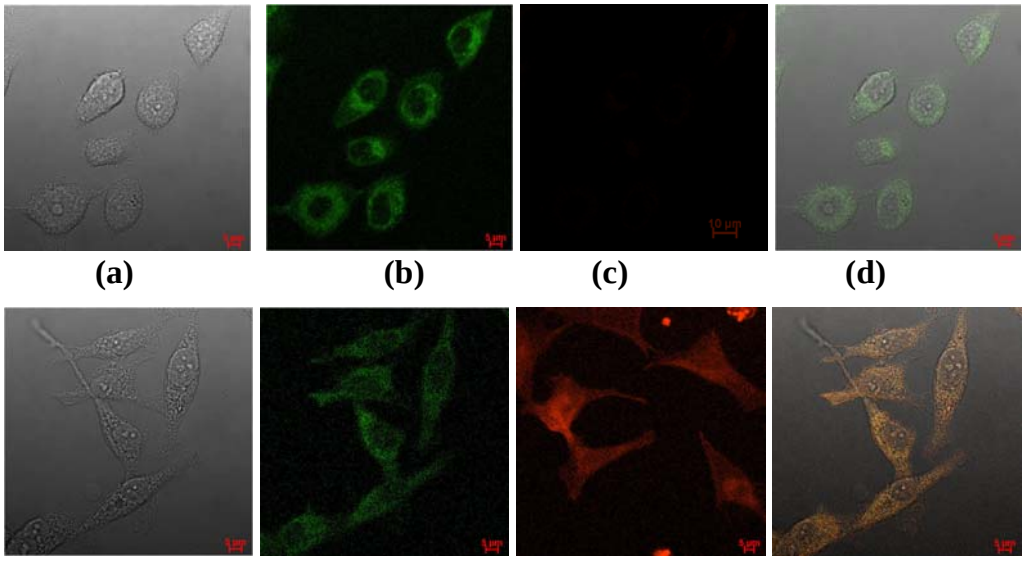

Figure 4.11. Single Photon Laser scanning confocal imaging of human prostate cancer cells(PC-3) incubated at 37 ^{o}C for 20 min where λ_{ex} = 488 nm with: **(a-d)** T12 (1.92 nM or 7 μg/mL in 5: 95% DMSO: EMEM), showing DIC (**a**), green channel (b), red channel (605-675 nm) (c) and DIC-green-red channel overlay (**d**). **(e-h)** T12@SWNT composite dispersion (in 5:99% DMSO: EMEM) containing 7 μg/mL T12 anchored onto 18 μg/mL SWNT: DIC (**e**), green channel (515-530 nm) (**f**), red channel (605-675 nm) (**g**) and DIC-green-red channels overlay (**h**), Scalebar 5 μm.

4.2.1.5 In vitro and in solution FLIM studies

In this work, Fluorescence lifetime imaging microscopy (FLIM) technique was used to visualize T12 and T12@SWNT taken up by cervical cancer cells (HeLa) and human prostate cancer cells (PC-3). FLIM was performed by using a confocal microscope (LSM 510, Carl Zeiss). A femtosecond mode locked Mira Ti:sapphire laser (Coherent Lasers Ltd) was tuned at 910 nm to generate two-photon luminescence from T12 and T12@SWNT. The laser pulse has a repetition rate of 75 MHz and duration of less than 180 fs. The intensity image shows that T12 and T12@SWNT were localised around nuclei of both PC-3 cells and HeLa cells imaged.

FLIM provides contrast according to the fluorescence decay time of each pixel compared to the traditional imaging methods based on fluorescence intensity. The fluorescence intensity distribution may have no differences in two environmentally distinct regions, but fluorescence lifetime distribution can reveal such regional differences. As well as being able to distinguish spectrally overlapping fluorophores,[49] imaging of the fluorescence lifetime can also be used to investigate the surroundings and dynamic processes of the fluorophore.[50,51]

FLIM images are showed under the intensity images are from the same samples with different coded colors representing different lifetime scales. The lifetime of each pixel is obtained by applying a single or multi-exponential fit; in this case a single exponential model was used. In PC-3 cells, the lifetime distributions of all the pixels are shown in Figure 4.12 e (T12) and Figure 4.12f (T12@SWNT). The main lifetime component of T12 is around 1713 ps. There are two lifetime components of T12@SWNT in PC3, one is 0.8±0.3 ns and another is 2.0±0.75 ns which indicate there are at least two types of T12@SWNTs with different lifetimes. In HeLa cells, T12 presents two lifetime components, one is 0.11±0.08 ns and another is 1.663±0.66 ns (major component) (Figure 4.12e). The most likely possibility is

that T12 binds to cell components (for example proteins) forming a complex, which then changes the lifetime of T12. Surprisingly, T12@SWNT (Figure 4.13f) shows only one lifetime component (around 0.77 ns) in HeLa cell. The lifetime distribution profiles of T12 and T12@SWNT show that both fluorophores have different interactions with the local environment in PC-3 cells and in HeLa cells: further investigations by the biophysicists at the Research Complex at Harwell would be needed, beyond the scope of this thesis to understand the different behavior of both fluorophores in a wider range of cells.

To probe the fluorescent nature of T12 and T12@SWNT in solution, fluorescence lifetime measurements were recorded for both compounds in DMSO using time-correlated single photon counting, with a 2-photon excitation wavelength of 910 nm. Two-photon emission lifetime decay spectra were recorded by time-correlated single photon counting using pulsed laser excitation (λ_{ex} = 910 nm in DMSO). DMSO was chosen as both T12 and T12@SWNT showed very good solubility and dispersibility in this solvent and also due to its low volatility. Both compounds exhibited only one lifetime component. The lifetime for T12 measured in DMSO is *ca.* 1.6 ns (χ^2=1.75), 1.2 ns for T12@SWNT (χ^2=1.78) (Figure 8.12, see Appendix). The faster fluorescent decay of T12 after stacking on the surface of SWNT (in DMSO) confirmed the fluorescence quenching by the SWNT surface (Figure 4.14).

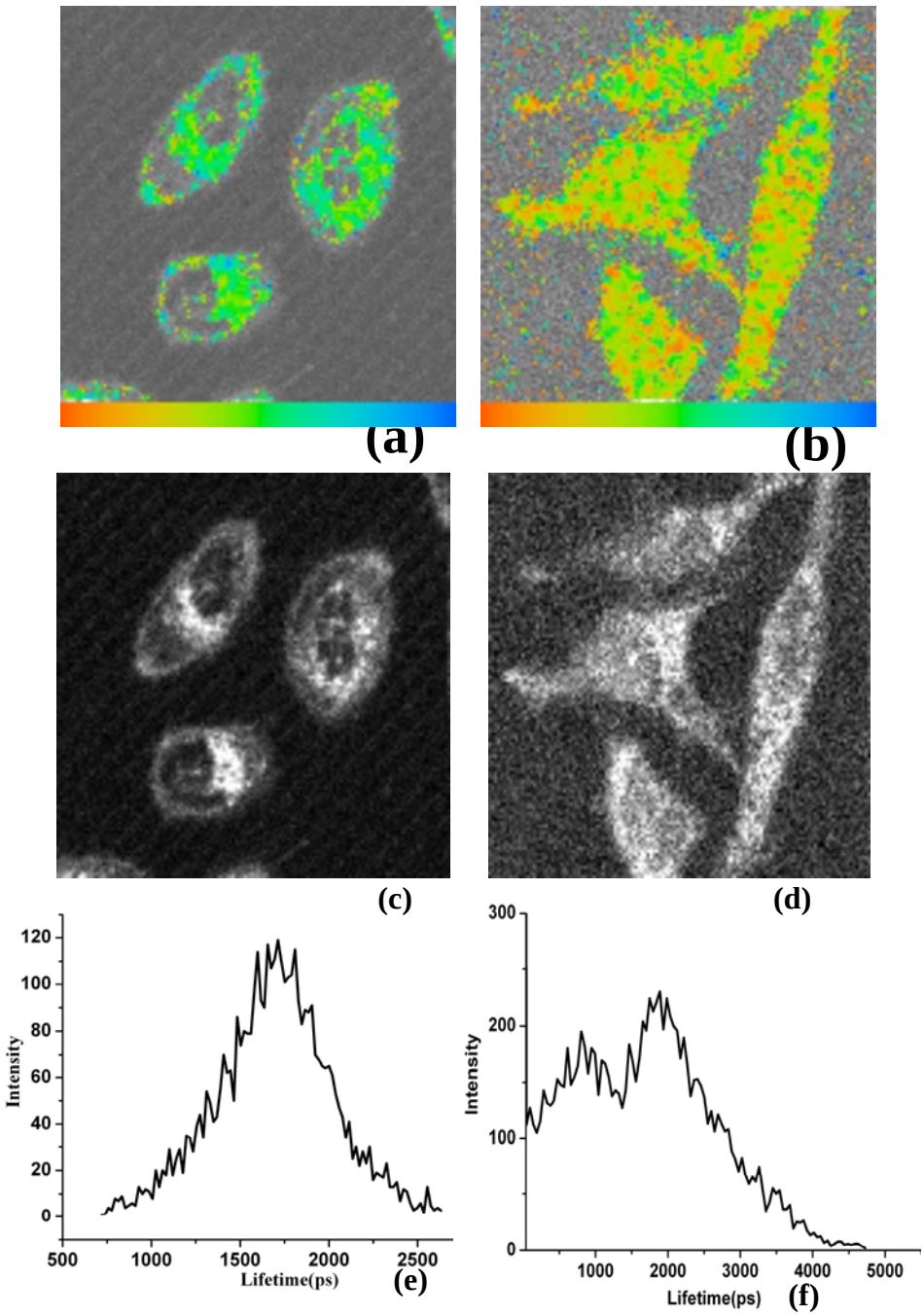

Figure 4.12. Two-photon laser confocal fluorescence (λ_{ex} = 910 nm):(**a,c,e)** Typical micrograph of PC-3 cells incubated for 20 min at 37 ^{o}C with T12 (1.92 nM or 7 μg/mL in 5: 95% DMSO: EMEM showing T12 mainly stay in cytoplasm surrounding nucleus, lifetime mapping and scalebar (**a**), intensity image (**c**), and corresponding lifetime distribution curve (**e**); **(b,d,f)** Typical micrographs of PC-3 cells incubated for 20 min at 37 ^{o}C with T12@SWNT composite dispersion (in 5: 95% DMSO: EMEM contained 7 μg/mL T12 (1.92 nM) 'anchored' onto 18 μg/mL SWNT. Intensity image (**d**), lifetime mapping and scalebar (**b**) and corresponding lifetime distribution curve (**f**).

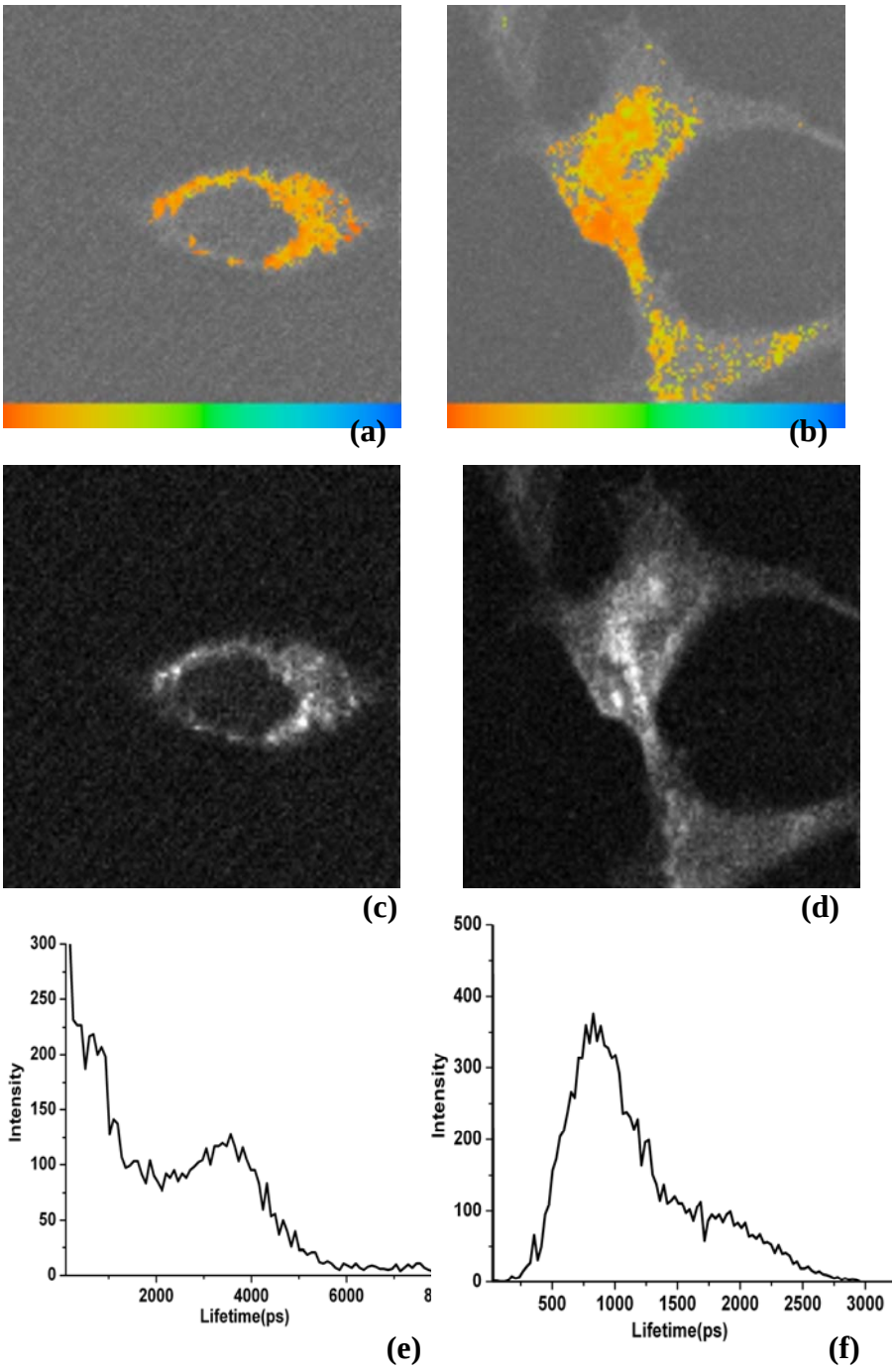

Figure 4.13. Two-photon laser confocal fluorescence (λ_{ex}= 910 nm):(**a,c,e)** Typical micrograph of HeLa cells incubated for 20 min at 37 ^{o}C with T12 (1.92 nM or 7 µg/mL in 5: 95% DMSO: EMEM showing T12 localizes in both cytoplasm and cell nucleus, lifetime mapping and scalebar (**a**), intensity image (**c**), and corresponding lifetime distribution curve (**e**); **(b,d,f)** Typical micrographs of HeLa cells incubated for 20 min at 37 ^{o}C with T12@SWNT composite dispersion (in 5: 95% DMSO : EMEM contained 7 µg/mL T12 (1.92 nM) 'anchored' onto 18 µg/mL SWNT. Intensity image (**d**), lifetime mapping and scalebar (**b**) and corresponding lifetime distribution curve (**f**).

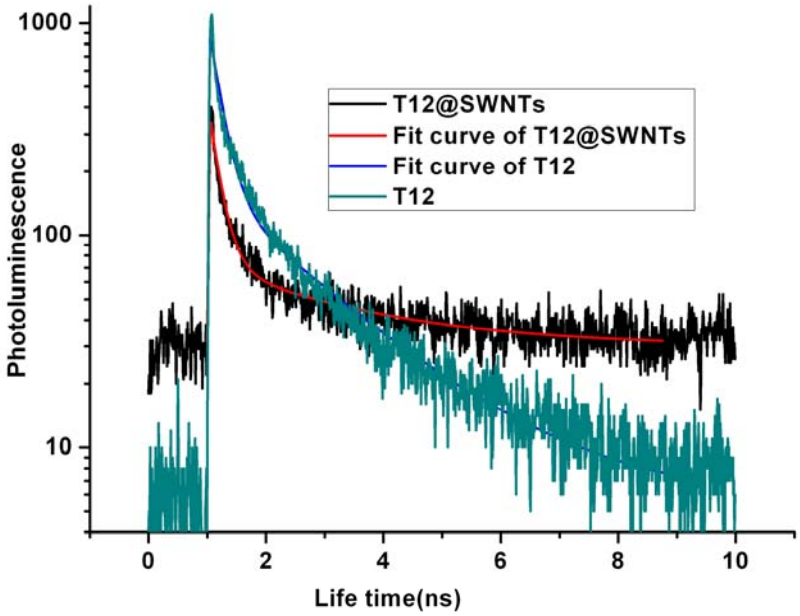

Figure 4.14. Two-photon fluorescence spectroscopy: fluorescence decay traces for the lifetime determinations (λ_{ex}= 910 nm, T12 concentration: 7.5 nM or 27.3 μg/mL in pure DMSO, T12@SWNT composite dispersion containing 27.3 μg/mL or 7.5 nM T12 anchored onto 70 μg/mL SWNT).

4.2.1.6 Diffusion-ordered 2D NMR (DOSY) as a tool for analysis of functionalisation of SWNTs

^{1}H NMR spectra of T12 in T12@SWNT (see Appendix Figure 8.22) composite material in $CDCl_3$ showed that the peaks corresponding to protons of ethylene glycol chain (3.55 ppm), alkyl chain (1.25-1.27 ppm) and thiophene (7.31 ppm) all become smaller compared with that of free polymer, indicating aromatic stacking interactions between T12 and SWNTs. As mentioned above, the majority of free, unbound, T12 was believed to be removed by three cycles of filtration/dispersion treatment. The tumbling motions of T12 are reduced strongly once conjugated to carbon nanotubes, which will have different magnetic-field environments.

Diffusion-ordered 2D NMR (DOSY) experiments have been used for analysis of the diffusive behaviour of mixtures,[52] as well as for characterization of aggregates.[53,54] A typical

DOSY experiment consists of a diffusion delay, flanked by two pulse field gradients. In the case of large and slowly moving molecules, the spin remains stationary during the time of these two pulses, the NMR signal is independent of the strength and length of the gradient pulse. But for small and fast moving molecules, the NMR signal will be affected. So, the NMR signal of rapidly moving, small molecule will be strongly attenuated, while the NMR signal of slowly moving, big molecule will be less attenuated. Therefore, DOSY technique can distinguish compounds according to their size.[55]

After 48 h of stirring at room temperature, the solution mix was subjected to centrifugation cycles at 10000 rpm, giving a black suspension. The black suspension was filtrated and dispersed in $CHCl_3$ 3 times. The resulting black complex was obtained by evaporating the solvent. A proton-detected DOSY of T12@SWNT $CDCl_3$ solution (1.54 mM) has been performed (see Figure 4.15).

The ^1H NMR spectrum of the conjugated T12 is shown in the horizontal axis: all signals are well resolved and consistent with the expected formula.

Figure 4.15 shows the signal intensity decays of the conjugated T12 after removing excess T12 through filtration, as a function of the increasing field gradient strength. We can calculate the diffusion coefficient of each proton signal by least-squares fitting of these decay plots. Subsequently the data can be presented in a 2D contour mode plot with NMR chemical shifts on the horizontal axis and diffusion coefficients on the vertical axis.

The numbers for the diffusion coefficients seem very small and further studies are necessary to elucidate the reasons for the rapid diffusion in solution: in the DOSY NMR of the T12@SWNT solution, three cross peaks were detected: the bottom one correspond to solvent/H_2O and other very small molecules, coming at about 2.46×10^{-9} m^2/s. The media peak may correspond to free, unbound T12 ($D=8.2\times10^{-10}$ m^2/s) present in dispersion. The top peak corresponds to T12 conjugated to very short functionalised carbon nanotubes

(T12=5.8×10^{-10} m^2/s). It clearly shows that T12 dot and T12@SWNT dot are very close with each other still can see the difference once zoom in. The precise size of the species was not estimated with precision as the behavior of this system is clearly very complex in the wet solvents used.

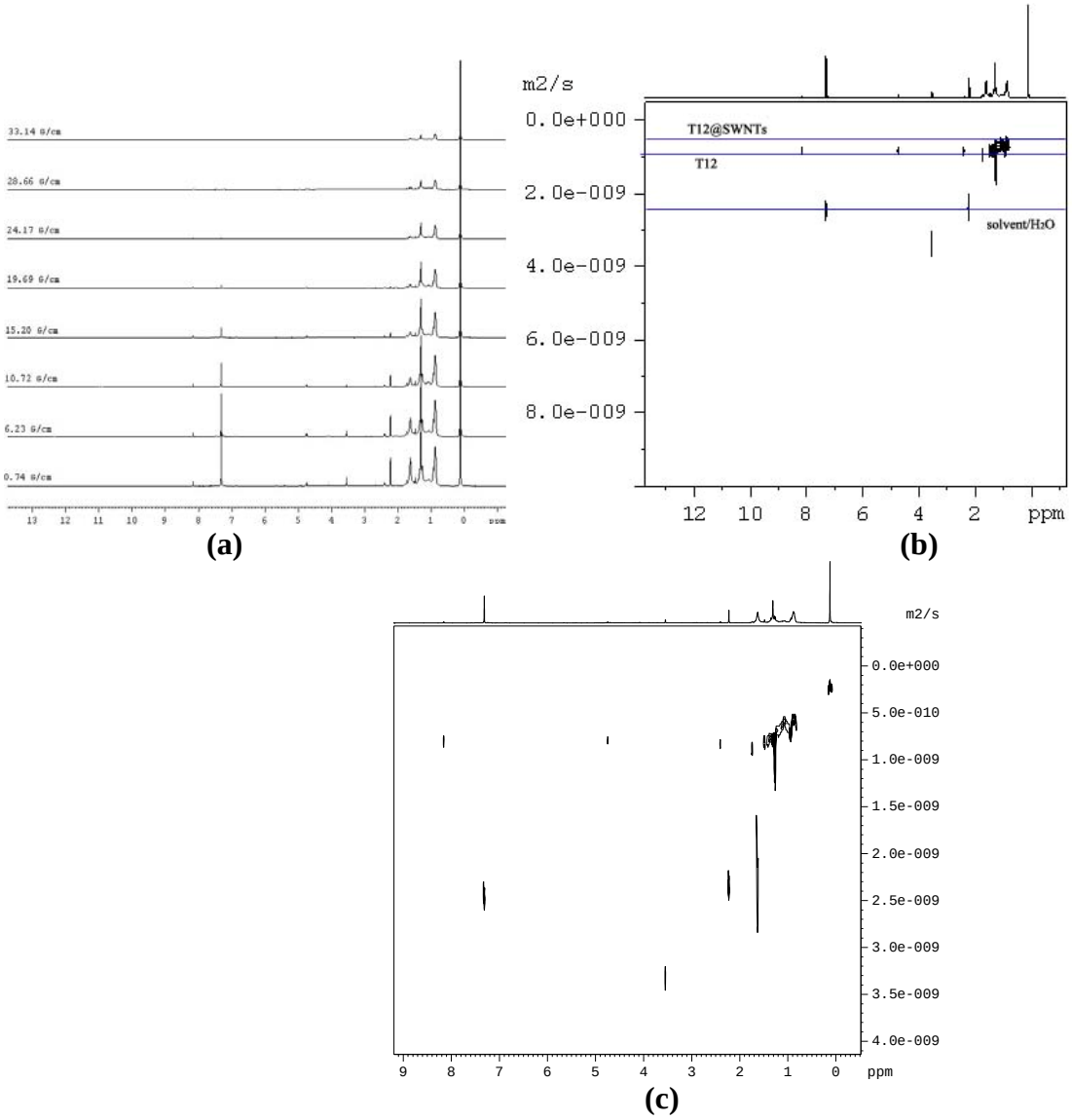

Figure 4.15. Signal intensity decay obtained with the 2D-DOSY analysis of the T12@SWNT in $CDCl_3$ after purification (**a**). 2D-DOSY contour mode plots (**b-c**), where the shift-resolved discrimination of the diffusion constant can be visualised, are reported for the same fractions (top and bottom right, F_1axis=$m^2/S\times10^{-9}$).

4.3 Conclusions for Chapter 4

In summary, a novel amphiphilic conjugated thiophene was used for noncovalent functionalisation of SWNTs. The interactions between the polythiophene and the SWNTs were studied by various characterization methods and the application of using this supramolecular structure as new molecular imaging probe was explored in this chapter. The non-covalent interactions (aromatic stacking, hydrophobic interactions) between SWNT and conjugated thiophene T12 are studied by UV-vis-NIR, fluorescence, Raman spectroscopic studies as well as surface analysis (AFM and TEM) study. The well resolved peaks of SWNTs in the NIR range suggest that SWNTs are de-bundled very well after interaction with T12 without large aggregated SWNTs in the solution, which was removed by the 3 cycles of dispersion/filtration treatment. The 90 nm blue-shift of maxima emission peak after complex with SWNTs which can be seen from 2D fluorescent contour plotting is due to the decreasing planarity of the conjugate T12 backbone after helical wrapping on the surface of SWNTs. The TEM and AFM studies show a good dispersibility of T12@SWNTs in organic solvents ($CHCl_3$), also the possibility of using T12@SWNTs for fabricating functional SWNTs films.

In order to investigate the intracellular imaging behavior of T12@SWNTs, we incubate cancer cells (HeLa and PC-3 cells) with T12@SWNTs DMSO solution and then image their intracellular localization and imaging by confocal laser scanning microscopy and also two-photon lifetime imaging microcopy. Lifetime imaging method provides the cellular information of T12@SWNTs and also free T12 based on fluorescent lifetime mapping and intensity imaging. Cellular imaging results show that the T12@SWNT complex acts as a very good potential candidate for molecular imaging nanoprobes.

4.4 Reference for Chapter 4

(1) Baker, M. *Nat. Methods* **2010**, *7*, 957.

(2) Kam, N. W. S.; Liu, Z. A.; Dai, H. J. *Angew. Chem.-Int. Edit.* **2006**, *45*, 577.

(3) Kam, N. W. S.; O'Connell, M.; Wisdom, J. A.; Dai, H. J. *Proc. Natl. Acad. Sci. U. S. A.* **2005**, *102*, 11600.

(4) Liu, Z.; Robinson, J. T.; Sun, X. M.; Dai, H. J. *J. Am. Chem. Soc.* **2008**, *130*, 10876.

(5) Prato, M.; Kostarelos, K.; Bianco, A. *Accounts Chem. Res.* **2008**, *41*, 60.

(6) De La Zerda, A.; Zavaleta, C.; Keren, S.; Vaithilingam, S.; Bodapati, S.; Liu, Z.; Levi, J.; Smith, B. R.; Ma, T. J.; Oralkan, O.; Cheng, Z.; Chen, X. Y.; Dai, H. J.; Khuri-Yakub, B. T.; Gambhir, S. S. *Nat. Nanotech.* **2008**, *3*, 557.

(7) Tasis, D.; Tagmatarchis, N.; Bianco, A.; Prato, M. *Chem. Rev.* **2006**, *106*, 1105.

(8) Carrillo, A.; Swartz, J. A.; Gamba, J. M.; Kane, R. S.; Chakrapani, N.; Wei, B. Q.; Ajayan, P. M. *Nano Lett.* **2003**, *3*, 1437.

(9) Petrov, P.; Stassin, F.; Pagnoulle, C.; Jerome, R. *Chem. Commun.* **2003**, 2904.

(10) Wang, H.; Zhou, W.; Ho, D. L.; Winey, K. I.; Fischer, J. E.; Glinka, C. J.; Hobbie, E. K. *Nano Lett.* **2004**, *4*, 1789.

(11) Chen, J.; Liu, H. Y.; Weimer, W. A.; Halls, M. D.; Waldeck, D. H.; Walker, G. C. *J. Am. Chem. Soc.* **2002**, *124*, 9034.

(12) Welsher, K.; Sherlock, S. P.; Dai, H. *Proc. Natl. Acad. Sci. U. S. A.* **2011**, *108*, 8943.

(13) Yang, S.-T.; Cao, L.; Luo, P. G.; Lu, F.; Wang, X.; Wang, H.; Meziani, M. J.; Liu, Y.; Qi, G.; Sun, Y.-P. *J. Am. Chem. Soc.* **2009**, *131*, 11308.

(14) Ray, S. C.; Saha, A.; Jana, N. R.; Sarkar, R. *J. Phys. Chem. C* **2009**, *113*, 18546.

(15) Yang, S.-T.; Wang, X.; Wang, H.; Lu, F.; Luo, P. G.; Cao, L.; Meziani, M. J.; Liu, J.-H.; Liu, Y.; Chen, M.; Huang, Y.; Sun, Y.-P. *J. Phys. Chem. C* **2009**, *113*, 18110.

(16) Wong, B. M.; Ye, S. H. *Phys.Rev. B* **2011**, *84*.

(17) Ramakrishna, G.; Bhaskar, A.; Bauerle, P.; Goodson, T., III *J. Phys. Chem. A* **2008**, *112*, 2018.

(18) Barbarella, G.; Zambianchi, M.; Pudova, O.; Paladini, V.; Ventola, A.; Cipriani, F.; Gigli, G.; Cingolani, R.; Citro, G. *J. Am. Chem. Soc.* **2001**, *123*, 11600.

(19) Gao, J.; Blondeau, P.; Salice, P.; Menna, E.; Bartova, B.; Hebert, C.; Leschner, J.; Kaiser, U.; Milko, M.; Ambrosch-Draxl, C.; Loi, M. A. *Small* **2011**, *7*, 1807.

(20) Aslund, A.; Sigurdson, C. J.; Klingstedt, T.; Grathwohl, S.; Bolmont, T.; Dickstein, D. L.; Glimsdal, E.; Prokop, S.; Lindgren, M.; Konradsson, P.; Holtzman, D. M.; Hof, P. R.; Heppner, F. L.; Gandy, S.; Jucker, M.; Aguzzi, A.; Hammarstrom, P.; Nilsson, K. P. R. *ACS Chemical Biology* **2009**, *4*, 673.

(21) Ali-Boucetta, H.; Al-Jamal, K. T.; McCarthy, D.; Prato, M.; Bianco, A.; Kostarelos, K. *Chem. Commun.* **2008**, 459.

(22) Arnold, M. S.; Guler, M. O.; Hersam, M. C.; Stupp, S. I. *Langmuir* **2005**, *21*, 4705.

(23) Balasubramanian, K.; Friedrich, M.; Jiang, C. Y.; Fan, Y. W.; Mews, A.; Burghard, M.; Kern, K. *Adv. Mat.* **2003**, *15*, 1515.

(24) Bayazit, M. K.; Coleman, K. S. *J. Am. Chem. Soc.* **2009**, *131*, 10670.

(25) Bianco, A.; Kostarelos, K.; Prato, M. *Expert Opin. Drug Deliv.* **2008**, *5*, 331.

(26) Bottini, M.; Bruckner, S.; Nika, K.; Bottini, N.; Bellucci, S.; Magrini, A.; Bergamaschi, A.; Mustelin, T. *Toxicol. Lett.* **2006**, *160*, 121.

(27) Bottini, M.; Cerignoli, F.; Dawson, M. I.; Magrini, A.; Rosato, N.; Mustelin, T. *Biomacromolecules.* **2006**, *7*, 2259.

(28) Chen, J. Y.; Collier, C. P. *J. Phys. Chem. B* **2005**, *109*, 7605.

(29) Cherukuri, P.; Gannon, C. J.; Leeuw, T. K.; Schmidt, H. K.; Smalley, R. E.; Curley, S. A.; Weisman, R. B. *Proc. Nat. Acad. Sci. U.S.A.* **2006**, *103*, 18882.

(30) Cui, D. X.; Tian, F. R.; Ozkan, C. S.; Wang, M.; Gao, H. J. *Toxicol. Lett.* **2005**, *155*, 73.

(31) Didenko, V. V.; Moore, V. C.; Baskin, D. S.; Smalley, R. E. *Nano Lett.* **2005**, *5*, 1563.

(32) Kubat, P.; Lang, K.; Janda, P.; Frank, O.; Matulkova, I.; Sykora, J.; Civis, S.; Hof, M.; Kavan, L. *J. Nanosci. Nanotech.* **2009**, *9*, 5795.

(33) Lee, Y.; Geckeler, K. E. *Adv. Mater.* **2010**, *22*, 4076.

(34) Lin, S. J.; Keskar, G.; Wu, Y. N.; Wang, X.; Mount, A. S.; Klaine, S. J.; Moore, J. M.; Rao, A. M.; Ke, P. C. *Appl. Phys. Lett.* **2006**, *89*.

(35) Pascu, S. I.; Kuganathan, N.; Tong, L. H.; Jacobs, R. M. J.; Barnard, P. J.; Chu, B. T.; Huh, Y.; Tobias, G.; Salzmann, C. G.; Sanders, J. K. M.; Green, M. L. H.; Green, J. C. *J. Mater. Chem.* **2008**, *18*, 2781.

(36) Porter, A. E.; Gass, M.; Muller, K.; Skepper, J. N.; Midgley, P. A.; Welland, M. *Nat. Nanotech.* **2007**, *2*, 713.

(37) Worle-Knirsch, J. M.; Pulskamp, K.; Krug, H. F. *Nano Lett* **2006**, *6*, 1261.

(38) Konig, K. *J. Microsc.* **2000**, *200*, 83.

(39) Suhling, K.; French, P. M.; Phillips, D. *Photochem. Photobiol. Sci.* **2005**, *4*, 13.

(40) Stutzmann, G. E.; Parker, I. *Physiology (Bethesda)* **2005**, *20*, 15.

(41) Oheim, M.; Michael, D. J.; Geisbauer, M.; Madsen, D.; Chow, R. H. *Adv. Drug. Deliv. Rev.* **2006**, *58*, 788.

(42) Bisby, R. H.; Crisostomo, A. G.; Botchway, S. W.; Parker, A. W. *Photochem. Photobiol.* **2009**, *85*, 353.

(43) Botchway, S. W.; Parker, A. W.; Bisby, R. H.; Crisostomo, A. G. *Microsc. Res. Tech.* **2008**, *71*, 267.

(44) Treanor, B.; Lanigan, P. M.; Suhling, K.; Schreiber, T.; Munro, I.; Neil, M. A.; Phillips, D.; Davis, D. M.; French, P. M. *J. Microsc.* **2005**, *217*, 36.

(45) van Rijn, P.; Savenije, T. J.; Stuart, M. C. A.; van Esch, J. H. *Chem. Commun.* **2009**, 2163.

(46) van Rijn, P.; Janeliunas, D.; Brizard, A. M. A.; Stuart, M. C. A.; Eelkema, R.; van Esch, J. H. *Chem.-Eur. J.* **2010**, *16*, 13417.

(47) Tolosa, L.; Gryczynski, I.; Eichhorn, L. R.; Dattelbaum, J. D.; Castellano, F. N.; Rao, G.; Lakowicz, J. R. *Anal. Biochem.* **1999**, *267*, 114.

(48) Bastiaens, P. I. H.; Squire, A. *Trends Cell Biol.* **1999**, *9*, 48.

(49) Brismar, H.; Trepte, O.; Ulfhake, B. *J. Histochem. Cytochem.* **1995**, *43*, 699.

(50) Ng, T.; Squire, A.; Hansra, G.; Bornancin, F.; Prevostel, C.; Hanby, A.; Harris, W.; Barnes, D.; Schmidt, S.; Mellor, H.; Bastiaens, P. I. H.; Parker, P. J. *Science* **1999**, *283*, 2085.

(51) Peter, M.; Ameer-Beg, S. M. *Biol. Cell* **2004**, *96*, 231.

(52) Van Lokeren, L.; Maheut, G.; Ribot, F.; Escax, V.; Verbruggen, I.; Sanchez, C.; Martins, J. C.; Biesemans, M.; Willem, R. *Chem.-Eur. J.* **2007**, *13*, 6957.

(53) Keresztes, I.; Williard, P. G. *J. Am. Chem. Soc.* **2000**, *122*, 10228.

(54) Jang, H. B.; Rho, H. S.; Oh, J. S.; Nam, E. H.; Park, S. E.; Bae, H. Y.; Song, C. E. *Org. Biomol. Chem.* **2010**, *8*, 3918.

(55) Viel, S.; Mannina, L.; Segre, A. *Tetrahedron Lett.* **2002**, *43*, 2515.

Chapter 5 Radio-metal filled and fluorescent SWNTs as synthetic platforms for multimodal imaging systems

5.1 Introduction

There is increased interest in improving our understanding of the interactions between nanomaterials and living systems, with regard to both the underlying chemistry and the physics of effects on the nanoscale. Imaging and therapeutic metallodrugs, including radioisotopes such as, for example, ^{64}Cu (positron emission tomography, PET, radiotracer $t_{1/2}$ = 2.7 h), ^{89}Zr (PET radiotracer, 78.4 h) or ^{186}Re (radiotherapy, $t_{1/2}$ =3.72 days). These building blocks when encased within inert carriers by rapid and simple chemistry based on non-covalent interactions, may lead to the construction of future nanomedicines.[1] Increased attention has also been drawn recently to new methods of drug delivery emerging from the new, interdisciplinary field of nanotechnology. To date, no single molecular imaging modality is sufficient to gain all the necessary information need for both *in vitro* and *in vivo*. Positron emission tomography (PET) has very high sensitivity but poor resolution although this continues to improve as image processing methods advance.[2,3] Both positron emission tomography and magnetic resonance imaging (MRI) require the imaging agents to accumulate in tumors without loss of the active species *en route* to target. The combination of multiple molecular imaging techniques can offer synergistic advantages over single modality imaging techniques (optical or PET alone).[2,3]

Design protocols leading to the 'smart' nano-theranostics of the future rely on synthetic advantages offered by molecular recognition principles as well as high resolution transmission electron microscopy (TEM) and surface analysis techniques such as atomic force microscopy (AFM) and molecular imaging on the nano- and micro-scale. Our recent

work in decorating carbon nanomaterials with biocompatible materials such as naphthyldiimides and porphyrin oligomers constituted a proof-of-principle study on how understanding and design at the molecular level could help develop research new diagnostics or therapeutics.[4]

Functionalisation methods for carbon nanomaterials(CNTs) have received huge attention over the past 5 years in the quest to clarify their role in biomedical applications. There are very few examples of radiolabeled nanotubes to date, and only one other study showing the entrapping or radioisotopes within carbon nanotubes. High-yield filling of single-walled carbon nanotubes (SWNTs) with inorganic compounds under harsh conditions (above 300 ^{o}C) leading to continuous crystalline filling has been demonstrated.[5-7] In typical endohedral filling methods via a molten salt route, the end of the nanotubes normally close under the reaction conditions used, which involve thermal annealing of the SWNTs under harsh conditions, *e.g.* as samples are heated at temperatures at least 20 ^{o}C above the melting point of the filling material.[5]

Designing nano-probes whereby PET imaging agents are anchored onto (or encapsulated within) nano-size carriers has become a topical issue.[8] This requires rapid radiolabelling methods under mild conditions suitable to work under the confines of most radiopharmacies or radiochemistry laboratories.[8] Combination of 'smart' fluorescent probes for cellular tracking with high resolution *in vivo* imaging methods such as PET coupled MRI constitutes an exciting prospect for future 'all-in-one' multimodality imaging applications. An additional current aim of our work is to design methods for the delivery of multiple molecules of an imaging reagent (encapsulated within a carrier) to a target while keeping the administered dose of the overall nanoprobe extremely small.

SWNTs have attracted growing interest due to their potential applications in the fields of cancer diagnosis and therapy.[9-13] To trace and diagnose the effects of the treatment in single cells or tissues, SWNTs have been derivatised with fluorescent tags.[14,15] Intrinsically, carbon nanotubes also exhibit weak near-infrared emissions, but to date, these are not considered intense enough in practice to be useful in functional in vivo imaging and diagnosis.[16] It is believed that appropriately functionalised SWNTs can efficiently reach tumor tissues in mice with limited or no apparent toxicity. The simultaneous radiolabeling (with 1,4,7,10-tetraazacyclododecane-1,4,7,10-tetraacetic acid (DOTA)-anchored ^{64}Cu) and fluorescence studies, coupled with biodistribution *in vivo* and *in vitro* has only been reported in two studies,[17,18] both involving the covalent functionalisation and hence the disruption of aromatic network. Under certain conditions, water-dispersed, functionalised carbon nanotubes have been shown to be non-toxic when taken up by cells. [19] These studies have been complemented by the recent PET imaging of water-soluble ^{86}Y-labeled carbon nanotubes *in vivo*[20], to explore the potential usefulness of carbon nanocarriers as scaffolds for drug delivery. Recent challenges in achieving the controlled translocation of carbon nanotubes in living cells and organisms have been reviewed recently.[21]

Covalent functionalisation with fluorophores attached directly onto the carbon nanotube surface may be problematic due to the strong quenching qualities of the electron rich SWNTs. The supramolecular tagging of the carbon nanotubes with fluorescent dyes attached via a continuous polymeric coating or via a very long linker (rather than directly onto the SWNTs) allows the separation of the fluorophore and the SWNT surface and was reported to be advantageous in minimising the fluorescence quenching.[22,23]

Dai et al. demonstrated the non-covalent functionalisation of SWNTs by fluorescein-polyethylene glycol (Fluor-PEG).[18,24] Water-soluble nanotube conjugates (Fluor-

PEG/SWNT), simultaneously attached to fluorescent labels have been developed. The same study showed that fluorescein, a widely used fluorophore, can strongly adsorb onto the sidewall of the SWNTs, likely by aromatic stacking, and the hydrophilic PEG chain imparts high aqueous solubility.[25] To date only a relatively small number of *in vitro and in vivo* studies have been carried out to determine the influence on cell toxicity mechanisms of the functionalities incorporated in these imaging probes, and a toolkit aiding their rational design has not yet been devised.[26] In this chapter aimed to validate our design principles for the assembly of the SWNTs-based imaging probes and hypothesise that bioimaging probes which rely exclusively on non-covalent interactions and molecular recognition methods can be synthesized and image in vivo and in vitro.

Our synthetic protocol reported hereby involves the following steps:

(a) Provision of single walled carbon nanotubes (SWNT) with open ends and a hollow cavity for the stable containment to prevent radionuclide loss en route to target, with lengths not exceeding 500 nm, and diameters up to 2 nm.

(b) Encapsulation of a PET metallic radioimaging agent within the SWNT cavity under mild conditions in aqueous media. A stopper molecule with a compatible outer diameter (C_{70}) is encapsulated within the inner cavity of the tubes simultaneously with the radiotracer to minimise the leaking of the payload in aqueous media.

(c) Rendering the entire surface of carbon nanotubes biocompatible *via* supramolecular wrapping which allows further (rapid and reversible) surface derivatisation with optical imaging agents, chemotherapeutic payloads and/or targeting units in water.

We are using a naturally occurring polysaccharide, β-D-glucan, known for its cancer therapeutic effect in traditional Chinese medicine,[27] as a dispersing agent having the ability to supramolecularly wrap the single strands of SWNts in water, having the potential to act

simultaneously as a biological targeting molecule and dispersing agent. A recent study by James and Shinkai showed that it is possible to attach small molecules to polysaccharide-coated SWNTs using boronic acids.[13] Here, diol groups act both as solubilising groups and as recognition units suitable for further synthetic modifications, by dynamic covalent chemistry involving boronic acids: attaching fluorescent tags as an additional assembly step or intrinsic to the supramolecular/covalent wrapping was also employed, such that the resulting fluorescent and biocompatible hybrid can be used for tracking in cells. To facilitate the cellular imaging of the targeted delivery probe, a fluorescein derivative incorporating aliphatic linkers and an additional cellular targeting agent (biotin, a well-known system used as a recognition motif for streptavidin) was used as a building block in our design protocol. Systematic studies leading to the devising of hierarchical protocols that range from design and synthesis to observing molecular imaging probes in vivo and in vivo are described. Surface analysis determinations such as AFM/SEM/HRTEM narrowed down the search for most stable imaging probe *in vitro* and help rationalise the mechanisms of interaction with cells and organelles, thus providing feedback to inform probe design. Furthermore, the long-term fate of nanomaterials in the body remains unknown and their biocompatibility and cytotoxicity (particularly for carbon nanotubes) is still much debated.[28] We also report hereby our observations for the in vivo (by PET imaging) and in vitro (by confocal fluorescence imaging) of the new functional materials for molecular imaging applications based on high purity single walled carbon nanotubes assembled using the steps (a)-(c) listed above.

An integrated methodology to build new biocompatible materials *via* a rational design and to elucidate their interactions with living cells *via* fluorescence imaging

techniques and ready for *in vivo* testing by Positron Emission Tomography, in future studies, was designed and is described below.

5.2 Results and discussions

5.2.1 Supramolecular nanoprobe scaffold C_{70}@ M@SWNT synthesis

The main factor in nanotube toxicity remains the metal catalyst particles from particle manufacture, (Fe, Ni, Y, Co etc.) which are typically ca.10 % by weight in most commercial samples. Removal of impurities from as-made SWNTs is crucial for the next step of biomedical applications. Amorphous carbon layers were also known to be present on the surface of as-made SWNTs and believe to shield the surface of nanotubes from further functionalisation. Popular purification methods (such as nitric acid, hydrogen peroxide, hydrogen[29,30]) can cause extensive damage of the SWNT tubular structure, thus rendering them potentially less suitable for small molecule encapsulation techniques, and form more amorphous carbon by oxidising whole SWNT structure. Here, the steam method was used for the purification and opening of single walled nanotubes (Elicarb©, Thomas Swann) following a method which was first reported by the research group of Professor Malcolm Green, University of Oxford with Thomas Swann Ltd. Steam acts as a mild oxidising agent to eliminate the graphitic coating without introducing defects and functional groups ready for biomedical applications.[31,32] The purification of as-made SWNTs (Thomas Swann, Elicarb) can be achieved by introducing steam carried by an argon flow through the reactor. (Scheme 5.1). SWNTs (500 mg -1 g) were introduced in a quartz reactor (9 mm diameter) placed inside of the quartz tube (5 cm diameter) and within the alumina lining of a furnace tube, which was flushed with argon at least 1 h prior to the experiment to minimise the presence of

air. Argon-degassed steam was introduced by bubbling argon through boiling water. The furnace temperature was gradually increased to 900 ^{o}C over ca. 30 min, and the reaction was maintained for at least 20 min and no longer than 2 h depending on the sample size. The resulting sample was refluxed in 16% HCl overnight, which removes most of the metal catalyst, and washed with NaOH and double distilled water on a 2 μm membrane filter until the filtrate was neutral pH. We introduced a further toluene washing/filtration step which allowed only the highest purity SWNTs samples to be recobered after filtration. We found that the overall yield of the purification procedure is lower than 20% so this method does not seem easily amenable to scale-up in commercial activities at present. However, the advanced purity of the samples used here was confirmed by exhaustive Raman and HRTEM/EDS analysis; this clearly shows that amorphous carbon and some graphitic particles entangling the as-made SWNTs were successfully removed leaving behind pristine SWNT surfaces (Figure 5.1b). HRTEM analysis and Raman spectroscopy indicated that the sample characteristics are consistent to those previously reported. This method gives rise to highly purified, opened carbon nanotubes, containing only SWNTs (when arc-made Carbolex-quality samples are used) but also SWNTs mixed with several traces of double walled CNTs (when CVD-made Elicarb Thomas Swann Ltd samples are used as a starting material) with dimensions ranging between 50-500 nm and diameters between 0.9 and 2 nm.

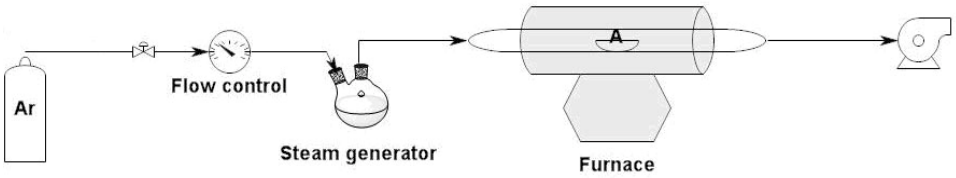

Scheme 5.1. Schematic drawing of the steam purification method of SWNTs by bubbling argon through boiling double-distilled H_20, **A**: SWNTs solid sample.

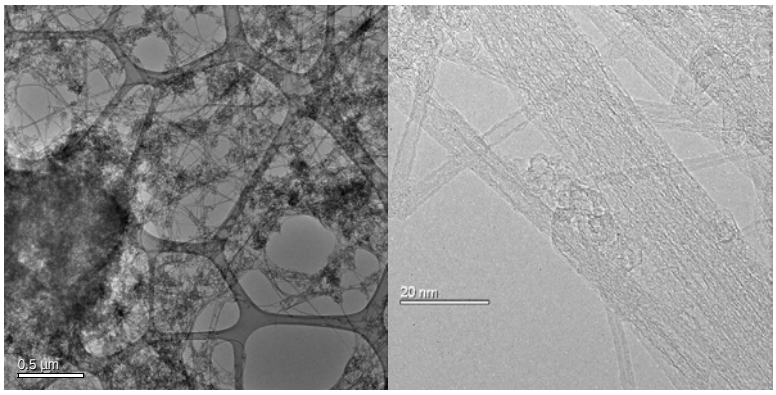

(a) (b)

Figure 5.1. HRTEM pictures of (a) as-made SWNTs, (b) steam purified SWNTs (900 °C, 2 h)

Although the filling of SWNTs with metal species is well established through the pioneering work of the Oxford Nanotube Group,[33-35] so far the encapsulation of $^{64}Cu^{2+}$ ions within SWNTs from aqueous solution, under the rapid and mild conditions applicable for tracer preparation for PET radioimaging was not demonstrated, particularly when working at the low concentrations (10^{-9} M) and time constrains (e.g. $t_{1/2}$ 12.7 h for ^{64}Cu) required for most radioisotope work. In our work SWNTs containing open ends prepared as above[31] have been exposed to aqueous solutions of simple metal salts, such as CuX_2, (X = Br^-, Cl^- or OAc^-) and their radiolabeled analogues ($^{64}CuX_2$), neat or using NaOAc as the filling support. The use of NaOAs in carrier-added experiments is known to be standard in PET tracer preparation and deemed not to hinder the in vivo imaging methods, as the pH is normally adjusted to 8 in the final tracer formulation, to simulate as closely as possible the conditions necessary prior to any *in vivo* work. The filling yield for $^{64}Cu(OAc)_2$ (supported by saturated solutions NaOAc) was estimated by radiochemistry to be in the range of 60 % over *ca* 4 h experiment time. For 'cold' Cu^{2+}@SWNT composites, obtained by filling with neat $Cu(OAc)_2$, the HRTEM analysis of showed encapsulation in the form of short crystals visible inside the SWNTs (Figure 5.2c). For a comparison, we also performed filling experiments of SWNTs with $CuBr_2$ *via* a molten salt route, and a similar yield (estimated by HRTEM) was

obtained only after *ca.* 8 h heating at 400 ^{o}C in accordance with literature reports.[35-37] (Figure 5.2 b) We thus found that the molten salt route is inadequate for radiochemistry work when this is performed under the confined environment of most clinical radiopharmacies, due to limitations in safe handling of radioactivity at high temperatures and the risk of potential release of radioactive vapours in the atmosphere.

To explore the generality of the solution filling method in this work, the Zr^{4+} filling experiment was also performed from aqueous solutions using $Zr(OAc)_4$ as the precursor, as a model for the PET radioisotope filling with ^{89}Zr. The zirconium filling experiments in aqueous solution showed that the successful filling can only be achieved when the pH was adjusted to 2 by adding small amount H_2SO_4 according to HRTEM/EDS imaging. However, the precise nature of the Zr clusters encapsulated is difficult to predict due to the complex aqueous chemistry of Zr(IV) (Figure 5.3 a). The Zr^{4+}@SWNT structures were analysed using High Resolution TEM. By lowering the accelerating voltage, the knock-on damage of the carbon nanomaterials can be minimised. From HRTEM observations, crystal-filled carbon nanotubes were only found in sample A (C_{70}@Zr^{4+}@SWNT saturated with NaOAc, see Chapter 7 experimental description) which means that make the solution saturated with OAc^- is a key fact for Zr filling. Zirconium clusters were formed after the hydrolysis of precursor $Zr(OAc)_4$ in acetic acid and the condensation of partially hydrolysed species after 48 h is likely to form a three-dimensional gel network. The zirconium complex structure is likely to change after addition of sulfuric acid at pH 2.4: the stoichiometry of Zr(IV) to the oxo-ions present in solutions are known to be strongly dependent on the pH. It is likely that the sulfate SO_4^{2-} ions bind to Zr^{4+} and this counterion is expected to replace the AcO^- ions, but the precise nature of the zirconium clusers present in this aqueous mixture could not be determined. Zirconium sulfate-based oxo-clusters are likely to be present in solution and

may be introduced into the open-ended SWNTs by solution filling. The filling experiment at low pH value seems to help convert the zirconium-aqueous gel-like material into more discrete species which in turn contributed to the successful filling SWNTs with Zr(IV) by solution method.

Interestingly, a rather high filling yield, ca. 60% (estimated by HRTEM, Figure 5.3 c) from aqueous media was obtained with $KReO_4$ ('cold' chemistry, as a model for $^{186/188}ReO_4^-$ or $^{99m}TcO_4^-$ therapeutic or SPECT diagnostic radiotracers). HRTEM reveals the presence of heavy atoms inside of carbon nanotubes with the high contrast compared with the un-filling SWNTs on the left side, which is corresponding to the Re compound (Figure 5.3 c, d). Also the HR-TEM revealed the absence of bulk ReO_4^- external to the SWNTs. The EDS analysis indicated the presence of Re in the sample as expected, a lower intensity of Re peaks was observed due to the removal of the external material by double-distilled H_2O washing.

The use of functionalised C_{60} was already shown to allow the removal of the excess free salts in water.[38] In our hands we found that the leaking of the encapsulated metallic species from open SWNTs may be prevented by the simultaneous encapsulation of C_{70} molecules (maximum van der Waals radii *ca.* 1.1 nm) rather than C_{60} (maximum external diameter = 0.7 nm) which remain stuck at the ends of SWNTs. Several C_{70} molecules act as stoppers of ideal size match for the SWNTs carriers used hereby: HRTEM images show that the open ends of SWNTs are filled by several C_{70} molecules by standard endohedral encapsulation methods.[38] We found that any free, un-bond C_{70} decorating the outside of the tubes can be removed via a simple toluene washing step followed by the filtration/redispersion steps. The inter-fullerene spacing (HRTEM, Figure 5.2 a) of C_{70}@SWNT is 10.4± 0.9 Å with the mean diameter of C_{70} encapsulated in tubes 7.4±0.5 Å. After fullerene encapsulation the mixtures containing M@C_{70}@SWNTs were then filtered

and the solid residue was washed several times with distilled water to remove the metal ions external to the SWNTs (M = Cu(II), Zr(IV) and Re(V). The water and toluene washing steps allowed the removal of most free C_{70} adhering to the walls of the SWNTs also the removal of any other of the bulk materials from filling step, external to the SWNTs cavity.

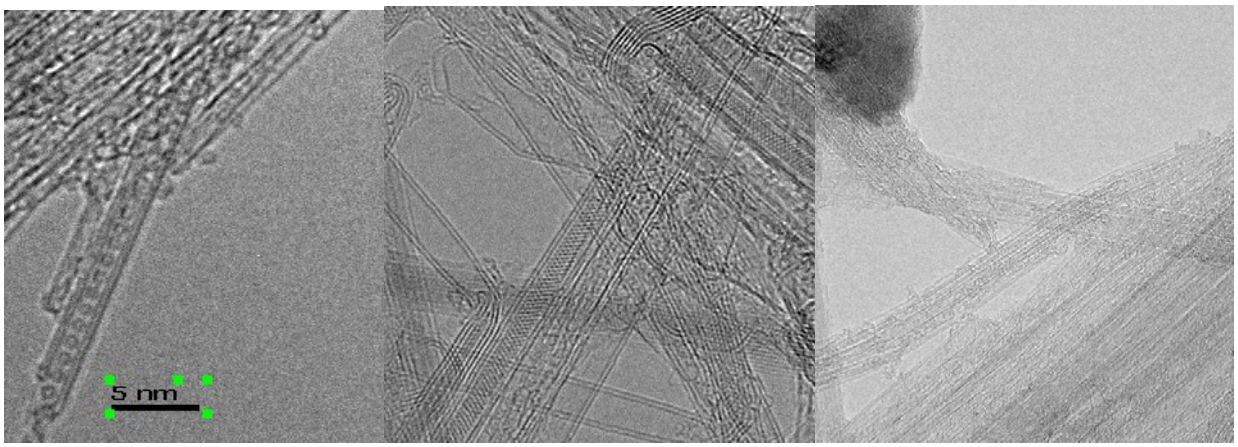

Figure 5.2. Typical HRTEM images of (**a**) C_{70}@SWNT observed in metal-filled and simultaneously corked samples, (b) molten salt $CuBr_2$@SWNT and (c) $Cu(OAc)_2$@SWNT(from neat Cu(OAc)2 filling experiment. Samples were imaged on a lacey copper based grid.

Raman spectroscopy studies showed that both sample A and B (Sample A: C_{70}@ Zr^{4+}@SWNTs saturated with NaOAc; Sample B: C_{70}@ Zr^{4+}@SWNTs without NaOAc, see Chapter 7 Experimental Description) exhibit characteristic radial breathing mode (RBM), G band and D band. (Figure 5.4) For both sample A and B, D-band intensities decrease with respect to those of purified SWNTs, indicating that functionalisation occurred. The I_D/I_G ratio of purified SWNTs, sample A and sample B are 0.121, 0.076 and 0.046, respectively. It shows that there is a decrease of the band intensity ratio after filling with zirconium.

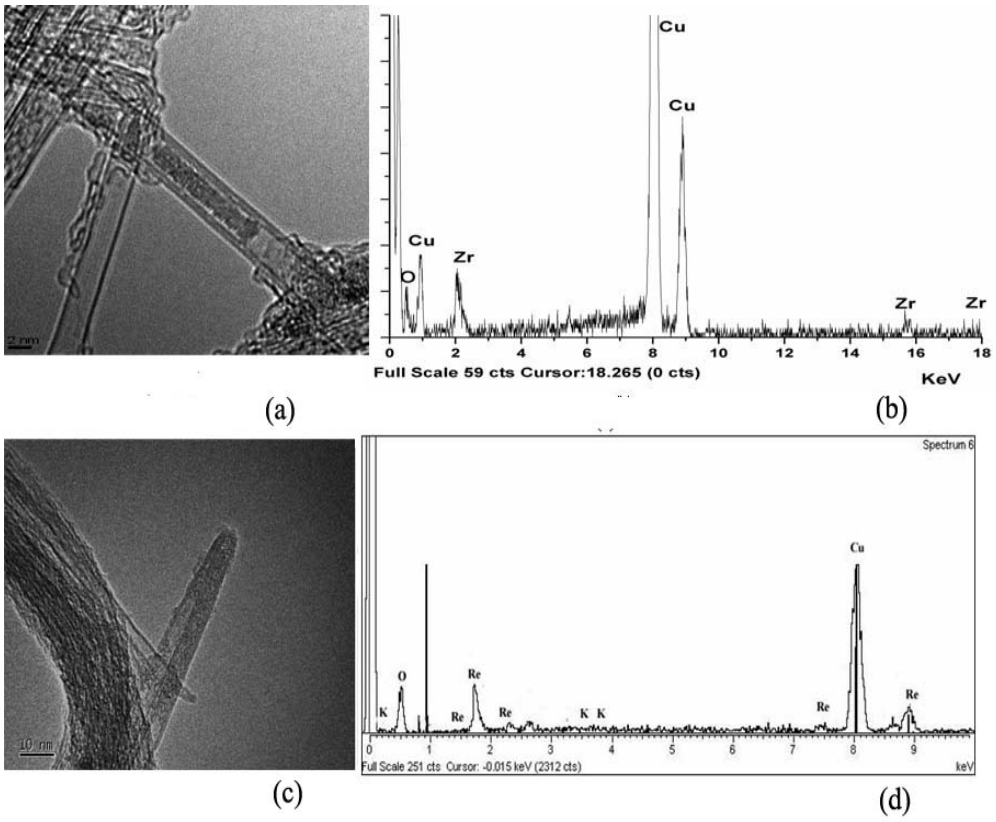

Figure 5.3. (**a**) HRTEM of Zr^{4+}encapsulated inside steam purified SWNTs.. (**b**) The EDS spectrum of Zr^{4+}@SWNT. (**c**) HRTEM of $KReO_4$@SWNT. (**d**)The EDS spectrum of $KReO_4$@SWNT. Samples were imaged on a lacey copper based grid.

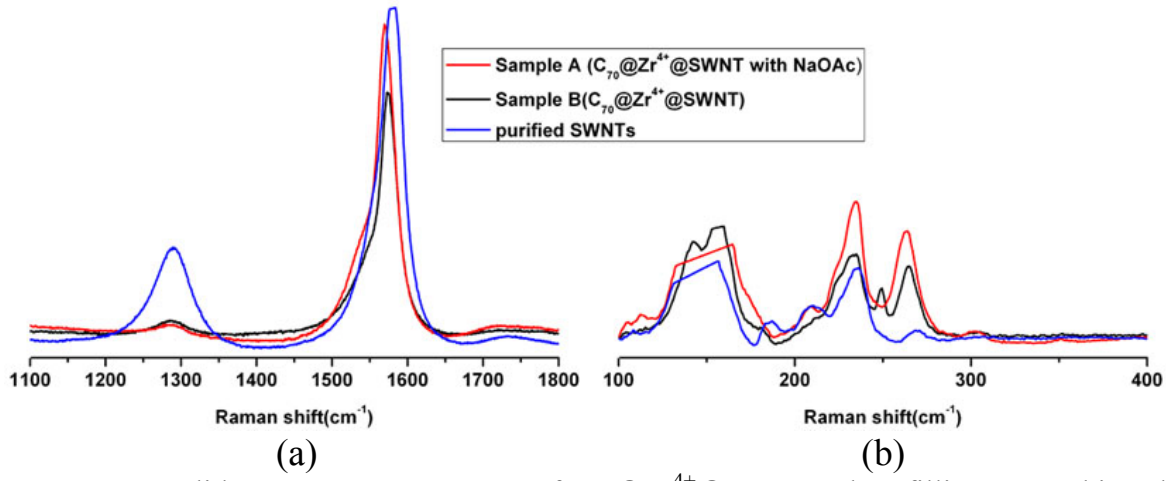

Figure 5.4. Solid state Raman spectrum of C_{70}@Zr^{4+}@SWNT when filling was achieved in the presence or absence of NaOAc (λ_{ex}=830 nm) showing the intensity of G and D bands vs Raman shift (cm^{-1}) (**a**) RBM frequency modes (**b**). Further Raman spectra are given in Appendix material.

.

5.2.2 Supramolecular wrapping of the filled carbon nanotubes surface: M@C_{70}@SWNT@glucan synthesis

The supramolecular wrapping of the tubular structure using polymers, polynuclear aromatic compounds, surfactants and biomolecules has become an important method to prepare well-dispersed SWNTs.[25,28] Polysaccharides such as *β*-D-glucans have been used in traditional Chinese and Japanese medicine from ancient time to enhance the immune system.[39-41] Numerous studies have demonstrated that *β*-D-glucan exhibit antitumor and antimicrobial activities in in vivo experiments.[42,43] Mechanistic studies reveal that *β*-D-glucan can activate macrophages, neutrophils, and natural killer cells to kill sensitive tumor cells[44] and that T cell responses to cellular antigens were potentiated.[45]. Here, stable dispersions (in aqueous PBS or cellular medium DMEM) of empty, pristine and filled SWNTs have been achieved using *β*-1,3-1,4-D-glucan (from barley, Aldrich, denote as *β*-D-glucan in this chapter) as a supramolecular coating. The hypothesis here was that the wrapping with *β*-D-glucan will further mediate the biomedical and clinical functions of metal-filled SWNTs. The wrapping procedure exploits the combination of hydrogen-bonding formation (in DMSO) and solvophobic interactions (in H_2O or NaOAc saturated aqueous solutions) which are known as the two main types of driving forces for *β*-D-glucan self-organisation into helical structures. Shinkai et al.[46] showed that these compounds exhibit hydrophobic cavities (acting as hosts) of shapes and dimensions perfectly adjustable to fit the SWNTs strands (acting as hydrophobic guests).

In this work the glucan@SWNT complex was prepared by mixing a solution of *β*-1,3-1,4-D-glucan from barley, dissolved in DMSO with an aqueous dispersion of the carbon nanotube and incubating the mixture at 40 ^{o}C with stirring, shaking or mild periodic sonication (*ca*. 5 min) alternating with standing periods, over 1 h. After removal of excess

glucan by a washing/filtration repeated procedure, and filtration over a 0.2 μm membrane filter the resulting composite (denoted glucan@SWNT) showed excellent stability over minimum 24 h, at 0.5 mg/mL concentrations, without precipitation in various aqueous phases (water and PBS). The non-covalent interaction between SWNTs and the coating material is based mainly on hydrophobic interactions in water, thus the supramolecular wrapping method allows the modification of the entire surface of SWNTs, without affecting the electronic network of the tubes.[11,12]

A simple molecular mechanics (MM+ Forcite)[13] optimisation model was carried out by Sofia Pascu and this suggests that these glucan strands are able to fit around SWNTs of appropriate diameters. The morphology of this glucan-functionalised SWNT composite was analysed by HRTEM, SEM and AFM. These studies showed that SWNT are entirely coated by *β*-D-glucan as the entire one-dimensional structure of the SWNTs strand is encapsulated inside of hollow cavity of the helical glucan network.

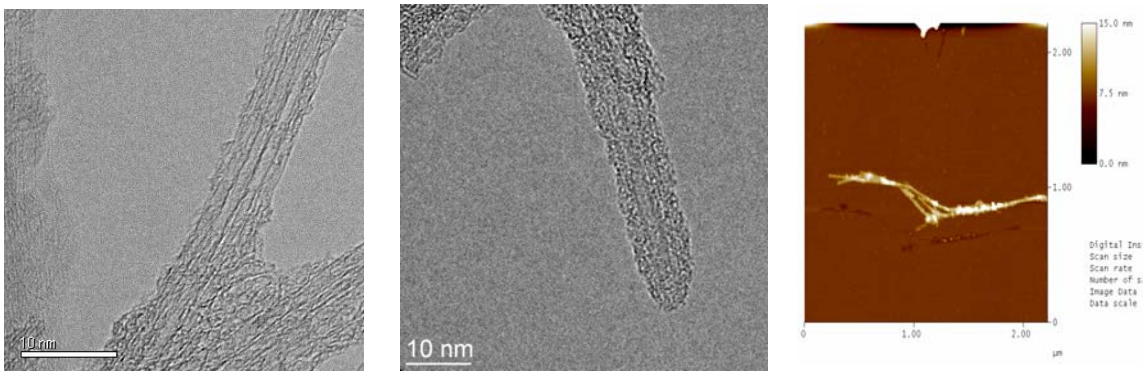

(a) **(b)** **(c)**

Figure 5.5. (**a**) HRTEM of Glucan@SWNT (**b**) HRTEM of glucan@Cu^{2+}@SWNT (**c**), AFM of Glucan@SWNT.

Figure 5.5 and Figure 5.6 show that single stands of SWNTs are uniformly coated by a soft layer or organic material, presumably *β*-D-glucan as imaged by tapping mode AFM (TM AFM). Solid samples were redispersed at 0.5 mg/mL concentration in EtOH and deposited on the relevant support needed for imaging: holey copper grids for HRTEM, mica

for TM AFM and HOPG (highly ordered pyrolitic graphite support) for SEM. The *β*-D-glucan@SWNTs hybrid strand determined by AFM images is *ca.* 15 nm overall indicating the formation of very small bundle on the mica substrates, comparable to the diameter of complexes observed by SEM images. The thickness of the coating is estimated to be ca. 5 nm. It was also found by HRTEM that *β*-D-glucan can seal the opening ends of SWNTs without the filling of the nanotube cavity. In DMSO or EtOH dispersions *β*-D-glucan wrapped SWNTs can still adhere to each other to form small bundles via the hydrogen bonding of OH groups. Raman spectroscopy in solution showed that these aggregates are significantly more dispersible in H_2O than pristine SWNTs.

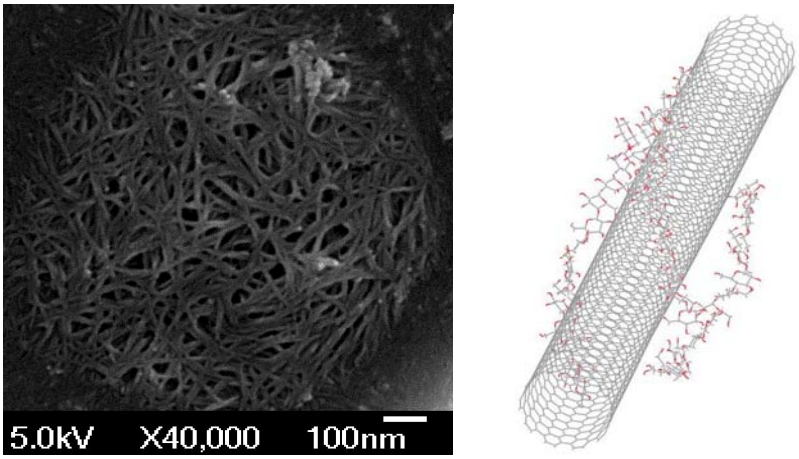

(a) **(b)**

Figure 5.6. SEM images of *β*-D-glucan@SWNT **(a)** and representation of the *β*-D-glucan@SWNT complex (MM+ Forcite) **(b)**. Calculations were performed by using the Materials Studio software.

Raman spectra shown in Figure 5.7 were recorded in solution and in the solid phase for dispersed samples deposited from double-distilled H_2O onto an aluminium sample holder using λ_{ex} = 830 nm. The G band (which corresponds to a splitting of the E2g stretching mode of graphite and reflects the structural intensity of the sp^2-hybridised carbon atoms) at ~1590 cm^{-1} and a disordered D band (generally attributed to the disordered graphite structure of the nanotubes) at ~1330 cm^{-1} were observed. For dried samples, a slight decrease in the I_D/I_G

band intensity ratio of the Cu^{2+}@SWNT and *β*-D-glucan@ Cu^{2+}@SWNT solid composite (9.1 % and 9.3 %) was observed compared to the I_D/I_G of free SWNTs and *β*-D-glucan@SWNT (12.1 % and 11.9 %). (Table 5.1)

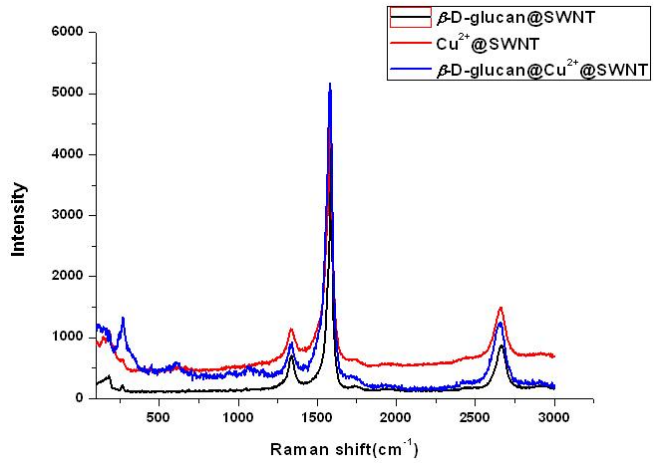

Figure 5.7. Raman spectrum of solid *β*-D-glucan@SWNT, Cu^{2+}@SWNT and *β*-D-glucan@ Cu^{2+}@SWNT (λ_{ex}=830 nm) showing the intensity of RBM frequency modes, G and D bands *vs* Raman shift (cm^{-1}). Solution spectrum of SWNT@glucan and of free glucan in H_2O.

Table 5.1. Raman data and I_D/I_G intensity ratio calculations

Compound	**D band absorbance**	**G band absorbance**	**I_D/I_G**
Purified SWNT	2547 (1302 nm)	21041 (1591 nm)	0.121
β-D-glucan@SWNT	468.74 (1336 nm)	3918.55 (1584 nm)	0.119
Cu^{2+}@SWNT	365.40 (1330 nm)	4011.90 (1582 nm)	0.091
β-D-glucan@Cu^{2+}@SWNT	438.52 (1325 nm)	4713.43 (1582 nm)	0.093

5.2.3 Biocompatibility and proliferation effects of *β*-D-glucan and *β*-D-glucan@SWNTs towards fibroblast cells

Cytotoxicity investigations of *β*-D-glucan and *β*-D-glucan@SWNTs in a healthy cell line, Fek-4, fibroblast cells, were investigated. Figure 5.8 shows the cytotoxicity of *β*-D-glucan to fibroblast Fek-4 cell line after incubation for 24 h. No significant cytotoxic effect

to Fek-4 cells can be seen after exposure to *β*-D-glucan with a limit concentration of 1 mg/mL in cell medium (precipitate can be seen if >1 mg/mL) (Figure 5.8 a). It also indicates that *β*-D-glucan can act as a stimulating agent to enhance the proliferation of Fek-4 cells compared to that of the non-treated control (Figure 5.8 b). Also the proliferation enhanced effect after exposure to *β*-1,3-1,4-D-glucan form barley used throughout was dose and time dependently. This phenomenon can be explained by that the normal human fibroblasts express pattern recognition receptors for *β*-1,3-D-Glucans in general.[38] It is known that highly purified, well characterised glucan stimulates the pro-collagen gene expression and collagen biosynthesis of fibroblasts.[47] Clinical report also shows that pediatric burns could be effectively and simply treated with glucan–collagen mixtures which can significantly decreased post-injury pain through stimulating fibroblast cells proliferation.[48]

In this work, MTT assay results of Fek-4 cells after exposure to *β*-D-glucan@SWNTs complex clearly showed that glucan can improve the biocompatibility of SWNTs in comparison with SWNTs alone,[49,50] which can be explained that glucan acts as an ideal material for covering the most of surface of SWNTs compared with other polymer functionalisation method. In our experiment, the upper concentration limit of *β*-D-glucan@SWNTs used for testing in cell medium was 100 μg/mL. Even at this limit concentration, Fek-4 cells still show considerable cell viability with more than 70 %. This experiment shows the biocompatibility of *β*-D-glucan@SWNTs to healthy cells within this concentration limit.

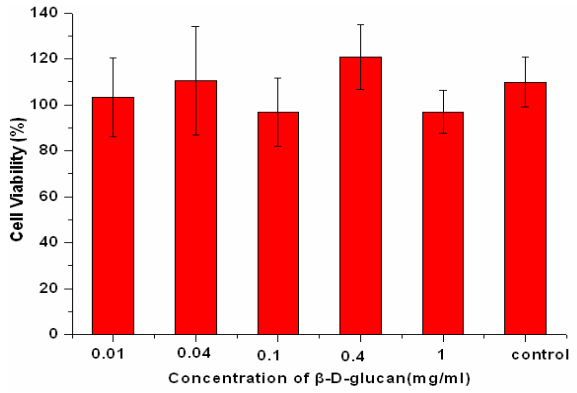

(a)

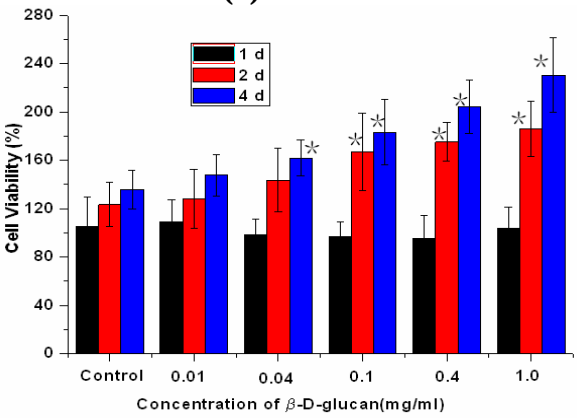

(b)

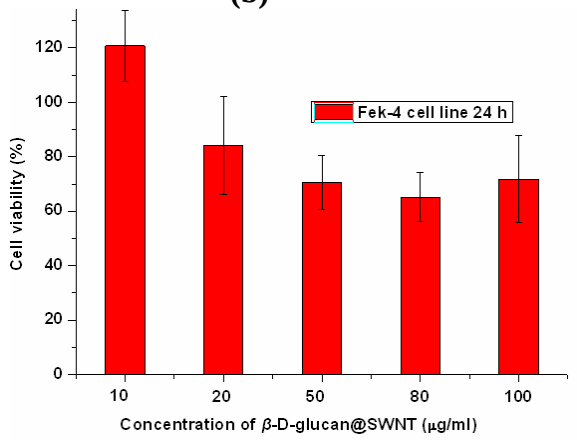

(c)

Figure 5.8. The cytotoxicity of *β*-D-glucan(**a**) and *β*-D-glucan@SWNTs(**c**) to fibroblast cell Fek-4 line, and also the proliferation effect of *β*-D-glucan to Fek-4 cells(**b**). The results are reported as a mean ± standard deviation (n = 3). The data was analysed by Student t-tests, and the values marked with asterisks are significantly ($p < 0.05$) different from the non-treated control.

5.2.4 Reversible covalent chemistry for the attachment of targeting units or fluorophors: Hierarchical nanoprobes flurophor@glucan@M@SWNT synthesis

The procedure for attaching fluorophore to the glucan coating was derived from the pioneering work of Prof Tony James at Bath University, where boronic acid fluorophores are bound to glucose or fructose under basic pH control.[51-54] The reaction mechanism is described in Scheme 5.1. Compounds **11**, **12** and **15** were synthesized as described in Chapter 7, coumarin-derivative (Compound 1**6**) was a generous loan from Professor Tony James and used for comparison purposes with **11, 12** and **15** which were synthesized hereby**.**

All fluorophor-tagged boronic acids showed fluorescent quenching upon addition of glucan with respect to free fluorophore emissions (Figure 5.10).

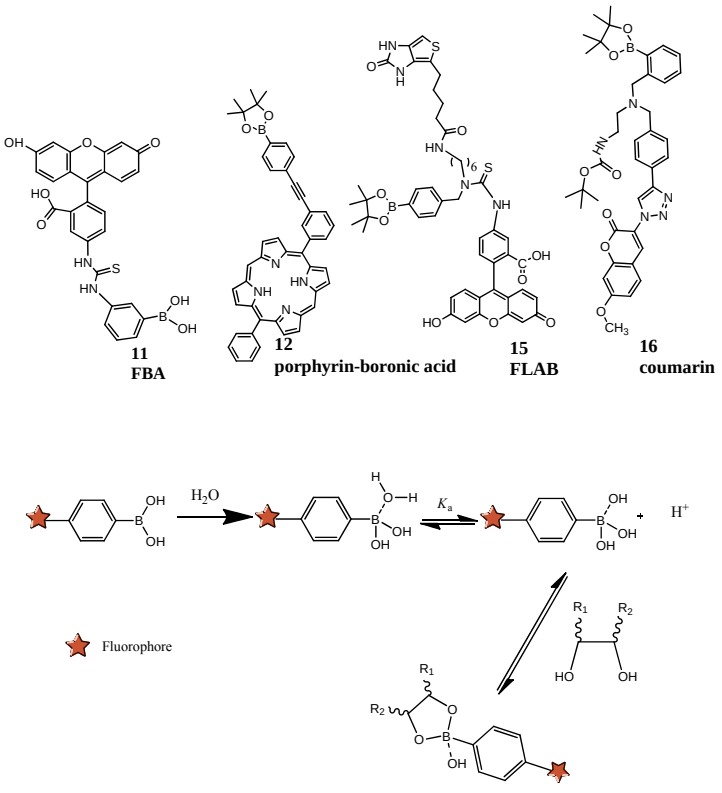

Scheme 5.1. Chemical structures of 4 boronic acid fluorophores (**11**: FBA; **12**: porphyrin-boronic acid. **15**: FLAB; **16**: coumarin) investigated in this chapter and the diagram of boronic acid fluorophore reversible binding with 1, 2-diol of glucan to form diol–phenylboronate complex with five membered ring.

There was virtually no fluorescence in control samples: glucan, glucan@SWNT, SWNT and solvent. The sequence of quenching efficiency was: PBS Buffer>DMSO> H2O. (Figure 5.10, Table 5.2) The final pH values of fluorophore@glucan@SWNT buffer, H_2O and buffer solution were 9.47, 7.04 and 11.24 respectively. Previous studies have shown that the borate ions form covalently-bonded complexes with 1,2-diol and 1,3-diol groups of the glucan at about pH 8-9.5 (Scheme 5.1). The binding constant of glucan with FBA (Compound **11**) was determined by fluorescence titrations as 4.53 $\times 10^3$ M^{-1} while for **12**, binding constant was 2.82 $\times 10^8$ M^{-1}. For compound **15**, the binding constant was 1.97 $\times 10^4$ M^{-1} whereas for **16** the binding constant was 3.0 $\times 10^6$ M^{-1} (Figure 5.9).

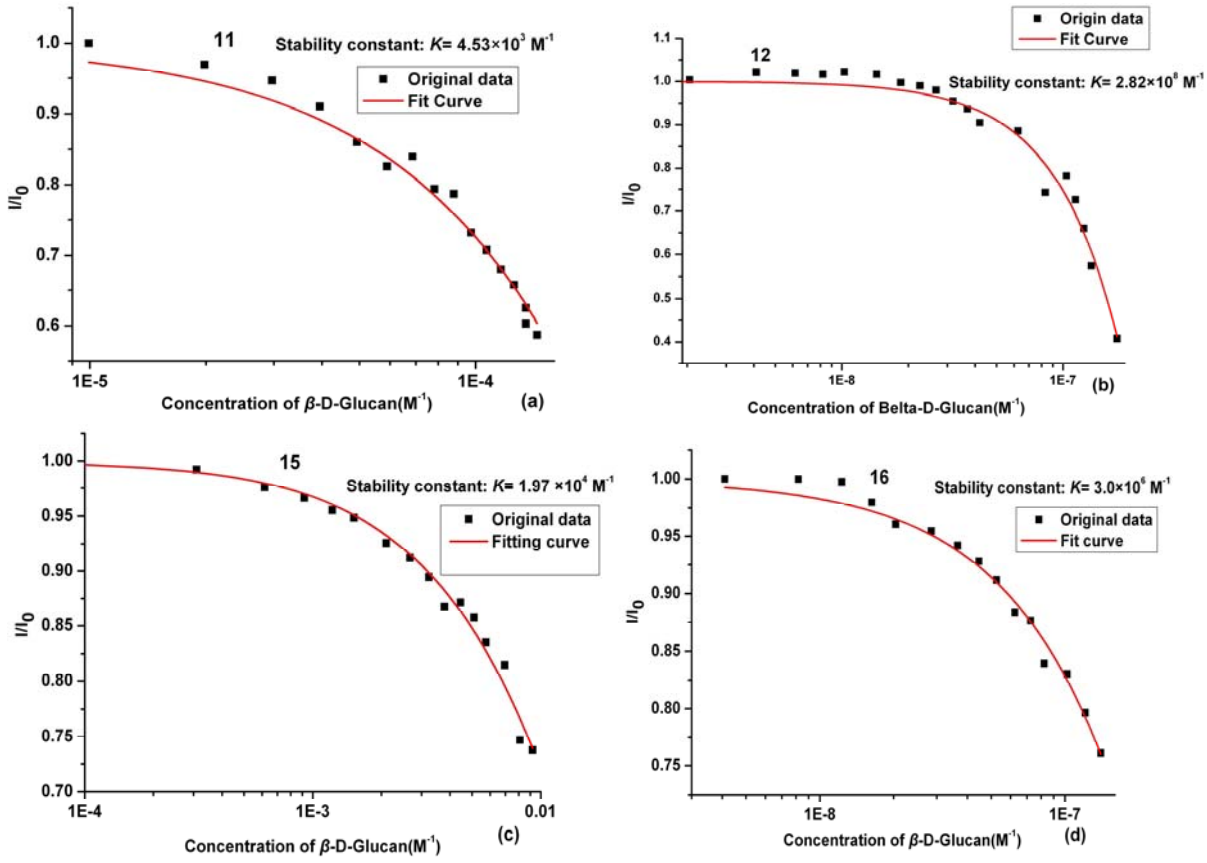

Figure 5.9. Relative fluorescence intensity versus glucan concentration profile of (**a**): **11** (25 μM, , λ_{ex} = 460 nm, λ_{em} = 543 nm), (**b**) **12** (33.7 μM, λ_{ex} = 490 nm, λ_{em} = 629 nm), (**c**) **15** (25 μM, λ_{ex} = 488 nm, λ_{em} = 514 nm) and (**d**) **16** (0.1 μM, , λ_{ex} = 350 nm, λ_{em} = 377 nm)in a pH 9.5 aqueous buffer.

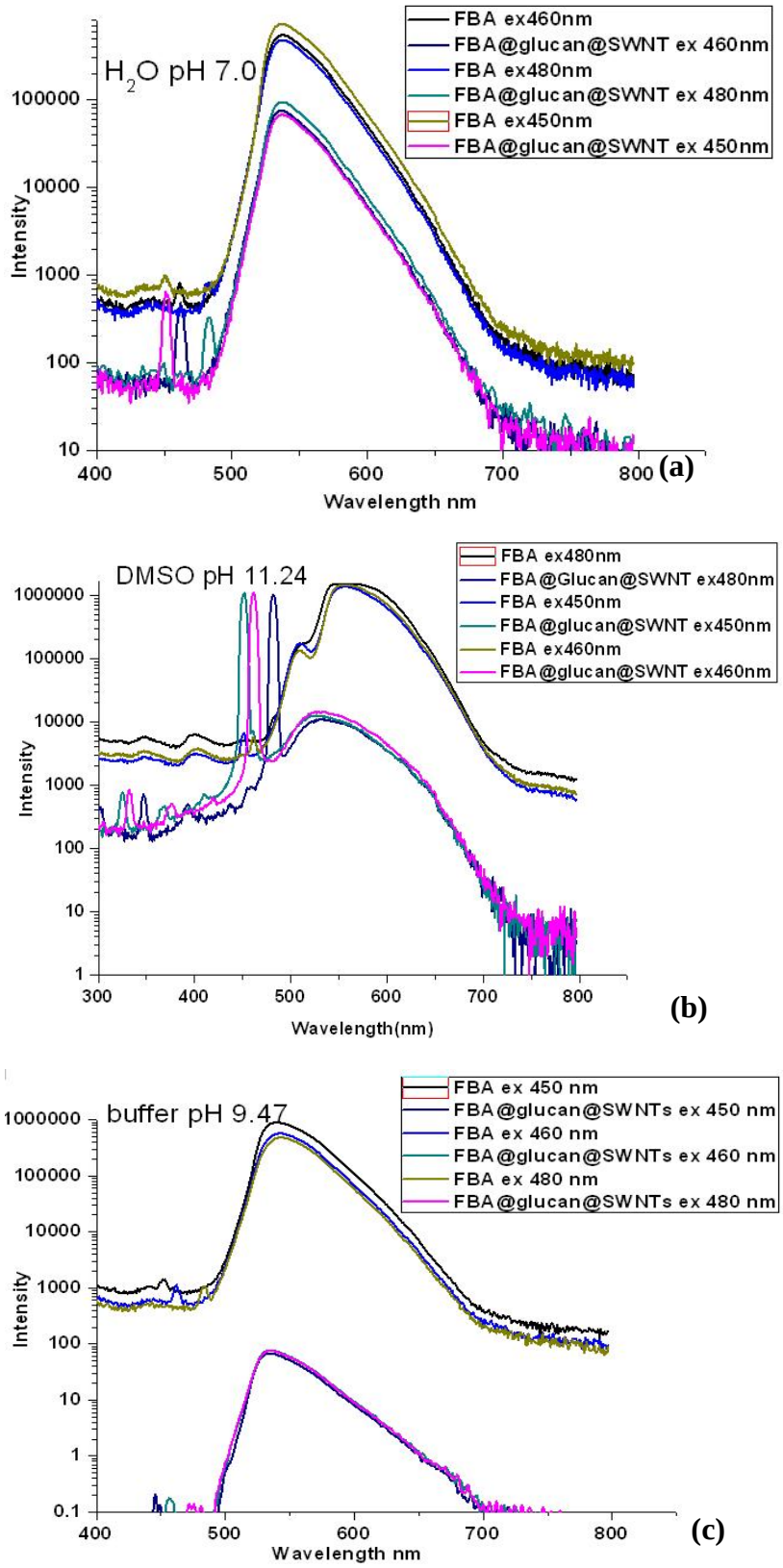

Figure 5.10. Overlay emission fluorescence spectra of free FBA and FBA@glucan@SWNT exciting at 450 nm, 460 nm and 480 nm in double-distilled H_2O (pH 7.0) (**a**), DMSO (pH 11.24) (**b**) and buffer (pH 9.5) (**c**) separately.

Table 5.2. Fluorescence intensity of FBA in FBA@glucan@SWNT solution and free FBA solution excite 450 nm, 460 nm and 480 nm

Solvent	*H_2O*			*Buffer*			*DMSO*		
Ex(nm)	450	460	480	450	460	480	450	460	480
FBA Intensity (AU,×10^5)	7.3	5.5	4.8	9	5.7	4.8	13.7	14.6	15.1
FBA@glucan @SWNT Intensity (AU,×10^4)	6.7	7.5	9.4	6.8×10^{-3}	7.7×10^{-3}	7.6×10^{-3}	1.3	1.5	1.1
Residual fluorescence percentage (%)	9.2	13.7	19.5	7.6×10^{-3}	1.35×10^{-2}	1.6×10^{-2}	0.9	1	0.72

*Each data point represents an average of three readings, errors were within 10% throughout.

Confocal imaging results (described below) confirmed that boronic acid fluorophore@glucan@SWNT can give sufficient residual emission to observe their uptake in cells using confocal fluorescence microscopy.

Multiphoton fluorescence imaging in solution and in vitro was used to characterise the resulting probe in vitro and in the solution phase. Interestingly, MCF-7 cells showed no uptake for both FBA@glucan and FBA@glucan@SWNT complexes: after rinsing the cells with PBS, any unbound FBA appeared to be just physically attached to the outer cell membrane. Imaging showed that FBA appears to stain the bottom glass of the commercial Petri dish (coated with polylysine) and seems to adhere strongly even after rinsing with PBS (see Appendix). Therefore, we replaced the fluorescent agent with the more hydrophobic systems FLAB, which incorporate a much longer alkyl chain. Simultaneously, this molecule was also designed to include a biotin tag for further cellular targeting possibilities.[55-59] Cell imaging shows the successful uptake of all probes in MCF-7 cells after incubation with FLAB, FLAB@glucan, and FLAB@glucan@SWNT (Figure 5.11). Bright-field imaging showed that black composites can be observed around the nucleus of MCF-7 cells for

FLAB@glucan@SWNT after 20 min incubation. This confirmed that the translocation of the composite into MCF-7 cells occured. Confocal fluorescence imaging of FLAB@glucan, and FLAB@glucan@SWNT showed that the glucan coating significantly enhances the cell membrane translocation of SWNTs. Presumably the glucan can efficiently attach to the cell membrane and lead to intracellular localization by recognising the cell membranes polysaccharides. The cellular uptake may be further mediated through the involvement of the biotin tag.[60]

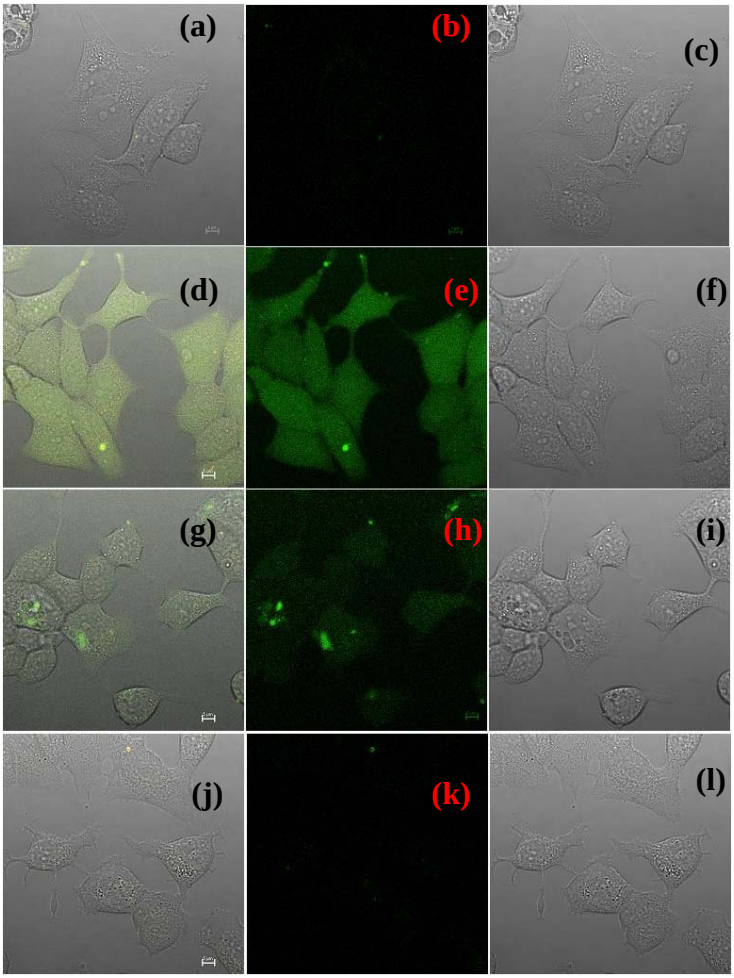

Figure 5.11. Fluorescent images of control (**a-c**), FLAB (d-f), FLAB tagged glucan (**g-i**), FLAB@SWNTs@glucan (**j-l**) in MCF7 cancer cells, (**a**) column represents a merged images of fluorescent images and non-fluorescent images, (**b**) column shows the fluorescent images excited at 488 nm and emission at 516-530 nm (**c**) bright-field images.

To explore the nano-hybrid integrity in cells we also used fluorescence-lifetime imaging microscopy (FLIM) using two photon excitation techniques. This allowed us to visualise FLAB, FLAB@glucan and FLAB@glucan@SWNT inside cells after uptake and probe their biodistribution. FLIM was performed using a confocal microscope (LSM 510, Carl Zeiss). A femtosecond mode locked Mira Ti:sapphire laser (Coherent Lasers Ltd) was tuned at 910 nm to generate two-photon luminescence from FLAB. The laser pulse has a repetition rate of 75 MHz and duration of less than 180 fs.

FLIM images are showed under the intensity images are from the same samples with different coded colors representing different lifetime scales. The lifetime of each pixel is obtained by applying a single or multiexponential fit; in this case a single exponential model was used. Figure 5.12 shows the lifetime emission maps for FLAB, FLAB@glucan and FLAB@glucan@SWNT in MCF-7 cells. Images are presented together with 2-photon intensity maps showing the spatial variations in fluorescence emission, the lifetime imaging maps and corresponding distribution plots for the predominant lifetime component (τ_1) and minor lifetime component (τ_2). Only one lifetime component of FLAB was found in cells after single exponential fitting, *i.e.* 2.24±0.64 ns, which is as expected for a fluorescein-derivative. Both FLAB@glucan and FLAB@glucan@SWNT showed two component lifetime in MCF-7 cells and the fitting proved significantly more complex. The major lifetime components for FLAB @glucan and FLAB@glucan@SWNT are much shorter, 0.697±0.14 ns (79.2%) and 0.567±0.16 ns (84.1%), as expected for a nanoparticle-bound fluorescein. The minor components for FLAB@glucan and FLAB@glucan@SWNT are 2.328±1.05 ns (20.8%) and 2.478±1.23 ns (15.9%) respectively, indicative of some minor dissociation of the fluorophor in cells.

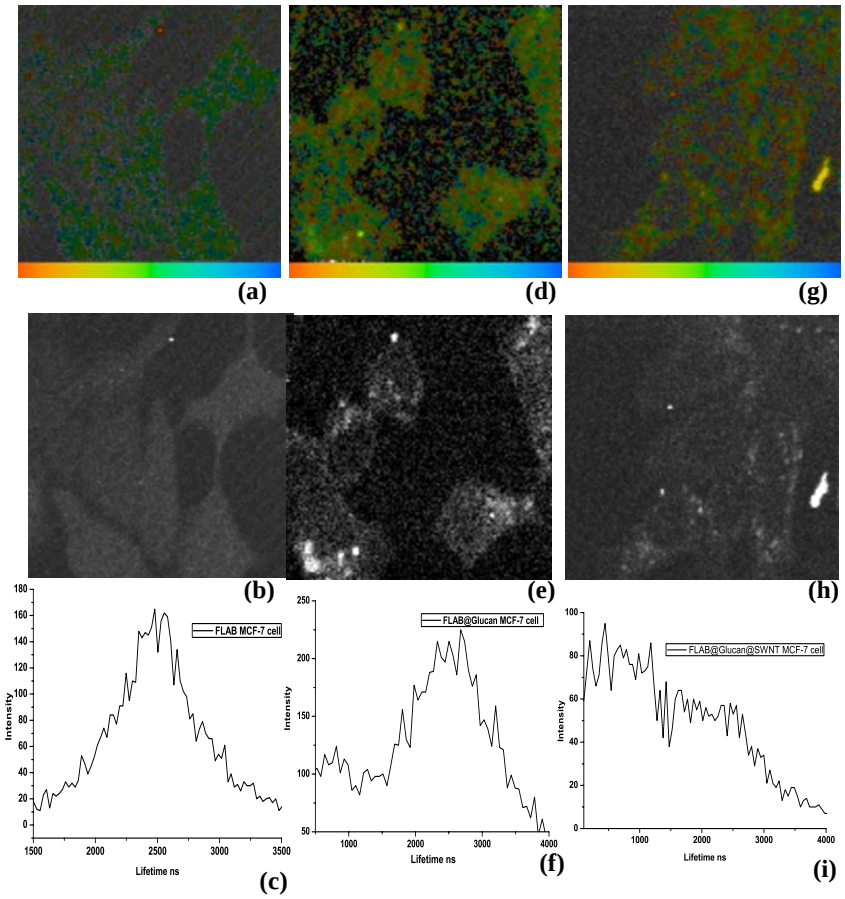

Figure 5.12. Two-photon laser confocal fluorescence (λ_{ex} = 910 nm):(**a-c)** Typical micrograph of MCF-7 cells incubated for 1 h at 37 ^{o}C with FLAB (26 μM or 21 μg/mL in 1: 99% DMSO EMEM) showing 2 just adhering onto the cell membrane but not entering into the cell, lifetime mapping(a), intensity image (**b**) and corresponding lifetime distribution curve (**c**); **(d-f)** Typical micrographs of MCF-7 cells incubated for 1 h at 37 ^{o}C with FLAB@glucan complex (dispersions in 1: 99% DMSO : EMEM contained 21 μg/mL NDI (26 μM) 'anchored' onto 35 μg/mL SWNT. lifetime mapping and scalebar (**d**), Intensity image (**e**) and corresponding lifetime distribution curve (**f**). Bright spots in cytoplasm region indicate that fluorescent FLAB@glucan complex translocated into cells as intact objects. **(g-i)** Typical micrographs of MCF-7 cells incubated for 1 h at 37 ^{o}C with FLAB@glucan@SWNT composite were recorded for dispersions in 1: 99% DMSO: EMEM. These contained 21 μg/mL NDI (26 μM) 'anchored' onto 35 μg/mL SWNT. Images show lifetime mapping and scalebar (**g**), intensity image (**h**) and corresponding lifetime distribution curve (**i**). The intensity image clearly shows that FLAB@glucan@SWNTs mainly concentrate in the cytoplasm region without nuclear uptake.

This data indicate there are at least two types of FLAB molecules present in cells, but that more than 80% of FLAB remains still bound to the glucan or glucan@SWNT hybrid. The differences of interactions of FLAB, FLAB@glucan and

FLAB@glucan@SWNTs with cellular local environments still need further investigation. There are several differences between the lifetime decay spectra profiles of free FLAB, FLAB@glucan and FLAB@glucan@SWNT and these were compared with the behaviour in solution. Figure 5.13 shows the fluorescence lifetime decay traces in PBS buffer: the long lifetime component decreased from 3.02 ns (71.6% weighting) in free FLAB in solution to 2.98 ns (77.9% weighting) in FLAB@glucan and to 2.65 ns (66.7% weighting) in FLAB@glucan@SWNTs, characteristic to the presence of fluorescein. But it was found that the short component lifetime increased from 6.08 ns (28.4% weighting) in free FLAB to 8.13 ns (22.1% weighting) in FLAB@glucan and 7.0 ns (33.3 % weighting) in FLAB@glucan@SWNTs. The decrease in fluorescence lifetime of FLAB confirmed the fluorescence quenching by glucan and glucan@SWNTs and also the successful binding of FLAB with glucan and glucan@SWNTs. It also indicates that glucan@SWNT has more quenching effect to FLAB than glucan alone. .

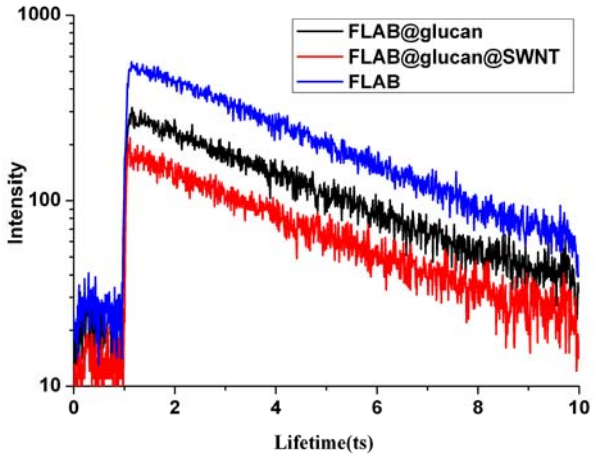

Figure 5.13. Two-photon fluorescence spectroscopy: fluorescence decay traces for the lifetime determinations (λ_{ex} = 910 nm, FLAB 26 µM, pH 8.2 buffer, FLAB@glucan complex dispersion containing 21 µg/mL FLAB (26 µM) anchored onto 35 µg/mL SWNT in pH 8.2 buffer, FLAB@glucan@SWNT complex dispersion containing 21 µg/mL FLAB (26 µM) anchored onto 35 µg/mL SWNT in pH 9.47 buffer).

5.2.5 PET Imaging tracer preparation by radioisotope filling using ^{64}Cu radioactivity encapsulation

The reactions described in Chapter 7 Experimental section using radioactive Cu in water were performed in order to determine the optimum protocol for encapsulation and glucan wrapping in order to formulate a radiotracer suitable for in vivo investigations.[38]

The procedure of preparation 5 samples ready for in vivo testing based on the sequence of addition glucan, radioactive $^{64}Cu^{2+}$ aqueous solutions (anchored onto NaOAc) and C_{70} is shown in Scheme 5.2 (Samples **a-e**).[38]

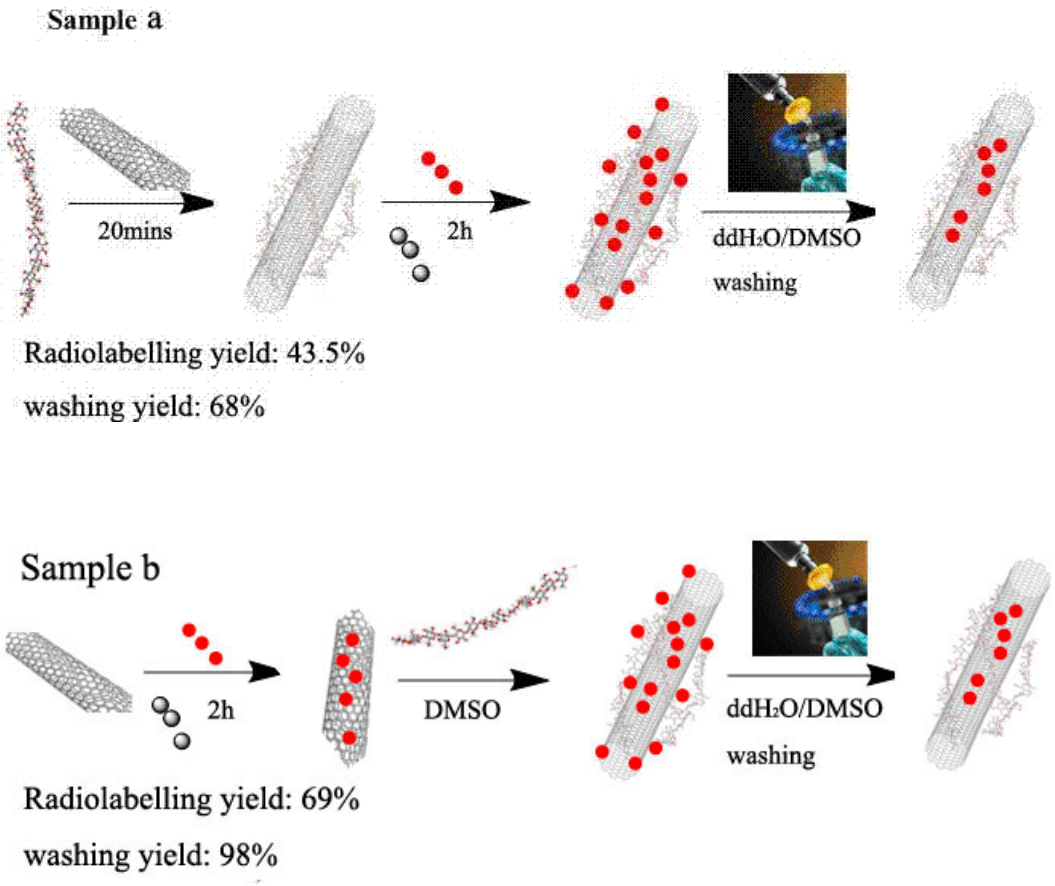

Sample c

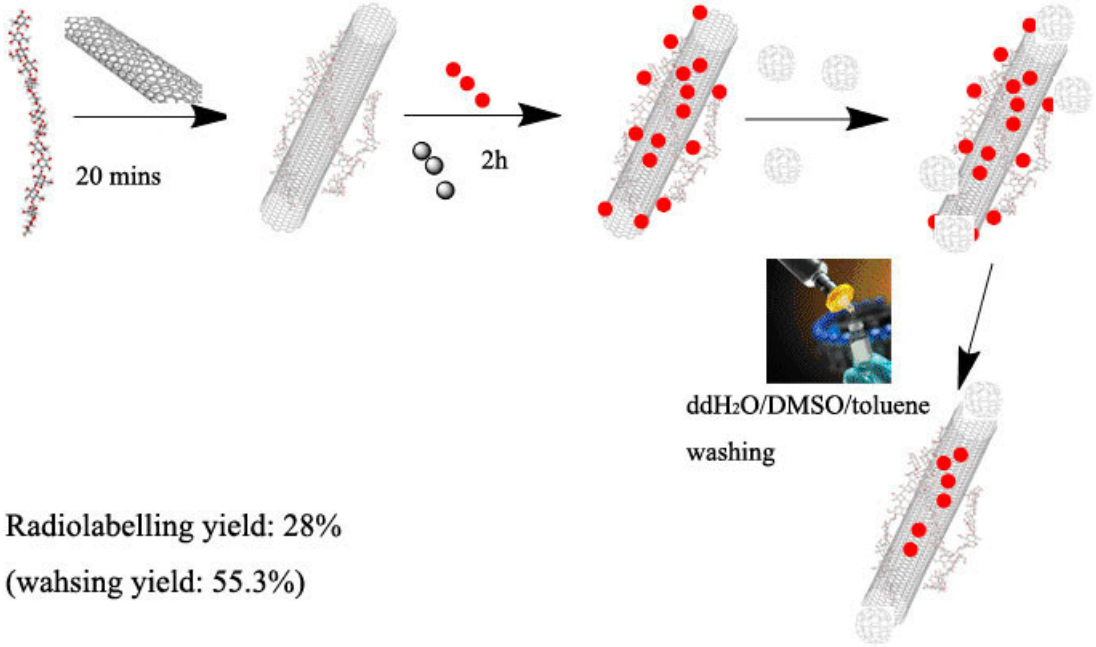

Radiolabelling yield: 28%

(wahsing yield: 55.3%)

Sample d

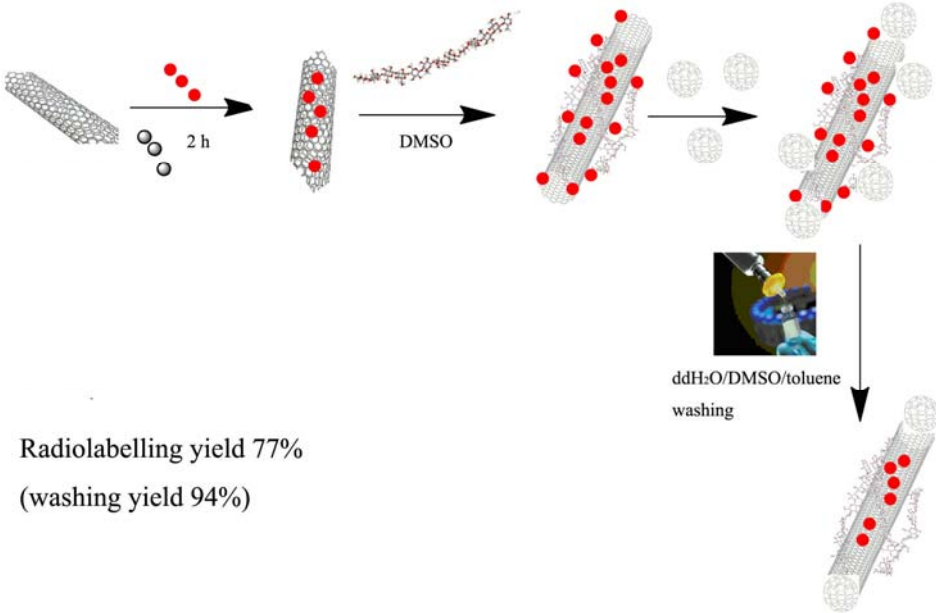

Radiolabelling yield 77%

(washing yield 94%)

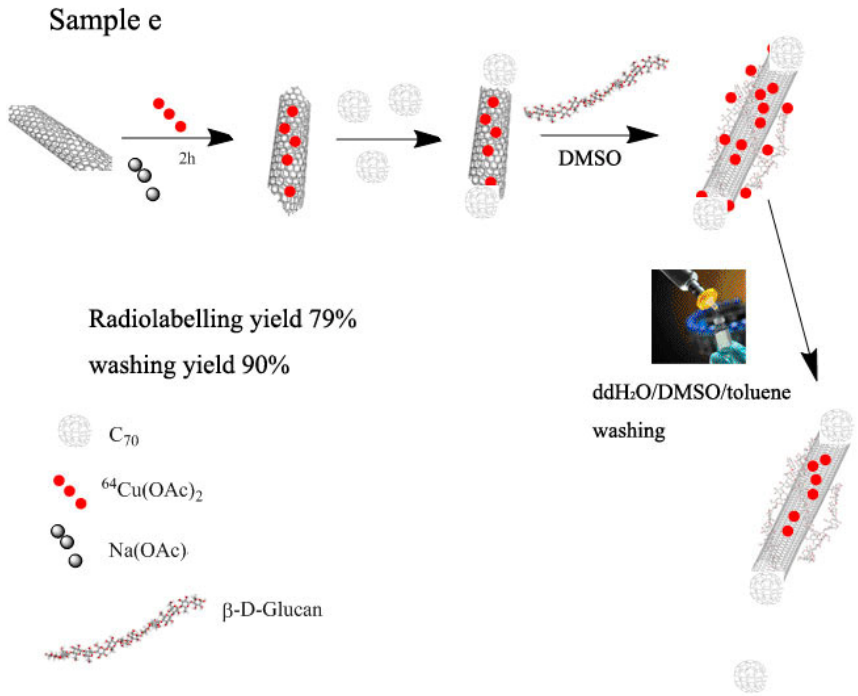

Scheme 5.2. Reaction diagram drawing of preparation of sample **a-b**, the conditions: glucan: 2 mg/mL in DMSO; SWNT: 0.5 mg/mL in H_2O; $^{64}Cu(OAc)_2$ (50 µL, about 10^{-9} M copper); NaOAc (10 mg); C_{70} (0.667 mg) suspended in 1 mL H_2O for each sample.

Table 5.3. Decay-corrected ^{64}Cu incorporation into glucan@SWNT complex using the encapsulation reaction routes **(a)-(e)**, $A = A_0 \times e^{-kt}$; k = ln2/ 12.7 h = 0.0546 (in h)

steps		Sample **a** (MBq)	Sample **b** (MBq)	Sample **c** (MBq）	Sample **d** (MBq）	Sample **e** (MBq)
Radio-reaction mixture		5.54	6.30	6.70	5.00	6.16
Filtration step:	solid	2.93	3.54	2.53	2.97	3.59
	solution	0.8	1.6	-	-	0.1
Toluene and H_2O wash:	solid	2.00	3.47	1.4	2.82	3.26
	solution	0.4	0.1	0.2	0.13	0.1
Estimated % ^{64}Cu associated with tubes at end of experiment		43 %	69 %	28%	77%	79%

*Each data point represents an average of three readings. Estimated errors are within 15%.
*One Bq is defined as one transformation (or decay) per second.

The order of ^{64}Cu radio-labelling efficiency was Sample **e** > Sample **d** > Sample **b** > Sample **a** > Sample **c** (Table 5.3). For Samples **b** and **d**, we performed the filling of SWNT with $^{64}Cu^{2+}$ aqueous solution first and adding *β*-D-glucan/DMSO for encapsulating with the ^{64}Cu radiolabeled SWNTs. The difference between samples **b** and **d** is that a slight variation in the C_{70} capping procedure was used for sample **d**. This induces a little increase of labelling efficiency compared with Sample 2 without C_{70} capping after glucan wrapping.

Sample **a** and **c** showed a lower radiolabelling efficiency than sample **d** and **b**. This could be due to encapsulating the SWNT with glucan before ^{64}Cu filling take place: glucan blocking both ends of the SWNT and reducing the filling efficiency. This result is in agreement with HRTEM experiments on glucan@SWNT in which a layer of glucan was clearly observed to coat an open end of a SWNT strand. (Figure 5.5 a) The results reveal that only 20 min interaction between SWNT and *β*-D-glucan can lead to more than 50% radioactivity retention even after the washing of the un-loaded radioisotope, and the highest radiochemical filling yield obtained can even reach 79%.

5.3 Conclusion to Chapter 5

We demonstrated the successful filling of SWNTs with Cu^{2+} (radiochemistry methods, using "hot" ^{64}Cu ions anchored onto NaOAc and also a "cold" optimised procedure for $Cu(OAc)_2$. Filling with other metal ions were also tested, for example $KReO_4$ (the 'cold' chemistry, as a model for $^{186/188}Re(V)$ radiotracers, of importance for radiotherapy and /or SPECT imaging or as a synthetic model for $^{99m}TcO_4^-$ for SPECT tracers encapsulation). The filling experiments with $Zr(OAc)_4$ in solution did not prove successful at normal pH but results were promising when pH was adjusted to *ca.* 2 using H_2SO_4. The filling efficiency of Cu^{2+} from a solution as the concentration of the metal salt is reduced to nano-molar

concentrations (by using 'hot' chemistry) and the radiochemistry yield has been optimised to above 70 %. Any significant leakage of metal ions from open SWNTs seems to be avoided by simultaneous encapsulation of C_{70} molecules at the ends of SWNTs. We also explore the functionalisation of SWNTs by the supramolecular wrapping the surface of SWNTs in aqueous media without affecting the electronic network with a naturally occurring glucan (*β*-1,3-1,4-D-glucan). The corresponding *in vivo* experiments by PET imaging are currently carried out at Wolfson Brain Imaging Center, Cambridge University by Dr. Franklin Aigbirhio.

Several boronic acid fluorophores were successfully synthesized and tested for the labeling of glucan@SWNTs by molecular recognition between boronic acids and *β*-D-glucan. Their cellular translocation behaviour and fluorescence properties were investigated by confocal fluorescence imaging and fluorescence lifetime imaging (FLIM). Both methods show that localization in sub-cellular (MCF-7 cells) regions and that the glucan coating significantly enhances the cell membrane translocation of SWNTs. This is likely due to the fact that glucans can be efficiently attached to the cell membrane by recognising cell membranes polysaccharides. The glucan coating can greatly mediate SWNTs' intracellular localization, and it appears to reduce the toxicity of carbon nanotubes. MTT assays showed that both *β*-D-glucan and *β*-D-glucan@SWNTs are biocompatible and have little cytotoxicity against fibroblast cells Fek-4.

5.4 References of chapter 5

(1) Ali-Boucetta, H.; Al-Jamal, K. T.; McCarthy, D.; Prato, M.; Bianco, A.; Kostarelos, K. *Chem. Commun.* **2008**, 459.

(2) Cai, W.; Chen, X. *J. Nucl. Med.* **2008**, *49*, 113S.

(3) Tian, J.; Bai, J.; Yan, X.-P.; Bao, S.; Li, Y.; Liang, W.; Yang, X. *IEEE Eng. Med. Biol. Mag.* **2008**, *27*, 48.

(4) Pascu, S. I.; Kuganathan, N.; Tong, L. H.; Jacobs, R. M. J.; Barnard, P. J.; Chu, B. T.; Huh, Y.; Tobias, G.; Salzmann, C. G.; Sanders, J. K. M.; Green, M. L. H.; Green, J. C. *J. Mater. Chem.* **2008**, *18*, 2781.

(5) Thamavaranukup, N.; Hoppe, H. A.; Ruiz-Gonzalez, L.; Costa, P.; Sloan, J.; Kirkland, A.; Green, M. L. H. *Chem. Commun.* **2004**, 1686.

(6) Bendall, J. S.; Ilie, A.; Welland, M. E.; Sloan, J.; Green, M. L. H. *J. Phys. Chem. B* **2006**, *110*, 6569.

(7) Ilie, A.; Bendall, J. S.; Kubo, O.; Sloan, J.; Green, M. L. H. *Phys. Rev. B: Condens. Matter* **2006**, *74*.

(8) Koo, O. M.; Rubinstein, I.; Onyuksel, H. *Nanomed. Nanotechnol. Biol. Med.* **2005**, *1*, 193.

(9) Kim, J.-W.; Shashkov, E. V.; Galanzha, E. I.; Kotagiri, N.; Zharov, V. P. *Lasers Surg. Med.* **2007**, *39*, 622.

(10) Liu, Z.; Li, X.; Tabakman, S. M.; Jiang, K.; Fan, S.; Dai, H. *J. Am. Chem. Soc.* **2008**, *130*, 13540.

(11) Liu, Z.; Peng, R. *Eur. J. Nucl. Med. Mol. Imag.* **2010**, *37*, S147.

(12) Xiao, Y.; Gao, X.; Taratula, O.; Treado, S.; Urbas, A.; Holbrook, R. D.; Cavicchi, R. E.; Avedisian, C. T.; Mitra, S.; Savla, R.; Wagner, P. D.; Srivastava, S.; He, H. *BMC Cancer* **2009**, *9*.

(13) Zhang, S.; Yang, K.; Liu, Z. *Sci China Chem* **2010**, *53*, 2217.

(14) Boghossian, A. A.; Zhang, J.; Barone, P. W.; Reuel, N. F.; Kim, J.-H.; Heller, D. A.; Ahn, J.-H.; Hilmer, A. J.; Rwei, A.; Arkalgud, J. R.; Zhang, C. T.; Strano, M. S. *Chemsuschem* **2011**, *4*, 848.

(15) Lin, S.; Keskar, G.; Wu, Y.; Wang, X.; Mount, A. S.; Klaine, S. J.; Moore, J. M.; Rao, A. M.; Ke, P. C. *Appl. Phys. Lett.* **2006**, *89*.

(16) Shi, D.; Guo, Y.; Dong, Z.; Lian, J.; Wang, W.; Liu, G.; Wang, L.; Ewing, R. C. *Adv. Mater.* **2007**, *19*, 4033.

(17) Zavaleta, C.; de la Zerda, A.; Liu, Z.; Keren, S.; Cheng, Z.; Schipper, M.; Chen, X.; Dai, H.; Gambhir, S. S. *Nano Lett.* **2008**, *8*, 2800.

(18) Liu, Z.; Tabakman, S. M.; Chen, Z.; Dai, H. *Nat. Proto.* **2009**, *4*, 1372.

(19) Kang, B.; Yu, D.-c.; Chang, S.-q.; Chen, D.; Dai, Y.-d.; Ding, Y. *Nanotechnology* **2008**, *19*.

(20) McDevitt, M. R.; Chattopadhyay, D.; Jaggi, J. S.; Finn, R. D.; Zanzonico, P. B.; Villa, C.; Rey, D.; Mendenhall, J.; Batt, C. A.; Njardarson, J. T.; Scheinberg, D. A. *Plos One* **2007**, *2*.

(21) McDevitt, M. R.; Chattopadhyay, D.; Kappel, B. J.; Jaggi, J. S.; Schiffman, S. R.; Antczak, C.; Njardarson, J. T.; Brentjens, R.; Scheinberg, D. A. *J. Nucl. Med.* **2007**, *48*, 1180.

(22) Chiu, C. F.; Dementev, N.; Borguet, E. *J. Phys. Chem. A*, *115*, 9579.

(23) Satishkumar, B. C.; Brown, L. O.; Gao, Y.; Wang, C.-C.; Wang, H.-L.; Doorn, S. K. *Nature Nanotechnology* **2007**, *2*, 560.

(24) Shi, D.; Guo, Y.; Dong, Z.; Lian, J.; Wang, W.; Liu, G.; Wang, L.; Ewing, R. C. *Adv. Mater.* **2008**, *20*, 1405.

(25) Britz, D. A.; Khlobystov, A. N. *Chem. Soc. Rev.* **2006**, *35*, 637.

(26) Pascu, S. I.; Arrowsmith, R. L.; Bayly, S. R.; Brayshaw, S.; Hu, Z. *Phil. Trans. R. Soc. A* **2010**, *368*, 3683.

(27) Chan, G. C.-F.; Chan, W. K.; Sze, D. M.-Y. *J. Hema. Oncl.* **2009**, *2*.

(28) Garg, A.; Sinnott, S. B. *Chem. Phys. Lett.* **1998**, *295*, 273.

(29) Liu, J.; Rinzler, A. G.; Dai, H. J.; Hafner, J. H.; Bradley, R. K.; Boul, P. J.; Lu, A.; Iverson, T.; Shelimov, K.; Huffman, C. B.; Rodriguez-Macias, F.; Shon, Y. S.; Lee, T. R.; Colbert, D. T.; Smalley, R. E. *Science* **1998**, *280*, 1253.

(30) Chiang, I. W.; Brinson, B. E.; Smalley, R. E.; Margrave, J. L.; Hauge, R. H. *J. Phys. Chem. B* **2001**, *105*, 1157.

(31) Tobias, G.; Shao, L.; Salzmann, C. G.; Huh, Y.; Green, M. L. H. *J. Phys. Chem. B* **2006**, *110*, 22318.

(32) Ballesteros, B.; Tobias, G.; Shao, L.; Pellicer, E.; Nogues, J.; Mendoza, E.; Green, M. L. H. *Small* **2008**, *4*, 1501.

(33) Hutchison, J. L.; Sloan, J.; Kirkland, A. I.; Green, M. L. *J. Electron Microsc. (Tokyo).* **2004**, *53*, 101.

(34) Xu, C. G.; Sloan, J.; Brown, G.; Bailey, S.; Williams, V. C.; Friedrichs, S.; Coleman, K. S.; Flahaut, E.; Hutchison, J. L.; Dunin-Borkowski, R. E.; Green, M. L. H. *Chem. Commun.* **2000**, 2427.

(35) Meyer, R. R.; Sloan, J.; Dunin-Borkowski, R. E.; Kirkland, A. I.; Novotny, M. C.; Bailey, S. R.; Hutchison, J. L.; Green, M. L. H. *Science* **2000**, *289*, 1324.

(36) Wilson, M.; Madden, P. A. *J. Am. Chem. Soc.* **2001**, *123*, 2101.

(37) Brown, G.; Bailey, S. R.; Sloan, J.; Xu, C. G.; Friedrichs, S.; Flahaut, E.; Coleman, K. S.; Hutchison, J. L.; Dunin-Borkowski, R. E.; Green, M. L. H. *Chem. Commun.* **2001**, 845.

(38) Yudasaka, M.; Ajima, K.; Suenaga, K.; Ichihashi, T.; Hashimoto, A.; Iijima, S. *Chem. Phys. Lett.* **2003**, *380*, 42.

(39) Brown, G. D.; Herre, J.; Williams, D. L.; Willment, J. A.; Marshall, A. S. J.; Gordon, S. *J. Exp. Med.* **2003**, *197*, 1119.

(40) Gantner, B. N.; Simmons, R. M.; Canavera, S. J.; Akira, S.; Underhill, D. M. *J. Exp. Med.* **2003**, *197*, 1107.

(41) Wasser, S. P. *Appl. Microbiol. Biotechnol.* **2002**, *60*, 258.

(42) Reynolds, J. A.; Kastello, M. D.; Harrington, D. G.; Crabbs, C. L.; Peters, C. J.; Jemski, J. V.; Scott, G. H.; Diluzio, N. R. *Infect. Immun.* **1980**, *30*, 51.

(43) Soto, E. R.; Caras, A. C.; Kut, L. C.; Castle, M. K.; Ostroff, G. R. *Journal of drug delivery* **2012**, *2012*, 143524.

(44) Taylor, P. R.; Brown, G. D.; Reid, D. M.; Willment, J. A.; Martinez-Pomares, L.; Gordon, S.; Wong, S. Y. C. *J. Immunol.* **2002**, *169*, 3876.

(45) Xia, Y.; Vetvicka, V.; Yan, J.; Hanikyrova, M.; Mayadas, T.; Ross, G. D. *J. Immunol.* **1999**, *162*, 2281.

(46) Numata, M.; Hasegawa, T.; Fujisawa, T.; Sakurai, K.; Shinkai, S. *Org. Lett.* **2004**, *6*, 4447.

(47) Bin Ibrahim, N.; Lawrence, K.; James, T. D.; Xia, F. J.; Pan, M.; Mu, S. C.; Mitchels, J. M.; Marken, F. *Sensor Actuat B-Chem* **2012**, *161*, 184.

(48) Kong, C.; Li, D. W.; Li, Y.; Partovi-Nia, R.; James, T. D.; Long, Y. T.; Tian, H. *Analyst* **2012**, *137*, 1094.

(49) Metola, P.; Anslyn, E. V.; James, T. D.; Bull, S. D. *Chem Sci* **2012**, *3*, 156.

(50) Shao, J. Y.; Sun, H. Y.; Guo, H. M.; Ji, S. M.; Zhao, J. Z.; Wu, W. T.; Yuan, X. L.; Zhang, C. L.; James, T. D. *Chem Sci* **2012**, *3*, 1049.

(51) Wu, Y. B.; Guo, H. M.; Zhang, X.; James, T. D.; Zhao, J. Z. *Chem-Eur J* **2011**, *17*, 7632.

(52) Elfeky, S. A.; Flower, S. E.; Masumoto, N.; D'Hooge, F.; Labarthe, L.; Chen, W. B.; Len, C.; James, T. D.; Fossey, J. S. *Chem-Asian J* **2010**, *5*, 581.

(53) Galbraith, E.; James, T. D. *Chem. Soc. Rev.* **2010**, *39*, 3831.

(54) Huang, Y. J.; Jiang, Y. B.; Bull, S. D.; Fossey, J. S.; James, T. D. *Chem. Commun.* **2010**, *46*, 8180.

(55) Fahrer, J.; Ng, D. Y. W.; Eisele, K.; Kuan, S. L.; Weil, T.; Barth, H. *Naunyn. Schmiedebergs Arch. Pharmacol.* **2012**, *385*, 25.

(56) Baugh, L.; Trong, I. L.; Cerutti, D. S.; Mehta, N.; Gulich, S.; Stayton, P. S.; Stenkamp, R. E.; Lybrand, T. P. *Biochemistry (Mosc).* **2012**, *51*, 597.

(57) Nguyen, T. T.; Sly, C. L.; Conboy, J. C. *Anal. Chem.* **2012**, *84*, 201.

(58) Du, L. Y.; Cheng, S.; Wang, S. H. *Lumin.* **2012**, *27*, 28.

(59) Lim, K. H.; Hwang, I.; Park, S. *Biotechnol. Progr.* **2012**, *28*, 276.

(60) Bradley, M.; Alexander, L.; Sanchez-Martin, R. M. *J.Fluo* **2008**, *18*, 733.

Chapter 6 Synthesis of thermally reduced graphene oxide and of its amino acid naphthalene diimide complex

6.1 Introduction

Graphene is one of the most exciting materials in recent years and this new material was discovered by Andre Geim and co-workers at the University of Manchester using the 'scotch tape method'. This has already switched on the new revolution in physics, chemistry and material.[1]

Graphene has a large theoretical specific surface area (2630 m^2 g^{-1}), high intrinsic mobility (200000 cm^2/Vs), high thermal conductivity (5000 $Wm^{-1}K^{-1}$), electrical conductivity, high Young's modulus (1.0 TPa) and also its advantageous optical transmittance (97.7%).[2]

All these properties determine that graphene has become considered as the next-generation material in the applications of nanoelectronic devices, transparent conductive films, fuel cells, electrical energy storage and also structural materials.

The popular approaches for producing graphene on a synthetic scale include mechanical exfoliation, chemical vapour deposition (CVD) and chemical or thermal reduction of graphite oxide.[3] The thermal reduction of graphite oxide method is considered not only the low-cost approach of mass-produced graphene but also the simple, non-chemical conversion of GO powder or film to graphene powder or film, respectively.[4]

Chemical reduction of GO, especially exposure to hydrazine in solution is the most widely used route to prepare reduced GO so far. However, the chemically reduced GO cannot reduce O atomic content efficiently.[5] The resulting material is still functionalised with O-residual groups on its aromatic surface.[6,7] Another disadvantage is hydrazine-treatment

forms nitrogen-functional groups with the toxicity of hydrazine.[8,9] Removal of the O-residual groups and N-functional groups could be carried out by either low temperature heating post-treatment (200-500 °C).[10,11] In comparison, thermal annealing reduction at high temperatures (900–1000 °C) is found to be an efficient route of producing graphene-like films with a significantly high C/O ratio, with no introduction of any residual groups on surface and do not need any toxic reagents.[12,13] However the thermal annealing treatment of GO is a very complex phenomenon because the thermal induced multi-step removal process of intercalated H_2O molecules and oxide groups of –COOH (carboxyl group), –OH (hydroxyl group), and >O (epoxy group).[14] Thermal reduced graphene produced in a wide range of organic solvent systems with the hydrazine derivatives can form very stable organic dispersions for at least 2 months.[15] The strong dispersibility of thermal reduced graphene in various of organic solvent is extremely useful for complex with other organic compounds or material with advantageous properties and applications of fabrication of organic-based composites then thin films. Inspired by our recent publication of interaction between SWNTs with amino acid tagged naphthalene diimide through a rapid, highly controllable supramolecular chemistry wrapping method,[16] we report here a novel and efficient approach of use thermal exfoliation and reduction of a graphite oxide (TRG) to complex with amino acid tagged naphthalene diimide through aromatic interactions.

6.2 Results and Discussion

In this work, graphene oxide (GO) was prepared using a modification of Hummers' method.[17] in a highly oxidising mixture of $KMnO_4$ /H_2SO_4 /KNO_3, oxygen functionalities such as hydroxyl, epoxide, carboxyl and other carbonyl groups were introduced on the edge and in the plane of the graphene sheet, resulting in good solubility of the GO in H_2O (Figure 6.1d). Digital photos of GO and steam thermal reduced graphene at 900 °C for 1 h clearly

showed that the colour of the GO suspension changed from yellow-brown in H_2O to black in $CHCl_3$ suggesting that the reduction of GO to graphene nanosheets has occurred.

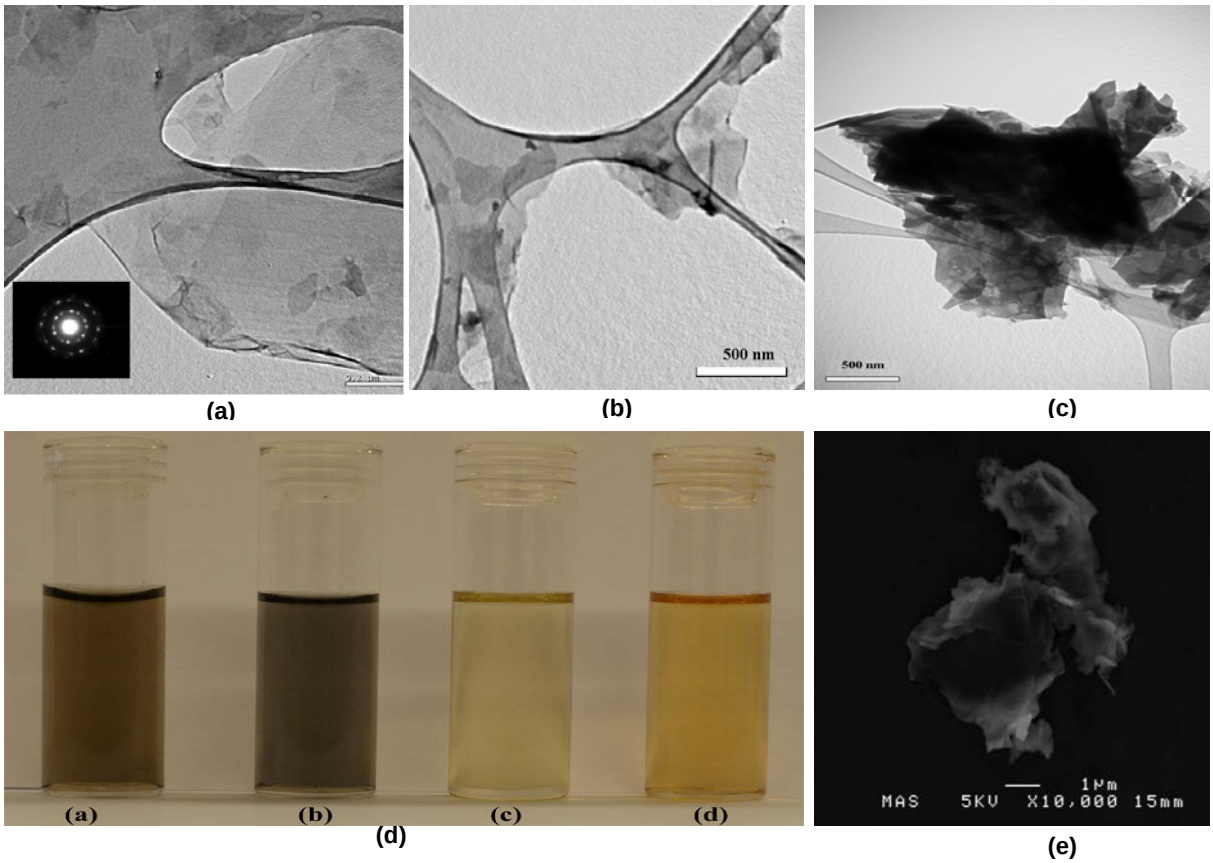

Figure 6.1. TEM images of (**a**) monolayer of graphene stacked with smaller flakes, image, scale bar =200 nm, the inset is SAED of GO; (**b**) annealing thermal treatment of GO in $CHCl_3$; (**c**) NDI@TRG after complex, several layer of TRG stacked with each other after complex with NDI; (**d**) digital photos of GO in H_2O(A), TRG in $CHCl_3$(B), NDI@TRG in $CHCl_3$ (C) and NDI in $CHCl_3$ (D); (**e**) SEM image of NDI@TRG in $CHCl_3$.

The thermal reducing of the GO was achieved by steam treatment at high temperatures (900 °C) generates graphene-like sheets (Scheme 6.1 and Figure 6.1b). Typical TEM images show that both GO and TRG are mono-layered or few-layered. TEM image of GO along with selected area electron diffraction (SAED) is shown in Figure 6.1a. The typical GO sheets can spread over a macroscopic region, and the SAED pattern indicates a crystalline structure, suggesting that the GO before reduction are not randomly oriented with respect to one another, and the interlayer coherence is not destroyed. The enormous differences between TRG and NDI@TRG in $CHCl_3$ are shown in Figure 6.1c and Figure

6.1b, in which clearly shows that after complex with NDI, TRG are less isolated and also form multi-layer NDI@TRG aggregate. Also the EDS measurements indicate that NDI successfully anchored on the graphene nanosheets compared with EDS spectrum of TRG.

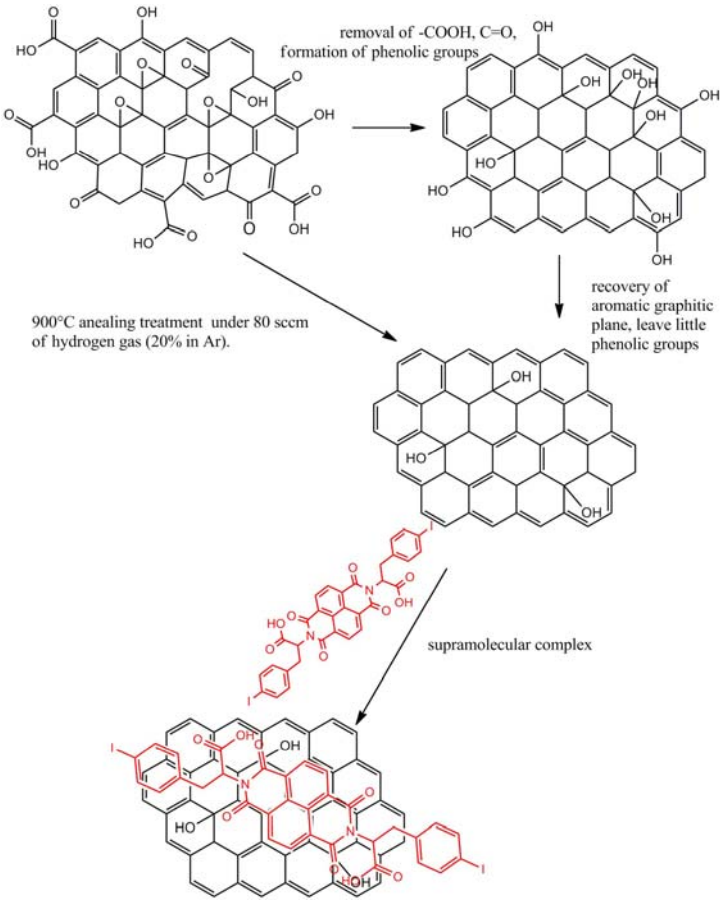

Scheme 6.1. Schematic diagram of the thermal reduce treatment of GO and TRG complex with NDI

The Raman spectra of graphite, GO and TRG are characterised by two prominent features (Figure 6.2)： a) the Brillouin zone-centered LO-phonon around 1590 cm^{-1}, named the G or graphite peak; b) the phonon peak around 1300 cm^{-1}, which corresponds to the double-resonance excitation of phonons close to the K point in the Brillouin zone, named the D or defect-induced peak.

The peak for GO (1591 cm^{-1}) at the G-band was up-shifted compared with that of graphite (1588 cm^{-1}). This was attributed to the presence of isolated double bonds that

resonate at frequencies higher than that of the G-band of the graphite. The G-band of TRG returned back to1588 cm^{-1}, which corresponds to the recovery of the hexagonal network of carbon atoms with defects. After thermal reduction, the Raman I_D/I_G intensity ratio of reduced GO is usually higher than the as-made GO, indicating an increase in the number of smaller graphene domains. In contrast, when our GO materials was reduced under 900 °C, the TRG showed an average I_D/I_G intensity ratio lower than that of the as-made GO (Table 6.1).

Since the Raman I_D/I_G intensity ratio is proportional to the average size of the sp^2 domains, the high temperature annealing actually increased the average size of the crystalline graphene domains in our GO.

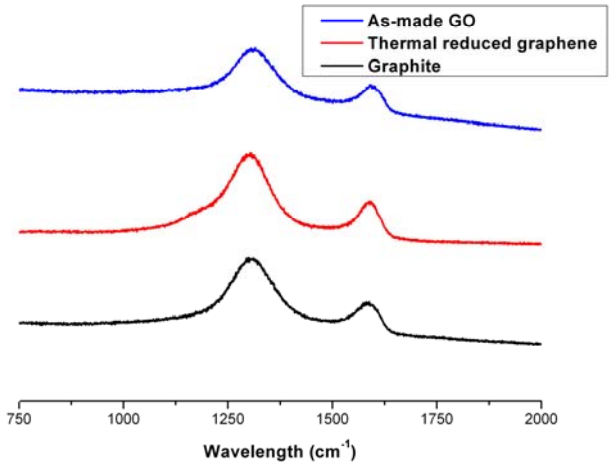

Figure 6.2. Raman characteristics of graphite, as-made GO and thermal reduced graphene (TRG).

Table 6.1. The percentage values of I_D/I_G ratios obtained by Raman spectroscopy

Samples	D band (cm^{-1})	G band (cm^{-1})	I_D/I_G
Graphite	1298	1588	3.31
As-made GO	1315	1591	3.05
TRG	1303	1588	2.78

FT-IR spectroscopic investigations confirmed the successful preparation of GO. Figure 6.3 shows the typical FT-IR spectrum obtained for three graphite materials. For GO, the broad, intense band at 3193 cm^{-1}, which corresponds to the O-H stretching vibrations

mode of intercalated water, the bands at 1717 cm^{-1} are due to C=O stretching vibrations from carbonyl and carboxylic groups, 1588 cm^{-1} corresponds to C=C skeletal vibrations from un-oxidised graphitic domains，1162 cm^{-1} corresponds to C-OH stretching vibrations and 1042 cm^{-1} corresponds to alkoxy groups. Thus, FT-IR spectroscopy provided evidence of the presence of abundant different types of oxygen functional on the graphite oxide material. The stretching vibrations of different types of oxygen functionalities in GO were significantly reduced (leaving a small peak at 2981 cm^{-1} corresponds C-H in aromatic ring) due to deoxygenation after thermal annealing treatment. The disappearance of characteristic peaks of oxygen functionalities groups in TRG indicates that such graphene oxides have been fully reduced to the graphene.

The FT-IR spectrum of NDI@TRG exhibits typical NDI absorption features, such as C=C-C of aromatic ring stretch(1450 cm^{-1}, 1484 cm^{-1}, 1580 cm^{-1}), C-N binding with aromatic ring (1335 cm^{-1}, 1246 cm^{-1}), C=O (1705 cm^{-1}), aromatic C-H out of plane bend (768 cm^{-1},881 cm^{-1},1006 cm^{-1},1177 cm^{-1}, 1246 cm^{-1}). These features confirm that the NDI has non-covalently been grafted with TRG sheet successfully.

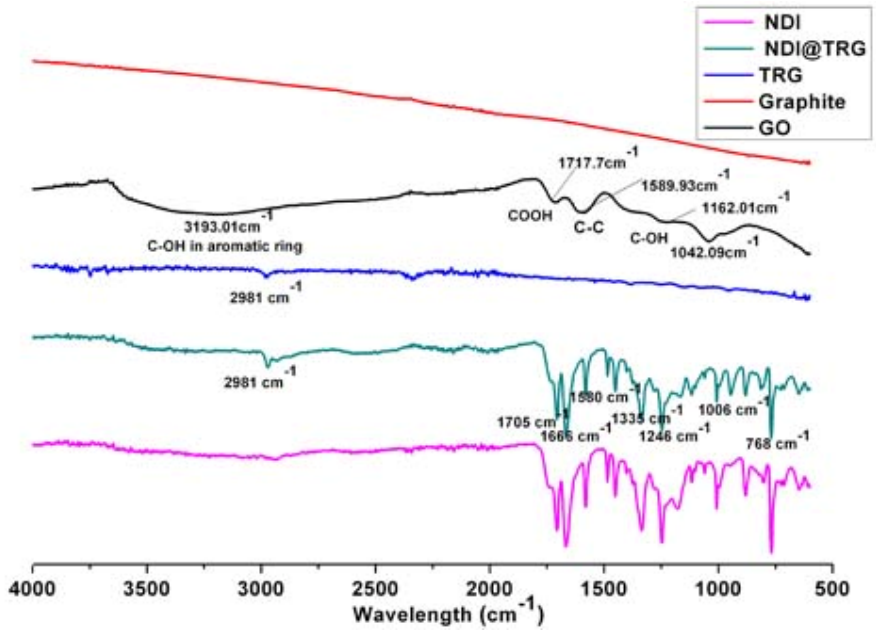

Figure 6.3. FTIR spectra of the graphite, GO, TRG, free NDI and NDI@TRG solids.

We have also examined the thermal stability of the prepared hybrids and compared it with that of pristine graphite and GO using thermogravimetric analysis (TGA). As shown in Figure 6.4 (blue line), the GO exhibits about 5.8 wt % loss below 100 °C and more than 70 wt % loss at 218 °C, resulting from the removal of the labile oxygen-containing functional groups such as CO, CO_2, and H_2O vapour. In contrast, the removal of the thermally labile oxygen functional groups by chemical reduction increased the thermal stability of graphene. It was shown a 30 wt % loss in a nitrogen atmosphere at 200 °C for the TRG (Figure 6.4 red line), which was much lower than that of the GO, indicating a decreased amount of oxygenated functional groups of TRG after thermal annealing treatment.

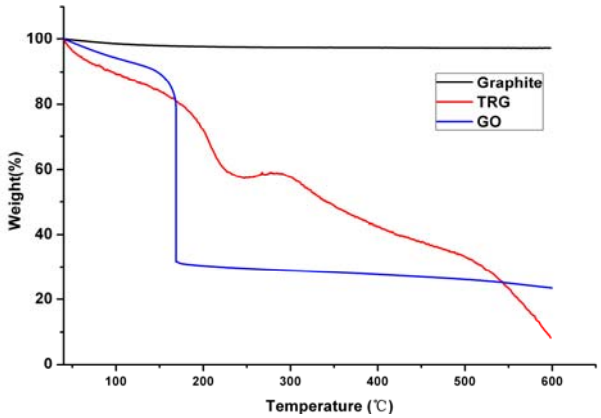

Figure 6.4. TGA curves of graphite (black), TRG (red) and GO (blue).

Fluorescence spectra of NDI show significant changes on the addition of TRG. The intensity of the fluorescence bands decrease markedly and the shape of peaks become broader with the increase in TRG concentration as illustrated in the Figure 6.5a. Such strong quenching of fluorescence of NDI by graphene can only be due to an excited state phenomenon since we do not observe ground state charge-transfer.

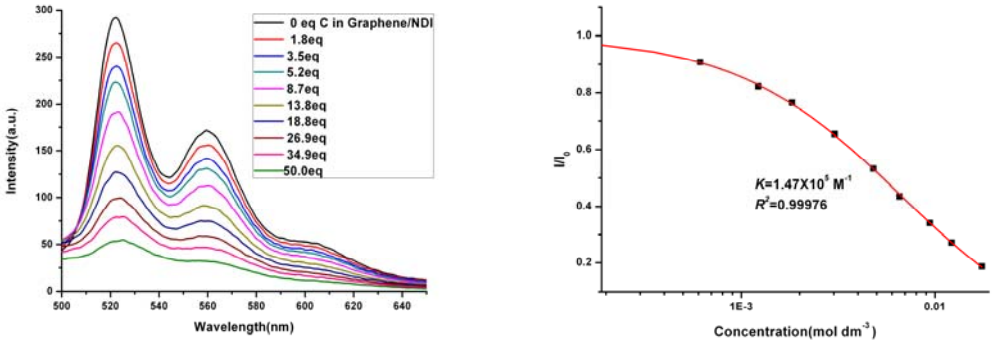

(a) **(b)**

Figure 6.5. (**a**) Fluorescence spectra of NDI recorded after the sequential addition of concentrated TRG accompanied by sonication 5 s and leave it 5 min for complete complex (molar fractions are given in the graph). (**b**) relative fluorescence intensity versus graphene concentration profile of NDI (1 μM, λ_{ex} = 488 nm, λ_{em} = 522 nm) in a $CHCl_3$ (1 mg/mL conc)

Two-dimensional fluorescence contour plotting for free NDI (Figure 6.6 a) and NDI@TRG (Figure 6.6 b, c) were recorded, respectively (excitation from 200 nm to 800 nm, emission from 200 nm to 800 nm) to investigate the excitation and emission behaviour differences of NDI before and after complex with TRG. Apart from the fluorescence peak of NDI, a strong Rayleigh scattering line is also observed from NDI 2D fluorescence contour plot (Figure 6.6 a), arising from the NDI dispersed in $CHCl_3$. After complexation of TRG with NDI in $CHCl_3$, it clearly shows that nearly most of free NDI was absorbed onto TRG, in which that free NDI peaks was disappeared in NDI@TRG contour plot. Also it shows that both the excitation wavelength and the emission wavelength of the peak maximum, experience a significant red-shift (excitation maximum wavelength moves from 250-350 nm to 400-450 nm, emission peak maximum wavelength moves from 350-450 nm to 450-550 nm). The plots also indicate that the intensity of NDI was severely quenched after complex with TRG. We postulate that these red-shifts and quenching of fluorescence occur as consequences of the adsorptive interaction between NDI with TRG through aromatic stacking.

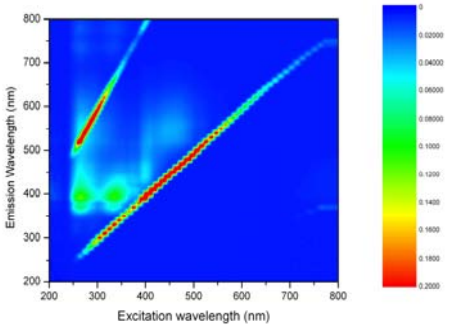

(a)

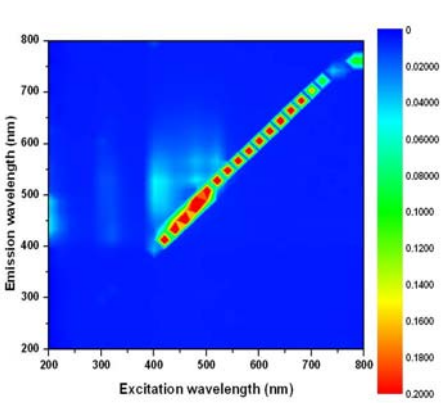

(b)

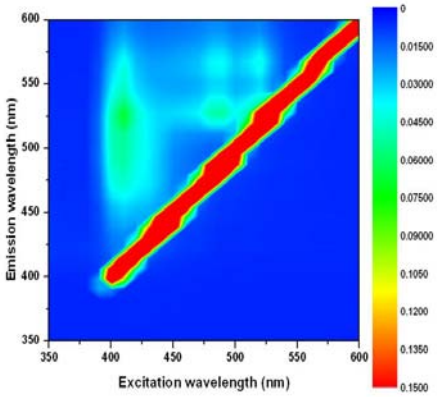

(c)

Figure 6.6. Two-dimensional fluorescence contour plots of (**a**) free NDI; (**b**) NDI@TRG; (**c**) Expansion of the NDI@TRG 2D fluorescence plot (Spectra recorded in $CHCl_3$).

Binding studies between TRG ("guest") with NDI ("host") were carried out by adding TRG stock solution in toluene (0.123 M, assuming that Mw of TRG is 1.48 mg/mL) to 2 ml NDI solution in fluorescent spectroscopy cuvette and leaving 5 minuets for the binding between "guest" and "host" completely then same volume of mixture was removed maintaining the total volume unchanged after each titration. Fluorescent spectra were recorded (λ_{ex}= 400 nm, λ_{em}= 522 nm) after each titration. The observed stability constants (*K*) with coefficient of determination (r^2) were calculated by the fitting of emission intensity at a single wavelength versus TRG concentration using custom written non-linear (Levenberg-Marquardt algorithm) curve fitting using Origin 8.0 software. Stability constants (*K*) determined by fitting a 1:1 binding model to I/I_0. The stability constant between TRG and NDI were calculated using equation (***1***) (see below). The curve from which the constant

was calculated is shown in Figure 6.5 b. TRG shows the fluorescence quenching effect to NDI with binding constant of $K = 1.47\times10^5$ M^{-1}.

$$I_F = (I_{F\min} - I_{F\max} \times K \times [guest]) / (1 + K \times [guest]) \qquad (\boldsymbol{1})$$

In Equation (***1***), $I_{F\ max}$ is the initial (maximum) fluorescence intensity, $I_{F\ min}$ is the final (minimum) fluorescence intensity, I_F is the fluorescence intensity for a particular guest concentration and K is the stability constant of the receptor with the guest.

6.3 Conclusion for Chapter 6

We studied the solution complexation of thermally reduced graphene with a naphthalene diimide to form a stable nanohybrid complex. Our observations and spectroscopic analysis confirm that making reduced graphene by thermal annealing is an important step leaving a more planar and clean aromatic surface for aromatic compound NDI stacking on. The efficient fluorescence quenching and significant red-shift of fluorescence of NDI was induced by the presence of the graphene-type material. The new complex was characterised by surface analysis (TEM and SEM), Raman spectroscopy, FT-IR and fluorescence microscopy. This complex will be useful for applications such as printable electronics, solar cells or future fuel lubricants.

6.4 References for chapter 6

(1) Geim, A. K.; Novoselov, K. S. *Nat. Mater.* **2007**, *6*, 183.

(2) Zhu, Y.; Murali, S.; Cai, W.; Li, X.; Suk, J. W.; Potts, J. R.; Ruoff, R. S. *Adv. Mater.* **2010**, *22*, 5226.

(3) Park, S.; Ruoff, R. S. *Nat. Nano.* **2009**, *5*, 309.

(4) Eda, G.; Lin, Y.-Y.; Miller, S.; Chen, C.-W.; Su, W.-F.; Chhowalla, M. *Appl. Phys. Lett.* **2008**, *92*.

(5) Compton, O. C.; Jain, B.; Dikin, D. A.; Abouimrane, A.; Amine, K.; Nguyen, S. T. *ACS Nano* **2011**, *5*, 4380.

(6) Stankovich, S.; Dikin, D. A.; Piner, R. D.; Kohlhaas, K. A.; Kleinhammes, A.; Jia, Y.; Wu, Y.; Nguyen, S. T.; Ruoff, R. S. *Carbon* **2007**, *45*, 1558.

(7) Bagri, A.; Mattevi, C.; Acik, M.; Chabal, Y. J.; Chhowalla, M.; Shenoy, V. B. *Nat. Chem.* **2010**, *2*, 581.

(8) Chen, W.; Yan, L.; Bangal, P. R. *J. Phys. Chem. C* **2010**, *114*, 19885.

(9) Fernandez-Merino, M. J.; Guardia, L.; Paredes, J. I.; Villar-Rodil, S.; Solis-Fernandez, P.; Martinez-Alonso, A.; Tascon, J. M. D. *J. Phys. Chem. C* **2010**, *114*, 6426.

(10) Wei, Z.; Wang, D.; Kim, S.; Kim, S.-Y.; Hu, Y.; Yakes, M. K.; Laracuente, A. R.; Dai, Z.; Marder, S. R.; Berger, C.; King, W. P.; de Heer, W. A.; Sheehan, P. E.; Riedo, E. *Science* **2010**, *328*, 1373.

(11) Gao, X.; Jang, J.; Nagase, S. *J. Phys. Chem. C* **2010**, *114*, 832.

(12) Eda, G.; Fanchini, G.; Chhowalla, M. *Nat. Nano.* **2008**, *3*, 270.

(13) Mattevi, C.; Eda, G.; Agnoli, S.; Miller, S.; Mkhoyan, K. A.; Celik, O.; Mostrogiovanni, D.; Granozzi, G.; Garfunkel, E.; Chhowalla, M. *Adv. Funct. Mater.* **2009**, *19*, 2577.

(14) Kim, C.-J.; Khan, W.; Park, S.-Y. *Chem. Phys. Lett.* **2011**, *511*, 110.

(15) Park, S.; An, J.; Jung, I.; Piner, R. D.; An, S. J.; Li, X.; Velamakanni, A.; Ruoff, R. S. *Nano Lett.* **2009**, *9*, 1593.

(16) Hu, Z.; Pantos, G. D.; Kuganathan, N.; Arrowsmith, R. L.; Jacobs, R. M. J.; Kociok-Koehn, G.; O'Byrne, J.; Jurkschat, K.; Burgos, P.; Tyrrell, R. M.; Botchway, S. W.; Sanders, J. K. M.; Pascu, S. I. *Adv. Funct. Mater.* **2012**, *22*, 503.

(17) Hummers, W. S.; Offeman, R. E. *J. Am. Chem. Soc.* **1958**, *80*, 1339.

Chapter 7 Experimental details

7.1 Instrumentation

7.1.1 Raman spectroscopy

Raman spectroscopy was performed at STFC CLF Facility in the Research Complex at Harwell using a Renishaw upright microscope using 830 nm for excitation, LWD objective 2 cm, operated at 50 × magnifications. Laser power magnification at the sample was 220 mW and spot size 100 micrometers.

7.1.2 Transmission electron microscopy (TEM) with energy dispersive X-ray (EDS) analysis

High resolution transmission electron microscopy (HR TEM) images were taken on a high resolution microscope JEOL 3000F coupled with EDS (point resolution, 0.16 nm) or a Jeol 4000F. Samples for HR TEM observation were ground and dispersed in EtOH and placed drop-wise onto a holey carbon support grid. A JEOL JSM-6500F instrument operating at 5 kV was used for scanning electron microscopic (SEM) measurements.

7.1.3 Ultrasonication

Ultrawave U-500 30 kHz or Agar Scientific S0080 Sonomatic 30 kHz, 80 W ultrasonic baths were used. It is recommended that the SWNTs used are sonnicated for no longer than 5 minutes followed by resting at the room temperature to avoid extensive fragmentation and tube damage.

7.1.4 Scanning electron microscopy (SEM)

All scanning electron microscopy (SEM) images and energy dispersive X-ray (EDS) spectra were obtained using a JEOL JSM-6500F field-emission SEM equipped with a JEOL EX-23000 BU EDS system.

7.1.5 Fluorescence lifetime imaging microscopy (FLIM)

Fluorescence lifetime experiments were carried out at the Rutherford Appleton Laboratory. Laser light at a wavelength of 580-630 nm was obtained from an optical parametric oscillator pumped by a mode locked Mira titanium sapphire laser (Coherent Lasers Ltd) producing 180 fs pulses at 75 MHz. this laser was pumped by solid state continuous wave 532 nm laser (Verdi V18, Coherent Laser Ltd). The oscillator fundamental output of 910 ± 2 was also used. The laser beam was focused to a diffraction limited spot through a water immersion ultraviolet corrected objective (Nikon VC ×60, NA1.2) and specimens illuminated at the microscope stage of a modified Nikon TE2000-U with UV transmitting optics. The focused laser spot was raster scanned using an X-Y galvanometer (GSI Lumonics). Fluorescence emission was collected without de-scanning, bypassing the scanning system and passed through a coloured glass (BG39) filter. The scan was operated in normal mode and line, frame and pixel clock signals were generated and synchronized with an external fast micro-channel plate photomultiplier tube used as the detector (R3809-U, Hamamatsu, Japan). These were linked via a Time-Correlated Single Photon Counting (TCSPC) PC module SPC830. Lifetime measurements were recorded using time correlated single photon counting with an excitation wavelength of 910 nm and measuring the emission at 360-580 nm.

Emission spectral detection was carried out using an Acton Research Component 275 spectrograph and an Andor iDus 740-BU CCD camera. The data included for each measurement the goodness of fit of the decay curves given by χ^2, the lifetime of each component and their respective weighting if more then one component was present. The χ^2 value of 1.0 indicates an optimal single exponential fit, whilst χ^2 value of more than 1.3 indicates an incomplete single exponential fit. As such, curves were subsequently fitted to two components. Lifetimes calculations were obtained using Becker and Hickl SPCImage analysis software.

7.1.6 Atomic Force Microscopy (AFM)

A Digital Instruments Multimode atomic force microscope (AFM) was used with a Nanoscope IIIa controller, operating in tapping mode with an 'E' scanner, having a lateral range of 12 μm and a vertical range of 3.5 μm. Silicon probes (Nascatec GmbH model NST-NCHFR), with resonant frequencies of approximately 320 kHz were used. X, Y, and Z calibration of the AFM was accomplished by scanning a 10 μm pitch 200 nm 3D reference from Digital instruments. The sample is dropped onto freshly cleaved mica surfaces using a Laurell Technologies WS-400 spin-coater (3000 rpm). The mica substrate was rinsed briefly with water, blow dry with air, and used for AFM imaging under the supervision of Dr Robert Jacobs (at Oxford University) and Dr John Mitchels (at Bath University).

7.1.7 UV/vis spectroscopy

Electronic absorption spectroscopy (UV/vis) was performed using a Perkin-Elmer Lambda 19 spectrometer, running UV Winlab software. Spectra were measured using 1.00 cm quartz cuvettes.

7.1.8 NMR spectroscopy

The NMR spectra were referenced to solvent and the spectroscopic solvents were purchased from Euriso-Top (C. E. Saclay). ^{1}H NMR data (300 MHz, 298K) are reported as follows: chemical shift in ppm on the δ scale, integration, multiplicity (s: singlet, d: doublet, t: triplet, q: quartet, dd: doublet of doublets, bs: broad singlet, bt: broad triplet), coupling constants (Hz) and assignment. TLC analyses were carried out using Merck silica gel 60 Å TLC plates. Column chromatography was performed on Breckland Scientific Supplies silica gel 60 Å (0.040-0.063 mm) for column chromatography.

7.2 Materials

Unless otherwise detailed, all chemicals and materials of the highest quality available were obtained from Aldrich or Agar. Carbon nanotubes (Elicarb) were provided by Thomas Swann Ltd (courtesy of Dr Marcello Motta) and further purified by standard stem purification methods.

7.2.1 Chemicals

Gases of the highest available purity were supplied by Air Products or BOC. High purity water was collected from a USF Elga water system with an output resistivity of 18.2 MΩcm. Otherwise, deionized water was obtained from the Inorganic Chemistry Laboratory (ICL) supply. 1-ethyl-3-(3-dimethylaminopropyl)carbodiimide (EDC, Fluka 03449) was stored at -18 ºC. Triethylamine (Et_3N, Sigma 471283) was dried with KOH.

7.2.2 Glassware

Glassware was cleaned by soaking in concentrated sodium hydroxide dissolved in isopropyl alcohol, then immersing in a dilute solution of hydrochloric acid, with water rinses after each soak. Finally, glassware was rinsed with acetone (lab grade) and allowed to dry.

Glassware used with solutions of 18.2 MΩcm water was cleaned with Decon® 90 surfactant and then washed extensively with 18.2 MΩcm water to remove surfactant. If drying was required, glassware was washed further with AR grade ethanol and blown dry with argon or nitrogen. Sterile containers (Sterilin), syringes, needles, and 0.20 μm syringe filters were also used with 18.2 MΩcm water.

7.3 Methods

7.3.1 TEM sample preparation

TEM samples were prepared by sonicating 0.1 mg of dried sample in 1-2 mL of EtOH and then depositing 3 drops of suspension onto copper grids (Agar) coated with holey carbon films.

7.3.2 Preparation of amino acid-tagged Naphthalenediimide functionalised Single Walled Carbon Nanotubes

7.3.2.1 Synthesis of NDI ((2S,2'S)-2,2'-(1,3,6,8-tetraoxobenzo[lmn][3,8]phenanthroline-2,7(1H,3H,6H,8H)-diyl)bis(3-(4-iodophenyl)propanoic acid)) (**1**) (Scheme 7.1)

1,4,5,8-Naphthalenetetracarboxylic dianhydride (200 mg, 0.746 mmol) and 4-iodophenylalanine (4.34 mg, 1.492 mmol) were suspended in 6 mL DMF in a pressure tight

8 mL microwave vial. To this suspension 0.2 mL dry Et_3N were added. The suspension was sonicated until the mixture became homogenous. The reaction mixture was heated for 5 min at 140 °C under microwave irradiation using a dedicated microwave reactor (CEM Discover). The solvent was removed under reduced pressure. The dark brown residue was taken up into CH_3CN (4 mL). This solution was added under stirring to 100 mL of 1M HCl. The resulting suspension was allowed to settle for 1 hour and then filtered using a Büchner funnel. The solid was then washed with 150 mL deionized water and dried *in vacuo*. The product was obtained in the form of a pale yellow solid in 87% yield.

^{1}H NMR (400 MHz, 1:1 $CDCl_3$:CD_3OD) δ(ppm): 8.63 (s, 4H, NDI-CH), 7.40 (d, J = 8.3, 4H, Ph-CH), 5.95 (dd, J_1 = 10.4, J_2 = 5.5, 2H, $C^{\alpha}H$), 3.61 (dd, J_1 = 14.4, J_2 = 5.5, 2H, $C^{\beta}H$), 3.45 (dd, J_1 = 14.4, J_2 = 10.4, 2H, $C^{\beta}H$); ^{13}C {^{1}H}NMR (100.61 MHz, DMSO-d_6) δ(ppm): 171.5, 163.1, 137.9, 137.4, 131.8, 131.6, 127.3, 126.8, 92.5, 55.0, 34.8. Mass spectrometry: Negative mode ES: *M/z* calcd: $C_{32}H_{20}I_2N_2O_8$ 813.9309 found: 813.9251 [M^-].

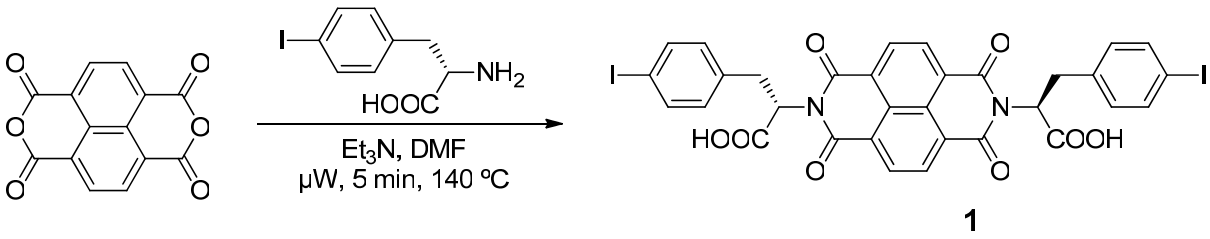

Scheme 7.1. Synthesis of iodine-derivatised NDI

7.3.2.2 Crystal structure determination

Single crystal X-ray diffraction data was obtained for NDI (Compound **1**) and tryptophan-derived NDI (Compound **9**). In both cases, crystals suitable for analysis were grown from THF layered with pentane (for Compound 1) or from DMSO:H_2O (for Compound **9**). In each case a typical crystal was mounted using the oil drop technique, in

perfluoropolyether oil at 150(2) K with a Cryostream N_2 open-flow cooling device. Single crystal X-ray diffraction data were collected using graphite monochromated Mo-Kα radiation (λ= 0.71073 Å) on a Nonius KappaCCD diffractometer.[1,2] The structures were solved by direct methods by using the program SHELXL97.[3] The refinement (on F^2) and graphical calculations were performed with the SHELXL97.[4] In general, coordinates and anisotropic displacement parameters of all non-hydrogen atoms were refined except where this was not possible due to the presence of disorder. Abbreviated crystal data and structure refinement parameters are included in below.

Compound **1**: NDI •2THF: $C_{40}H_{36}I_2N_2O_{10}$: M = 814.319, Z = 2, monoclinic P_{21} space group a = 12.7594(4)Å, b = 9.2119(3)Å, c = 16.3278(6)Å, β = 103.4340(10)º, U = 1866.63(11)Å^3, T = 150 (2) K, μ = 1.747 mm^{-1}, λ = 0.71073 Å. Of 28017 reflections measured, 8439 were independent (Rint = 0.0953). Final R = 0.0486 (6146 reflections with I > 2σ (I)) and wR = 0.0812.

Crystallographic data (excluding structure factors) for the structure reported in this paper have been deposited with the Cambridge Crystallographic Data Centre as supplementary publication no. CCDC.736937. Data can be obtained free of charge from The Cambridge Crystallographic Data Centre via http://www.ccdc.cam.ac.uk/cgi-bin/catreq.cgi.

Compound **9**: Try-NDI •3H_2O•3DMSO: $C_{36}H_{24}N_4O_8$, 3(C_2H_6OS), 3H_2O:

M = 911.02, Z = 4, orthorhombic P $_{21\ 21\ 21}$ space group, a = 8.6884(8) Å, b = 19.6749(18) Å, c = 25.149(2) Å, α=β=γ = 90º, U = 4299.06 Å^3, T = 150 (2) K, μ = 0.243 mm^{-1}, λ = 0.71073 Å. Of 35763 reflections measured, 6841 were independent (Rint = 0.065). Final R = 0.0529 (4973 reflections with I > 3σ (I)) and wR = 0.0569.

7.3.2.3 Computational methods

First-principles computational studies using density functional theory (DFT) were performed on a naphthalene diimide (NDI) molecule anchored onto a model single strand of a [10. 10] SWNT by Dr Navaratnarajah Kuganathan (UCL). All calculations were performed using the SIESTA code,[5] which solves the standard Kohn–Sham (KS) equations using numerical atomic orbitals (NAO) basis sets. The exchange–correlation term was modeled using the local density approximation (LDA) parameterized by Ceperley and Alder.[6] Standard norm conserving Troullier–Martins pseudopotentials were used to model the core electrons of carbon, nitrogen, oxygen, iodine and hydrogen.[7-10] The reference electronic configuration, cut-off radius and partial core cut-off radius for all pseudopotentials employed here are listed in Table 7.1. For nitrogen and iodine, a partial core correction was necessary to account for nonlinearity of the exchange and correlation potential between core and valence charge densities. The iodine pseudopotential was generated with scalar relativistic effects. To test the quality of the pseudopotential, comparisons were made with the eigenvalues and excitation energies of all-electron calculations on the same series of atomic configurations. The cross-excitation energies for both carbon and nitrogen pseudopotentials were not more than 0.09 eV, for oxygen and iodine were 0.06 eV and for hydrogen were 0.04 eV, indicating the excellent transferability of these pseudopotentials. The one electron Kohn–Sham eigenstates were expanded in a basis of strictly localized numerical atomic orbitals.[9] For carbon, nitrogen and oxygen, a double ζ basis set for the 2s and 2p valence states and a single ζ basis set for the 3d state were used. For iodine, a double ζ basis set for the 5s, 5p and 6p and a single ζ basis set for 5d and 6s orbitals were used. For hydrogen a double ζ basis set for 1s and a single ζ basis set for the 2p orbitals were used. Structure optimizations were performed using a conjugate gradient algorithm and the forces on the atoms were obtained from the Hellman–Feynmann theorem including Pulay corrections. For

all optimized geometries, the forces on the atoms were smaller than 0.06 eV $Å^{-1}$ and the stress tensor was less than 0.02 GPa. To represent the charge density a cut-off of 200 Ry for the real space grid integration was used in all calculations. We have used super cells with 25 Å and 45 Å vacuum spaces along the x, y and z directions for a NDI interacting with a model SWNT. A single k-point (Γ) was used for all calculations.

This modeling approach has been successful in earlier studies modeling the charge transfer in the gas phase for the interaction between porphyrins and C_{60} molecules and within the supramolecular structure of porphyrin@SWNT nanohybrids, whereby SWNTs acted as an acceptor molecule. Previously, a close agreement was obtained using this method between the experimental structure and the optimised geometry of the complex formed between C_{60} and a porphyrin host whereby the shortest C–C distances between porphyrin unit and C_{60} ranged between 3.27 and 3.71 Å compared with a range of experimental values of 3.35 to 3.67 Å.[11]

The binding energy between the NDI and the C_{60} or SWNT guest would be ideally described by the difference between the total energy of the C_{60} or SWNT@NDI composite and the total energies calculated for an isolated C_{60}/SWNT unit and an isolated NDI unit. Subtraction of the energy quantities of both C_{60}/SWNT and NDI unit from the composite with localized basis sets gives an uncorrected binding energy, $E_b(unc)$, defined by equation *(1)*

$$E_{b(unc)} = E_{C_{60}/SWNT\_NDI} - E_{NDI} - E_{C_{60}/SWNT} \qquad (1)$$

where $E_{C_{60}/SWNT\_NDI}$ is the total energy of C_{60} or SWNT complexed by the NDI and $E_{C_{60}}$ and E_{NDI} are the total energies of C_{60} (or SWNT) and an isolated NDI respectively. The error in binding energy due to basis set superposition errors (BSSE) can be high and must be corrected in DFT calculations employing localized basis sets. The true binding energy can be determined by the counterpoise correction (CP) method of Boys and Bernardi [12] using

''ghost'' atoms. The ''ghost'' molecule corresponds to additional basis wave functions centred at the atomic positions of C_{60}, SWNT or the NDI, but without any atomic potential.

$$E_{b(CP)} = E_{C_{60}/SWNT\_NDI} - E_{C_{60}/SWNT+NDIghost} - E_{C_{60}/SWNTghost+NDI} \qquad (2)$$

Table 7.1. Reference configuration and cut-off radii (a.u.) of the pseudopotentials used in this study.

Atom		C	N	O	I	H
Reference		$2s^2 2p^2 3d^0 4f^0$	$2s^2 2p^3 3d^0 4f^0$	$2s^2 2p^4 3d^0 4f^0$	$5s^2 5p^5 5d^0 4f^0$	$1s^2 2p^0 3d^0 4f^0$
Core radius (a.u.)	*s*	1.25	1.25	1.15	1.80	1.25
	p	1.25	1.25	1.15	1.90	1.25
	d	1.25	1.25	1.15	3.00	1.25
	f	1.25	1.25	1.15	2.10	1.25
Core cutoff (a.u.)		0.00	1.37	0.00	2.50	0.00

7.3.2.4 Cell culture (FEK-4, MCF-7 and HeLa) and fluorescence imaging

Cells were cultured at 37 °C in a humidified atmosphere of 5% CO_2 in air and split once confluence had been reached, using EMEM medium (Eagle's Modified Essential Medium) with foetal calf serum (FCS) (10% for HeLa and MCF-7 and 15% for FEK-4, 200 U mL^{-1} L-glutamine and 100 U mL^{-1} penicillin. The medium contained no fluorescent indicator dyes such as phenol red and was therefore suitable for use in fluorescence imaging studies. Samples for fluorescence imaging were prepared in the following way: surplus supernatant after culturing (containing dead cell matter and excess proteins) was discarded. The live adherent cells were then washed with two 5 mL aliquots of phosphate buffer saline solution

to remove any remaining medium containing FCS since this contains protease inhibitors which inactivate trypsin, thus inhibiting the resuspension of the cells. For re-suspension in solution, the cells were incubated in 3 mL of trypsin–EDTA (500 mg L^{-1} trypsin, 200 mg L^{-1} EDTA) solution for 5 min at 37 °C. After trypsinizing, fresh EMEM (15% FCS) was added to the suspended cells to give a sufficient concentration of cells (ca. 50000 cells/mL). The concentration of cells required varied slightly between cell lines and is chosen to be optimal for achieving sufficient coverage on the Petri dish for optimal imaging (between 40-60% coverage). The cells were plated in a Petri dish with a glass cover slip (Mattek) and left for 24 h to adhere before fluorescence imaging measurements were made. Final concentrations on cell plates used, in 1: 99 DMSO: EMEM, were: a) 21 μg/mL (26 μM) NDI; b) NDI@SWNT composite dispersion containing 21 μg/mL NDI (26 μM solution used to 'anchor' NDI onto 35 μg /mL SWNT); c) 35 μg /mL dispersion of free SWNT. Cells were incubated for maximum 2 h followed by washing prior to imaging. Cell viability prior to the experiment was tested by optical microscopy and MTT assays. The uptake of the NDI@SWNT composite was imaged by laser-scanning confocal microscopy (LSM 510 META, Zeiss) of live cells, as well as in fixed cells, using the 488 nm line of an argon ion laser for excitation. The emission was long pass filtered (515 nm) and detected with a photomultiplier tube (PMT). The intensity of the laser was modified to reduce the possibility of photo-bleaching of the fluorophore over time and the PMT voltage adjusted to be just above the auto-fluorescence limit of the starting conditions (for imaging of living cells) thus recording a background image before addition of compound, whilst maximizing sensitivity and ensuring optimal focusing. A similar standard procedure was used for imaging fixed cells, and for these an additional background image was collected (using fixed, but untreated cells) at the end of experiment. The confocal imaging of the cells using λ_{ex}=405 nm did not show significant fluorescence emission for either free NDI or NDI@SWNTs thus allowing

colocalization tests with nuclear staining dyes such as Hoechst or DAPI (Invitrogen). A strong fluorescence emission was observed in the green (515-530 nm) and red (605-675 nm) channels upon single-photon laser confocal microscopy using excitation with a green laser (488 nm). Upon incubation with the NDI@SWNT probe, formation of endosomes of ca. 0.5-1 μm seems to be suggested by both bright field and fluorescence imaging inside the cells' cytoplasm. The largest of NDI@SWNT aggregates (ca. 4 μm) did not appear to cross the outer membrane and remained attached to the outside membrane of the cell. After exposure to NDI@SWNT the cell membrane did not show any significant disruption or changes in morphology within 1 h incubation time at 37 °C. In contrast, when the experiment was repeated using either free NDI or pristine SWNT imaging showed that these distributed rapidly both inside the cells throughout the cytoplasm and in the nucleus and visibly altered the cell membrane morphology within 1 h of incubation.

7.3.2.5 Cell viability tests in FEK-4 and MCF-7 cell lines by MTT assays

Cell viability studies were carried out under conditions closely comparable with the imaging experiments. Stock solutions were prepared as follows: samples containing 42 μg NDI, 42 μg NDI anchored onto 70 μg SWNT (mass ratio NDI: SWNT = 0.6) and 70 μg purified SWNT were each treated with 2 mL $CHCl_3$: EtOH (4:1) and sonicated for ca 20 min. After sonication, the solvent was completely removed and 100 μL DMSO was added to each of the residues, followed by further sonication for ca 20 min. Aliquots from each of the stock solutions were added to EMEM and immediately added to the wells containing cells ready for treatment such that the final DMSO content in EMEM was 1%. The final concentration of the probes added to each well was: a) 42 μg free NDI, b) NDI@SWNT composite, formed by anchoring 42 μg NDI onto 70 μg SWNT and c) 70 μg SWNT, each dispersed in 100 μL solvent (1: 99 DMSO : EMEM). Two control groups were used consisting of 100 μL

solvent/well, i.e 1%: 99% EMEM, as well as 100% EMEM. FEK-4 and MCF-7 cell lines (cultured using standard procedures[13]) were incubated at 37 °C with the samples prepared as above for 1 h, 3 h, 6 h and 24 h. After incubation, wells were aspirated and solvents replaced by 100 μL of 0.5 mg/mL MTT (3-(4,5-dimethylthiazol-2-yl)-2,5-diphenyltetrazolium bromide) in EMEM:PBS 9:1, followed by a further incubation (at 37 ^{o}C) for 2 h.[14] The MTT solution was then aspirated and 100 μL of DMSO was added. Absorbance of resulting samples (directly proportional to cell viability) was measured at 570 nm using a plate reader. Cell viability (%) was estimated as [experiment group OD value] ×100 /[control group OD value].

7.3.2.6 Epifluorescence Microscopy

FEK-4 cells and MCF cells cultured in glass bottom dishes (0.1 million cells/dish) were incubated with NDI (42μg), SWNT(35μg) or NDI@SWNT(42μg@35μg).Fluorescence spectra were measured in a fluorescence spectrophotometer equipped with a xenon lamp (Nikon XB0 100, Tokyo, Japan) and a CCD camera Cool SNAP fx photometrics 193 (20 MHz, 1300 × 1030 pixels). The fluorescence ratio was recorded every 0.1 s using Lambda 10-2 Sutter Instrument (Nikon CO. Tokyo, Japan) and Fluorescence Analysis was performed with the Software Metafluor® 5.0.

7.3.2.7 MTT assays for MI_{50} determinations

The MI_{50} (24 h) of NDI, NDI@SWNT and SWNT was assessed following an adaptations of literature methods. Briefly, suspensions of 5 $\times 10^4$ cells/mL Fek-4 or MCF-7 cells were aliquotted into 96-well plates and incubated in triplicate with NDI (in concentrations ranging from 1×10^{-3} to 1 μmol/mL), NDI@SWNT prepared as above (in concentrations containing from 1×10^{-3} to 1 μmol/mL NDI keeping the mass proportion of

NDI and SWNT constant $R_{NDI/SWNT}$= 0.6) and SWNT (in concentrations ranging from 1 to 1000 μg/mL) for 48 h and analyzed using a 3-(4,5-dimethylthiazole-2-yl)-2-5-diphenyl tetrazolium bromide (MTT) assay. Three independent experiments were performed and MI_{50} was calculated. Software Origin 8.0 version was used to calculate the MI_{50} value. The mathematical model used for nonlinear curve fitting was a logistic fit.

Equation used: $y = A_2 + (A_1 - A_2)/(1 + (X / X_0)\text{^ } p))$ *(3)*

7.3.2.8 Calculate Fluorescence Quantum Yields of NDI

A comparative method to that Williams et al. was used for the determination of quantum yield (Φ),[15] It is based on the ratio of five experimentally determined values and characterised standard samples with known ΦF values are well characterised. It is an un-direct measurement. The standard sample should have the same excitation wavelength as the test sample to ensure standard sample absorb after excitation. If possible, standard sample emit in the same region to the test sample. Standard 10 mm path length fluorescence cuvettes were used for running the fluorescence measurements. Use $[Ru(bpy)_3][PF_6]_2$ (ruthenium trs-bipy) dionised solution as a reference sample. This compound has a quantum yield of 0.042. $[Ru(bpy)_3][PF_6]_2$ solution and samples must be measured on the same day otherwise it is not possible to compare the estimated Qys. UV/vis absorbance of Rubpy is below 0.06 for a standard.

The quantum yield (the ratio of photons emitted to photons absorbed) is calculated by the following expression;

$$\Phi_s = \Phi_r \times (\frac{D_s}{D_r}) \times (\frac{A_r}{As}) \times (\frac{I_r}{I_s}) \times (\frac{n_s}{n_r})^2 \qquad (4)$$

Φ = quantum yield

D = integrated area under emission peak (on fluorimeter)

s = sample

A = absorbance of solution at excitation wavelength

r = reference

n = refractive index of (pure) solvent

I = maximum intensity of emission peak

$[Ru(bipy)_3][PF_6]_2$ water solution was used as the reference material, where Φ_r = 0.042. Absorbance is calculated according to the Beer Lambert Law with $A=\varepsilon cl$ where ε= molar absorptivity of sample ($Lmol^{-1}cm^{-1}$ – from UV-Vis spectra, c= concentration ($molL^{-1}$) and l= path length (cm – cuvette dimension).

7.3.2.9 Staining for nuclear co-localisation studies

Cells were cultured using standard protocols, as described above, in EMEM. Prior to addition of the commercial co-localisation dye, cells were washed 5 times with PBS. Protocols adapted from *Invitrogen* were used throughout. Hoechst A stock solution of 100 μg mL^{-1} Hoechst 33342 (*Invitrogen*) was prepared in sterile MilliQ water. To 10 μL of the stock solution, a volume of 990 μL was added giving a final concentration of 1 μg mL^{-1}. After cells were incubated with this solution for 30 min a further 5 washings with PBS were carried out, before the addition of 2 mL of serum free medium (SFM). Subsequently, a small volume of SFM was removed (e.g. 10 μL) and compound in DMSO was added in equal volume to what was removed, to obtain a final volume of 1 mL and the desired concentration and 1% DMSO). After 2 h incubation with the compound cells were washed 3 times with PBS and fresh serum free medium was added (1 mL) and images were recorded immediately. A similar method was used for the DAPI staining, and cells were fixed prior to imaging using standard protocols and images were recorded immediately.

7.3.3 Synthesis of Bombesin-Naphthalenediimide conjugate functionalised Single Walled Carbon Nanotubes

7.3.3.1 Reagents

HPLC-grade water (Millipore); acetonitrile (ACN) (Sigma; cat. no. 34967-1L); HPLC-grade formic acid (Sigma; cat. no. 27001-500ML-R);

7.3.3.2 Equipment

250-μL HPLC vial (Dionex; cat. no. 6820.0029); Ultimate 3000 nano HPLC system (Dionex); Chromelon 6.7 software (Dionex); C18 PepMap100 solid-phase extraction μ-Precolumn cartridge (particle size 5 μm, pore size 100 Å, 300 μm inner diameter) (Dionex; cat. no. 160454); Nano-column PepMap C18 reversed-phase material (particle size 3 μm, pore size 100 Å, 75 μm inner diameter) (Dionex; cat. no. 160321);

7.3.3.3 Reagent setup

Solution A 0.01% formic acid (wt/vol) in water; **Solution B** 0.01% formic acid (wt/vol) in CH_3CN

7.3.3.4 Semi-preparative HPLC system

HPLC system Chromatographic system: UltiMate 3000 LC system was used for separate sample. Injection system: FAMOS μ–autosampler equipped with a 500 μL sample loop, a user-defined injection method was used. HPLC detection system: UltiMate UV Detector, 3 μL flow cell, 214-nm detection wavelength. Separation column: PepMap C18,

75 μm ID ×150 mm length, 3 μm particle size, 100 Å pore size. Mobile phase for column: 95 % 0.01% water; 5 % CH_3CN. Loading solvent for HPLC is DMSO. RP-column flow rate: 0.300 μL min^{-1}. Load sample to a Pepmap C18 Precolumn from 0 min to 30 min, switch on the collector from 8 min to 18 min.

7.3.3.5 Flow gradient for semi-preparative HPLC

The initial proportion of **B** was kept at 5 % (v/v). (Figure 7.1) The **B** was successively increased up to 95 % (v/v) from 0 to 7.5 min. The **B** proportion was kept at 95 % (v/v) for 9 min (from 7.5 min to 16.5 min) in order to appropriately separate compounds **5** and **11**. After that, the proportion **B** was successively decreased back to 5 % (v/v) from 16.5 min to 30.0 min. During the whole procedure, the flow rate was maintained 2 mL/min.

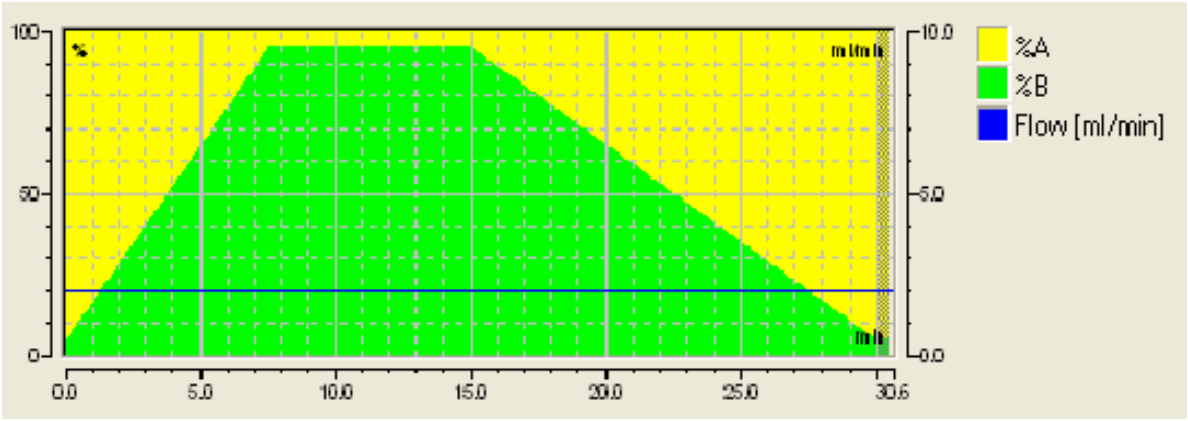

Figure 7.1. Detail of elution and flow-rate gradient.

7.3.3.6 Synthesis of bombesin [7-13] peptide (2) (Scheme 7.2)

The bombesin (Gln-Trp-Ala-Val-Gly-His-Leu-NH_2) [7-13] peptide sequence was made by SPPS (Solid Phase Peptide Synthesis), involving the coupling of coupled fluorenylmethoxycarbonyl (Fmoc) amino acids onto Rink Amide Resin. Leucine, glycine, alanine and valine were used unprotected, Fmoc-Leu-OH, Fmoc-Gly-OH, Fmoc-Ala-OH and Fmoc-Val-OH. The side chain functional group of histidine and glutamine were protected

by trityl and tert-butoxycarbonyl(Fmoc-His(Trt)-OH, Fmoc-Gln(Boc)-OH)and tryptophan protected by tert-Butyloxycarbonyl, Fmoc-Trp(Boc)-OH. The first amino acid Fmoc-Leu-OH coupling onto resin is normally the hardest to attach and hence as a precaution the HOBt/DIC coupling method was used**.** But for the next amino acids coupling, HBTU and DIPEA were used. Deprotection of the Fmoc group was achieved by 3×3 min treatment with 20% piperidine in DMF and then washed by 3× DCM and 3×DMF. A Kaiser-test was used for confirming the free amine after deprotection which the beads should turn blue. After all amino acids were coupled to this sequence, peptide can be cleaved from resin and also amino acid protective groups can be deprotected by mixing resins with a cocktail of TFA/TIS/water 95:2.5:2.5 in a round-bottom flask stirring 3 h. The solution then was filtrated and filtration liquid was collected and evaporated. Dichloromethane was added to the product and extracted with double-distilled H_2O 3 times. The aqueous layer is recovered and evaporated again. The product was then freeze-dried and stored in the fridge for further analysis. The white powder after freeze-drying was analyzed by mass spectroscopy:

ESI/MS: *m/z* 809.44 $[M + H]^+$, 405.38 $[M +2H]^{2+}$

HPLC Rt: 5.35 min. **(**flow gradient, see section 7.3.3.5)

7.3.3.7 Swelling the resin

The resin, Rink Amide MBHA, is swelled in the peptide vessel, using DCM, for 20 min.

7.3.3.8 Deprotection

The deprotection was achieved by washing resin with a solution of 20% piperidine in DMF 4 × 4 min. Then the resin was washed by 4 ×DMF and 4 × DCM.

7.3.3.9 Kaiser-test

The Kaiser test is a qualitative test for monitoring deprotection in solid phase peptide synthesis[16]. The test is based on reaction of Ninhydrin (2,2-Dihydroxyindane-1,3-dione) with primary amines can give a dark blue colour. A small amount of beads are taken and deposed in a small vial. Then several drops from ninhydrin (5%, w/v) in ethanol, phenol (4:1, w/v) in ethanol and potassium cyanide (2%, v/v, of a 1 mmole/liter aqueous solution) in pyridine are taken separately and added to vial. Then the vial was heated by heating gun. If the beads turn dark blue, then there is a free amine present, confirming deprotection was successful. If the beads are still colorless, then the deprotection failed and procedure needs to be repeated.

7.3.3.10 Coupling

A mixture of the amino-acid (3 eq), coupling reagent (3 eq) and the base (6 eq) in DMF was added to the resin. For the first amino acid Leucine was coupled to resin by standard HOBt/DIC coupling. For the next amino acids, HBTU and DIPEA were used.

7.3.3.11 Loading efficiency of the fist amino acid to the resin

The loading efficiency of the fist amino acid to resin is very important to the last product field. We calculated the loading efficiency of the first amino acid based on the Beer-Lambert law:

$$A = \varepsilon l C \qquad (5)$$

Where **A** is the absorbance, **ε** the absorption coefficient, which is 3800 for Fmoc-H, **C** is the concentration and **l** the path length of UV cuvette, which is 1 cm.

The concentration of Fmoc- first amino acid was calculated and compared to the theoretical loading.

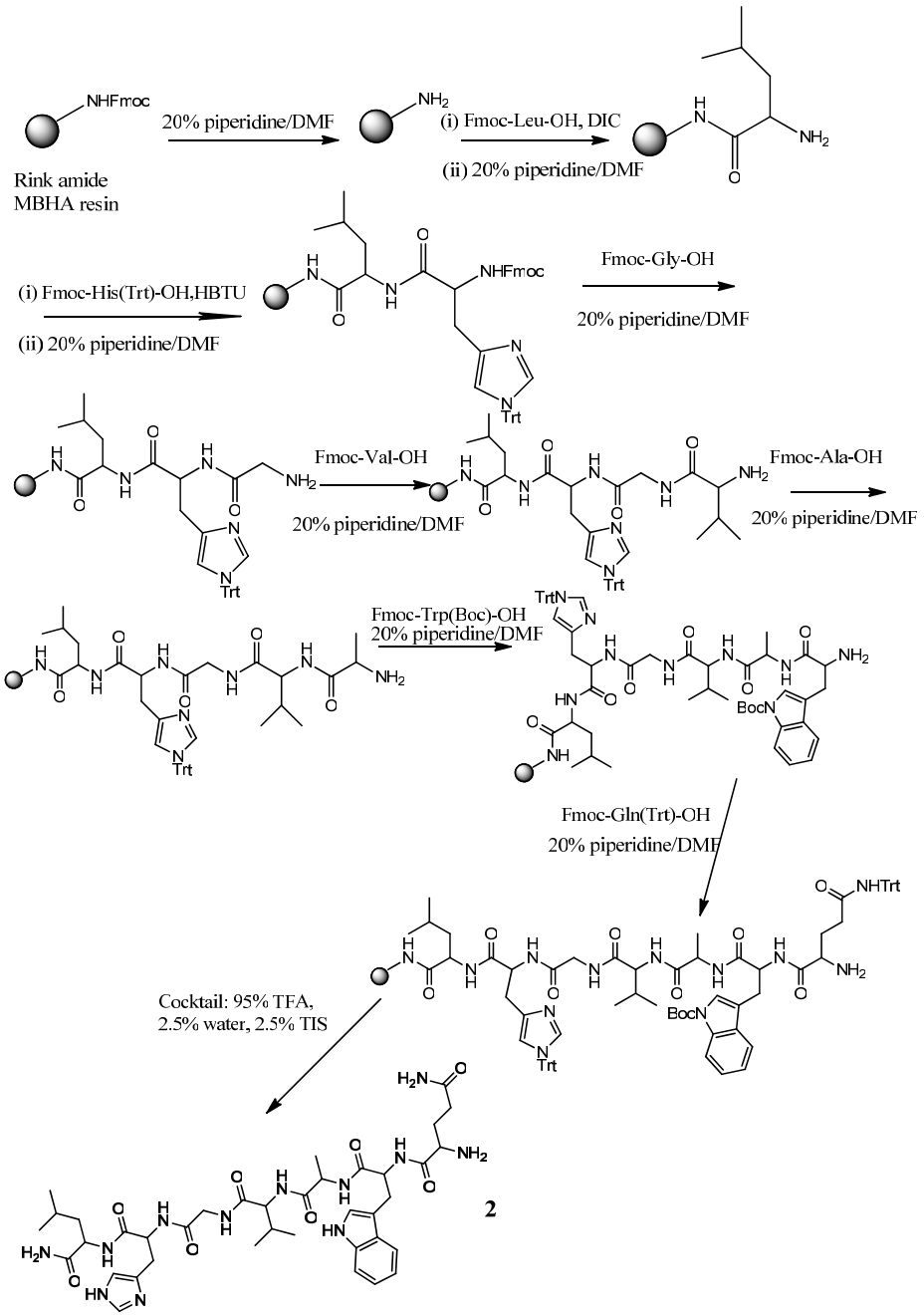

Scheme 7. 2: Procedure for the synthesis of bombesin[7-13]: Gln-Trp-Ala-Val-Gly-His-Leu-NH_2

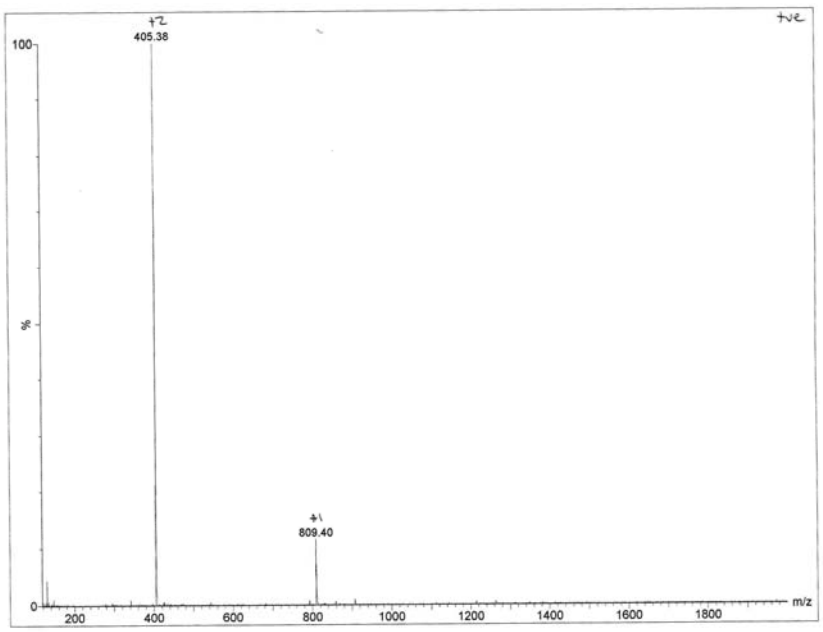

Figure 7.2. The ESI/MS spectrum of Bombesin[7-13] showing two peaks at *m/z* 809.44 and 405.38 corresponding to$[M]^{2+}$ and $[M]^{+}$.

7.3.3.12 Synthesis of Naphthalene diimide-Bombesin Conjugates

7.3.3.12.1 Method 1: The first route of synthesis of naphthalene diimide-Bombesin conjugates (mono-substituted naphthalene diimide-Bombesin) (**3**) (Scheme 7.3)

INDI (11.4 mg, 0.014 mmol, 1 eq) was dissolved in DMF (100 μL), and the solution was cooled to 4 in ice bath. EDC·HCl(N-(3-dimethylaminopropyl)-N'-ethylcarbodiimide hydrochloride) (6.71 mg, 0.035 mmol, 3 eq) and HOBt·H_2O(1-hydroxybenzotriazole hydrate)(6.62 mg, 0.049 mmol) was added sequentially to NDI solution and allowed to stir for 40 min in ice bath and to this solution was added bombesin peptide (34 mg, 0.042 mmol, 3 eq). The pH value of solution was adjusted to 9 with DIPEA. Then the ice bath was removed and the solution was stirred at room temperature for one night. After reaction, the solvent was removed under reduced pressure, leaving behind a pale white residue. The residue was dissolved in $CHCl_3$ (125 mL), washed with H_2O (2×20 mL) and saturated aqueous Na_2CO_3 Solution (2 ×20 mL). The organic layer was dried over anhydrous $MgSO_4$, and evaporated to dryness under reduced pressure and yellow powder was obtained (18 mg, 53.7% yield).

Mono-substituted NDIBBN Mass Spectrometry: Positive mode ES: *m/z* calcd for $C_{70}H_{74}I_2N_{14}O_{15}Na^+$:1627.35 $[M+Na]^+$; found: 1627.0; calcd for $C_{70}H_{74}I_2N_{14}O_{15}K^+$:1643.35 $[M+K]^+$; found: 1643.0).

HPLC Rt: 8.31 (flow gradient, see section 7.3.3.5)

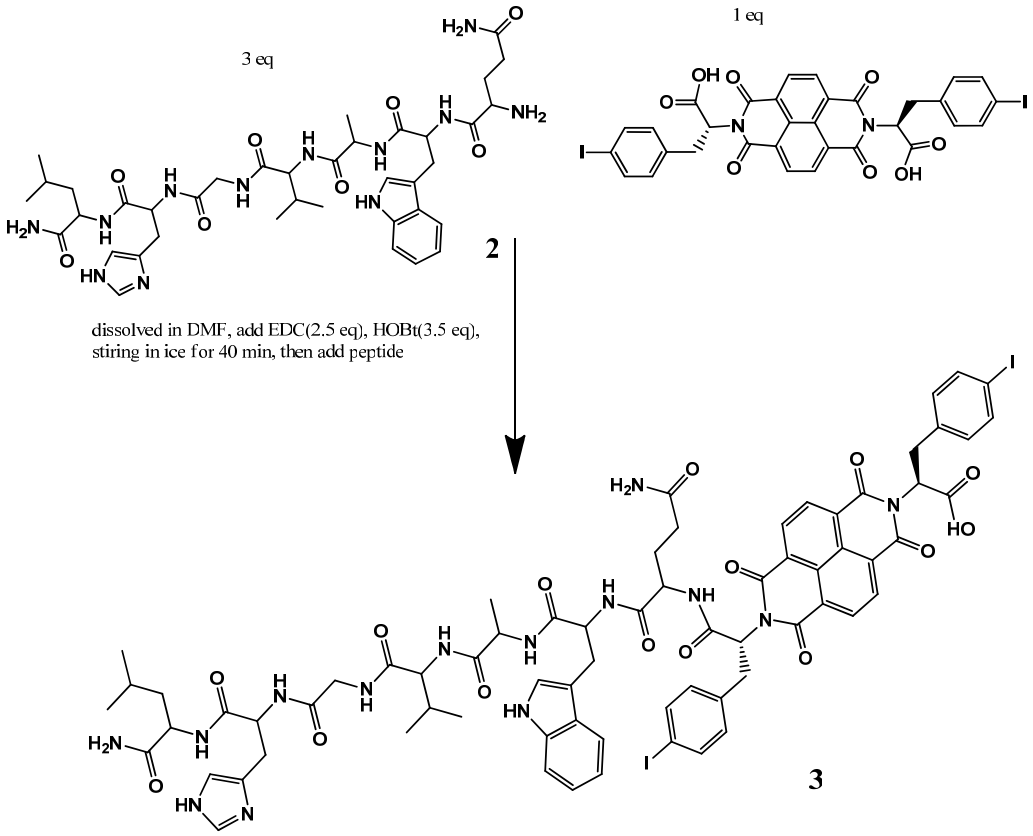

Scheme 7.3: The first route synthesis of mono-substituted NDI-bombesin (**3**)

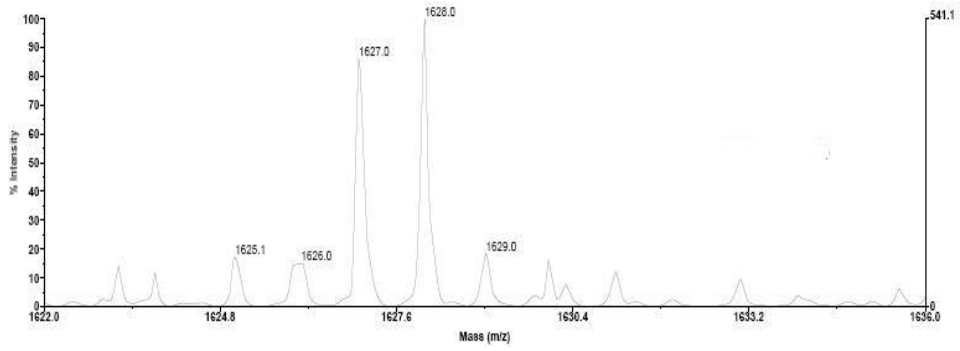

(a)

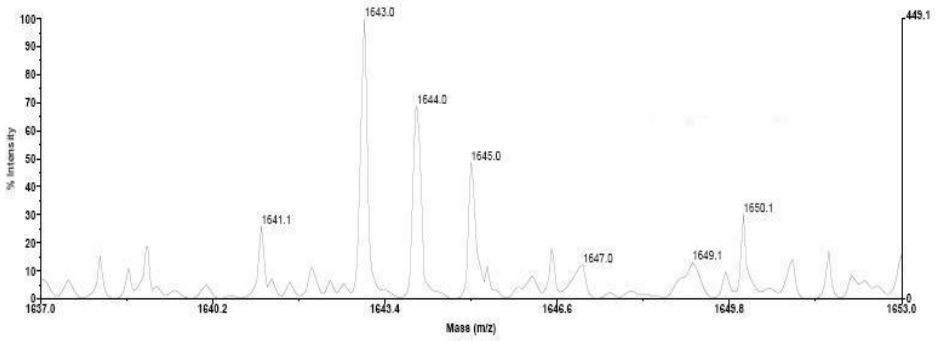

(b)

Figure 7.3. The ESI/MS spectrum of mono-NDIBBN showing peaks at *m/z* 1628.0 and 1643.0 corresponding to $[M+Na]^+$ and $[M+K]^+$.

7.3.3.12.2 Method 2: The second route of synthesis of naphthalene diimide-Bombesin conjugates (double-substituted naphthalene diimide-Bombesin) (**5**)

7.3.3.12.2.1 Synthesis of NDI-OSu (**4**) (Scheme 7.4)

NDI and *N*-hydroxylsuccinimide was dissolved in DMF with stirring in ice bath for 15 min. EDC・HCl was dissolved in DMF and then added to the solution which was stirring in ice bath for another 15 min. Then ice bath was removed and the solution was continually stirring at room temperature for 8 h. The DMF was removed by evaporating and a small amount of acetonitrile was added for dissolving the resulting product. Then the solution was added to stirring double-distilled H_2O from which precipitate was formed. The precipitate was collected by filtration and fine powder was formed by adding pentane to precipitate in bottom flask and then dried in vacuum. Yield: 0.76 g, 88%. ^{1}H NMR (500 MHz, DMSO-d6, 300 K) δ(ppm): 8.76 (s, 4 H, NDI), 7.51 (d, J = 8.3, 4H, Ph-CH), 7.00 (d, J

= 8.28, 4H, Ph-CH), 6.37 (dd, J_1 = 9.9, J_2 = 5.9, 2H, $C^{\alpha}H$), 3.74 (dd, J_1 = 14.4, J_2 = 6.5, 2H, $C^{\beta}H$), 3.61 (dd, J_1 = 15.3, J_2 = 10.2, 2H, $C^{\beta}H$); 2.82 (s, 8 H, NC(O)CH_2). ^{13}C {^1H}NMR (100.61 MHz, DMSO-d_6) δ(ppm): 176.2, 169.1, 159.2, 139.8, 137.6, 129.5, 90.8, 25.8. (Positive mode ES: *m/z* calcd for $C_{40}H_{26}I_2N_4O_{12}Na^+$: 1030.96 $[M+Na]^+$.; found: 1030.95).

HPLC Rt: 12.56 (flow gradient, see section 7.3.3.5)

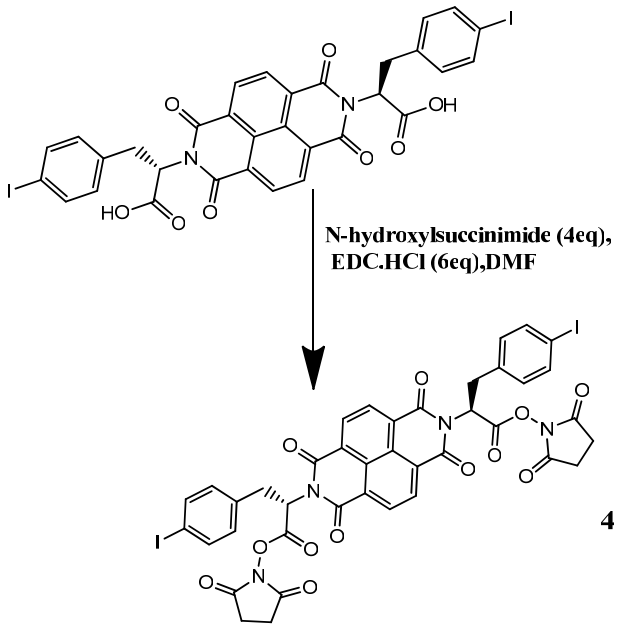

Scheme 7.4: Synthesis of NDI-OSu (**4**).

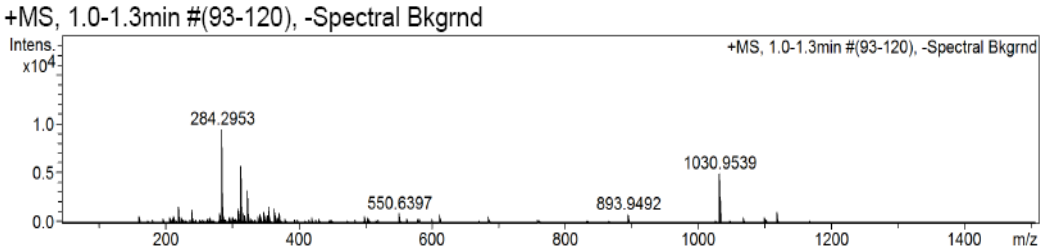

Figure 7.4. The ESI/MS spectrum of NDI-OSu showing peaks at *m/z* 1030.95 corresponding to $[M+Na]^+$.

7.3.3.12.2.2 Synthesis of naphthalene diimide-Bombesin conjugates by coupling of NDI-OSu with bombesin[7-13] (**5**) (Scheme 7.5)

To a mixture of NDI-OSu (10 µmol, 10 mg) and bombesin (21µmol, 17 mg) in DMF was added Et_3N (2.93 mg). The solution was stirred under N_2 for 8 h at room temperature. Solvent was removed and acetone was added to the residue. The acetone mixture was added

dropwise to a vigorously stirred solution of 1 M HCl (200 mL). The precipitate was collected by filtration and dried. Mass spectroscopy and analytical HPLC methods were used for analyzing the resulting compound. Both methods confirm that there are two products, one is) and another is double-substituted. The product was purified by semipreparative HPLC (reverse phase).

NDI-Bombesin (Positive mode ES: *m/z* calcd for $C_{108}H_{128}I_2N_{26}O_{22}K^+$: 2433.78 $[M+K]^+$; found: 2433.47) (Figure 7.5**)**.

HPLC Rt: 8.71 (flow gradient, see section 7.3.3.5)

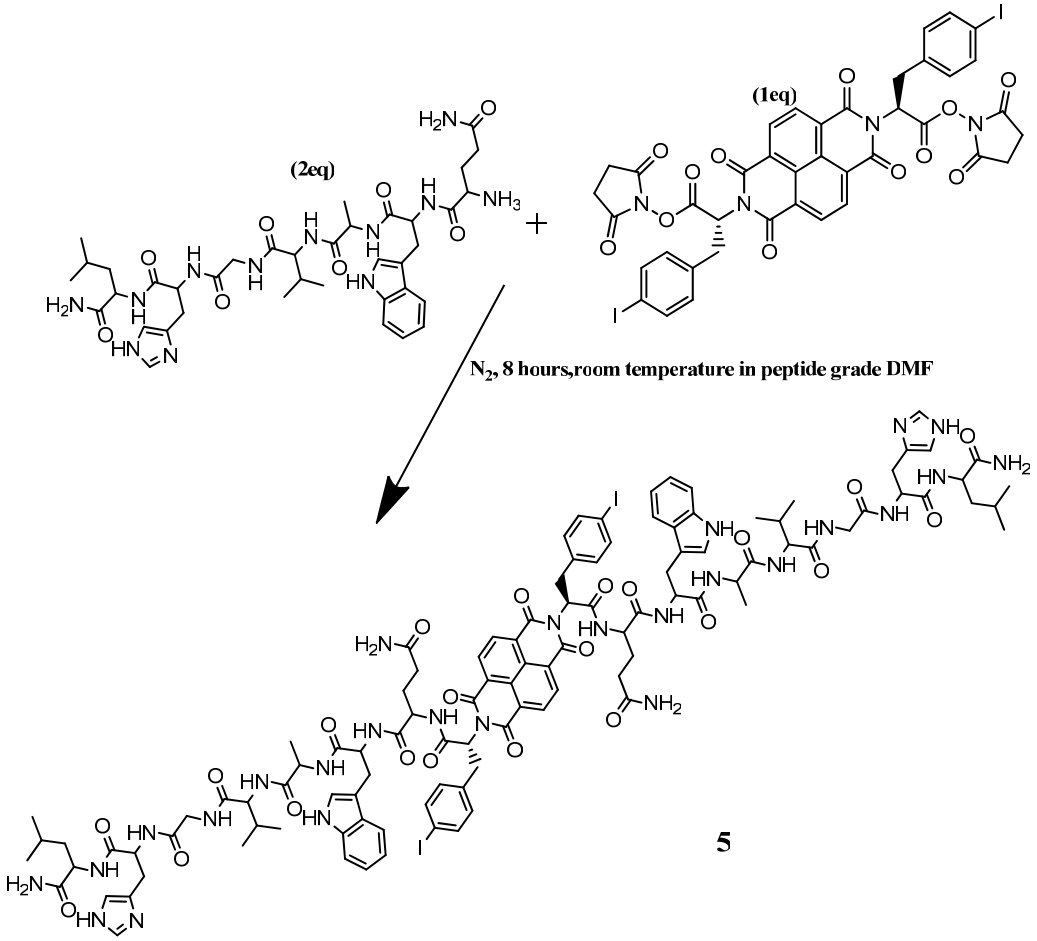

Scheme 7.5. Synthesis of double substituted NDIBBN (**5**).

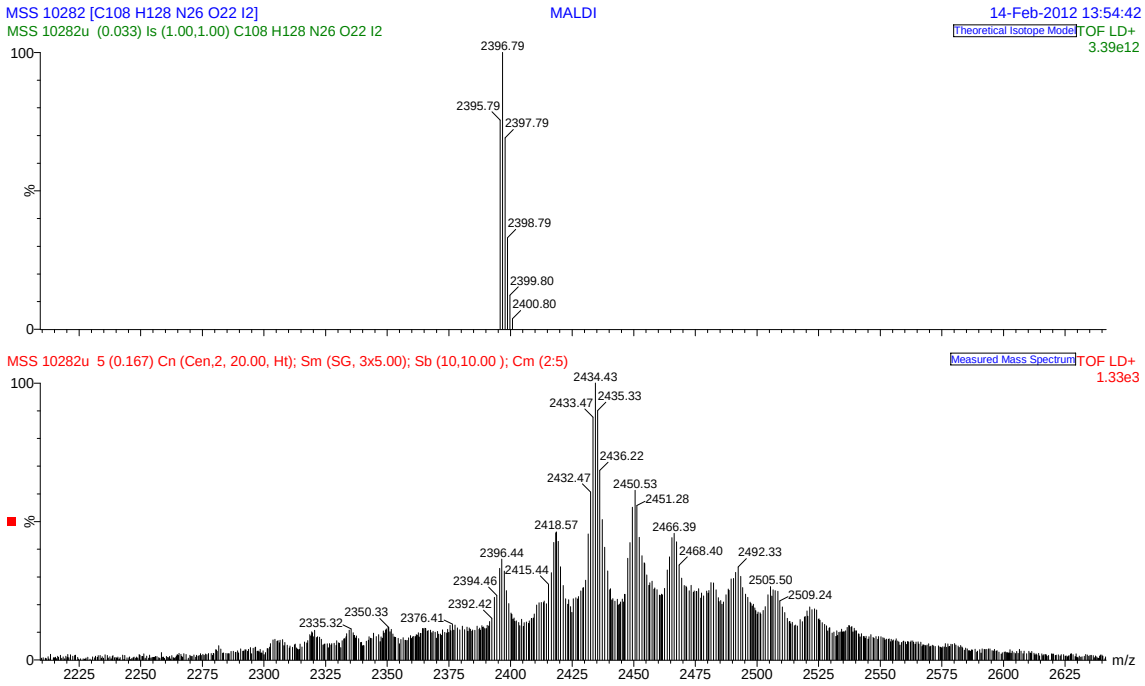

Figure 7.5. The MALDI spectrum of double substituted NDIBBN (**5**) showing peaks at *m/z* 2433.47 corresponding to $[M+K]^+$.

7.3.3.12.3 Isolation of mono-substituted NDI-Bombesin and double-substituted NDI-Bombesin from impurities by semipreparative HPLC

HPLC system Chromatographic system: UltiMate 3000 LC system was used for separate sample. Injection system: FAMOS μ-autosampler equipped with a 500 μL sample loop, a user-defined injection method was used. HPLC detection system: UltiMate UV Detector, 3 μL flow cell, 214-nm detection wavelength. Separation column: PepMap C18, 75 μm ID ×150 mm length, 3 μm particle size, 100 Å pore size. Mobile phase for column: 95% 0.01%water; 5% CAN. Procedure: (a) Loading solvent for HPLC: DMSO. RP-column flow rate: 0.300 μL min^{-1}. (b)Load sample to a Pepmap C18 Precolumn from 0 min to 30 min, (c) Switch on the collector from 8 min to 18 min.

7.3.3.13 Preparation of **5**@SWNT complex, denoted as NDIBBN@SWNT

The NDI-Bombesin@SWNT complex was prepared by mixing mono-substituted NDIBBN (**3**) water solution (2.4 mg, 1.5 μmol, 2 mL) with SWNT (0.25 mg, 2 mL) EtOH

dispersion, then sonicating 20 min, solution was stirring 2 days. Dialysis of NDI-Bombesin and SWNTs mixture against phosphate-buffered saline (PBS, 50 mM, pH 7.4) was carried out at 37 °C, which results in removal of unbound NDI-Bombesin. Centrifuge was performed to remove the aggregate which size is not suitable for biomedical application. The procedure results a very clear NDI-Bombesin@SWNT complex dispersion. (Figure 7.6 b).The UV-Vis analysis concluded that 1.44 mg **5** (0.9 μmol) bind with 180 μg SWNTs.

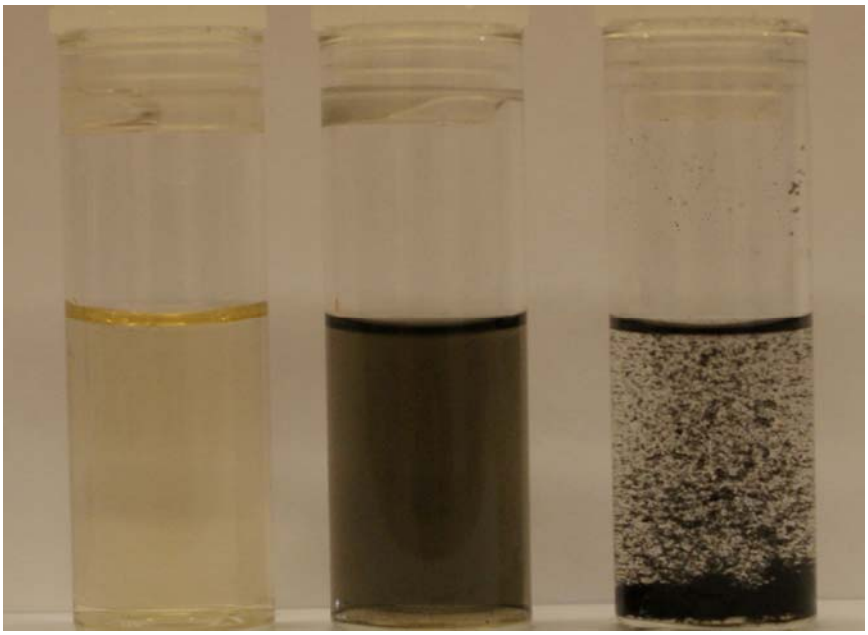

(a) **(b)** **(c)**

Figure 7.6. a) Mono-NDIBBN H_2O solution, 2.4 mg, 1.5 μmol, 2 mL b)mono-NDIBBN@SWNT H_2O solution obtained on a preparative scale after buffer dialysis, and redispersed at 0.1 mg/mL conc. (1.44 mg mono-NDIBBN (0.9 μmol) anchored onto 180 μg SWNTs), c) 0.25 mg SWNT dispersed in H_2O, 2 mL.

7.3.3.14 Fluorescence imaging of NDI-Bombesin and NDI-Bombesin@SWNTs

Final concentrations of compounds added to PC-3 cell and Hela cell plates in 1: 99 DMSO: EMEM, were: a) 3 μM NDI-Bombesin; b) 3 μM NDI-Bombesin@SWNT composite dispersion (3 μM solution used to 'anchor' 3μmol NDI-Bombesin onto 6 mg SWNT). Cells were incubated for maximum 2 h followed by washing prior to imaging. Cell viability prior to the experiment was tested by optical microscopy, standard trypan blue tests and MTT

assays. The uptake of the NDI-Bombesin@SWNT composite was imaged by laser-scanning confocal microscopy (LSM 510 META, Zeiss) of live cells, as well as in fixed cells, using the 405 nm, 488 nm and 543 nm line of an argon ion laser for excitation. The emission was detected with a photomultiplier tube (PMT). The intensity of the laser was modified to reduce the possibility of photobleaching of the fluorophore over time and the PMT voltage adjusted to be just above the auto-fluorescence limit of the starting conditions (for imaging of living cells) thus recording a background image before addition of compound, whilst maximizing sensitivity and ensuring optimal focusing. A similar standard procedure was used for imaging fixed cells, and for these an additional background image was collected (using fixed, but untreated cells) at the end of experiment.

7.3.4 Synthesis RGDfK-Naphthalene diimide conjugate

7.3.4.1 Synthesis of linear RGDfK(Arg(Pbf)-Gly-Asp(OtBu)-D-Phe-Lys(Boc)) (**6**) (Scheme 7.6)

Loading of the resin was achieved by swelling 2-chlorotrityl polystyrene resin (1.0 g) for 20 min in DCM. After swelling, the resin was treated with a solution of Fmoc-Gly-OH (2 eq, 3 mmol) and DIPEA (4 eq, 1 mL) in DCM (10 mL) by agitating for 90 min. The first amino acid attached resin was then washed with a solution of DCM / MeOH / DIPEA (10 mL; 17: 2: 1 v/v/v) for 3 ×15 min and with DCM (3 × 10 mL), DMF (2 × 10 mL), and DCM (2 × 10 mL). The other amino acids coupling were performed using Fmoc-amino acid (2 eq, 3 mmol), PyBOP (2 eq, 3 mmol), and DIPEA (4 eq, 6 mmol) in DCM (10 mL) for 90 min. Fmoc deprotection before next amino acid coupling was achieved by treatment with piperidine/DMF (1:4 v/v) for 4 × 3 min. The deprotection reaction was monitored by

ninhydrin test and chloranil test. Washing of the resin after coupling were deemed complete by DMF (2 × 8 mL), Et_2O (2 × 8 mL) and DCM (2 × 8 mL).

Cleavage from the resin was achieved by treatment with TFA / DCM (7 mL; 1 : 99 v/v) for 10 × 2 min. Before aspirating cleavage solution from vessel, the cleavage solution were neutralised by addition to pyridine / MeOH (10 mL; 1: 9 v/v). The mixture was concentrated in vacuum, dissolved in a minimum volume of MeOH, then the crude peptide was precipitated by adding Millipore water, collected by centrifugation, dissolved in DCM (100 mL), washed with water (100 mL). The DCM layer was collected and evaporated in vacuum to give **6** as a white solid (1.18 g; 85%). ESI-MS: *m/z* calcd for $C_{49}H_{74}N_9O_{13}S$ 1028.52 $[M+H]^+$; found 1028.4936.

HPLC Rt: 8.54 min (flow gradient, see section 7.3.3.5)

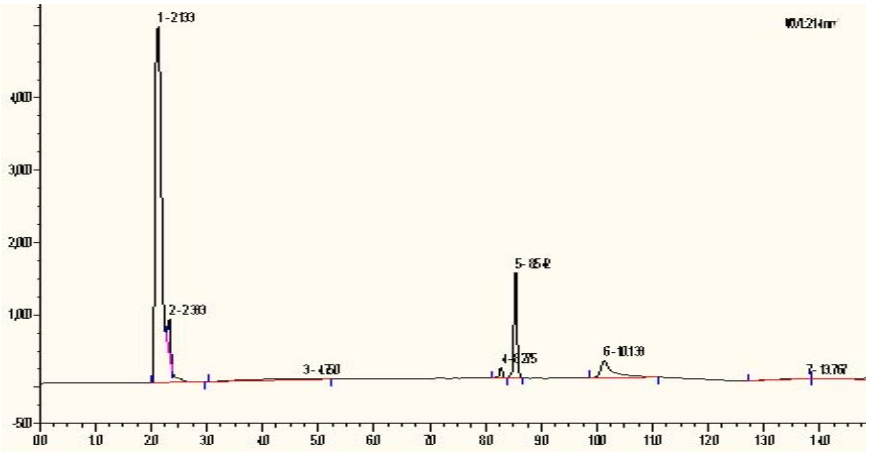

(a)

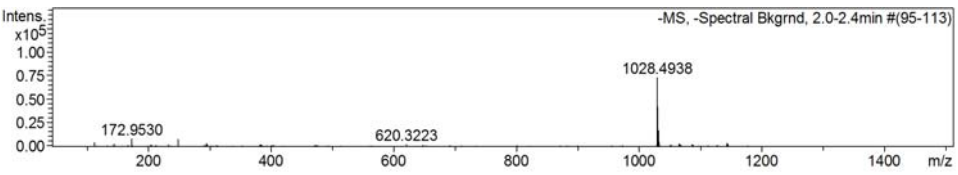

(b)

Figure 7.7. Analytic HPLC trace(Rt: 8.58 min) **(a)** and ESI/MS spectrum**(b)** showing peaks at *m/z* 1028.49 corresponding to $[M+H]^+$ of linear RGDfK

7.3.4.2 Cyclisation of protected RGDfK peptide (Cyclo(-RGDfK), **7**)

6 (139 mg; 0.13 mmol) and PyBOP (0.083 g; 0.161 mmol) were dissolved in DCM (135.5 mL) and the solution was adjusted to pH 8 by the addition of DIPEA (0.382 mL) and allowed to stir for 24 h. The reaction mixture was then concentrated in vacuum. The crude product was dissolved in DCM (20 mL) and washed with a saturated solution of $NaHCO_3$ (4 × 20 mL) and with brine (75 mL). The crude peptide was then precipitated in cold Et_2O, and centrifuged to give **7** as a white solid (127 mg; 94%).

HPLC R_t: 10.19 min (flow gradient, see section 7.3.3.5).

ESI-MS : *m/z* calcd for $C_{49}H_{73}N_9O_{12}SNH_4^+$ 1029.51 $[M+NH_4]^+$; found 1030.53.

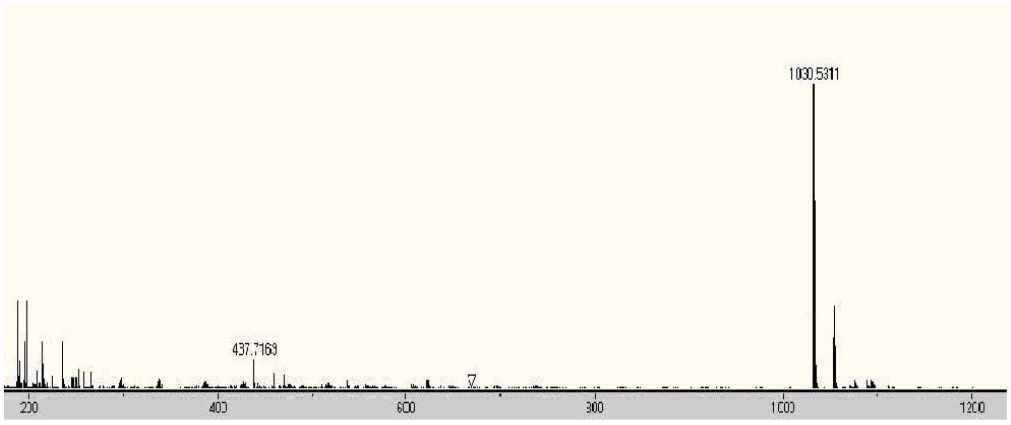

Figure 7.8. ESI MS spectrum of cyclic protected RGDfK **7** showing peaks at *m/z* 1030.49 corresponding to $[M+NH_4]^+$.

7.3.4.3 Cyclic deprotected RGDfK peptide (**8**).

Protected Cyclo(-RGDfK) **7** (0.2 g; 0.198 mmol) was dissolved in a TFA deprotection cocktail (TFA/CH_2Cl_2, 1: 1, 5 mL), and the solution was stirred for 2 h. The majority of the TFA can be removed by purging N_2 gas. The crude peptide was precipitated in cold Et_2O, then centrifuged to give the desired product as a light green solid (0.122 g; 67%).

HPLC R_t : 7.95 min (flow gradient, see section 7.3.3.5);

ESI-MS: *m/z* calcd for $C_{27}H_{42}N_9O_7$: 604.31 $[M+H]^+$; found 604.3910.

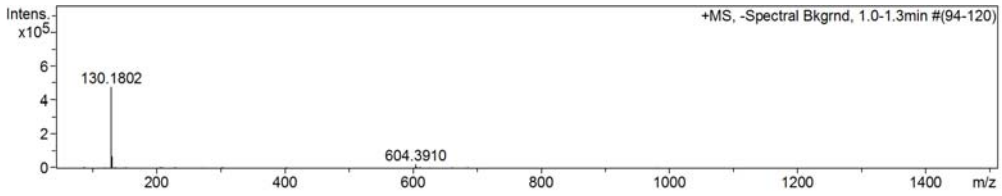

Figure 7.9. ESI/MS spectrum of cyclic deprotected RGDfK showing peak at *m/z* 604.39 corresponding to $[M+H]^+$.

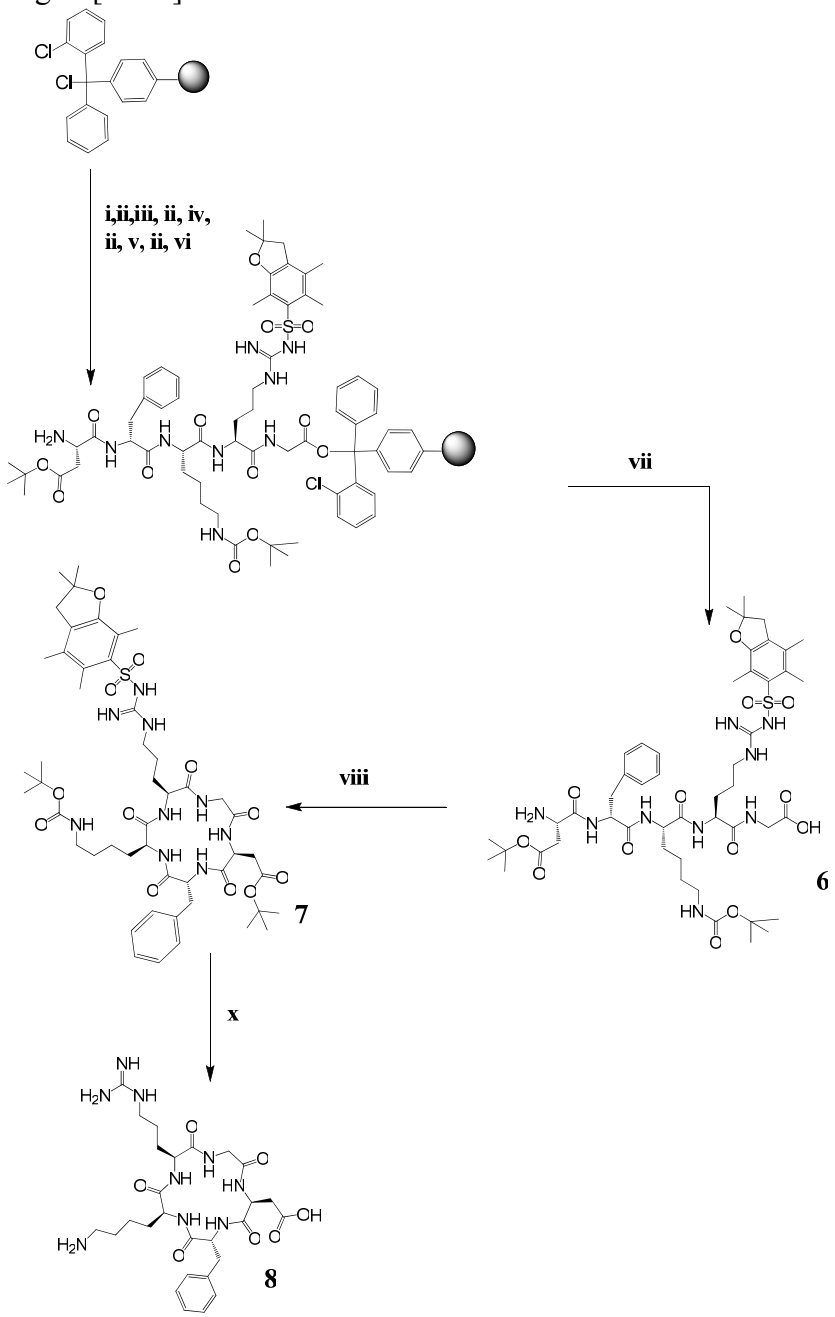

Scheme 7.6. Synthesis of deprotected cyclic RGDfK peptide **8**, (i):Fmoc-Gly-OH, DIPEA,CH_2Cl_2 (ii):20%(v/v) piperidine in DMF; (iii):Fmoc-Arg(Pbf)-OH, PyBop, DIPEA,CH_2Cl_2; (iv): Fmoc-Lys(Boc)-OH, PyBop, DIPEA, CH_2Cl_2; (v): Fmoc-D-Phe-OH PyBop, DIPEA,CH_2Cl_2; (vi):Fmoc-Asp(OtBu)-OH, PyBop, DIPEA,CH_2Cl_2; (vii):TFA/ DCM (10 mL; 1 : 99 v/v) for 10×2 min, pyridine/MeOH (10 mL ; 1 : 9 v/v); (viii): PyBOP, DIPEA, 72 h rt; (x):TFA/CH_2Cl_2 (1:1), rt, 2 h.

7.3.4.4 Synthesis of tryptophan-NDI (TNDI) (9) (Scheme 7.7)

1,4,5,8-Naphthalenetetracarboxylic dianhydride(200 mg, 0.746 mmol) and the L-Tryptophan (1.491 mmol, 304.5 mg) were suspended in 8 mL of DMF in a pressure-tight 15-mL microwave vial. To this suspension was added 0.2 mL of dry Et_3N. The suspension was sonicated until the mixture became homogeneous. The reaction mixture was heated for 5 min at 140°C under microwave irradiation using a dedicated microwave system.

The solvent was removed under reduced pressure. The dark brown oil was taken up into MeOH (6 mL). This solution was added under stirring to 400 mL of 1M HCl. The resulting suspension was allowed to coagulate overnight and then filtered through a glass funnel. The solid was then washed with 100 mL deionized water and dried under reduced pressure. The product was obtained in the form of a brown solid in 88% yield.

^{1}H NMR (400 MHz, DMSO-*d*$_6$) δ(ppm): 10.48(s, 2H), 8.54(s, 4H), 7.4(d, 2H, *J*=7.8), 7.11(d,2H, *J*=8), 6.91(d,2H, *J*=2.2), 6.86(dd,2H, *J*=7.1), 6.74(dd,2H,*J*=8), 5.8(t, 2H), 3.64-3.45(m, 4H) ^{13}C NMR{^{1}H} (100.61 MHz, DMSO-*d*$_6$) δ(ppm): 169.2, 161.8, 137.2, 131.3, 128.9, 128.1, 126.4, 125.9, 125.5, 54.2, 52.3, 34.0; ESI/MS calcd. for: $C_{36}H_{24}N_4O_8K^+$ $[M+K]^+$ (*m/z*): 679.16, found: 680.09.

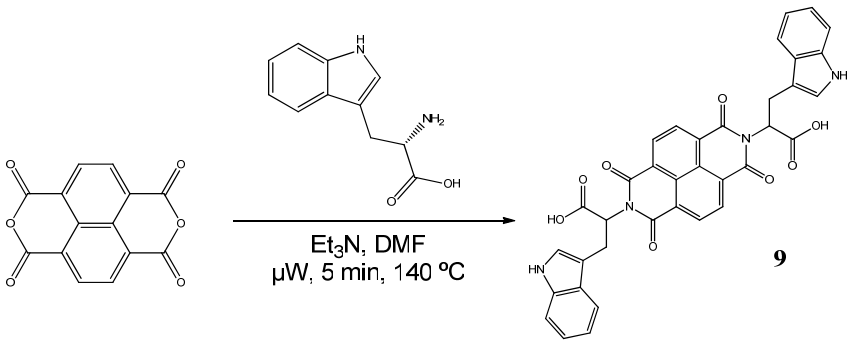

Scheme 7.7. Synthesis of **Compound 9.**

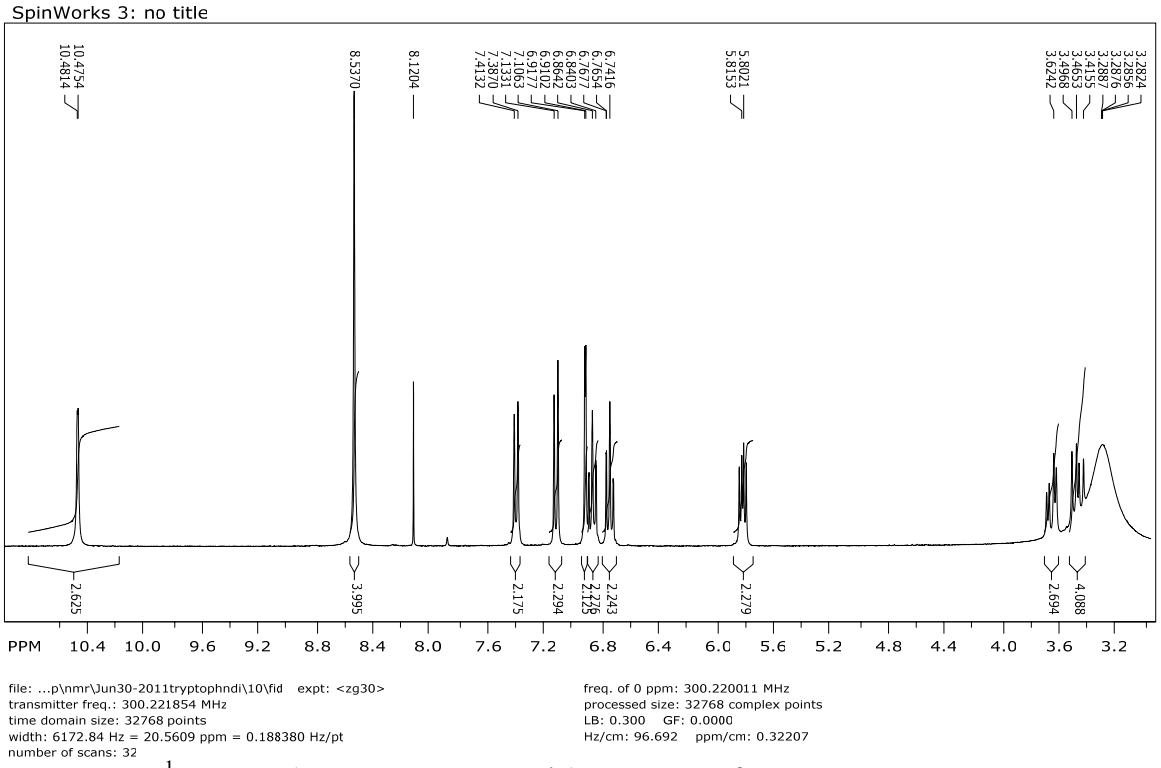

Figure 7.10. ^{1}H NMR (400 MHz, DMSO-d6) spectrum of **9.**

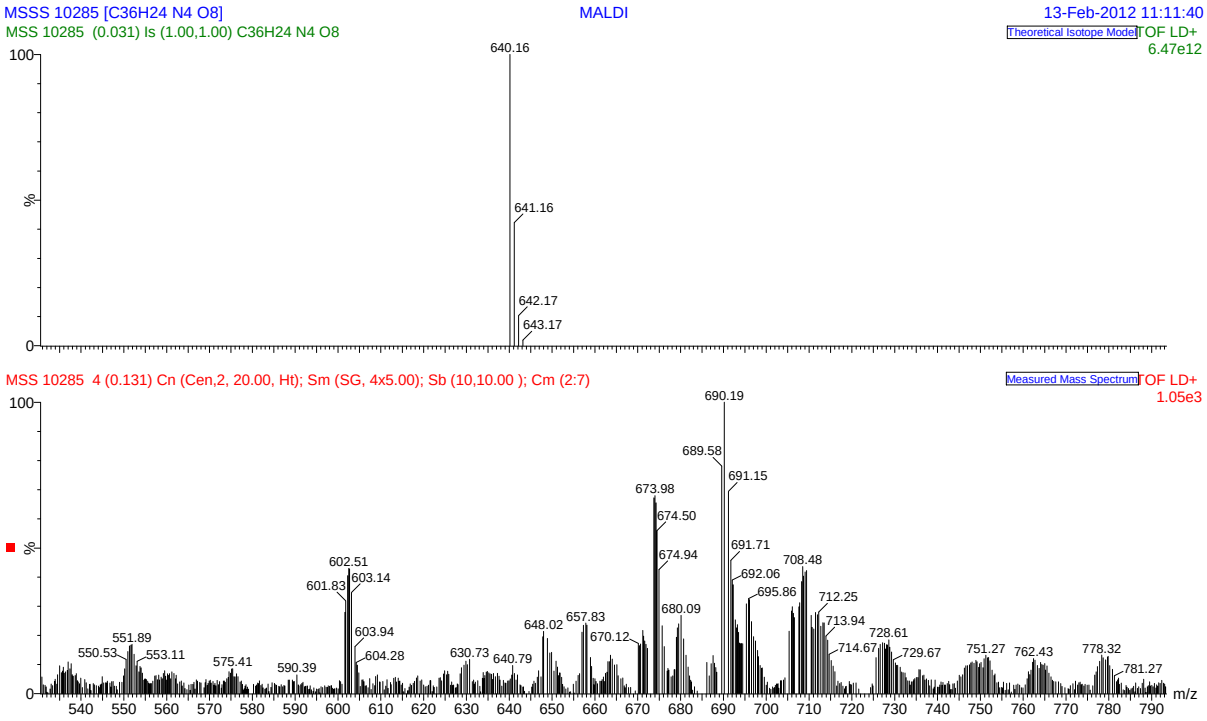

Figure 7.11. MALDI spectrum of TNDI showing peaks at *m/z* 680.09 corresponding to $[M+K]^{+}$.

7.3.4.5 Synthesis of tryptophan-NDI-OSu (TrypNDI-OSu) (10) (Scheme 7.8)

Tryptophan-NDI (0.2 mmol, 128.12 mg) and *N*-hydroxysuccinimide (0.8 mmol, 92 mg) were dissolved in DMF and stirred in ice bath for 15min. EDC・HCl (0.8 mmol, 153.36 mg) was dissolved in 20 mL DMF and then added to the solution which was stirred in ice bath for another 15 min. Then ice bath was removed and the solution was continually stirring at room temperature for 8 h. The DMF was removed by evaporating and a small amount of acetonitrile was added for dissolving the resulting product. Then the solution was added to stirring double-distilled H_2O from which precipitate was formed. The precipitate was collected by filtration and fine powder was formed by adding pentane to precipitate in the bottom of the flask and then dried in vacuum.

Yield: 160.2624 mg, 96%. ^{1}H NMR (300 MHz, DMF-d1, 300 K) δ(ppm): 11.7 (s, 1 H, NH), 8.7(s,4H, NDI), 7.54(d, 2H, *J*7.5), 7.1(d, 2H, *J*9.8),6.8(m, 6H), 5.3(t, 2H, *J*6.1 and 4.1), 3.67(m, 4H), 2.76(s,1H), 2.64(s,1H). ^{13}C {^{1}H} NMR (100.61 MHz, DMF-d1) δ(ppm): 162.91, 162.71, 162.13, 107.92, 67.15, 35.85, 34.47, 30.74, 29.91 and 24.18.

Positive mode ESI MS: *m/z* calcd: $C_{44}H_{30}N_6O_{12}Na^+$ 857.19 $[M+Na]^+$; found: 857.45. calcd: $C_{44}H_{30}N_6O_{12}K^+$ 873.19 $[M+K]^+$; found: 873.46. (Figure 7.12)

Scheme 7.8. Synthesis of TrypNDI-OSu **10.**

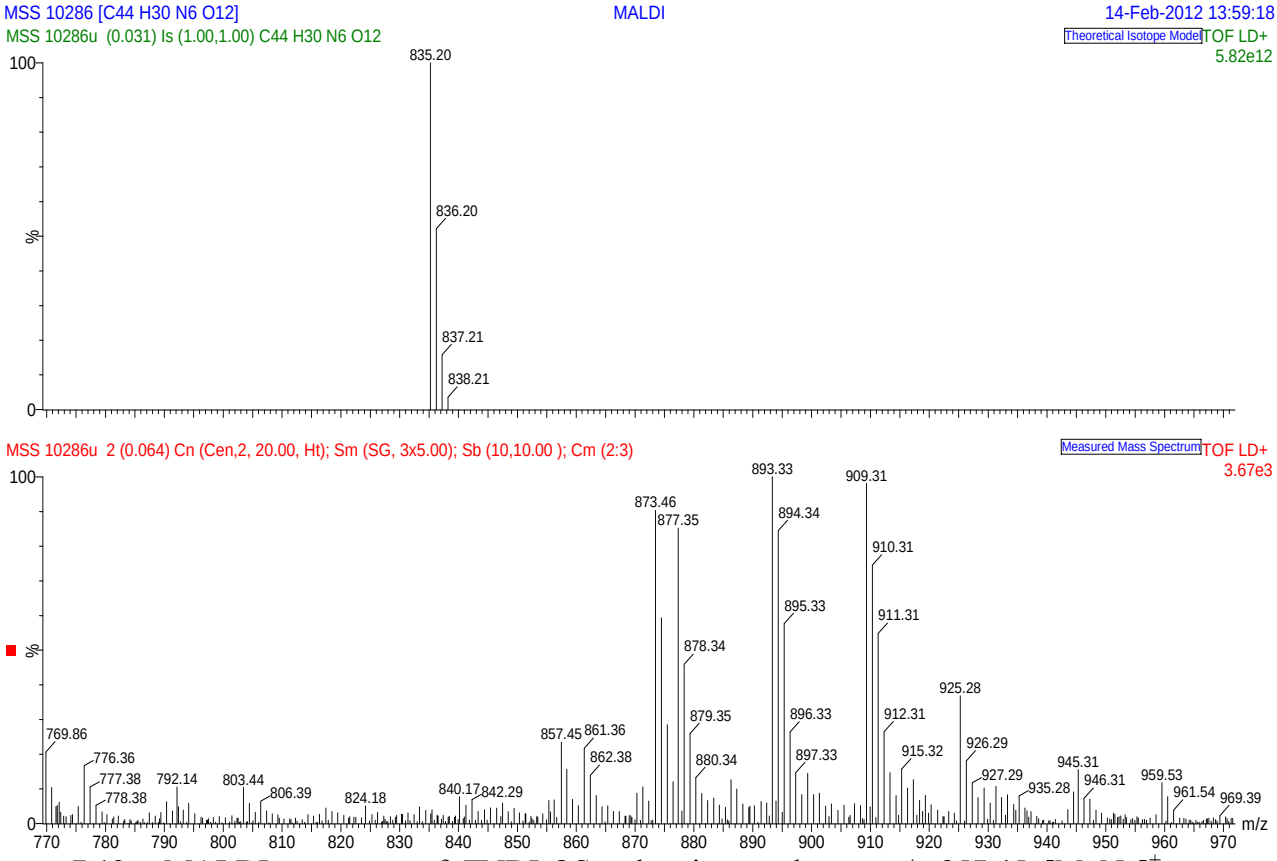

Figure 7.12. MALDI spectrum of TNDI-OSu showing peaks at *m/z* 857.45 $[M+Na]^+$, 873.46 $[M+K]^+$.

7.3.4.6 Synthesis Trypotophan-tagged naphthalene diimide-RGDfK conjugates 11 by coupling reaction (Scheme 7.9)

To a mixture of **10 (**10 µmol, 10 mg) and **8** (21 µmol, 17 mg) in DMF was added Et_3N (2.93 mg). The solution was stirred under N_2 for 8 h at room temperature. Solvent was removed and acetone was added to the residue. The acetone mixture was added dropwise to a vigorously stirred solution of 1 M HCl (200 mL). The precipitate was collected by filtration and dried (Scheme 8). Mass spectrometry and analytical HPLC methods were used for analyzing the resulting compound. MALDI and HPLC confirm that the product is double-substituted NDI-RGDfK **(11)**. The product was purified by semi-preparative HPLC. Positive mode ESI MS: *m/z* calcd: $C_{90}\ H_{103}\ N_{22}\ O_{20}^+$, 1811.76 $[M+H]^+$; found: 1811.76 (Figure 10).

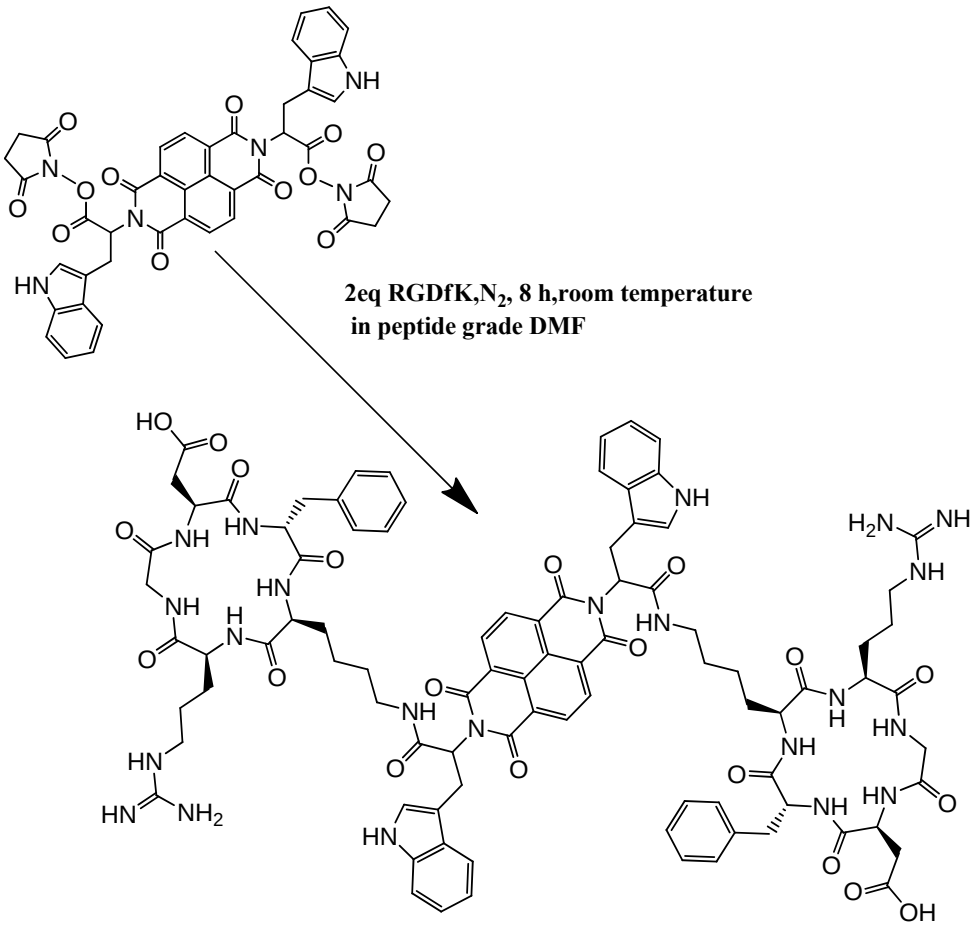

11

Scheme 7.9. Synthesis of TNDI-RGDfK **11**

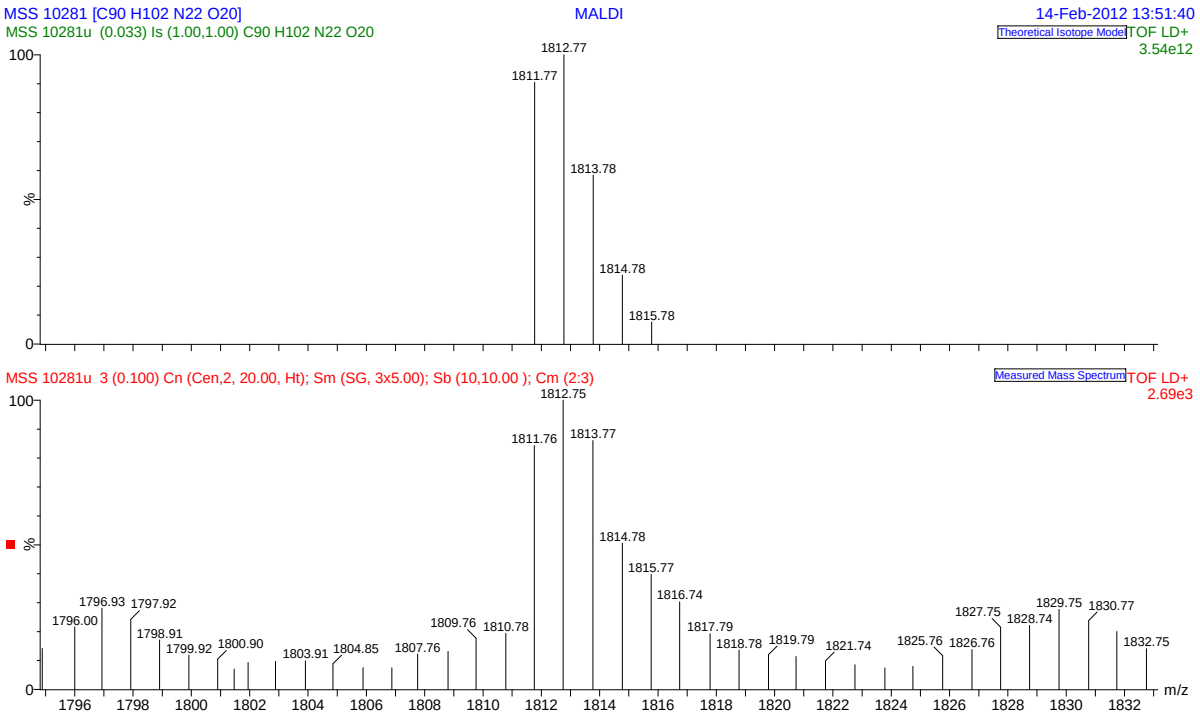

Figure 7.13. MALDI spectrum of **11** showing peaks at *m/z* 1811.76 $[M+H]^+$.

7.3.5 Functionalisation of SWNTs with a dodecathiophene (denoted T12)

7.3.5.1 Materials

All solvents (HPLC grade) were used without further purification. All starting materials were purchased from Aldrich, Acros, or Fluka and used without further purification. T12 was synthesized by Patrick van Rijn from Delft University of Technology and used as provided. The purity and identity of this compound was confirmed by NMR and Mass spectroscopy at Bath.

^{1}H NMR (300 MHz, $CDCl_3$): δ=0.80 (t, *J*=7.0 Hz, 12H), 1.09-1.26 (m, 104 H), 1.47–1.75 (m, 8H), 3.22–3.33 (m, 24H), 3.40–3.49 (m, 16 H), 3.50–3.74 (m, 112 H),4.57 (s, 16H), 6.84 (s, 1 H), 7.19 ppm (s, 11H), 7.53 (s, 2H) ^{13}C NMR (75 MHz, $CDCl_3$): δ=14.23 (CH_3), 29.12 (CH2), 29.68 (CH_2), 29.88 (CH_2), 31.08 (CH_2), 76.59 (CH_2), 77.01 (CH_2), 77.22 (CH_2), 77.44 (CH_2), 126–140 ppm (broad overlapping signals corresponding to 14 CH and 34 C); ESI-TOF: *m/z* calculated for $C_{192}H_{314}O_{40}S_{12}$; 3643.92 (mono-isotopic) found: 1844.9081 $[M+2Na]^{2+}$,1237.6293 $[M+3Na]^{3+}$.

7.3.5.2 Preparation of T12@SWNT nanohybrid

A typical procedure for preparing T12@SWNT dispersions is as follows: a mixture of SWNTs (0.1 mg) and the T12 polymer (0.1 mg) in $CHCl_3$ (4 mL) was sonicated for 20 min and stirred for 2 days. After centrifugation (10000 rpm) of the resultant yellow-brown suspension for 30 min, the supernatant was taken and filtrated and washing with $CHCl_3$ three times. The black complex on PTFE filter membrane was collected and dried in oven 60 °C overnight. The T12@SWNT composite can be dissolved again in $CHCl_3$, DCM and DMSO easily.

7.3.5.3 Cell culture and fluorescence imaging

For microscopy, cells were seeded onto chambered coverglass slides and incubated for 12 h to ensure adhesion. Prior to imaging, the solution was replaced with 1 mL fresh EMEM. Background autofluorescence was measured by imaging the cells in 1 mL of EMEM medium only. Final concentrations on cell plates used were: a) 7 μg/mL T12 (1.92 μM in 5: 95% DMSO: EMEM); b) T12@SWNT composite dispersion (in 5: 95% DMSO: EMEM) containing 7 μg/mL T12 (1.92 μM T12 'anchored' onto 18 μg/mL SWNT);

7.3.6 Preparation of metal radiopharmaceuticals filling and biocompatible fluorescent material coating Carbon Nanotubes

7.3.6.1 Buffer and Solvents

The fluorescence titrations of boronic acid fluorophore with *β*-D-Glucan were carried out in in a pH 8.21 aqueous methanolic buffer. The buffer was prepared as Perrin and Dempsey method[17]: 52.1 wt% HPLC grade methanol in deionised water with KCl (10.0 mM), KH_2PO_4 (2.75 mM), and Na_2HPO_4 (2.75 mM) and was stored in the dark in fridge when not in use. PBS buffer was made by dissolving each tablet of PBS with 100 mL of distilled water. This buffer contains 10 mM phosphate, 150 mM sodium chloride, pH 7.3 to 7.5.

7.3.6.2 Steaming purification of SWNTs (Figure 7.14)

This method was based on literature method by Malcolm L H Green.[18,19] 250 mg arc-discharge made SWNTs (CarboLex) was kept in a glove box fed with argon gas for two days to remove oxygen absorbed on surface of carbon nanotubes.

Distilled water was first flushed with argon to remove dissolved oxygen. SWNTs were placed in a silica tube (9 mm diameter) and immobilised with silica wool at both sides. The sample was then put in the middle of quartz furnace tubes. The sample was kept under argon for 30 min. The steam was introduced by bubbling argon through boiling water (98 °C). After the whole system was purged by argon for 2 h, then the furnace was gradually then heated to 900 °C (15 °C/min). After 2 h steaming treatment, the steam was turned off, and the furnace was switched off, but argon flow was kept on until furnace decreased to room temperature to protect the sample from thermal oxidation. After steam treatment, sample was stirring in 16 % HCl overnight, and then the carbon nanotubes was filtered after the solution diluted with access distilled water, the solid was washed with access distilled water. Obtained carbon nanotubes solid was dried in oven at 60 °C overnight.

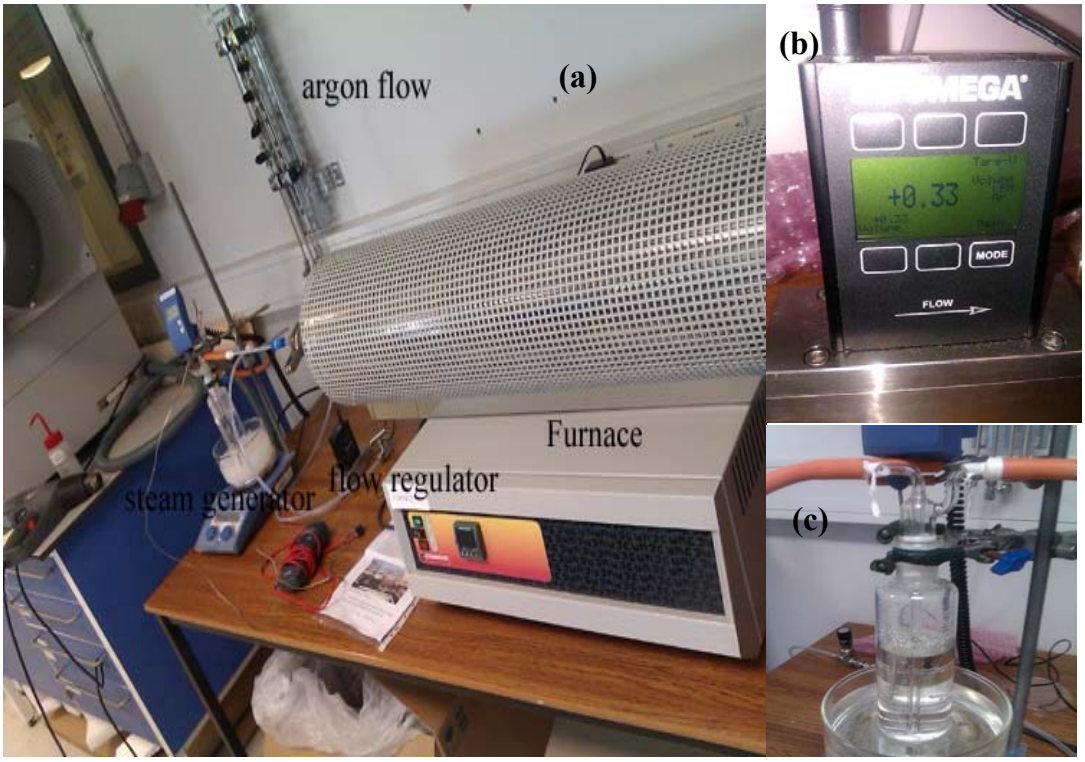

Figure 7.14. (a) Equipment setup for SWNTs steaming purification. (b) Argon flow regulator. (c) Steam generator.

7.3.6.3 "Cold" filling steam-purified SWNTs using the orecursors: $Cu(AcO)_2$, $KReO_4$ and $Zr(OAc)_4$

7.3.6.3.1 Filling with Copper Acetate

In a typical procedure, 0.8 mg of steam purified open SWNTs were suspended into a saturated $Cu(OAc)_2$ and NaOAc (1:10 ratio) solution and then sonicated for 30 min. The solution was kept stirring at 50 °C for 2 h. Then the $Cu(AcO)_2$@SWNTs solution was evaporated to remove the H_2O. 0.66 mg C_{70} was sonicated in EtOH for 2 min. $Cu(OAc)_2$ @SWNTs precipitate was added to this solution and the mixture was sonicated for 1 min and left stirring for 30 min, to allow the C_{70} to enter the SWNTs, in a similar mechanism called "nano-extraction" method for the encapsulation of fullerenes. After "corking", the solution was filtered, and washed several times with distilled water to remove the excess of copper acetate external to the SWNTs. The solid residue on the filter membrane was washed again with toluene (5 mL) to remove C_{70} sticking on the external surface of SWNTs. The solid residue was dying under reduced pressure. A very small amount of the sample (less than 1 μL) was dropped on a copper grid for HRTEM.

7.3.6.3.2 Filling with Zirconium Acetate $Zr(OAc)_4$

Open-ended SWNTs (1.6 mg) was added to 20 mL of ethanol and then ultrasonicated in a water bath for 20 min. SWNTs ethanol solution was splitted into 2 samples (A and B). 23.4 mL of zirconium acetate solution (30 mg) was added to each vial. 10 mg of sodium acetate was added into B sample. $Zr(OAc)_4$ formed gel in both samples after two days room temperature stirring. H_2SO_4 was added into both samples in dropwise until the pH value was adjusted to 2.4 for avoiding the gel formation of $Zr(OAc)_4$. Ethanol was removed by evaporation and then 10-15 mL double-distilled H_2O was added into each sample without the gel forming by dropping H_2SO_4. Samples were kept under constant stirring at 50 °C for 48 h.

The solution was filtered through a 0.2 μm polycarbonate membrane and washed with excess distilled water to remove the large excess of $Zr(OAc)_4$ and sodium acetate. The sample was then dried under vacuum giving zirconium acetate filled SWNTs, designated as $Zr(OAc)_4$@SWNTs. Also the unwashed $Zr(OAc)_4$@SWNTs solution can be "corked" with C_{70}. Prior to washing, C_{70} (0.4 mg) was added, stirred and heated at 50 ^oC overnight. After 24 h, the solution was filtered, and washed several times with excess double-distilled H_2O, followed by a toluene wash to remove the C_{70} left in solution.

7.3.6.3.3 Filling with Potassium Perrhenate ($KReO_4$)

In a typical procedure, 0.8 mg of steam purified open SWNTs were suspended into a saturated $KReO_4$ solution and then sonicated for 30 min. The solution was kept stirring at 70 °C for 2 h. Then the $KReO_4$@SWNTs solution was evaporated to remove the H_2O. 0.5 mg C_{70} were sonicated in EtOH for 2 min. $KReO_4$@SWNTs solid was added to this solution and the mixture was sonicated for 1 min and left stirring at 80 °C for 2 days. After "corking", the solution was filtered, and washed several times with distilled water to remove the excess of $KReO_4$ external to the SWNTs. The solid residue on the filter membrane was washed again with toluene (5 mL) to remove C_{70} sticking on the external surface of SWNTs. The solid residue was dying under reduced pressure. A very small amount of the sample (less than 1 μL) was dropped on a copper grid (lacey carbon) for HRTEM imaging.

7.3.6.4 Synthesis of fuorescein-5-[thioureidyl-(3-phenylboronic acid)] (FBA) (Scheme 7.10)(**12**)

Fluorescein isothiocyanate (130 mg, 0.33 mmol), *m*-aminophenylboronic acid (45.2 mg, 0.33 mmol) were added into a methanol (12 mL) and distilled water (2 mL) mixture solvent. Triethylamine (1 mg) was dropped into this reaction. The solution was stirred for 1 h

at room temperature and then another 45.2 mg of *m*-aminophenylboronic acid was added. Stirring for another 1 h, the product was then purified by thin layer chromatography (eluent dichloromethane:methanol, 9:1). ^{1}H NMR (300 MHz, MeOD d4+D_2O) δ: 7.97 (1H, d, J 2.7), 7.74 (1H, dd, J 8.5 and 2.7), 7.71 (1H, s), 7.6 (1H, d, J 8.5), 7.36 (1H, m), 7.19-7.15 (2H, m), 6.63-6.59 (5H, m), 3.35 (2H, NH). ^{13}C NMR (75 MHz, D_2O) δ: 182.2, 179.9, 160.0, 159.9, 141.9, 141.8, 139.7, 133.1, 132.9, 132.1, 131.7, 131.5, 129.7, 128.2, 127.1, 126.6, 123.6, 123.4, 115.5, 114.9, 104.7, 104.5. ^{11}B NMR (D_2O, 96 MHz): 19.17. HRMS (ESI)- calcd for: $C_{27}H_{18}BN_2O_7S^-$,525.10 [M-H]$^-$; found: *m/z* 525.0946.

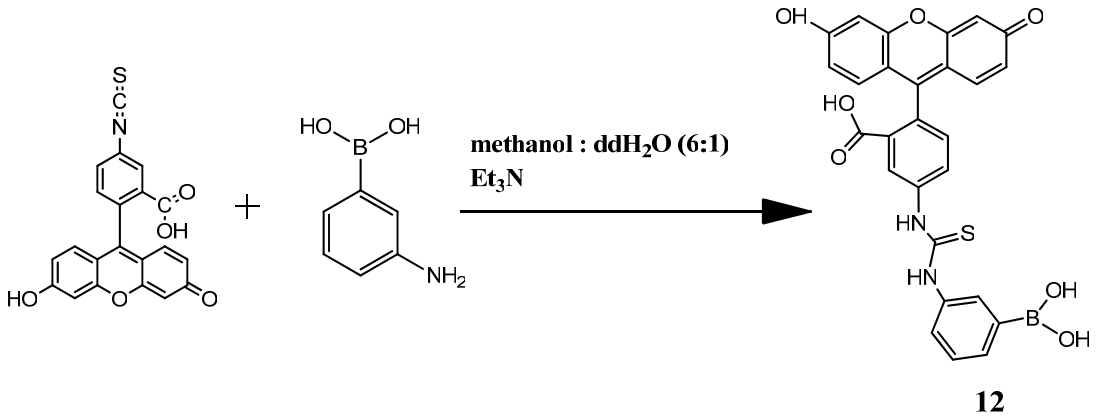

Scheme 7.10. Synthesis of **12.**

7.3.6.5 Synthesis of porphyrin-boronic acid (Scheme 7.11) (**13**)

2-(4-ethynylphenyl)-4,4,5,5-tetramethyl-1,3,2-dioxaborolane (27.13 mg, 0.119 mmol), 5-(3-iodophenyl)-15-phenylporphyrin(70 mg, 0.119 mmol), $Pd_2(dba)_3$ (13.5 mg, 0.0148 mmol) and $AsPh_3$ (36.4 mg, 0.119 mmol) were dissolved in toluene (8 mL) and Et_3N (4 mL). The solution was saturated with argon (three freeze thaw cycles) and stirred at room temperature for 3 days, after which the solvent was removed under reduced pressure. The reaction mixture was purified by preparative TLC on silica gel eluted with Hexane/CH_2Cl_2 (1/4) to yield **13** as black-red solid (71.29 mg, 87%). ^{1}H NMR (500 MHz, CD_3OD) 10.4 (2H, s, meso-CH), 9.50 (2H,d,*J*4.7, pyrrole-H_β), 9.49 (2H,d, *J*4.7, pyrrole-H_β), 9.15 (2H, d, *J*4.5,

pyrrole-H_β), 9.14 (2H,d, *J*4.5, pyrrole-H_β), 8.51 (1H, m), 8.31(2H, m), 8.06 (1H, d, *J*8.2), 7.88 (6H, m), 7.79 (2H, d, *J*8.4), 7.63 (2H, d, *J*8.4), -3.3 (2H, br s,NH), 1.36 (12H, s, CH). MALDI-TOF MS (*m/z*) Calcd for: $C_{46}H_{37}BN_4O_2Na^+$, 711.30 $[M+Na]^+$, found 711.18; Calcd for: $C_{46}H_{41}BN_5O_2K^{3+}$, 745.30 $[M+NH_4+K]^{3+}$; found: 745.17. (Figure 7.15).

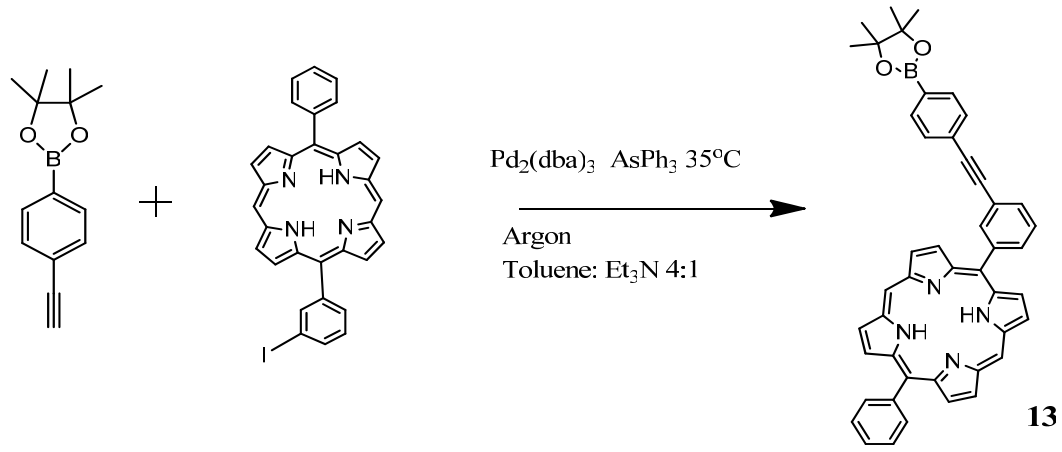

Scheme 7.11. Synthesis of porphyrin-boronic acid **13.**

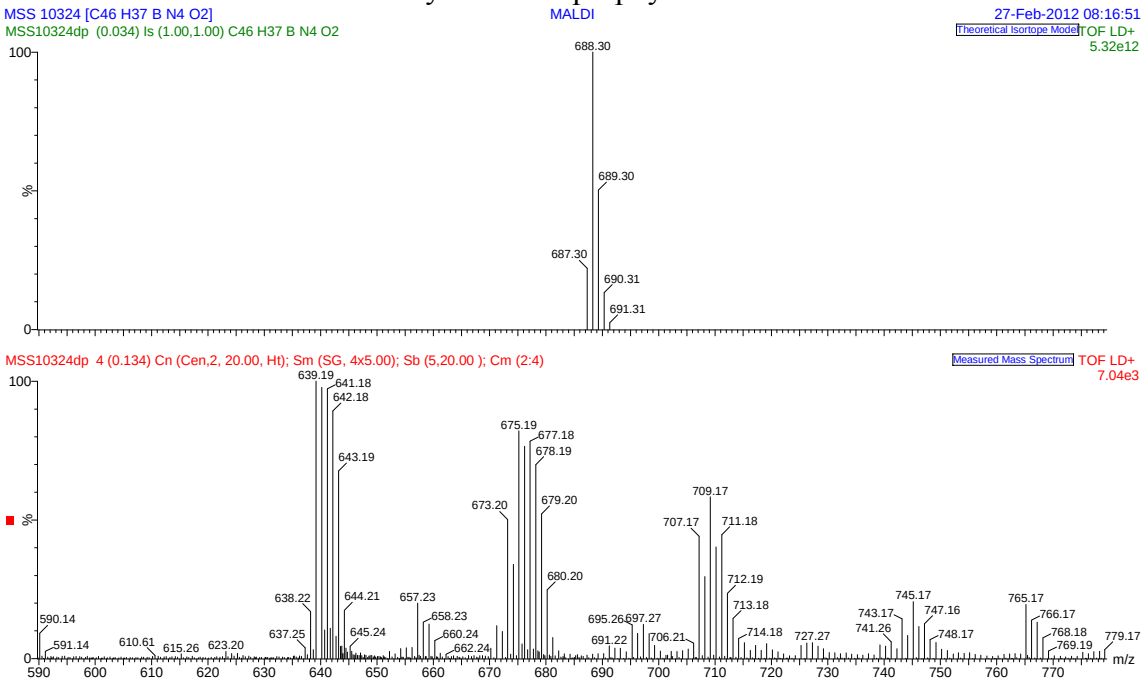

Figure 7.15. MALDI spectrum of porphyrin-boronic acid showing peaks at *m/z* 711.18 $[M+Na]^+$, 745.17 $[M+NH_4+K]^{3+}$.

7.3.6.6 Synthesis of FLAB (**16**) (Scheme 7.12)

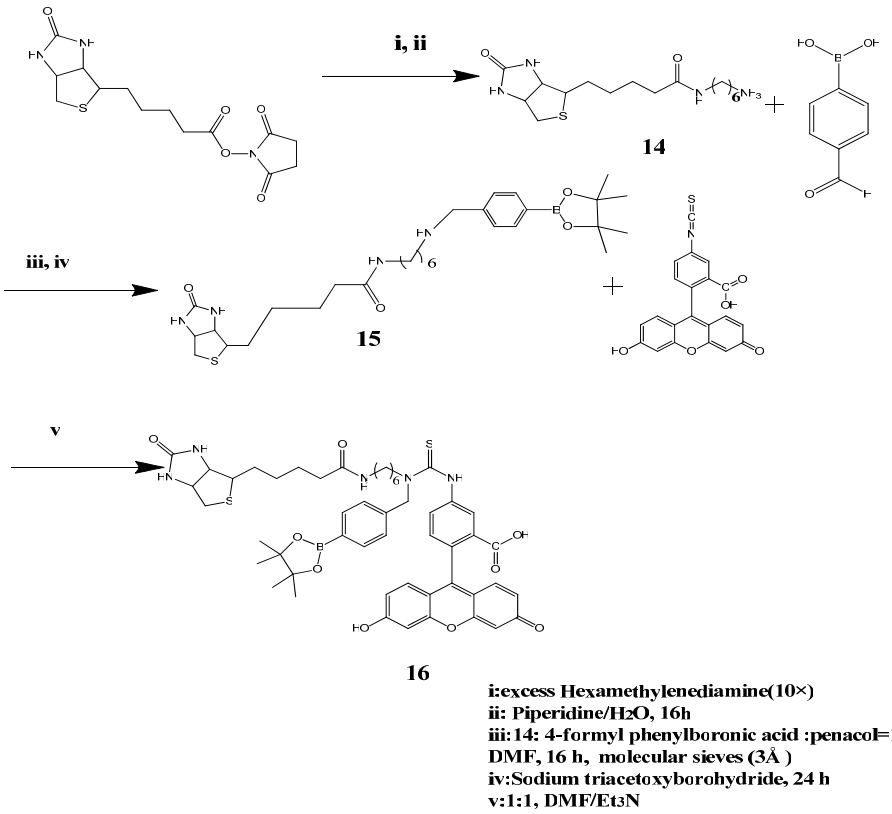

Scheme 7.12. Synthesis of FLAB **16**.

Synthesis of intermediate Compound 14

Biotin *N*-hydroxysuccinimide ester (500 mg) was mixed with excess hexamethylene diamine (5 g) in piperidine/H_2O. The mixture was then stirred overnight. The precipitate thus formed was collected by filtration, washed with diethyl ether and a little dichloromethane, and dried *in vacuo* to give a white solid of **14** (quantitative yield, >90%).

HRMS-ESI$^+$: Calculated for $C_{16}H_{31}N_4O_2S^+$, 343.21 $[M+H]^+$, found: 343.2.

Compound 15

Dried, powdered molecular sieves (3 Å), DMF (10 mL) and compound 13 (490.5 mg, 1.45 mmol) were added to a flask purged with nitrogen. To this flask, 4-formyl phenylboronic acid (217.4 mg, 1.45 mmol) and pinacol (171.35 mg, 1.45 mmol) were added. The mixture was next stirred under nitrogen for 16 h. Sodium triacetoxyborohydride (461 mg,

2.175 mmol) was then added, and then the mixture was stirring for another 24 h. Ethyl acetate was added to this solution for neutralizing and the solvents were evaporated under a high vacuum to give 342.5 mg of crude white solid of compound **15**.

HRMS-ESI+: Calculated for $C_{29}H_{48}BN_4O_4S^+$: 559.34 $[M + H]^+$; found: 559.3.

Compound 16

Fluorescein isothiocyanate (194.69 mg, 0.5 mmol) was dissolved in DMF (20 mL), to which **7** (236 mg, 0.5 mmol) was added, followed by triethylamine (2 mL). The mixture was stirring overnight under nitrogen while being protected from light. Subsequent drying *in vacuo* delivered desired compound **16** as a yellow solid.

^1H {^{13}C}NMR (300 MHz, D4-MeOD) δ: 8.09(1H, s, NH), 7.8(2H, d, *J*2.3), 7.77(1H, d, *J*2.2), 7.11(3H,d, *J*7.5), 6.8(1H,d,*J*9.2), 6.58(1H, d, *J*2.7), 6.49(1H,dd, *J*2.3 and 8.7), 3.24(1H, s), 3.21(2H, m), 3.05(2H, q, *J*7.4 and 14.7), 1.83(2H, d, *J*1.4), 1.2(12H, s), 1.18(4H, d, *J* 14.5). ^{13}C NMR (75 MHz, D4-MeOD) δ: 180.2, 169.1, 172.8, 160.3, 155.9, 145.1, 135.7, 132.3, 129.6, 105.8, 56.9, 36.0, 32.5, 31.9, 30.1, 28.9, 24.6.

^{11}B NMR (d^4-MeOD, 96 MHz): 160.46 ppm.

MALDI-TOF MS (*m/z*) Cacld: $C_{50}H_{57}BN_5O_9S_2^-$, 947.38 $[M-H]^-$, found 947.

Cacld for: $C_{50}H_{58}BN_5O_9S_2Cl^-$, 982.38 $[M+Cl]^-$, found 982.

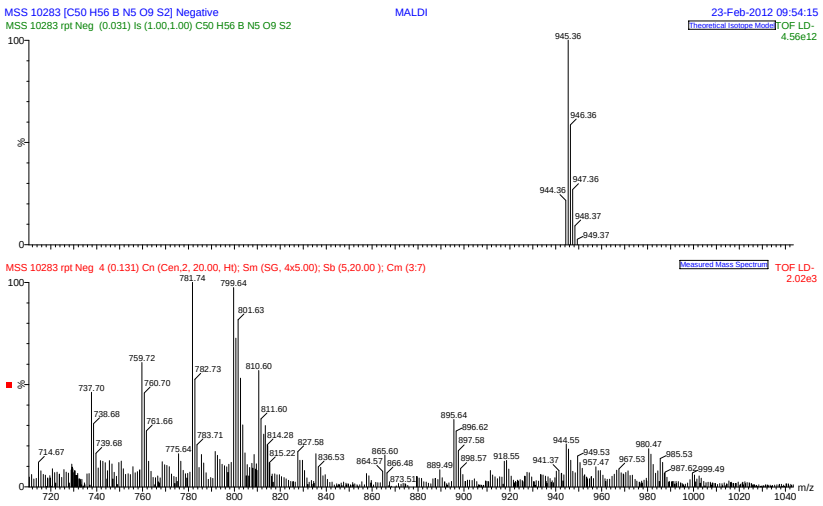

Figure 7.16. MALDI spectrum of **16** showing peaks at *m/z* 947$[M-H]^-$, 982 $[M+Cl]^-$.

7.3.6.7 Fluorescence Titrations of boronic acid fluorophors FLAB, FBA, Coumarin- and porphyrin-boronic acid and *β*-D-glucan

Coumarin was provided by the Prof Tony James group and used as a comparison to prove the generality of the boronic acid-glucan tagging method.

Stock solution of "receptor" (FLAB, FBA, Coumarin and porphyrin-boronic acid) with known molarity was made by dissolving fluorophores in pH 8.21 aqueous buffer. 50 mL working solutions (25 μM FLAB**,** 25 μM FBA, 0.1 μM Coumarin and 33.7 μM porphyrin-boronic acid) were prepared by diluting stock solution with pH 8.21 aqueous methanolic buffer separately.

β -D-Glucan was completely dissolved in pH 8.21 aqueous buffer by heating (50 °C) generated 0.031 mM "guest" solution. Increasing volumes of guest were transferred to 1 mL receptor solution in fluorescent spectroscopy cuvette and leaving 5 minuets for the binding between guest and receptor completely, then same volume of mixture was removed maintaining the total volume unchanged after each titration.

Fluorescence emission spectra were recorded (FLAB (λ_{ex}= 488 nm, λ_{em}= 514 nm), FBA (λ_{ex} = 460 nm, λ_{em}= 543 nm), Coumarin (λ_{ex} = 350 nm, λ_{em} = 377 nm) and porphyrin-boronic acid (λ_{ex} = 490 nm, λ_{em} = 629 nm) after each titration.

7.3.6.8 Titration Data Analysis

The observed stability constants (*K*) with coefficient of determination (r^2) were calculated by the fitting of emission intensity at a single wavelength *versus polys*accharide concentration using custom written non-linear curve fitting (equation *6*) using Origin 8.0 software. Binding constant (*K*) was determined by fitting a 1:1 binding model to I_F/I_{Fmax}.

$$y = (1 + A_1 * A_2 * x) / (1 + A_1 * x) \qquad (6)$$

y: I_F/I_{Fmax}

A_1: K (binding constant of the receptor with the guest)

A_2: I_{Fmin}/I_{Fmax}

x : the concentration of glucan added to fluorophore

I_{Fmin} is the final (mimimum) fluorescence intensity; I_{Fmax} is the initial (maximum) fluorescence intensity; I_F is the fluorescence intensity after addition of particular glucan (guest) concentration.

7.3.6.9 Boronic acid fluorophore binding with β-D-glucan, β-D-glucan@SWNTs or β-D-glucan@metalical atom@SWNT

An aqueous solution containing boronic acid fluorophore was added to the aqueous solution containing glucan@SWNT composites at 7.0 pH and at 9.4 pH. As the borate ion forms covalently bonded complexes with 1, 2-diol and 1, 3-diol groups, it should also form complexes with the side-chain glucose in β-D-glucan from barley used. Scheme7.13 shows the procedure for preparing glucan@SWNT complex and the bonding the fluorescent boronic acid to glucan through the interaction between boronic acid and diol groups.

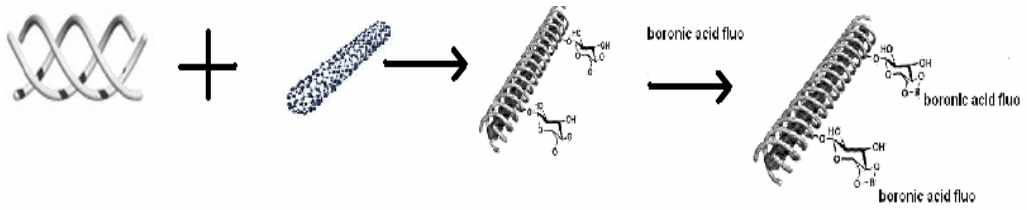

Scheme. 7.13. Basic principle for preparing boronic acid fluorophore@glucan@SWNT, diagram adapted from paper[20].

1M boronic acid fluorophore solutions were prepared by dissolving boronic acid fluorophores (FBA, FLAB, prophyrin boronic acid or coumarin) in pH 8.2 buffer. β-D-glucan, β-D-glucan@SWNT or β-D-glucan@M^{n+}@SWNT composites were dispersed in pH

8.2 buffer. Boronic acid fluorophore buffer solutions were mixed with β-D-glucan, β-D-glucan@SWNTs or β-D-glucan@M^{n+}@SWNT separately . Maintain the reaction stirring at the room temperature for 2 days. Excess fluorophore was removed by filtrate boronic acid fluorophore@β-D-glucan@SWNTs and boronic acid fluorophore@β-D-glucan@M^{n+}@SWNT solution through 2 μm membrane. The black solid on membrane was collected and dried in oven overnight (60 °C).

7.3.6.10 Preparation of glucan-wrapped SWNTs and encapsulation of radio-metal ions from aqueous media

All the "cold" (non-radioactive metal ions) and "hot" (radioactive isotopes of same metals) chemistries were performed in collaboration with the Radiopharmaceutical Chemistry Laboratory of Wolfson Brain Imaging Center (WBIC), University of Cambridge. The SWNTs dispersion before wrapping and filling was carried out in "cold" chemistry laboratory using a sonicator. The β-D-glucan DMSO solution (2 mg/mL) was prepared before radioisotope-filling experiments performed in "hot" cell.

^{64}Cu was produced at the WBIC by the irradiation of a thin layer of ^{64}Ni electroplated on a solid gold internal target plate of the GE PETtrace cyclotron utilizing the nuclear reaction ^{64}Ni(p,n)^{64}Cu and separated from the target material as [^{64}Cu]-$CuCl_2$ by anion chromatography as previously described.[21-24]

The radioactive $^{64}CuCl_2$ was converted to $^{64}Cu(OAc)_2$ a by diluting 0.2 mL $^{64}CuCl_2$ in 0.1 mol dm^{-3} HCl with 0.1 mol mL^{-3} sodium acetate (1.8 mL, pH 5.5).

The radioisotope ions filling and C_{70} capping after filling were performed in standard lead lined "hot cells". Each cell is provided with monitored air extract to protect against gaseous radio-activity leaks into the atmosphere. The radioactivity of radiolabelling samples was counted on a γ-counter (1480 Wizard 3, Perkin–Elmer, Boston, MA). Before

radiolabelling, 2.4 mg purified SWNTs were sonicated in 8 mL EtOH for 30 min and then split into 4 fractions. Solvent was removed by evaporation.

Sample a: Sugar wrapping before radio-metal filling without C_{70} capping the ends of SWNTs.

0.8 mg SWNTs in one fraction were dispersed in 2 mL ddH_2O through sonicating 30 min. SWNTs solution was mixed with 2 mg/mL β-D-glucan DMSO solution and the mixed solution was sonicated for 20 min (mild sonication using a water bath). 50 μL of ~10^{-9} M ^{64}Cu $(OAc)_2$ and 10 mg NaOAc were mixed with glucan@SWNTs solution. Leave radiolabelling reaction stirring at the room temperature for 2 h. After reaction, the un-loaded radioisotope was removed by filtration through syringe 0.45μm membrane. The radioactivities of solid on membrane and filtrate solution were measured by γ- counting. The radiolabelling solid on membrane was washed with excess double-distilled H_2O. The radioactivities of solid on membrane and eluting solution were measured again by γ-counting. Experiment steps above were repeted 4 times and an average measurement reported.

Sample b: Sugar wrapping after radio-metal filling without C_{70} capping the ends of SWNTs

0.8 mg SWNTs in one fraction was dispersed in 2 mL double-distilled H2O through sonicating 30 min. 50 μL of ~10^{-9} M ^{64}Cu $(OAc)_2$ and 10 mg NaOAc were added to SWNTs solution and the radio-reaction continued 2 h. Radiolabeled SWNTs solution was mixed with 2 mg/mL β-D-glucan DMSO solution and the mixed solution was sonicated for 20 min (mild sonication using a water bath). The un-loaded radioisotope was removed by filtration through syringe 0.45μm membrane. The radioactivities of solid on membrane and

filtrate solution were measured by γ- counting. The radiolabelling solid on membrane was washed with excess double-distilled H_2O. The radioactivities of solid on membrane and eluting solution were measured again by γ- counting. Experiment steps above were repeted 4 times and an average measurement reported.

Sample c: Sugar wrapping SWNTs before both radio-metal filling and C_{70} capping the ends of SWNTs

0.8 mg SWNTs in one fraction was dispersed in 2 mL double-distilled H_2O through sonicating 30 min. 50 μL of ~10^{-9} M $^{64}Cu(OAc)_2$ and 10 mg NaOAc were added to SWNTs solution and the radio-reaction continued 2 h. Radiolabeled SWNTs solution was mixed with 0.67 mg/mL C_{70} H_2O dispersion and the mixed solution was sonicated for 5 min (mild sonication using a water bath) and leave it stirring another 1 h. The un-loaded radioisotope was removed by filtration through syringe 0.45μm membrane. The radioactivities of solid on membrane and filtrate solution were measured by γ- counting. The radiolabelling solid on membrane was washed with excess double-distilled H_2O. The radioactivities of solid on membrane and eluting solution were measured again by γ- counting. Experiment steps above were repeated 4 times and an average measurement reported.

Sample d: Sugar wrapping SWNTs after radio-metal filling but before C_{70} capping the end of SWNTs

0.8 mg SWNTs in one fraction was dispersed in 2 mL double-distilled H_2O through sonicating 30 min. 50 μL of ~10^{-9} M $^{64}Cu(OAc)_2$ and 10 mg NaOAc were added to SWNTs solution and the radio-reaction continued 2 h. Radiolabeled SWNTs solution was mixed with 2 mg/mL β-D-glucan DMSO solution and the mixed solution was sonicated for 20 min (mild sonication using a water bath). 0.67 mg/mL C_{70} H_2O dispersion was added to the above

radiolabeled glucan@SWNTs and sonicating for 5 min (mild sonication using a water bath) and leave it stirring another 1 h. The un-loaded radioisotope was removed by filtration through syringe 0.45μm membrane. The radioactivities of solid on membrane and filtrate solution were measured by γ-counting. The radiolabelling solid on membrane was washed with excess ddH_2O. The radioactivities of solid on membrane and eluting solution were measured again by γ- counting. Experiment steps above were repeated 4 times and an average measurement reported.

Sample e: Sugar wrapping SWNTs after both radio-metal filling and C_{70} capping the end of SWNTs

0.8 mg SWNTs in one fraction was dispersed in 2 mL double-distilled H_2O through sonicating 30 min. 50 μL of ~10^{-9} M $^{64}Cu(OAc)_2$ and 10 mg NaOAc were added to SWNTs solution and the radio-reaction continued 2 h. Radiolabeled SWNTs solution was mixed with a 0.67 mg/mL C_{70}/H_2O dispersion and sonicated for 5 min (mild sonication using a water bath) . Mixture was left stirring another 1 h. The above radiolabeled C_{70}@SWNTs solution was mixed with 2 mg/mL β-D-glucan DMSO solution and the mixed solution was sonicated for 20 min (mild sonication using a water bath). The un-loaded radioisotope was removed by filtration through syringe 0.45 μm membrane. The radioactivities of solid on membrane and filtrate solution were measured by γ-counting. The radiolabelling solid on membrane was washed with excess double-distilled H_2O. The radioactivities of solid on membrane and eluting solution were measured again by γ- counting. Experiment steps above were repeated 4 times and an average measurement reported.

7.3.6.11 Cells fluorescence imaging and In vitro fluorescence lifetime imaging (FLIM) of Fluorophores@glucan@SWNTs

Cells (MCF-7 and HeLa cell lines) were seeded in a Petri dish with a glass cover slip (Mattek) and left for 24 h to adhere before fluorescence imaging measurements were made. Prior to imaging, the solution was replaced with 1 mL fresh medium. Fluorophore stock solutions were prepared for live cells fluorescence imaging. 5% v/v stock sample was added to dish. Cell dish was incubated in a 5 % CO_2 humidified atmosphere for 20 min. Surplus supernatant was removed after culturing (containing dead cell matter and excess proteins). Adherent cells were washed with two 5 mL aliquots of phosphate buffer saline solution to remove any remaining medium containing FCS. The uptake of the fluorophore@glucan@SWNTs and fluorophore@glucan by cells were imaged and monitored by using laser-scanning confocal microscopy (LSM 510 META, Zeiss) by tuning the argon ion laser excitation wavelength to 405 nm, 488 nm and 543 nm separately.

After confocal lasing imaging, cells in the same dish was scanned with an external fast microchannel plate photomultiplier tube as the detector.The multiphoton excited image of cell with the associated characteristic decay at each pixel position was generated by a time-correlated single-photon-counting PC module SPC830 (Becker and Hickl) These were linked via a time-correlated single-photon-counting PC module SPC830 (Becker and Hickl) to generate the multiphoton excited image with the associated characteristic decay at each pixel position. The scan was operated in normal mode and line, frame and pixel clock signals were 20 generated and synchronized with an external fast microchannel plate photomultiplier tube used as the detector. FLIM data can be analysed using the SPCImage analysis software (Becker and Hickl).

7.3.7 Synthesis of a thermal reduced graphene oxide-amino acid naphthalene diimide complex

7.3.7.1 Graphene oxide (GO) synthesis, thermal exfoliation and reduction of GO to give TRG

Graphite oxide is synthesized from graphite powder (SP-1 grade 325 mesh, Bay Carbon Inc.) by the modified Hummers method.[25] Graphite oxide is synthesized from natural graphite powder (Fluka 50870) by the Hummers method using $NaNO_3$, H_2SO_4, and $KMnO_4$. 10 g of powdered graphite and 5 g $NaNO_3$ was added to concentrate H_2SO_4 (50 mL). The mix was cooled to 0 °C using an ice bath. 30 g of $KMnO_4$ was added to the suspension slowly while maintaining the suspension vigorous agitation and controlling the temperature of suspension not exceeding 20 °C. The temperature went up to 35 °C after remove ice-bath and keeping the stirring 30 min. After oxidation, 500 mL double-distilled H_2O was added carefully and temperature was increased to near 100 °C. The color eventually turned to brown from dark. After 15 min, the diluted suspension was continuing diluted to 1.5 L. Then the suspension was treated with 30% H_2O_2 for reducing the MnO_4 and MnO_2 to soluble manganese sulfate. The suspension was filtered 3 times with total 4.5 L double-distilled H_2O. The filter flake was dispersed in double-distilled H_2O again and dried in vacuum oven overnight. The dried product was diluted to make a 2% w/v dispersion that is put through dialysis for 2 weeks to remove any remaining salt. This product was dehydrated in at 40 °C over phosphorus pentoxide under *vacuum***.** For the preparation of graphene oxide dispersions in H_2O, the dried product was diluted with double-distilled H_2O to make a 2 % w/v dispersion and sonicated in an ultrasound bath cleaner (J. P. Selecta Ultrasons system, 40 kHz) for 1 h. The suspension was centrifuged at 3000 rpm 5 h. The supernatant was taken and left settling for 1 month after which the clear supernatant was used for next experiments.

2 mg of GO powder was made by freeze drying of GO suspension overnight. GO powder was then thermally exfoliated and reduced in a tubular furnace under N_2 flow (300 mL min^{-1}) to 900 °C (15 °C min^{-1}), to obtain graphene-oxide annealed, labeled TRG.

7.3.7.2 Synthesis of the complex NDI@TRG

1 mg of TRG synthesized as above was dispersed in 5 mL toluene or $CHCl_3$ through 1 h ultrasonication treatment (50/60 Hz), and then the mixture was centrifuged with ×10000 rpm speed to remove the aggregate leaving the supernatant for next use. 4 mg of NDI was added to this clear TRG suspension then sonicate for another 5 min and then leave it stirring for overnight. Then the solution was filtered through a 0.22 μm PTFE membrane which can be use to redisperse readily the deposited solid in organic solvents by ultrasonication.

7.3.7.3 Thermogravimetric analyses (TGA)

Thermogravimetric analyses (TGA) of sample was performed on a Pyris Diamond TG/DTA Thermogravimetric Analyzer (Perkin-Elmer Thermal Analysis). Sample was heated under nitrogen atmosphere (gas flow 20 mL/min) from 45 °C temperature to 600 °C at 5 °C min^{-1}.

7.4 References for Chapter 7

(1) Cosier, J.; Glazer, A. M. *J. Appl. Crystallogr.* **1986**, *19*, 105.

(2) Otwinowski, Z.; Minor, W. *Methods Enzymol.* **1997**, *276*, 307.

(3) Altomare, A.; Cascarano, G.; Giacovazzo, C.; Guagliardi, A. *J. Appl. Crystallogr.* **1993**, *26*, 343.

(4) Sheldrick, G. M. *Acta Crystallogr., Sect. A: Found. Crystallogr.* **2008**, *A64*, 112.

(5) Frederiksen, T.; Paulsson, M.; Brandbyge, M.; Jauho, A.-P. *Phys. Rev. B: Condens. Matter* **2007**, *75*.

(6) Ceperley, D. M.; Alder, B. J. *Phys. Rev. Lett.* **1980**, *45*, 566.

(7) Hamann, D. R.; Schluter, M.; Chiang, C. *Phys. Rev. Lett.* **1979**, *43*, 1494.

(8) Troullier, N.; Martins, J.; eacute; Luriaas *Phys. Rev. B: Condens. Matter* **1991**, *43*, 1993.

(9) Junquera, J.; Paz, Ó.; Sánchez-Portal, D.; Artacho, E. *Phys. Rev. B: Condens. Matter* **2001**, *64*, 235111.

(10) Hebenstreit, J.; Heinemann, M.; Scheffler, M. *Phys. Rev. Lett.* **1991**, *67*, 1031.

(11) Pascu, S. I.; Kuganathan, N.; Tong, L. H.; Jacobs, R. M. J.; Barnard, P. J.; Chu, B. T.; Huh, Y.; Tobias, G.; Salzmann, C. G.; Sanders, J. K. M.; Green, M. L. H.; Green, J. C. *J. Mater. Chem.* **2008**, *18*, 2781.

(12) Boys, S. F.; Bernardi, F. *Mol. Phys.* **1970**, *19*, 553.

(13) Pascu, S. I.; Waghorn, P. A.; Conry, T. D.; Betts, H. M.; Dilworth, J. R.; Churchill, G. C.; Pokrovska, T.; Christlieb, M.; Aigbirhio, F. I.; Warren, J. E. *Dalton Trans.* **2007**, 4988.

(14) Mosmann, T. *J. Immunol. Methods* **1983**, *65*, 55.

(15) Caspar, J. V.; Meyer, T. J. *J. Am. Chem. Soc.* **1983**, *105*, 5583.

(16) Zwick, W. R.; Velicer, W. F. *Psychol. Bull.* **1986**, *99*, 432.

(17) Perrin, D. D.; Dempsey, B. In *Buffers for pH and Metal Ion Control* 1974, p 176.

(18) Ballesteros, B.; Tobias, G.; Shao, L.; Pellicer, E.; Nogues, J.; Mendoza, E.; Green, M. L. H. *Small* **2008**, *4*, 1501.

(19) Tobias, G.; Shao, L.; Salzmann, C. G.; Huh, Y.; Green, M. L. H. *J. Phys. Chem. B* **2006**, *110*, 22318.

(20) Tamesue, S.; Numata, M.; Kaneko, K.; James, T. D.; Shinkai, S. *Chem.Commun.* **2008**, 4478.

(21) McCarthy, D. W.; Shefer, R. E.; Klinkowstein, R. E.; Bass, L. A.; Margeneau, W. H.; Cutler, C. S.; Anderson, C. J.; Welch, M. J. *Nucl. Med. Biol.* **1997**, *24*, 35.

(22) Obata, A.; Kasamatsu, S.; McCarthy, D. W.; Welch, M. J.; Saji, H.; Yonekura, Y.; Fujibayashi, Y. *Nucl. Med. Biol.* **2003**, *30*, 535.

(23) Avila-Rodriguez, M. A.; Nye, J. A.; Nickles, R. J. *Appl. Radiat. Isot.* **2007**, *65*, 1115.

(24) Hou, X. L.; Jacobsen, U.; Jorgensen, J. C. *Appl. Radiat. Isot.* **2002**, *57*, 773.

(25) Hummers, W. S.; Offeman, R. E. *J. Am. Chem. Soc.* **1958**, *80*, 1339.

Chapter 8 Appendix

8.1 Appendix for Chapter 2

8.1.1 General experiments

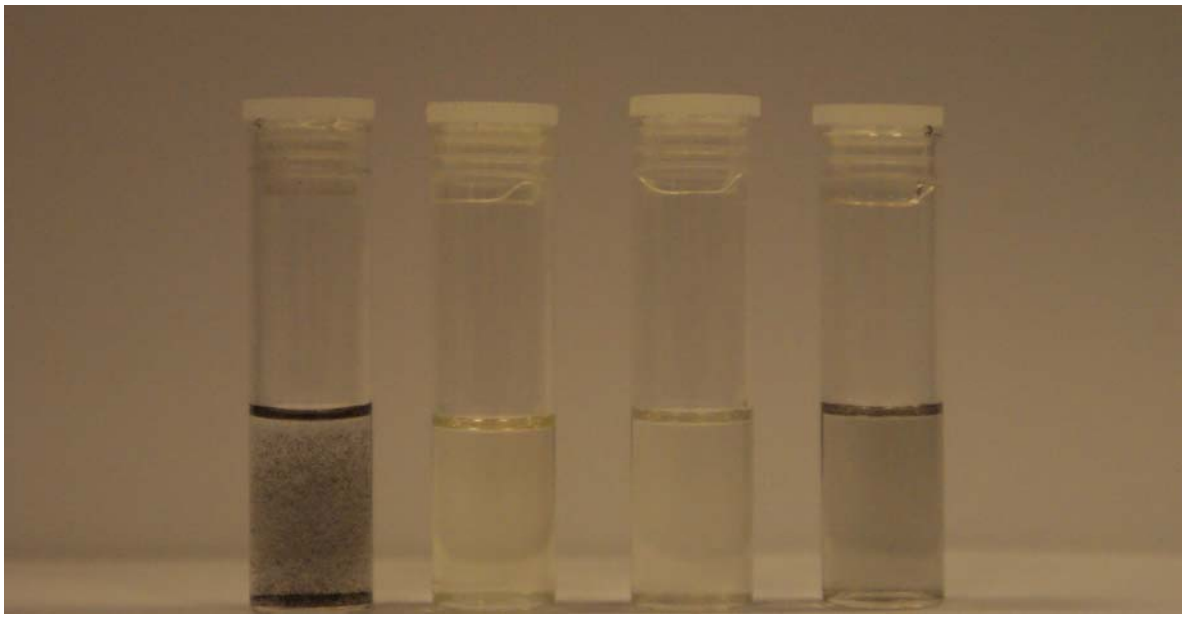

a **b** **c** **d**

Figure 8.1. Materials studied as solutions (NDI) or dispersions in 2 mL $CHCl_3$:EtOH 4:1. **a**) 0.7 mg SWNT; **b**) 42 μg NDI (26 μM); **c**) NDI@SWNT composite obtained on a preparative scale after 4 cycles of filtration, and redispersed at 0.2 mg/mL conc. **d**) NDI@SWNT 'fresh' composite formed in situ by anchoring 42 μg NDI (26 μM) onto 70 μg SWNTs.

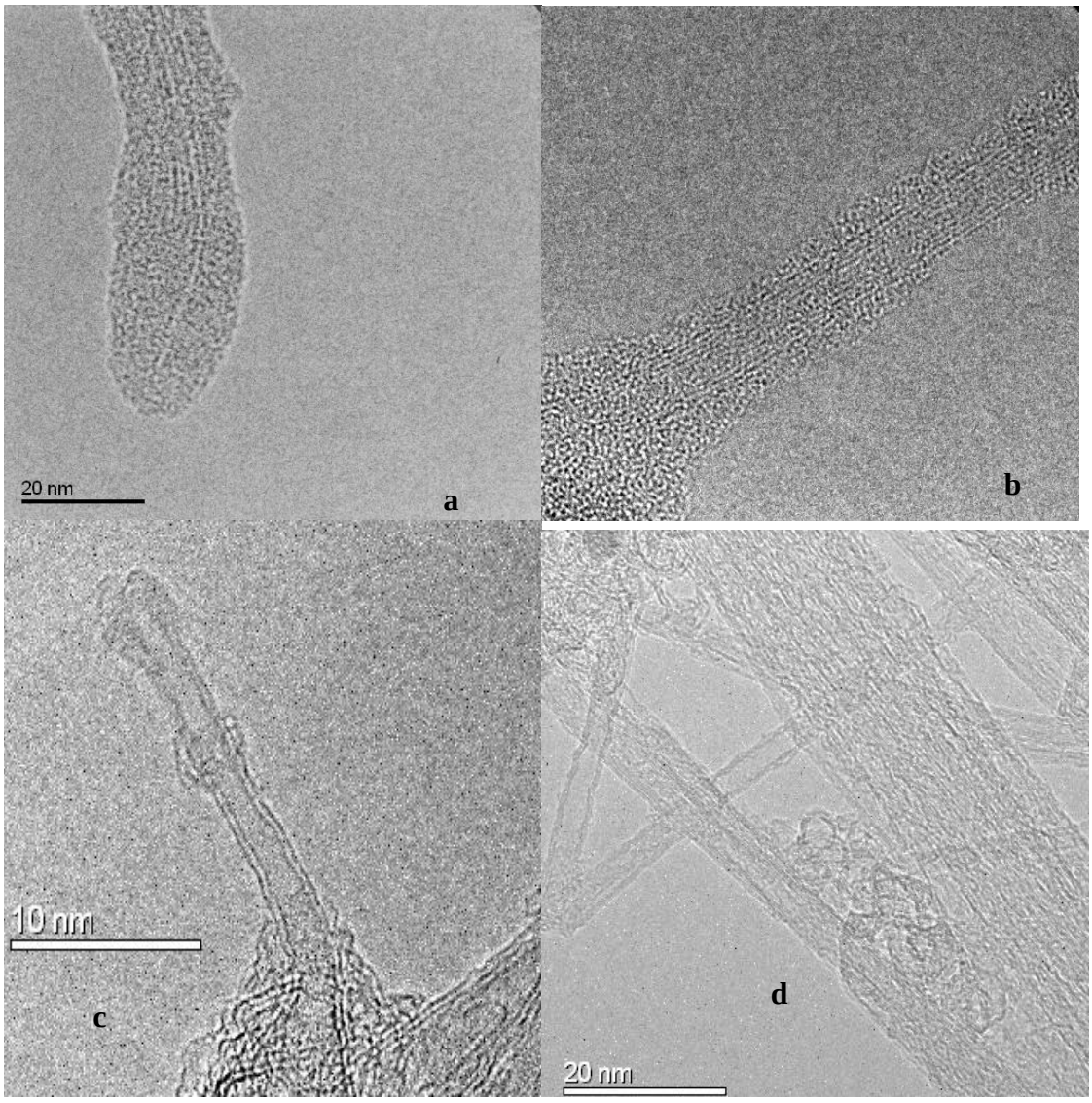

Figure 8.2. High resolution transmission microscopy: **a-c:** Typical HR TEM images of the NDI@SWNT composite showing the uniform coating of SWNTs, including its tips (**a** and **b**), and the presence of 'dark dots' assignable to the heavy element iodine (Z = 53) in uniform layers on the aromatic surface; **d:** TEM of free, purified, SWNT used.

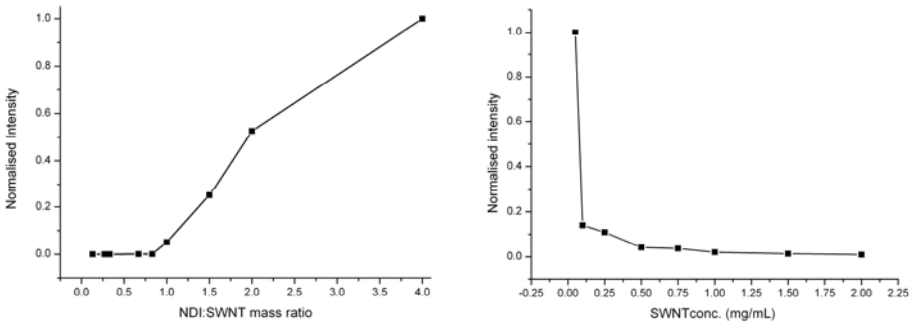

a **b**

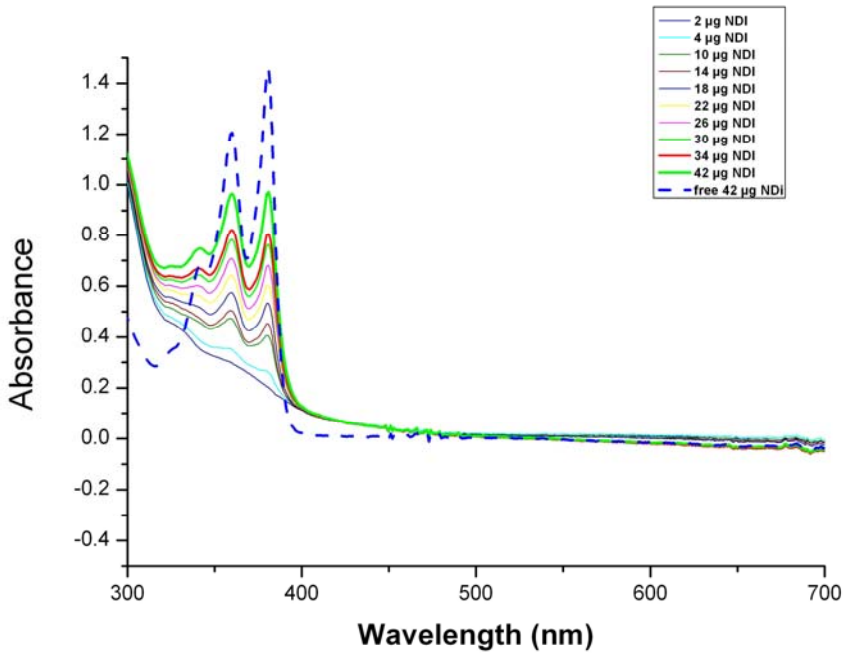

c

Figure 8.3. Fluorescence titrations ($CHCl_3$: EtOH) of NDI onto SWNTs dispersions (**a**) and of SWNTs (total 35 µg/mL, added as 10 µl aliquots) onto a 26 µM solution of NDI (**b**). UV-Vis titrations of NDI onto SWNTs dispersions (35 µg/mL SWNT in $CHCl_3$: EtOH 4:1) (**c**). Fluorescence spectroscopy showed a qualitatively full quenching of fluorescence was observed when a small amount of SWNT was added (**b**). This qualitative observation is indicative of close NDI–SWNTs contacts but the titration data did not allow reliable estimation of the association constant. Data was used to estimate a NDI: SWNT mass ratio which allowed complete coverage and minimum free (unbound) NDI in solution. The proposed ratio NDI: SWNT =0.6 was further verified by UV-Vis titrations (**c**) of NDI onto SWNTs dispersions and used in further experiments.

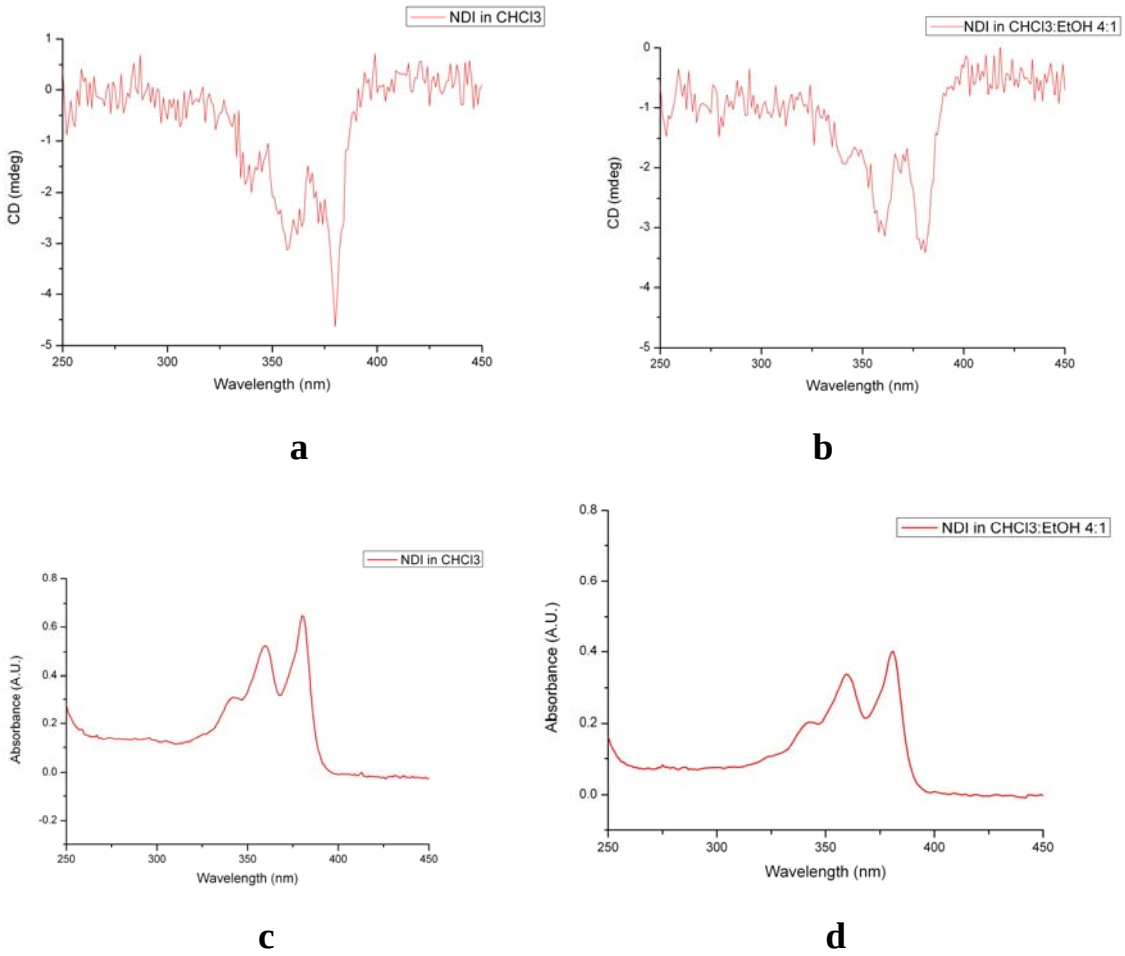

Figure 8.4. Circular Dichroism (top row, **a** and **b**) and UV-Vis (bottom row, **c** and **d**) spectroscopy for fresh solution (recorded within 20 min in solution) of free NDI, 26 μM in $CHCl_3$: EtOH 4:1 and in pure $CHCl_3$ solutions.

8.1.2 Cell culture and fluorescence imaging for FEK-4, HeLa, HT801 and MCF-7 cell lines

In general cells were cultured at 37 ^{o}C in a humidified atmosphere of 5% CO_2 in air and split once confluence had been reached. Cells were cultured in EMEM medium (Eagle's Modified Essential Medium) with foetal calf serum (FCS) (10% for HeLa and MCF-7 and 15% for FEK-4, 200 U mL^{-1} L-glutamine and 100 U mL^{-1} penicillin. The medium contained no fluorescent indicator dyes such as phenol red and was therefore suitable for use in fluorescent studies.

Samples for live cells fluorescence imaging were prepared as described below. Surplus supernatant after culturing (containing dead cell matter and excess proteins) was discarded. The live adherent cells were then washed with two 5 mL aliquots of phosphate buffer saline solution to remove any remaining medium containing FCS (since this contains protease inhibitors which inactivate trypsin, thus inhibiting the resuspension of the cells). To re-suspend the cells in solution, they were incubated in 3 mL of trypsin–EDTA (500 mg L^{-1} trypsin, 200 mg L^{-1} EDTA) solution for 5 min at 37 ^{o}C. After trypsinizing, fresh EMEM was added to the suspended cells to give a sufficient concentration of cells. The concentration of cells required varies between cell lines and is chosen to be optimal for achieving sufficient coverage and optimal imaging. Cells were maintained at 37 °C in a 5 % CO_2 humidified atmosphere and grown to approximately 85 % confluence before being split using 0.25 % trypsin. For microscopy, cells were seeded onto chambered coverglass slides and incubated for 12 h to ensure adhesion. Prior to imaging, the solution was replaced with 1 mL fresh EMEM. Background autofluorescence was measured by imaging the cells in 1 mL of EMEM medium only. Final concentrations on cell plates used:

a) 21 μg/mL NDI (26 μM in 1: 99% DMSO: EMEM);

b) NDI@SWNT composite dispersion (in 1: 99% DMSO : EMEM) containing 21 μg/mL NDI (26 μM 'anchored' onto 35 μg/mL SWNT);

c) 35 μg/mL free SWNT scaffold (dispersed in 1: 99% DMSO: EMEM).

Fixed cell imaging: Cells cultured as above were plated in a Petri dish containing a glass cover slip. Before fluorescence imaging, the serum containing medium was replaced with SFM. After addition of compound, cells were fixed by inverting the coverslip placing it onto 50 μL of paraformaldehyde dissolved in PBS (4%). After 15 min, the coverslip was mounted to a slide using Vectashield®, hard set mounting medium with DAPI (Vector Laboratories, Inc.). A similar standard procedure to that described above was used for

imaging fixed cells, and for this an additional background image was collected (using untreated cells) at the end of experiment.

The uptake of the NDI@SWNT composite was imaged by single-photon laser-scanning confocal microscopy (TCS NT, Leica), using the 488 nm line of an argon ion laser for excitation and the emission was long pass filtered (515 nm) and detected with a photomultiplier tube. The intensity of the laser was modified to reduce the possibility of photobleaching of the florophore over time and the PMT voltage adjusted to be just above the auto-fluorescence limit of the starting conditions (for imaging of living cells) effectively recording a background image before addition of compound, whilst maximizing sensitivity and ensuring optimal focusing.

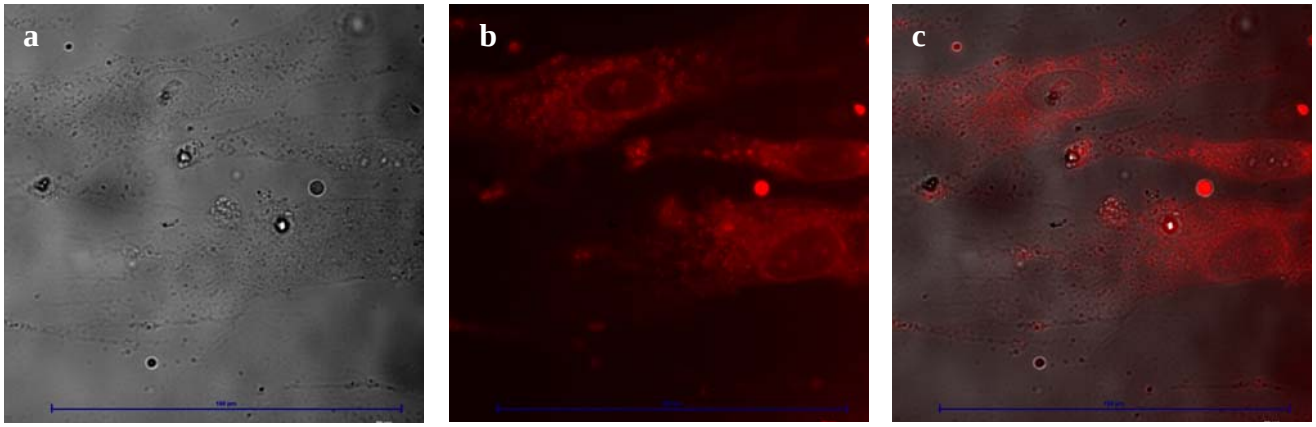

Figure 8.5. Epifluorescence imaging λ_{ex} = 450-500 nm of healthy FEK-4 cells incubated for 2 h at 37 ^{o}C with an NDI@SWNT composite dispersion (in 1: 99% DMSO: EMEM) containing 21 μg/mL NDI (26 μM) 'anchored' onto 35 μg/mL SWNT. Scalebar = 100 μm. Brightfield, fluorescence emission and overlaid micrograph

For both live cells, or fixed cells, formation of endosomes of ca. 300-400 nm was evident by both brightfield and fluorescence imaging inside the cytoplasm, but the largest NDI@SWNT aggregates (ca 1 μm) did not appear to cross the outer membrane and remained attached to the outside of the cell. After exposure to NDI@SWNT the cell membrane did not show any significant disruption. The composites do not seem to cross the perinuclear

membrane within 24 h uptake. In contrast, when the experiment was repeated using free NDI, this distributed both inside the cytoplasm and cell nucleus and visibly altered the cell membrane morphology within 1 h. Notably, the confocal imaging of the same cells using λ_{ex} 405 nm did not show fluorescence emission for either free NDI or NDI@SWNTs.

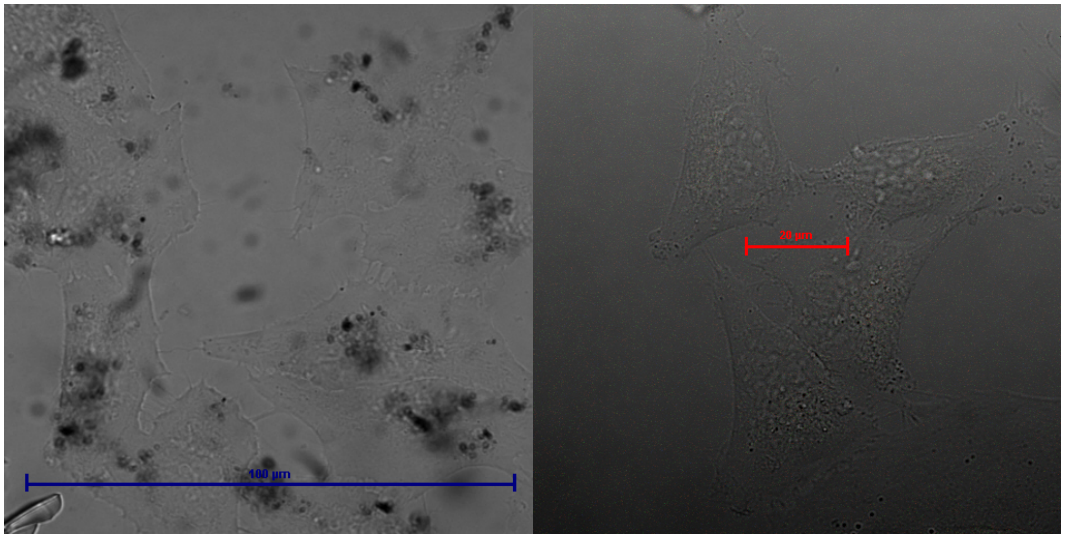

Figure 8.6. DIC images of HeLa cells incubated for 2 h at 37 ^{o}C in 1: 99% DMSO : serum free medium EMEM containing 0.35 µg/mL SWNT (left) and control experiment showing live HeLa cells prior to imaging, after incubation 37 ^{o}C in cells medium containing with 1% DMSO (right)

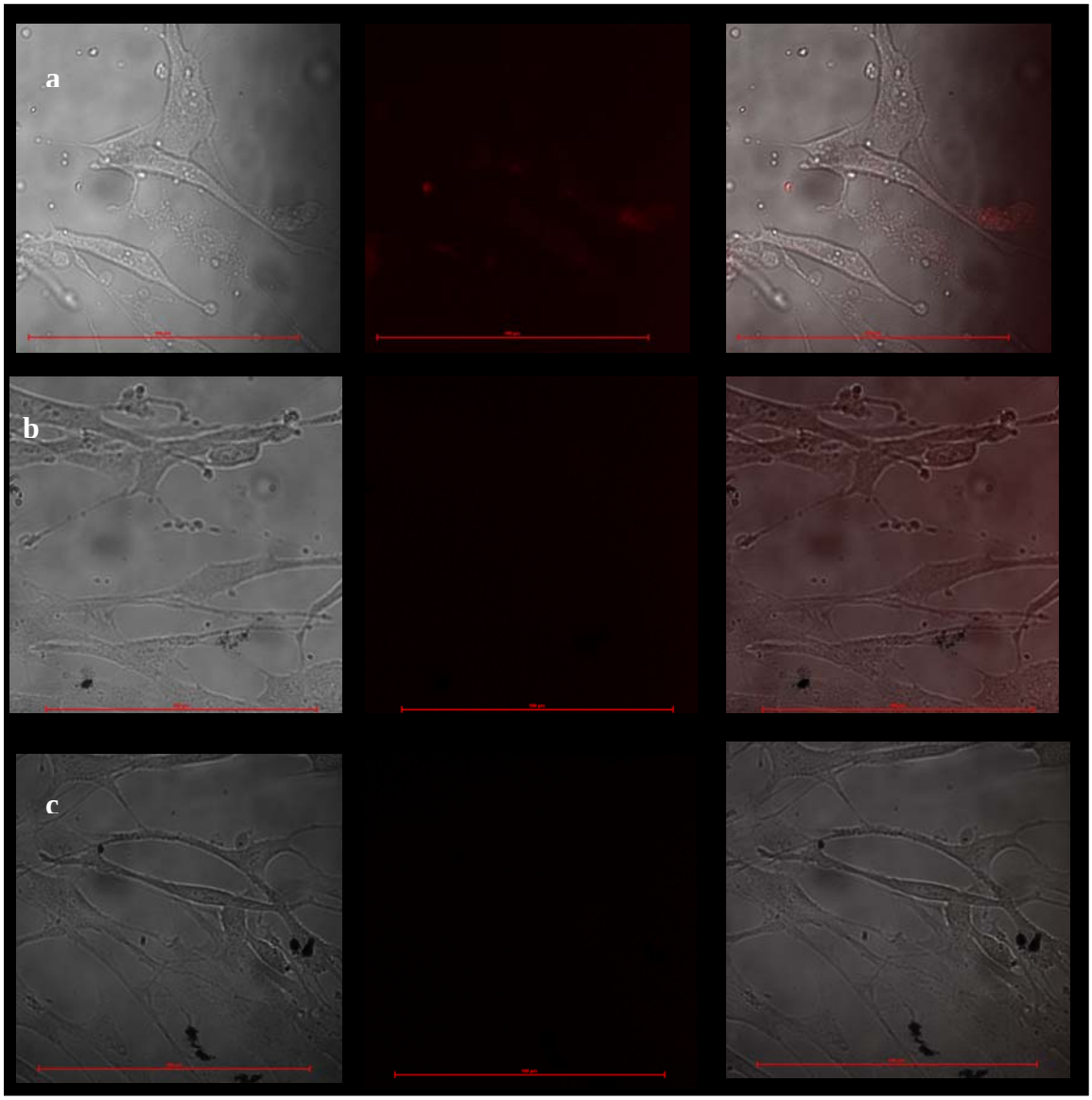

Figure 8.7. Epifluorescence images showing brightfield, fluorescence emission and overlaid micrographs (λ_{ex} = 450-500 nm) of FEK-4 cells incubated for 2 h at 4 ^{o}C with: **a**) 21 μg/mL NDI (26 μM in 1: 99% DMSO : EMEM); **b**) NDI@SWNT composite dispersion (in 1: 99% DMSO : EMEM) containing 21 μg/mL NDI (26 μM) 'anchored' onto 35 μg /mL SWNT; **c**) 35 μg /mL free SWNT scaffold (dispersed in 1: 99% DMSO : EMEM). Scalebar = 100 μm.

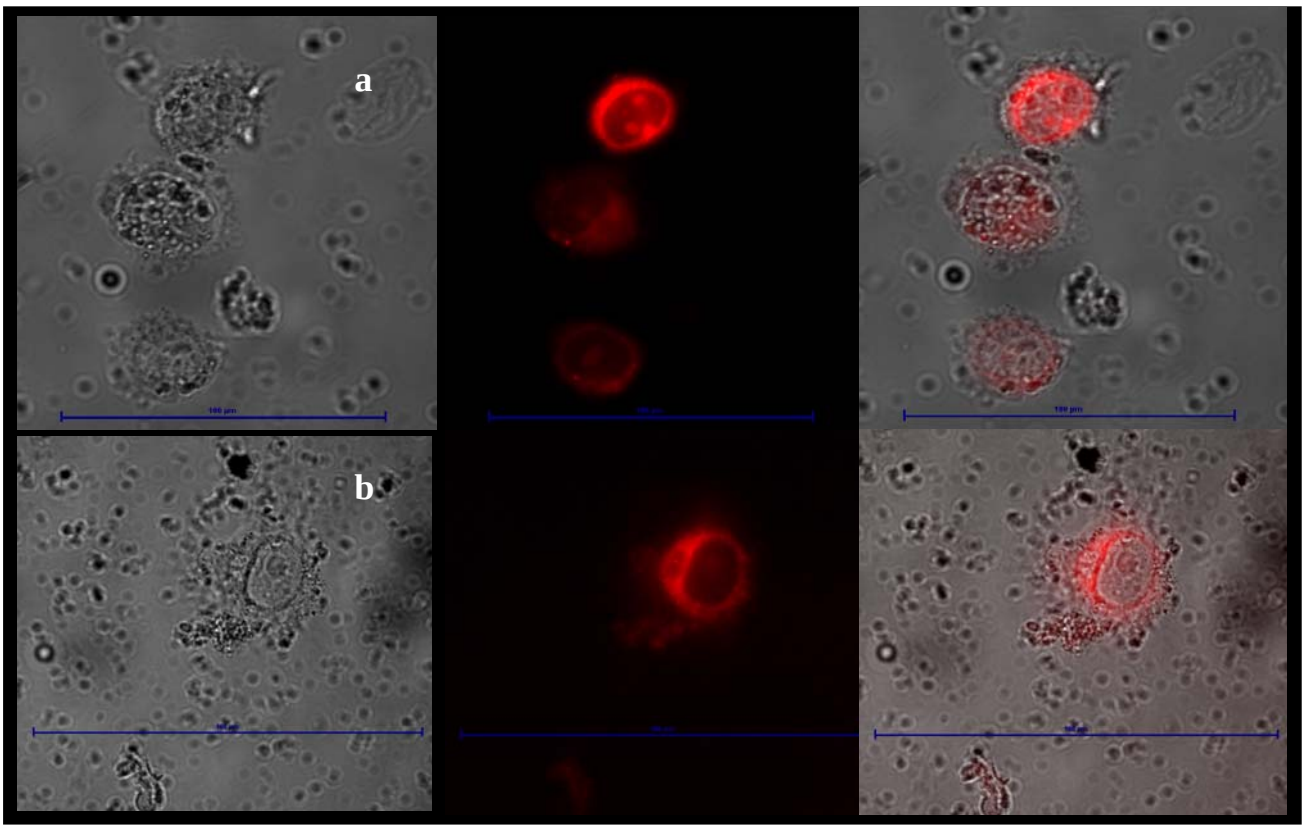

Figure 8.8. Epifluorescence imaging showing brightfield, fluorescence emission and overlaid micrographs (λ_{ex} = 450-500 nm) of MCF-7 cells incubated for 2 h at 37 ^{o}C with: **a)** 21 μg/mL NDI (26 μM in 1: 99% DMSO: EMEM); **b)** NDI@SWNT composite dispersion (in 1: 99% DMSO: EMEM) containing 21 μg/mL NDI (26 μM 'anchored' onto 35 μg/mL SWNT). Scalebar = 100 μm. Images show nuclear uptake for free NDI and the deterioration of cell morphology within 2 h incubation..

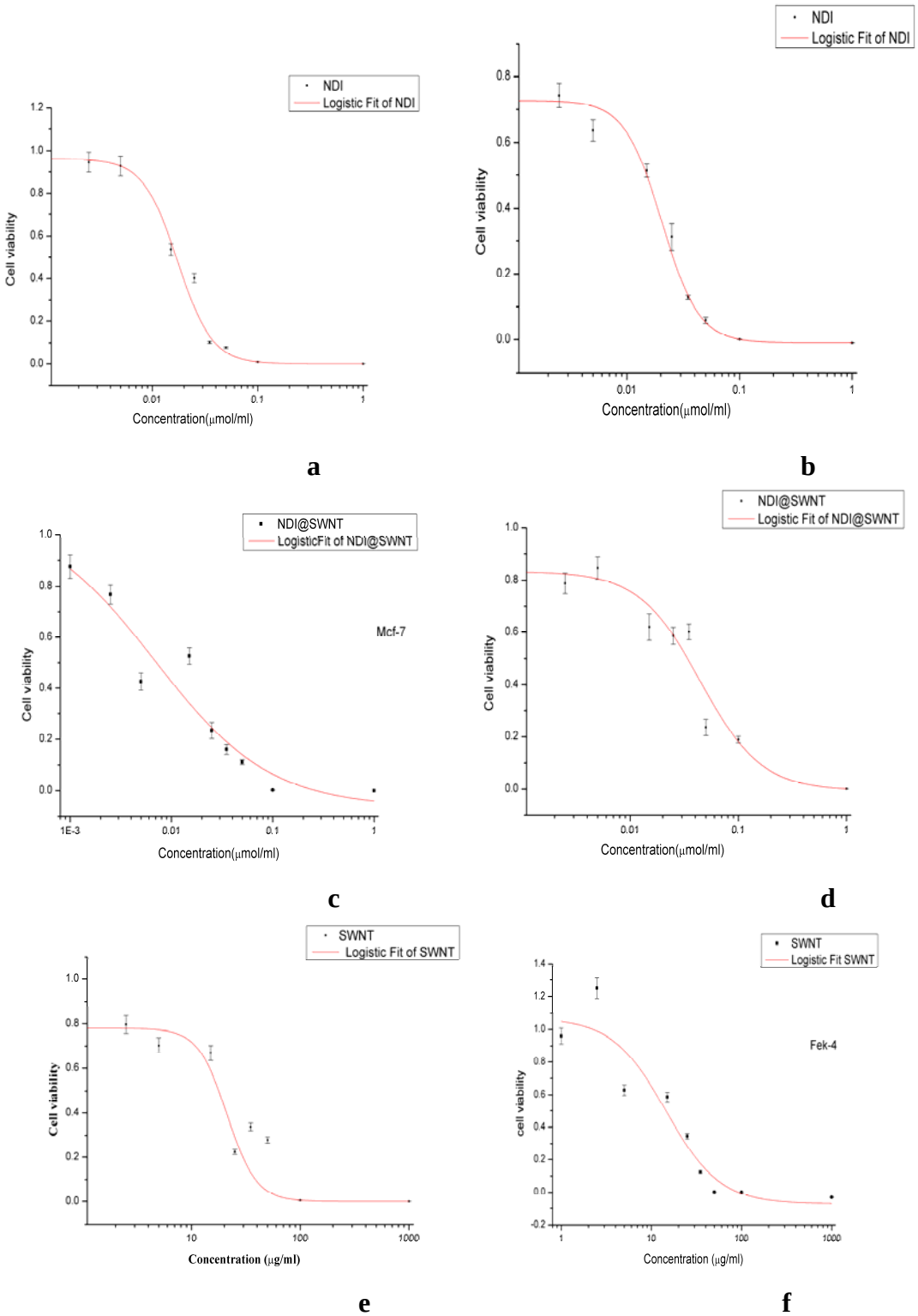

Figure 8.9. MI_{50} determinations from MTT assays in healthy and in cancerous cells: **a)** NDI uptake in MCF-7 cells by MTT assays, **b)** NDI uptake in FEK-4 cells by MTT assays, **c)** NDI anchored onto SWNT (NDI@SWNT): uptake in MCF-7 cells by MTT assays (mass ratio was kept constant over the range of concentrations used, NDI:SWNT = 0.6),**d)** NDI anchored onto SWNT (NDI@SWNT): uptake in FEK-4 cells by MTT assays (mass ratio was kept constant over the range of concentrations used was NDI:SWNT = 0.6),**e)** SWNTs uptake in MCF-7 cells by MTT assays **f)** SWNTs uptake in MCF-7 cells by MTT assays

8.2 Appendix for Chapter 3

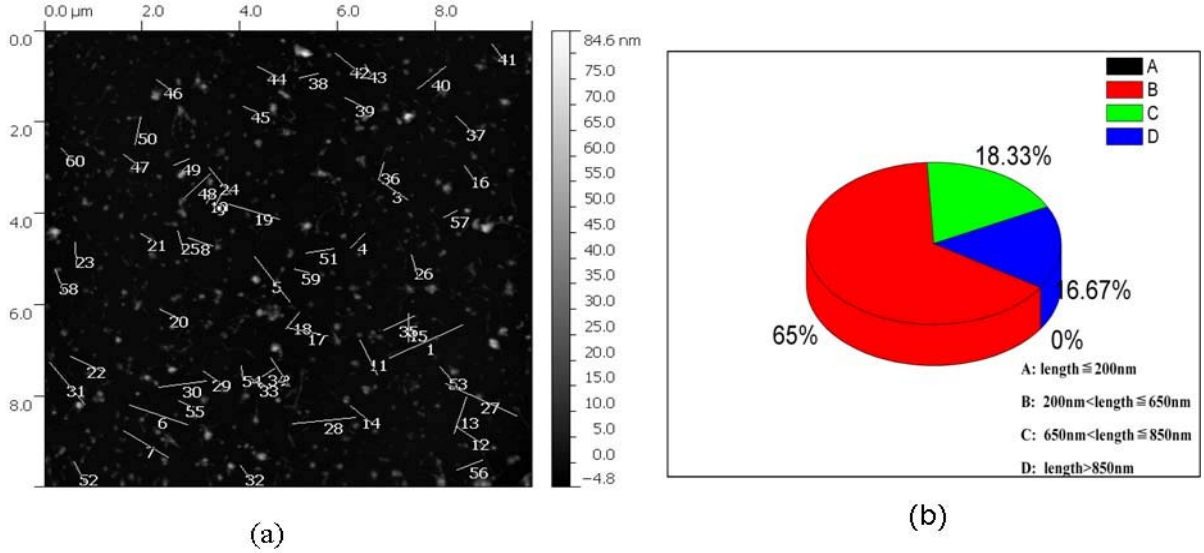

Figure 8.10. Distribution of T12@SWNT length in this AFM imaging.

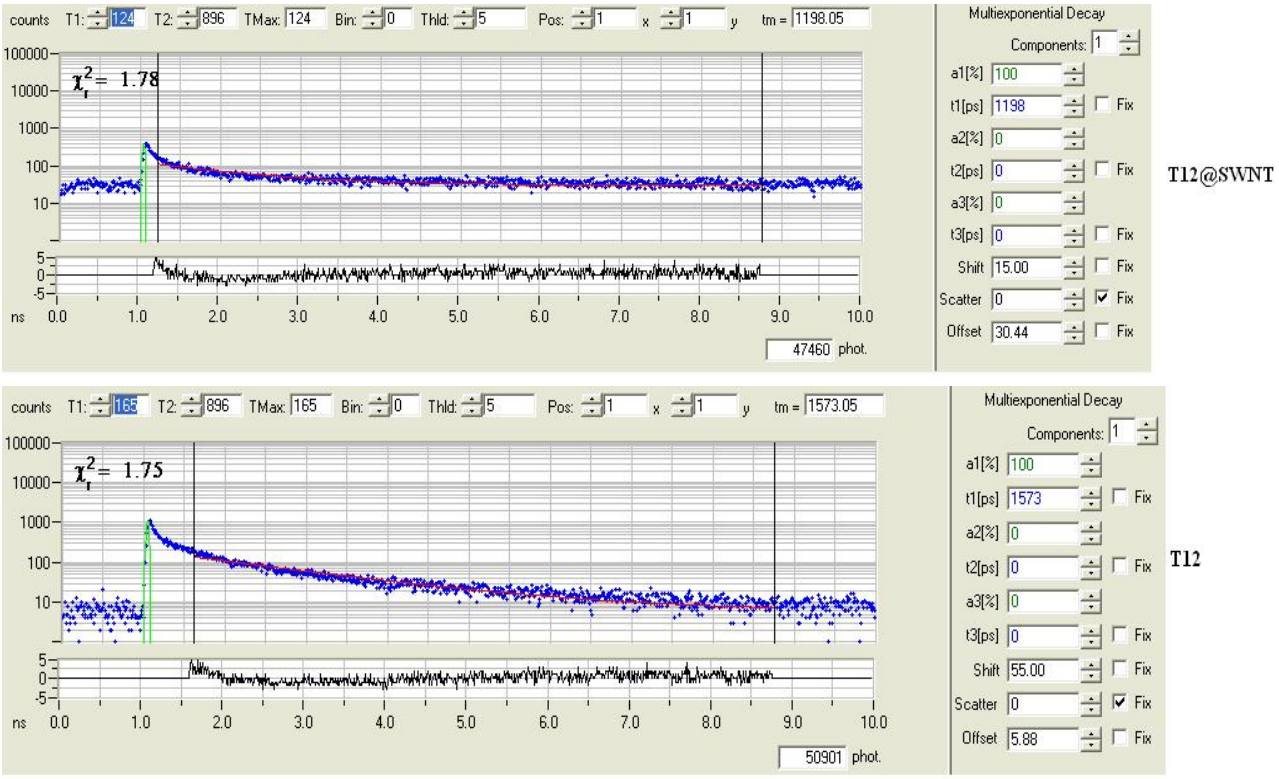

Figure 8.11. Fitted 2 photon excitation (λ_{ex}= 910 nm) FLIM decay curves for T12@SWNT and T12 in DMSO. (T12: 7.5 nM or 27.3 µg/mL T12 in pure DMSO, T12@SWNT composite dispersion containing 27.3 µg/mL T12 (7.5 nM) anchored onto 70 µg/mL SWNT).

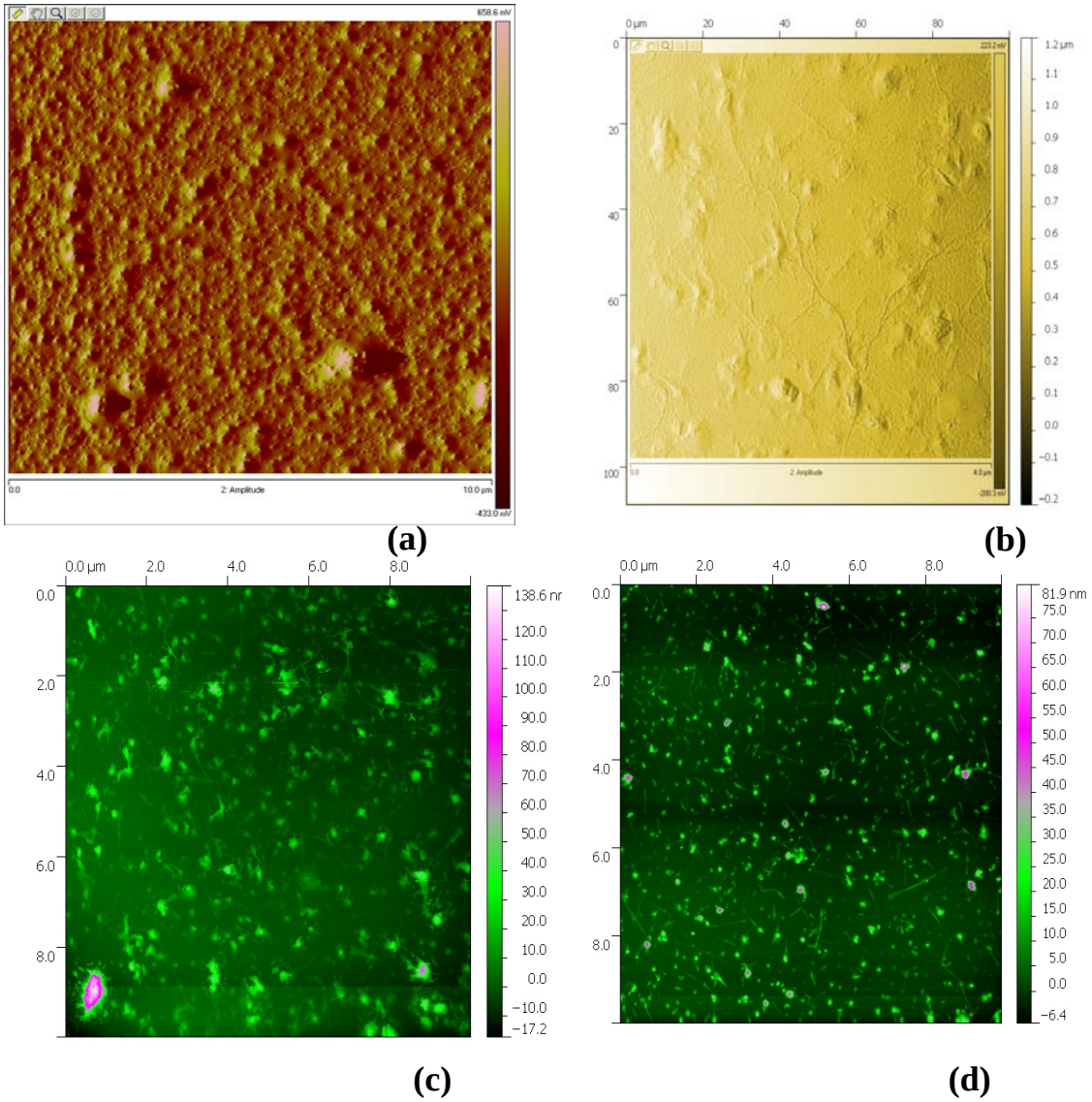

Figure 8.12. AFM imaging of T12@SWNT **(a)** original solution(mixture of SWNTs (0.1 mg) and the T12 polymer (0.1 mg) in $CHCl_3$ (4 mL), **(b)** after the first filtration/dispersion treatment, **(c)** after the second filtration/dispersion treatment and **(d)** after the third filtration/dispersion treatment

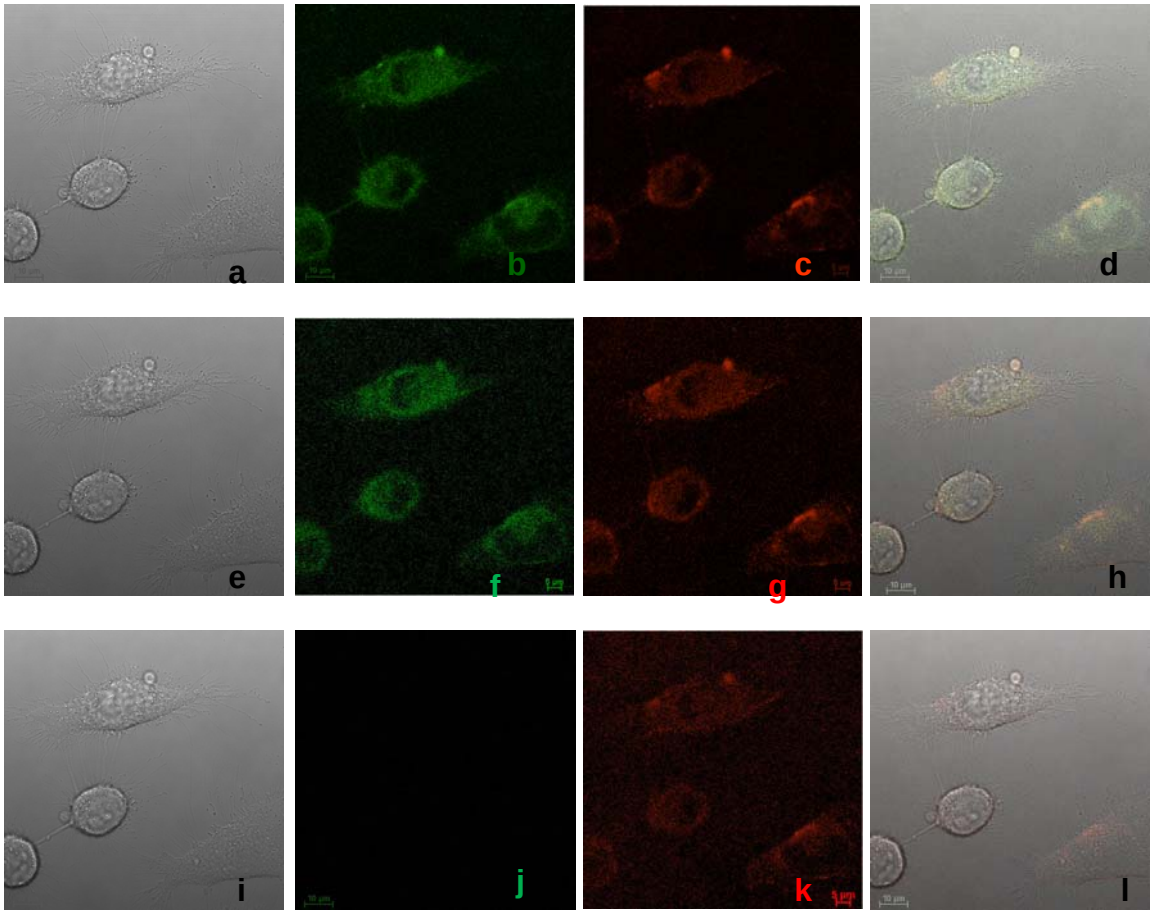

Figure 8.13. Single Photon Laser scanning confocal imaging of cancerous (HeLa) cells incubated at 37 ^{o}C for 20 min with T12 (1.92 nM or 7 µg/mL in 5: 95% DMSO: EMEM), **(a-d)** λ_{ex} = 405 nm, showing DIC (**a**), green channel (b), red channel (605-675 nm) (c) and DIC-green-red channel overlay (**d**). **(e-h)** λ_{ex}= 488 nm, showing DIC (**e**), green channel (515-530 nm) (**f**), red channel (605-675 nm) (**g**) and DIC-green-red channels overlay (**h**). **(i-l)** λ_{ex} = 543 nm, showing DIC (**i**), green channel (515-530 nm) (**j**), red channel (605-675 nm) (**k**) and DIC-green-red channels overlay (**l**), Scalebar 5 µm.

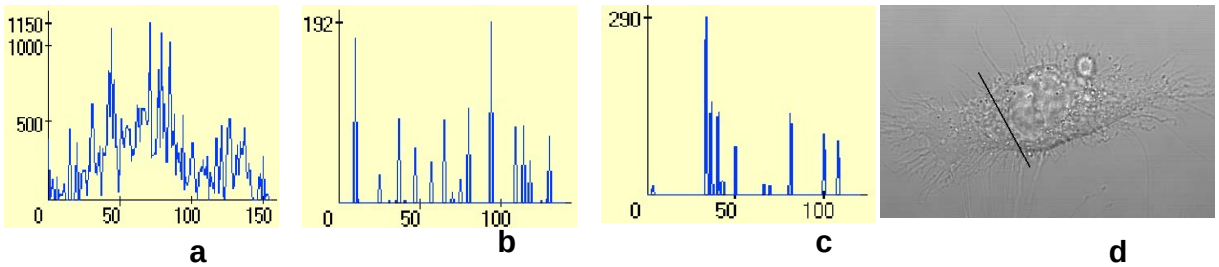

a **b** **c** **d**

Figure 8.14. Fluorescent Intensity profile of HeLa cells **(d)** incubated at 37 ^{o}C for 20 min with T12 (1.92 nM or 7 µg/mL in 5: 95% DMSO: EMEM**) (a)** λ_{ex} = 405 nm, **(b)** λ_{ex} = 488 nm and **(c)** λ_{ex} = 543 nm

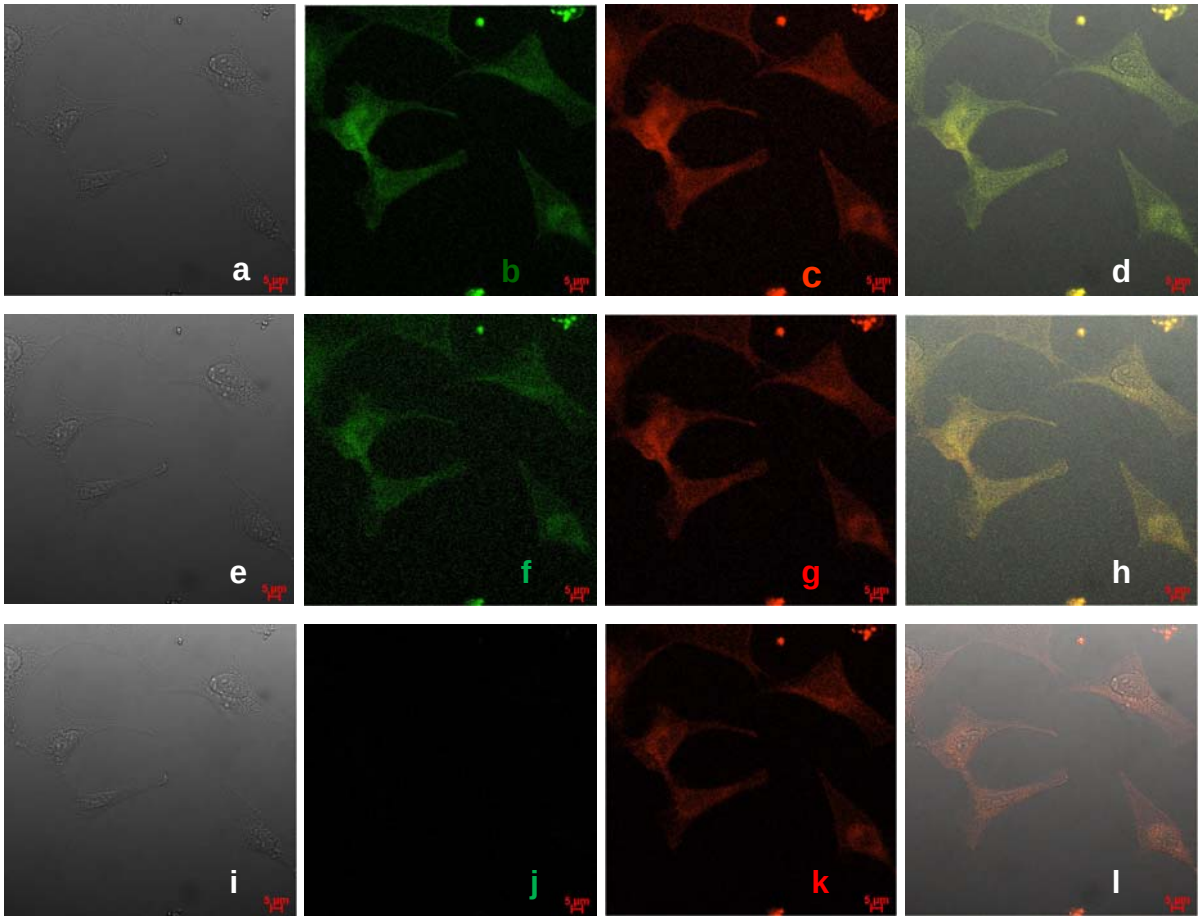

Figure 8.15. Single Photon Laser scanning confocal imaging of cancerous (HeLa) cells incubated at 37 ^{o}C for 20 min with T12@SWNT composite dispersion (in 5:99 % DMSO:EMEM) containing 7 µg/mL T12 anchored onto 18 µg/mL SWNT, **(a-d)** λ_{ex} = 405 nm, showing DIC (**a**), green channel (b), red channel (605-675 nm) (c) and DIC-green-red channel overlay (**d**). **(e-h)** λ_{ex} = 488 nm, showing DIC (**e**), green channel (515-530 nm) (**f**), red channel (605-675 nm) (**g**) and DIC-green-red channels overlay (**h**). **(i-l)** λ_{ex} = 543 nm, showing DIC (**i**), green channel (515-530 nm) (**j**), red channel (605-675 nm) (**k**) and DIC-green-red channels overlay (**l**), Scalebar 5 µm.

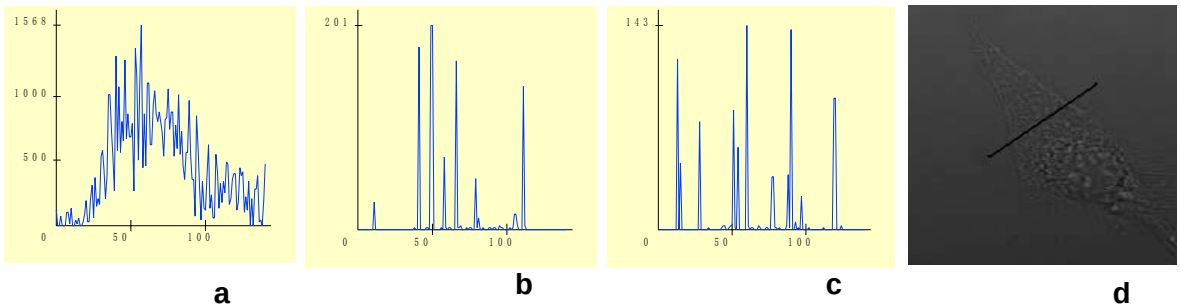

Figure 8.16. Fluorescent Intensity profile of HeLa cells **(d)** incubated at 37 ^{o}C for 20 min with with T12@SWNT composite dispersion (in 5:99% DMSO:EMEM) containing 7 µg/mL T12 anchored onto 18 µg/mL SWNT, **(a)** λ_{ex} = 405 nm, **(b)** λ_{ex} = 488 nm and **(c)** λ_{ex} = 543 nm

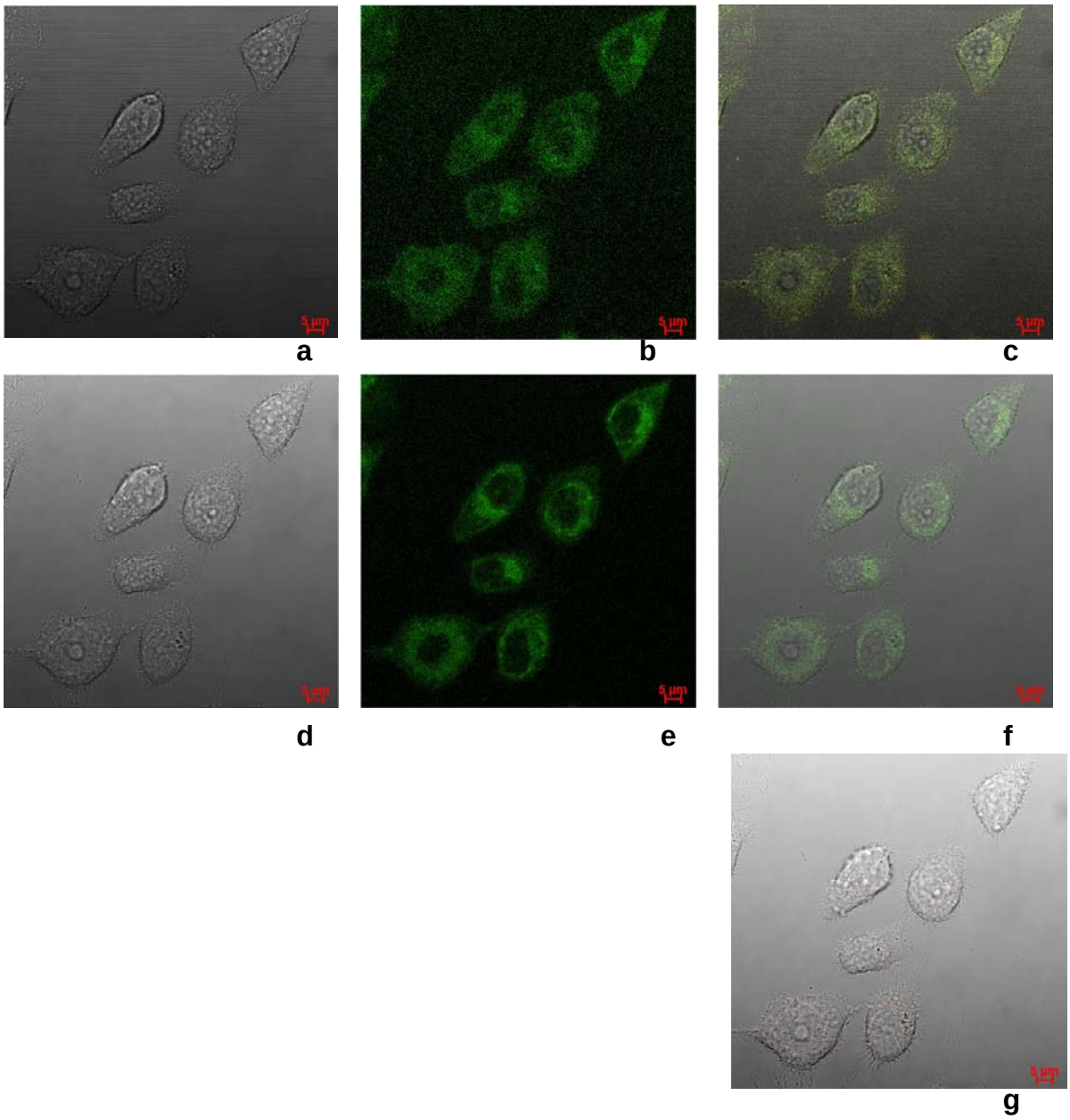

Figure 8.17. Single Photon Laser scanning confocal imaging of PC-3 cells incubated at 37 ^{o}C for 20 min with T12 (1.92 nM or 7 μg/mL in 5: 95% DMSO: EMEM**)**, **(a-c)** λ_{ex} = 405 nm, showing DIC (**a**), green channel (b) and DIC-green-red channel overlay (**c**). **(d-f)** λ_{ex} = 488 nm, showing DIC (**d**), green channel (515-530 nm) (**e**) and DIC-green-red channels overlay (**f**). **(g)** λ_{ex} = 543 nm, showing DIC-green-red channels overlay (**g**), Scalebar 5 μm.

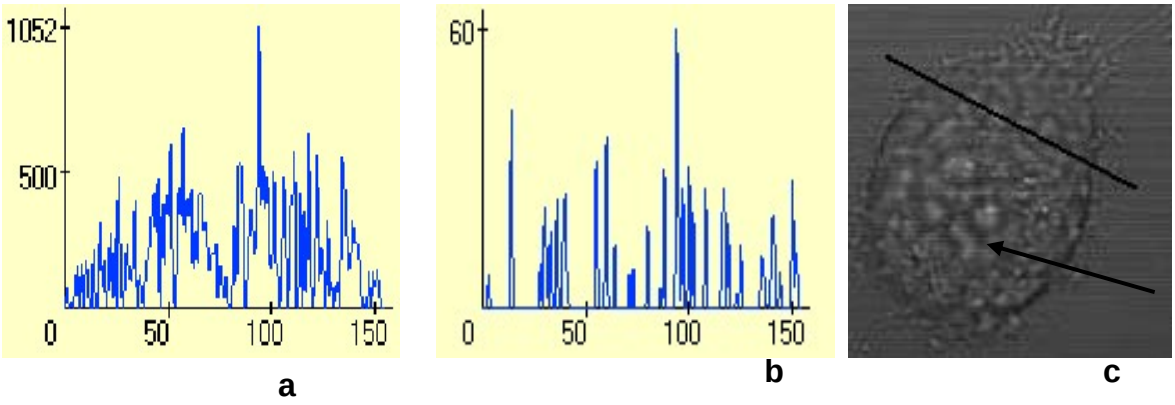

Figure 8.18. Fluorescent Intensity profile of PC-3 cells **(c)** incubated at 37 ^{o}C for 20 min with T12 (1.92 nM or 7 µg/mL in 5: 95% DMSO: EMEM**) (a)** λ_{ex} = 405 nm and **(b)** λ_{ex} = 488 nm.

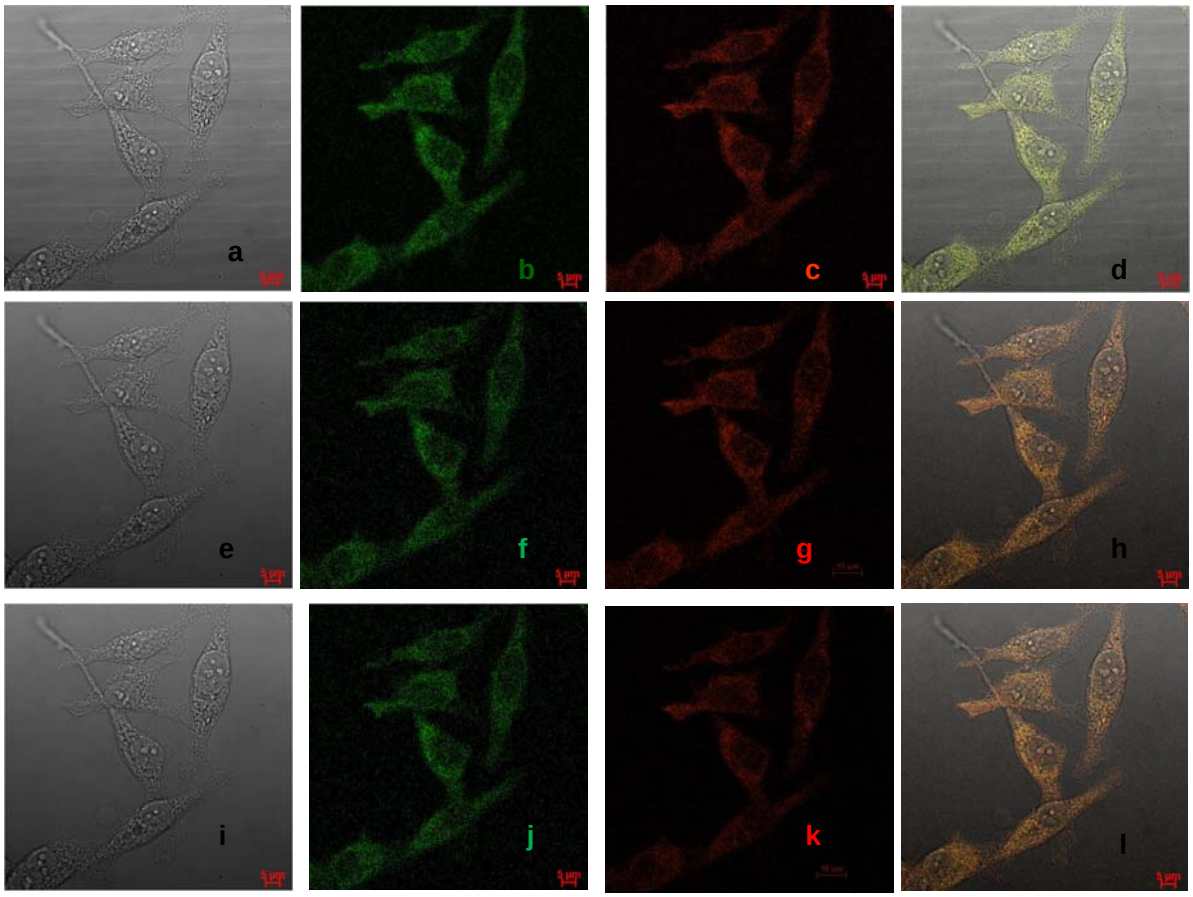

Figure 8.19. Single Photon Laser scanning confocal imaging of PC-3 cells incubated at 37 ^{o}C for 20 min with T12@SWNT composite dispersion (in 5:99% DMSO:EMEM) containing 7 µg/mL T12 anchored onto 18 µg/mL SWNT, **(a-d)** λ_{ex} = 405 nm, showing DIC (**a**), green channel (b), red channel (605-675 nm) (c) and DIC-green-red channel overlay (**d**). **(e-h)** λ_{ex} = 488 nm, showing DIC (**e**), green channel (515-530 nm) (**f**), red channel (605-675 nm) (**g**) and DIC-green-red channels overlay (**h**). **(i-l)** λ_{ex} = 543 nm, showing DIC (**i**), green channel (515-530 nm) (**j**), red channel (605-675 nm) (**k**) and DIC-green-red channels overlay (**l**), Scalebar 5 µm.

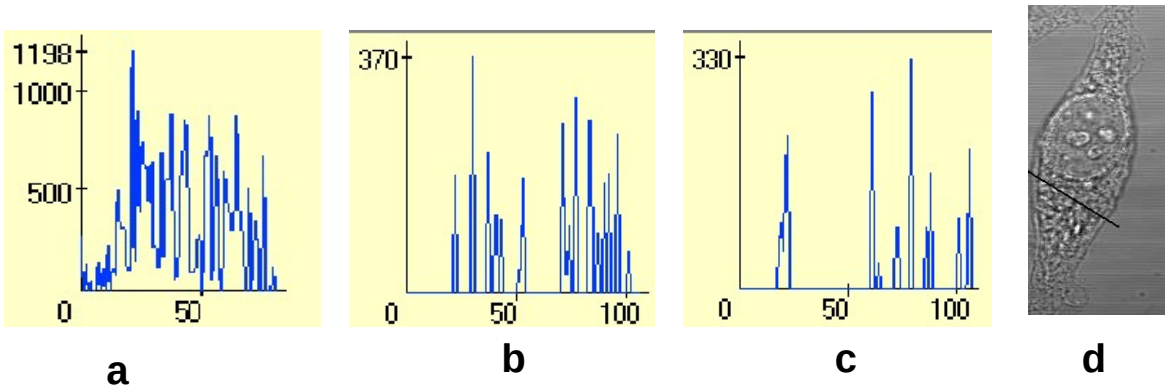

Figure 8.20. Fluorescent Intensity profile of PC-3 cells **(d)** incubated at 37 ^{o}C for 20 min with with T12@SWNT composite dispersion (in 5:99% DMSO:EMEM) containing 7 µg/mL T12 anchored onto 18 µg/mL SWNT, **(a)** λ_{ex} = 405 nm, **(b)** λ_{ex} = 488 nm and **(c)** λ_{ex} = 543 nm

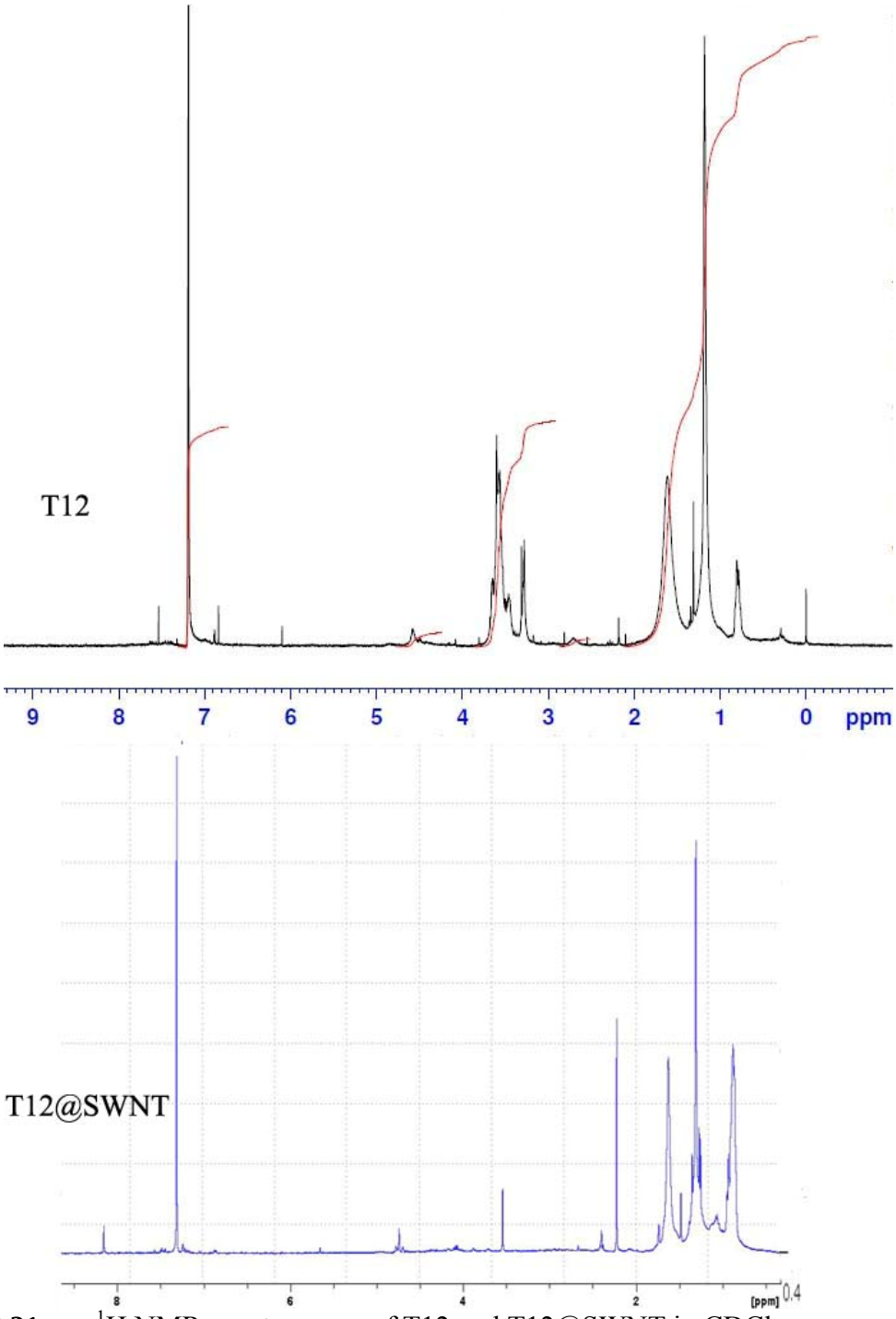

Figure 8.21. ^{1}H NMR spectroscopy of T12 and T12@SWNT in $CDCl_3$

8.3 Appendix for Chapter 5

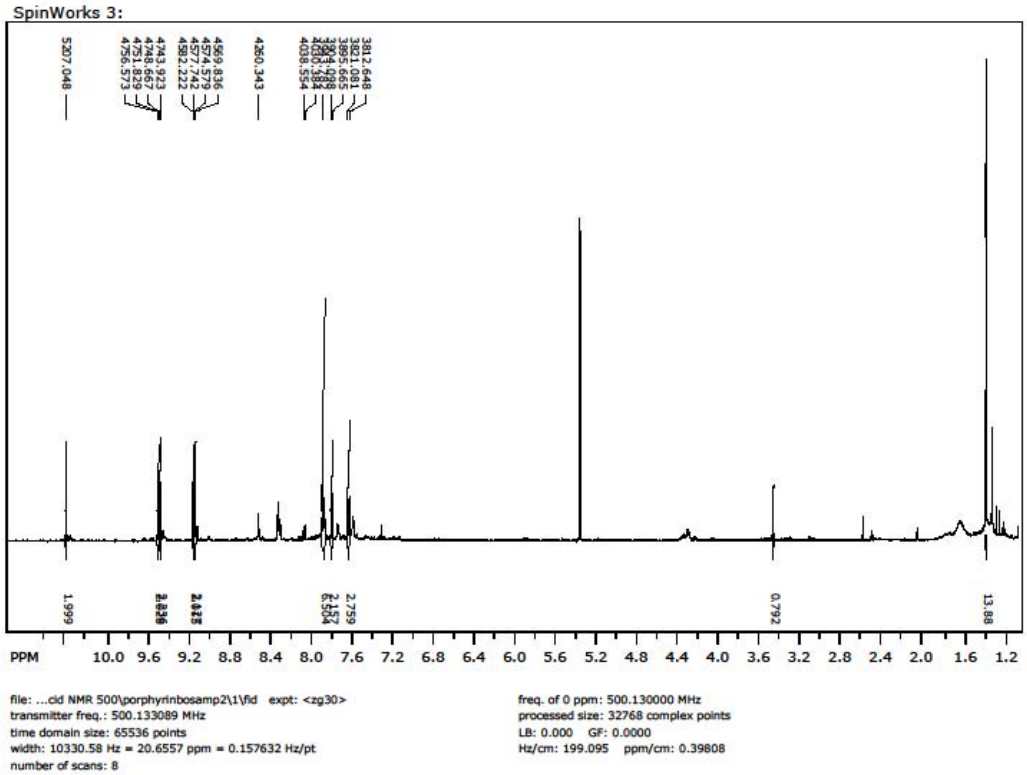

Figure 8.22. ^{1}H NMR spectroscopy of porphyrin-boronic acid in CD_3OD

8.4 References for chapter 8

1. W.L.F. Armarego, D.D. Perrin, *Purification of Laboratory Chemicals*, Fourth ed., Butterworth-Heinemann, Oxford, **1996**.
2. W. Jahn, *Journal of Microscopy* **1995**, *179*, 333.
3. A.G. Rinzler, J. Liu, H. Dai, P. Nikolaev, C.B. Huffman, F.J. Rodriguez-Macias, P.J. Boul, A.H. Lu, D. Heymann, D.T. Colbert, R.S. Lee, J.E. Fischer, A.M. Rao, P.C. Eklund, R.E. Smalley, *Appl. Phys. A: Mater. Sci. Process.* **1998**, *67*, 29.
4. J. Wang, M. Li, Z. Shi, N. Li, Z. Gu, *Anal. Chem.* **2002**, *74*, 1993.
5. D. Voet, J.G. Voet, *Biochemistry*, Second ed., John Wiley & Sons, Inc., New York, **1995**.